2015

Perovskite titanium nitride oxides and vanadium phosphates: synthesis and characterization

Spencer Hampton Porter
University of Wollongong

Perovskite Titanium Nitride Oxides and Vanadium Phosphates: Synthesis and Characterization

Spencer Hampton Porter, M.S.

Presented as part of the requirements for the conferral of the degree:

Doctor of Philosophy

Institute for Superconducting and Electronic Materials
Australian Institute for Innovative Materials
University of Wollongong

2015

Thesis Committee

Dr. Zhenguo Huang, Co-advisor

Dr. Shi Xue Dou, Co-advisor

Dr. Young-Il Kim, Yeungnam University

Dr. Graham King, Los Alamos National Laboratory

Abstract

The synthesis, crystal structures, ordering, magnetic, optical, water oxidizing, and electronic properties of RTiNO$_2$ (R = La – Nd) have been investigated. Neutron powder diffraction indicates that CeTiNO$_2$ and PrTiNO$_2$ crystallize with orthorhombic *Pnma* symmetry (Ce: a = 5.5580(5), b = 7.8369(7), and c = 5.5830(4) $\AA$; Pr: a = 5.5468(5), b = 7.8142(5), and c = 5.5514(5) $\AA$) as a result of $a^-b^+a^-$ tilting of the titanium octahedra. Careful examination of the NPD data, confirms the absence of long range anion order in both compounds, while apparent superstructure reflections seen in transmission electron microscopy provide evidence for short range anion order. Inverse susceptibility plots reveal that the RTiNO$_2$ (R = Ce, Pr, and Nd) compounds are paramagnetic with Weiss constants that vary from –28 to –42 K. Effective magnetic moments for RTiNO$_2$ (R = Ce, Pr, and Nd) are 2.43 μB, 3.63 μB, and 3.47 μB, respectively, in line with values expected for free rare-earth ions. Deviations from Curie-Weiss behavior at low temperatures are driven by magnetic anisotropy, spin-orbit coupling, and crystal field effects. CeTiNO$_2$, PrTiNO$_2$, and NdTiNO$_2$ have band gaps that fall in the range of 2.0 – 2.1 eV, very similar to LaTiNO$_2$, which enables them to absorb a significant fraction of the visible spectrum. Photocatalytic oxygen evolution studies under visible light irradiation in the presence of a sacrificial electron acceptor (Ag^+) show that the activity of NdTiNO$_2$ (16 μmol/g/h) is comparable to that of LaTiNO$_2$ (17 μmol/g/h), while PrTiNO$_2$ (11 μmol/g/h) and CeTiNO$_2$ (5 μmol/g/h) have activities that are only 65% and 30% that of LaTiNO$_2$. X-ray photoelectron spectroscopy measurements reveal the presence of partially occupied f-orbital states that lie in the band gap for CeTiNO$_2$, and near the valence band maximum for PrTiNO$_2$. As evidenced by time resolved infrared kinetic decay, these

localized f-orbital states act as electron-hole recombination centers that inhibit the photocatalytic activities of both compounds. $NdTiNO_2$, where the f-orbital energies fall below the valence band maximum, does not suffer from this effect. The synthesis, crystal structures, ordering, magnetic, and optical properties of $A_3V_4(PO_4)_6$ (A = Mg, Mn, Fe, Co, and Ni) have also been explored. Combined synchrotron and neutron powder diffraction indicates that $A_3V_4(PO_4)_6$ (A = Mg, Mn, Fe, Co, and Ni) crystallize with triclinic $P\bar{1}$ symmetry. Lattice parameters expand as expected with successive ionic radii increases, and cation disorder scales as A- and B-site ionic radii converge. DC magnetic susceptibility measurements suggest that all compounds with A = transition metal are antiferromagnetic and have complex magnetic structures. Effective magnetic moments for $A_3V_4(PO_4)_6$ (A = Mg, Mn, Fe, Co, and Ni) are 5.16 μB, 11.04 μB, 10.08 μB, 9.76 μB, and 7.96 μB, respectively, in line with calculated values for high spin transition metal ions. d-d transitions drive the colors of the compounds which are sequentially light lime green, brown, brown, green, and tan.

To my family, given and chosen

Acknowledgements

To my parents, for being excellent role models, parents, and friends exactly when I need them. They have imbued in me all of the Porter Principles: persistence, patience, precaution, and planning. Life would be much more arduous without these principles. To Dr. Zhenguo Huang for his encouragement, financial support, and hospitality during my time in his lab. To Dr. Patrick Woodward for his willingness to undertake an international collaboration, for his keen editing, advice, and hospitality. To Dr. ShiXue Dou, for his support, leadership, and encouragement. Thank you all. I am grateful for everything each of you have done for me. To Dr. Julie Stefanski for her 40-love, dedication, and willingness to listen as well as laugh. Here is to a lifetime of good live music, adventure, and great home-cooked food! To the University of Wollongong for awarding me a University Postgraduate award as well as an International Postgraduate Tuition Award. I am grateful for the support during my time at UOW as a Higher Degree Researcher. Young researchers are the catalyst for innovative outcomes. To Dr. Maxim Avdeev, Dr. Zhenxiang Cheng, and Dr. Zhixin Chen for hard work and countless hours with instrumentation during our collaboration. To Dr. Samantha Brown-Xu for her willingness to take TRIR data even as her imminent departure for Northwestern lingered. To Tianyang Li and Dr. Joshua Goldberger for seeing in me the potential to aid in your endeavours. To my dear friends, who despite my repeated efforts to thwart their affection and embarrass them into submission have provided me with a true family-by-choice. I am eternally grateful and forever indebted. To my previous advisers, Dr. Douglas Keszler (Oregon State University) and Dr. Shane Snyder (SNWA/University of Arizona), for encouraging and supporting me in my endeavours then and now. To Dr. Huang's future students, may

good fortune reign eternal. Thank you, Australian Government, for deciding science is important enough to subsidize tuition in science as well as engineering and for funding grants for research (i.e. Dr. Huang's DECRA). Lastly, thank you to all the people along the way who have taken their time to shape and mold me, if even in the most subtle way. I am grateful for your efforts and hope this work will show that it was not in vain.

VITA

2001-2005
B.S. ACS Adv. Chemistry
Oregon State University
Adviser: Dr. Douglas Keszler
Research (3 yrs): Spin coated, thin film TCOs and VUV phosphors for PDPs
GPA: 3.10

2008-2012
M.S. Chemistry
Ohio State University
Adviser: Dr. Patrick Woodward
Thesis: *Perovskite and Pyrochlore Tantalum Nitride Oxides: Synthesis and Characterization*
GPA: 3.42

2012-2015
Higher Degree Researcher
Univ. of Wollongong, AUS

Publications

- **Porter, Spencer H.**; Xiong, Jie; Huang, Zhenguo; Merz, David; Shi Xue Dou; Woodward, Patrick M.; The Structural, Magnetic, And Optical Properties Of $A_3V_4(PO_4)_6$ (A = Mg, Mn, Fe, and Ni); *In Preparation; intended submission to Inorganic Chemistry*, **2015**, [Impact Factor (IF) = 4.8]
- **Porter, Spencer H.**; Huang, Zhenguo; Shi Xue Dou; Woodward, Patrick M.; Electronic structure and photocatalytic activity of RTiNO$_2$ (R = Ce, Pr and Nd) perovskite nitride oxides; *Chem. Mater.*, **2015**, 27 (7), pp 2414-2420 [Impact Factor (IF) = 8.5]

- **Porter, Spencer H.**; Zhenxiang Cheng; Zhixin Chen; Avdeev, Maxim; Woodward, Patrick M.; Huang, Zhenguo; Shi Xue Dou; Structural and Magnetic Properties of $R\mathrm{TiNO_2}$ (R = Ce, Pr, Nd) perovskite nitride oxides; *J. Solid State Chem.*, **2015**, 226, 279 [IF = 2.3]

- **Porter, Spencer H.**; Huang, Zhenguo; Woodward, Patrick M.; Study of Anion Order/Disorder in $R\mathrm{TaN_2O}$ (R = La, Ce, Pr) Perovskite Nitride Oxides; *Crystal Growth and Design*, **2014**, 14(1), 117-125. [IF = 4.7]

- Balaz, Snjezana; **Porter, Spencer H.**; Woodward, Patrick M.; Brillson, Leonard J.; Electronic Structure of Tantalum Oxynitride Perovskite Photocatalysts; *Chem. Mater.*, **2013**, 25(16), 3337-43. [IF = 8.5]

- Huang, Zhenguo; Lingam, Hima K.; Chen, Xuenian; Du, Aijun; **Porter, Spencer**; Woodard, Patrick M.; Shore, Sheldon G.; Zhao, Ji-Cheng; Synthesis, structural analysis, and thermal decomposition studies of $[(\mathrm{NH_3})_2\mathrm{BH_2}]\mathrm{B_3H_8}$; *RSC Advances*, **2013**, 3(20), 7460-5. [IF = 2.6]

- Li, Tianyang; Liu, Yi-Hsin; **Porter, Spencer**; Goldberger, Joshua E.; Dimensionally Reduced One-Dimensional Chains of $\mathrm{TiSe_2}$; *Chem. Mater.*, **2013**, 25(9), 1477-9. [IF = 8.2]

- Huang, Zhenguo; Eagles, Mitch; **Porter, Spencer**; Sorte, Eric G.; Billet, Beau; Corey, Robert L.; Conradi, Mark S.; Zhao, Ji-Cheng; Thermolysis and solid state NMR studies of $\mathrm{NaB_3H_8}$, $\mathrm{NH_3B_3H_7}$, and $\mathrm{NH_4B_3H_8}$; *Dalton Transactions*, **2013**, 42(3), 701-8. [IF = 3.8]

- Liu, Yi-Hsin; **Porter, Spencer**; Goldberger, Joshua E.; Dimensional Reduction of a Layered Metal Chalcogenide into a 1D Near-IR Direct Band Gap Semiconductor; *J. Am. Chem. Soc.*, **2012**, 134(11), 5044-7. [IF = 10.7]

- Day, Bradley E.; Bley, Nicholas D.; Jones, Heather R.; McCullough, Ryan M.; Eng, Hank W.; **Porter, Spencer**; Woodward, Patrick M.; Barnes, Paris W.; Structures of ordered tungsten- or molybdenum-containing quaternary perovskite oxides; *J. Sol. St. Chem.*, **2012**, 185, 107-116. [IF = 2.3]

Contents

List of Figures

List of Tables

1

Introduction

Full understanding of this subject material will be addressed by compartmentalizing this thesis into smaller, bite-size pieces. There are two primary research thrusts: perovskite nitride oxides of the form $R\mathrm{TiNO_2}$ where R = La – Nd and quaternary vanadium (III) phosphates in the form $A_3\mathrm{V_4(PO_4)_6}$ where A = Mg, Mn, Fe, Co, and Ni. First, the perovskite nitride oxides are presented. The conditions required to create a perovskite are followed by the historical context for them. The concepts familiar to the study of perovskites are introduced, such as tolerance, tilting, distortion, and pseudosymmetry. This segues into the design and birth of the nitride oxide perovskite class via aliovalent substitution on the oxide lattice. Anion ordering of this mixed anion system is addressed and so are the implications beyond synthesis (applications). Second, the quaternary vanadium (III) phosphates are laid out. The historical uses and applications of V-P-O containing compounds are bracketed by discussions about pigments, batteries, and magnetism. The justification for exploration within this system is presented. Lastly, the above mentioned compounds are prepared for the first time and are (almost) completely uncharacterized. A substantial number of instrumental techniques are employed and the generated data must be understood to identify the physical properties of these compounds.

1.1 Perovskite Nitride Oxides

1.1.1 History and Background

1.1.1.1 What is a Perovskite?

In a perfect perovskite example, ABX_3, the A-site is a cube octahedron (twelve coordinate), the B-site is an octahedron (six coordinate) and the X-site is (distorted) six coordinate. Because of this convention, the cation that is larger in size is typically designated as the A-site cation. The octahedra are corner sharing and extend in every direction throughout three dimensional (3D) space. The A-site cations rest in the center of the cavities that remain within this structural motif. The structure is crystallographically cubic and is commonly depicted in two ways: with the A-site cations at the corners of the cube and the B-site octahedron centered in the middle or vice versa (Figure 1.1).

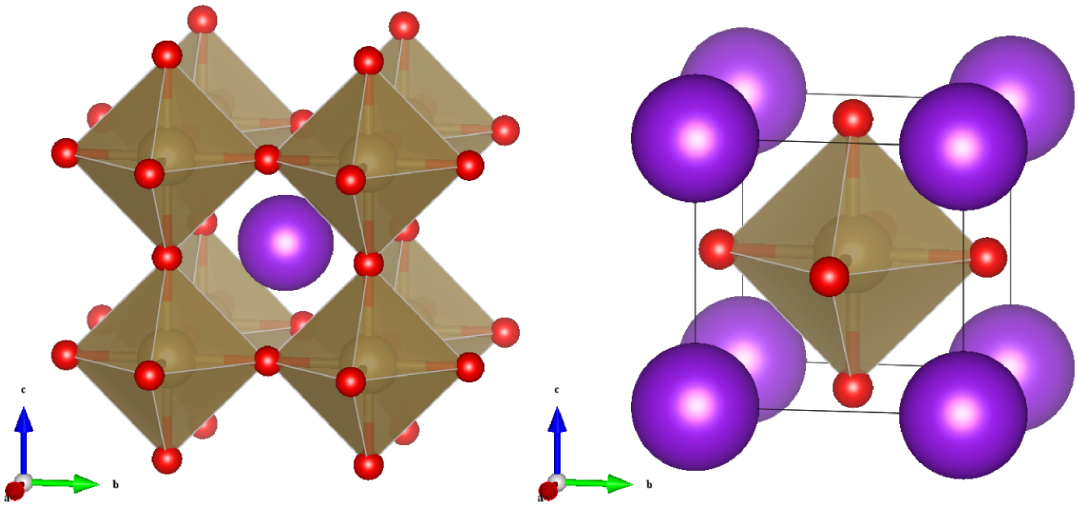

Figure 1.1: Origin choices for a simple ABX_3 perovskite - A cations (purple), B cations (tan), and X anions (red). B-site at (0,0,0)(left) and A-site at (0,0,0)(right).

1.1.1.2 Historical Context

$CaTiO_3$ as a mineral was originally named after L. Perovski, for which the entire class has been named. The perovskite class of compounds is abundant, and the structure type has been made to include elements that span the entire periodic table. The

structural requirements are complex enough to allow for diversity in creation but simple enough to be thermodynamically stable. This attribute results in reported properties in this class of compounds that are just as varied as the elements contained within. Dielectrics, ferroelectrics, magnetism, superconductivity, metals, half-metals, multiferroics, semiconductors, and insulators are just some of the examples that have all been demonstrated using the perovskite structure as a template. There are several exhaustive and encyclopedic reviews on the compounds that lie within the perovskite structural class. [(1, 2, 3, 4)] Further pursuit of this general topic is left to the reader.

1.1.1.3 Goldschmidt's Tolerance Factor

The first description of the tolerance factor, τ, for perovskite was given by Victor Goldschmidt in 1926. [(5)] It is an indicator for the stability and distortion of a crystal structure. Comparing the ionic radii of the elements within the compound, (1.1), this metric can be helpful in determining the possible existence of a perovskite phase and also in determining if the compounds may have distortions in the form of octahedral tilting.

$$\tau = (r_a + r_x)/(\sqrt{2} \times (r_b + r_x)) \tag{1.1}$$

where r_a, r_b, and r_x are the ionic radii of a 12-coordinate A cation, 6-coordinate B cation, and a 6-coordinate X anion, respectively. Weighted averages are used accordingly. Values of τ indicate how well the A-cation fits into the BX_6 network. A value of one is ideal, less than one means the (larger) A-cation is too small, and greater than one means that the A-cation is too big. The typical stability regime to stabilize perovkite-related structures, ABX_3, ranges from about 0.71 – 1.1. When τ is less than 0.71 the A- and B-site cations have sizes that are too similar. Structures like ilmenite are prone to form. As τ increases form there, perovskite-related rhombohedral structures begin to dominate (0.71 – 0.85). When τ is > 0.85, enough cation size discrepancy exists to stabilize the orthrhombic-related perovskite structure type, although it is usually distorted. [(6)] From 0.85 – 0.97 the size contrast between the A-site and the B-site cations grows but still allows fluxionality in tilting of the corner connected octahedral network. When τ is 0.97 – 1.03, the fit results in a cubic perovskite. Notably, when τ grows to 1.03 – 1.1, the A-site cation becomes too big to fit into the interstitial cavities of the corner-connected octahedral network and tetragonal (*e.g.* $BaTiO_3$) or hexagonal

cells begin to dominate. When τ is ideal, the resulting bond angle (B-X-B) between octahedra is 180 degrees. Deviation from this results in the distortion of the corner-connected octahedral manifold. As τ decreases in value from ideal, the octahedra begin to synergistically tilt to optimize the bond distances between all coordinating ligands at both the A- and B-site. The cage of octahedra effectively clamps down upon the A-site cation.

1.1.1.4 Type of Tilting and Pseudosymmetry

When the octahedra tilt to better accommodate the size of the A-site cation these tilts can be ordered systematically down an axis, as in- or out-of-phase. Sequential octahedra down a given axis can be rotated in the same direction (in-phase) or in the opposite direction (out-of-phase) (Figure 1.2). These tilting designations can be different for each axis (but not within an axis), as can the magnitude of the tilting. A convention for indicating these types of distortions has been created by Glazer: $p^x q^y r^z$. The positions of p,q, and r are used to indicate the magnitude of the tilting down the a, b, and c-axes. If the tilts down two axes are identical the letter assigned to the two axes would be the same. In the superscripts, the position x, y, and z are used to signal the tilting type down that axis where "0" is for no tilts, "+" is for in-phase, and "–" is for out-of-phase. For example, perovskites with the space group *Imma* correspond to $b^- a^0 b^-$. There are two out-of-phase tilts of equal magnitude that can be viewed down the a- and c-axes. The various different combinations of the directions and magnitudes of these tilts have already been initially compiled, [(7)] studied thoroughly, [(8, 9, 10)] and adapted for various applications such as ferroelectric distortions [(11)] or anion ordering. [(12)]

The compounds in this work (described below) require an orthorhombic designation, *Pnma*, which is also the most prevalent perovskite lattice type, to represent the unit cell. There are many ways to create a orthorhombic unit cell, but in this case, it can be related to the initial cubic primitive cell, where $a_p \sim 4.0$ $\mathring{A}$, by an expansion to: $\sqrt{2}a_p \times 2a_p \times \sqrt{2}a_p$. The corners of the connected network of octahedra are oriented along the a-c plane face diagonals in this layout (Figure 1.3). This space group corresponds to a tilting of $b^- a^+ b^-$

Superstructures can arise from clamping of the cage of corner-sharing B-site octahedra, which results from the need for the structure to accommodate the varied size of

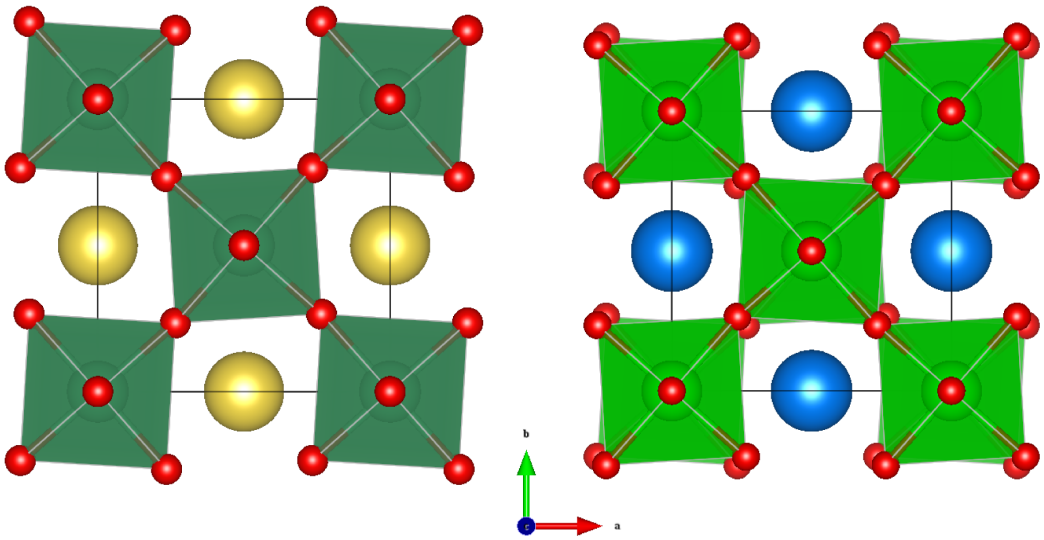

Figure 1.2: Tilting in perovskites - In-phase tilting in $a^0a^0c^+$ $P4/mbm$ (left) and out-of-phase tilting in $a^0a^0c^-$ $I4/mcm$ (right).

the A-site cation. For a perovskite where the size of the A-site cation adequately fills the cage, there is little buckling of the cages, so the B-X-B angles are 180 degrees and the space group $Pm\bar{3}m$ is assigned. As the cation size decreases in the cage, it bends and distorts to optimize bond distances, which lowers the symmetry of the space group assignment. This changes the space group assignment, which, in turn, can result in the growth of very subtle peaks in X-ray diffraction patterns (XRD). These peaks represent new reflection conditions associated with symmetry changes arising from the tilting of the octahedra which also requires re-specification of the lattice parameters. The new lattice parameters are often multiples of the initial unit cell, $\#a_p$, or a mulitple of the face diagonal, $\#\sqrt{2}a_p$, where $\#$ is an integer. Auto indexing programs for the structure solution or Rietveld refinement of X-ray diffraction powder data on perovskites historically perform quite poorly. To combat this, a methodology for assignment of a space group has been laid out in these systems for oxide single and double perovskites. [(13)]

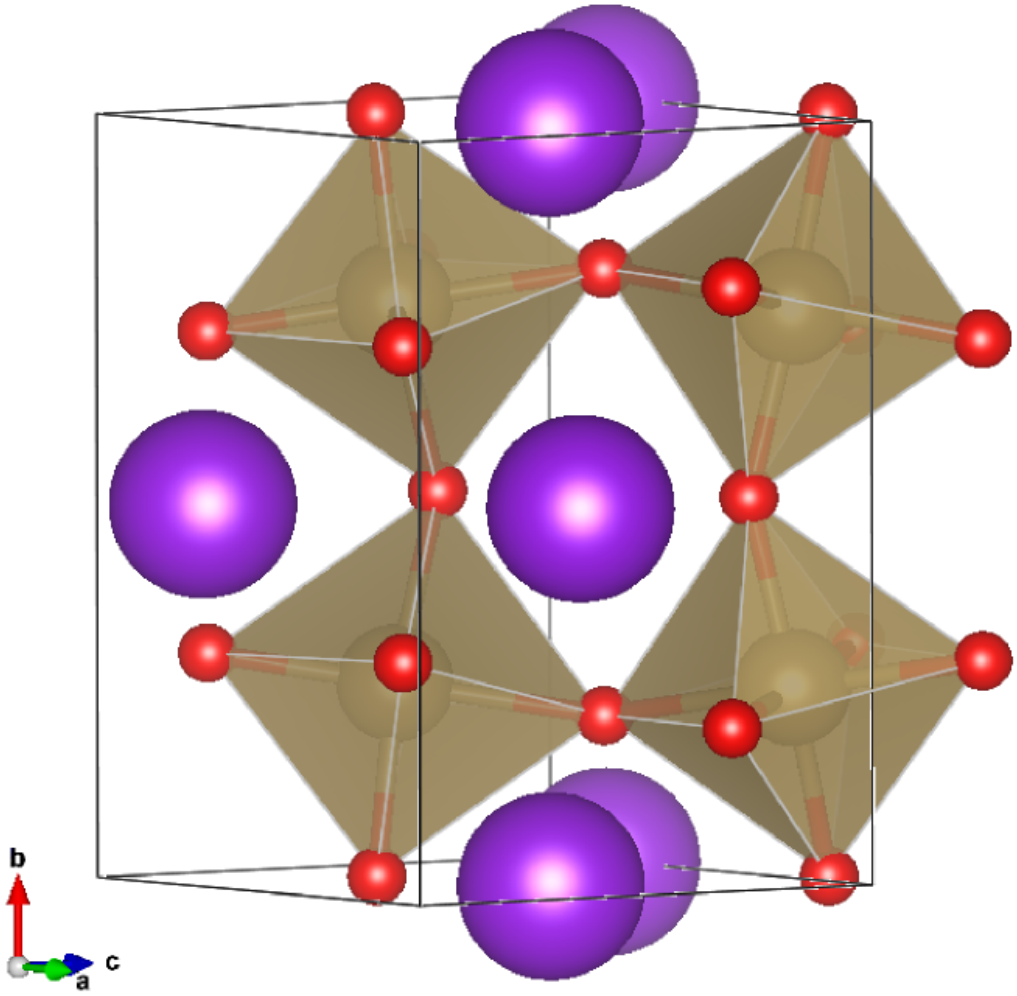

Figure 1.3: Origin choices for a *Pnma* ABX_3 perovskite - A cations (purple), B cations (tan), and X anions (red). B-site at $\sim$ ($\frac{1}{2}$,0,0).

1.1.1.5 Baur's Distortion Index

Up until the 1940s, the bonding environment about a polyhedron was thought to be rigid and fixed for a given AX_n example. [(14)] Over time, this view changed as empirical evidence began to pile up. Bond data for a catalogue of geometric atomic polyhedra were compiled and analysed for parity by W. H. Baur, and the outpouring of this work is his distortion index, *D*. This is represented by the compilation of the variability of the bond lengths about a given central atom of a polyhedron.

$$D = \frac{1}{n} \sum_{i=1}^{n} \frac{\mid l_i - l_{avg} \mid}{l_{avg}} \tag{1.2}$$

where l_i is distance from the central atom to the i^{th} coordinating atom and l_{avg} is the average bond length. A perfect polyhedron has a distortion index of 0. Deviation from this initial value indicates increasing levels of irregularity. This information can help to give information on the relative stability of the environment about a given site or how well the bonding is optimized for a given coordination. Polyhedra that are severely over-bonded in one part of the coordination environment and also under-bonded in another portion are also indicated by this index. This technique can be applied to any type of polyhedron. In the solid state, the most commonly occurring shapes are the octahedon and the tetrahedron, and therefore they will be the focus of our studies here, to be discussed later (1.2.1.1). Perovskites varying from perfect to heavily distorted have distortion indexes that vary from 0 – 5%. [(15)]

1.1.2 Aliovalent Substitution: From Oxides to Nitride Oxides

Chemical control of electronic band structure has been demonstrated extensively through cation manipulation. The effects of this have implications in the physical properties of materials, enabling contributions including, but not limited to, the fields of phosphors,(16) giant magnetoresistance,(17) p– and n-type semiconductors,(18, 19, 20) superconductivity,(21) dielectrics,(22, 23) and photocatalysts.(24) Across the entire spectrum of material applications listed above, perovskite is a structure type that can be found in all of them. Perovskites, though varied across the entire periodic table for the cations, are mostly oxide-based when anions are considered. Along a similar vein to cation doping, is the notion of anion doping: the replacement of oxygen in the lattice with another charge-negative ion, nitrogen for example. Doing so introduces a class of

compounds called nitride oxides (also called oxynitrides or oxide nitrides). Relative to simple perovskites, ABX_3, there are two whole number substitutions of nitrogen for oxygen that can be made: a single replacement, -NO_2, and a double, -N_2O. Greater complexity is added when cations of variable oxidation state are used. Inquiry into anion doping, specifically via nitrogen-based substitution occurred as early as 1970.[(25)] These early examples of oxynitrides were comprised mainly of silicon.[(26)] Compounds synthesized later, in 1986, were the first examples of perovskite oxynitrides, referring to the structure and the anions present.[(27)] The basis for this research was to start with $NaTaO_3$, a known perovskite, and implement aliovalent replacement simultaneously on both the cation and anion sites. This same concept can be applied to the $SrTiO_3$ starting material, and the substitution process is represented pictorially in Figure 1.4, which has titanium on the B-site, strontium on the A-site and oxygen (and later nitrogen) on the X-site. By replacing either the A or B cation with an atom that has a more positive oxidation state, nitrogen can be added to charge compensate. To maintain the structure, similar chemistry and ion size should be selected. Further consideration should be made in selecting a cation that is stable under reducing conditions, because nitrogen is added by decomposition of ammonia at elevated temperatures. The alkaline earth (AE) elements are a good starting place, with calcium, strontium, and barium being front runners after size considerations are made. Rare earths (R) also are stable versus reducing atmospheres. Cations with noble gas configurations or filled valence shells should be paired with each other to limit reduction to lower valencies. Reillustrated, $AE^{+2} \rightarrow R^{+3}$ and $O^{-2} \rightarrow N^{-3}$. The result is RTiNO_2. Mental exercises and ideation such as this are how new classes of materials are expanded and, in this case, how new perovskite nitride oxides are added to the library of existing compounds! Nonetheless a list of the known nitride oxide perovskites reported in the literature [(28, 29, 30, 31)] is valuable for reference (Table 2.1).

1.1.3 Anion Order

Structural characterization of these compounds provides information that will allow a deeper understanding of the material properties of this class. For instance, anion stoichiometry can influence the local symmetry of the metal octahedra, affecting the polarity and dielectric permittivity. There are three length scales that anion ordering can occur at: short, medium, and long. Going from oxides to nitrides, a full spectum

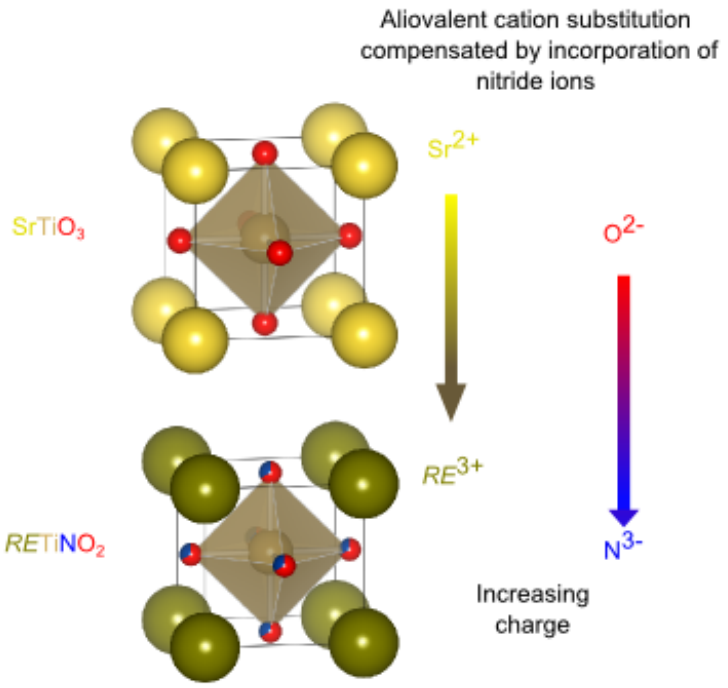

Figure 1.4: Aliovalent substitution of nitrogen on the oxide lattice of $SrTiO_3$(top) - nitride oxide formed (bottom).

		A-site										
		Ca	Sr	Ba	La	Ce	Pr	Nd	Sm	Eu	Gd	Dy
B-site	Ti				✓	TW	TW	✓				
	Zr				✓	✓	✓	✓	✓			
	V				NS			✓				
	Nb	✓	✓	✓	✓		NS	NS		✓	✓	✓
	Ta	✓	✓	✓	✓	✓	✓		✓	✓	✓	
	Mo	NS	NS		NS							
	W		✓		NS			NS		NS		

Table 1.1: Library of existing simple perovskite nitride oxides, $AB(O,N)_3$, that have been synthesized and structurally characterized (check mark) compounds, as well as ones that are non-stoichiometric (NS), are presented in this work (TW).

of aliovalent substitutions can occur at the octahedron to impart short range order (Figure 1.5). Only half of the substitutions need to be shown. The other half is just mirrored, i.e. the MO_4N_2 octahedron has identical anion ordering classifications as the one with MN_4O_2 ordering. For these aforementioned octahedral configurations, there are three possible anion configurations: cis, trans, and disordered. In an attempt to find out which of these orderings are most favorable, geometry optimization calculations have shown the cis conformation to be the most thermodynamically stable product for $BaTaO_2N$.[(32)]

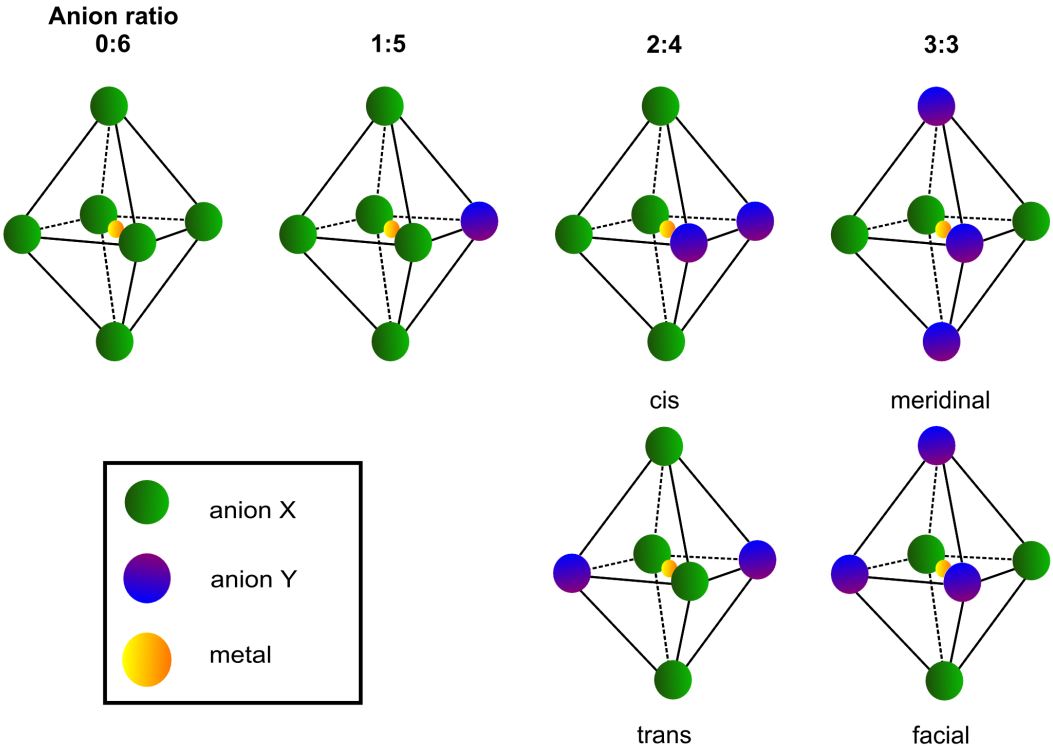

Figure 1.5: Mixed anion configurations about an octahedron - Increasing substitution going from left to right.

The implications of local anion order can have an effect on the assigned space group of a system if it extends coherently enough to long ranges. Long-range anion order cannot be represented in the simple cubic perovskite unit cell ($Pm\bar{3}m$) due to symmetry restrictions. This effectively lowers the crystallographic symmetry of the cell. A supercell with this disorder incorporated generates results that better reflect

those given for the optical properties of bulk powders.[(33)] The order/disorder of the anions can therefore determine the symmetry and space group assignment of a given compound. If a nitride oxide system is completely disordered in terms of the long range (short range order still possible), then the space group assignment is dominated only by tilting arguments (ordering arguments are averaged out). The compounds presented in this work are believed to be *Pnma* tilted, but what would happen to the space group symmetry if the anions were locally and long-range ordered? Luckily, this has already been worked out for *Pnma* (Figure 1.6) and other common tilt systems. [(12)] Aside from the cis, trans, and disordered arrangements of the anions, there is another consideration for the ordering: relativity to tilting. To best describe the arrangement in the unit cell then, the ordering is benchmarked versus the tilting axes, and if necessary a coordinate axis.

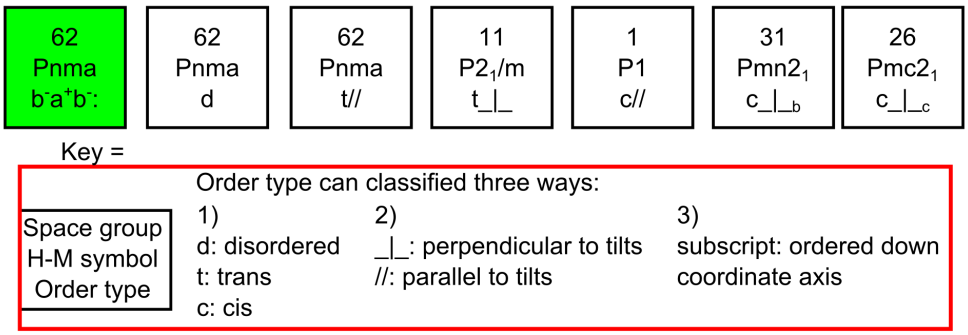

Figure 1.6: Classification of the space group imposed by -X_2Y anion ordering types in *Pnma* perovskites - 5 possible space groups.

The intermediate case, medium range order, was first reported by Fuertes *et al.* [(34)] and is best described as two dimensional (2D)-cis partial order. It is driven by the corner connectivity of the locally ordered cis-coordinated octahedron. The cis-arrangement of anions on an octahedron influences the anion orientation of the octahedra coordinated/connected to it and is best visualized by a 2D depiction (Figure 1.7) of the perovskite. If a line is imagined between the cis coordinated anions in the 2D example, the orientation of this line at the adjacent octahedron is either a continuation of the line or an orthogonal change in direction. The short-range order dictates the medium range order interactions, which, in turn, are similar to a random walk and have been likened to quasi-order. This 2D order is not readily observed on the long

range, but anion occupancies from neutron powder diffraction (NPD) can give some indication of its occurrence.

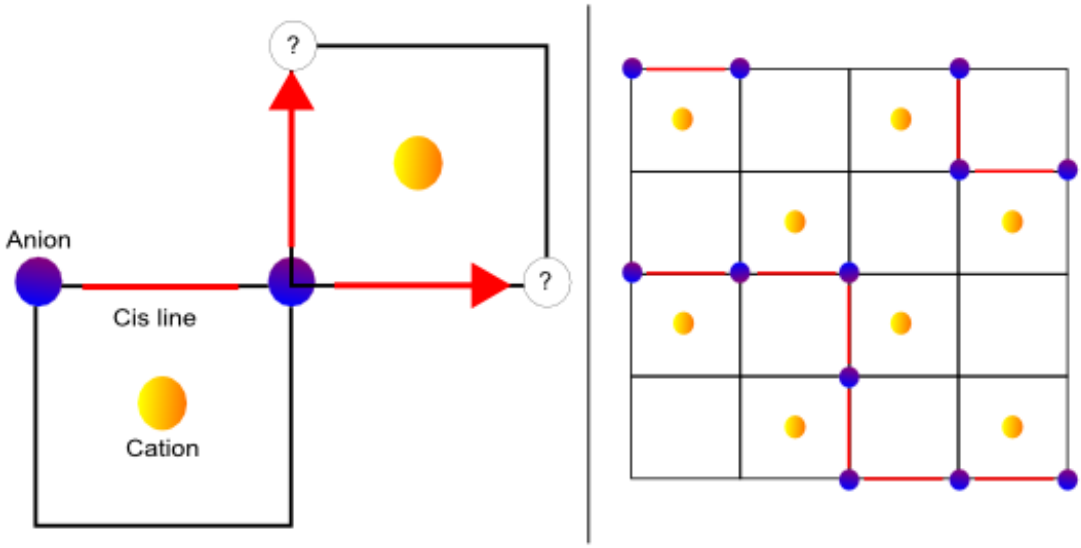

Figure 1.7: 2D cis order on the equatorial perovskite anion square net plane - Adjacent octahedra have cis-related connections (left), which impart a random walk-like medium range order in the crystal structure (right). The cis-driven medium range ordering mechanism can also extend out of the 2D plane to include the axial anions but they are not included for clarity.

Perovskite oxide nitrides from the literature have been reported as being ordered, (35, 36) partially ordered, (32, 34, 37) and completely disordered models. (36, 38) Chronologically, the nitride oxides were initially reported as being fully ordered by NPD studies. This caused a stir in the scientific community, because polar compounds have applications as ferroelectrics. Subsequent studies, however, have rebutted that statement. Side note: Fully ordered nitride oxide analogues do exist for the perovskite-related Ruddlesden-Popper phases, which is driven by the extra AO_2 layer. [(39)]. Further investigation of anion ordering in the perovskite class has concluded that full ordering is unlikely, with partial order or disorder thermodynamically favorable. To probe the extent and length scales of ordering, a variety of techniques are used, typically transmission electron microscopy/electron diffraction (TEM/ED) and neutron powder diffraction (NPD). Recently, it was determined that $PrTaN_2O$ and $CeTaN_2O$ show a slight preference for ordering, based on NPD work. [(40)] These compounds are

solved in the *Pnma* space group, which has two anion related Wyckoff positions. The dominant anion species (N, in this case) has a preference for the site of higher multiplicity. In the $SrTaO_2N$ case, oxygen favours the 8d site by 75% to 25% nitrogen, while on the 4c site the ratio is 50:50 (preserving stoichiometry). Conversely, for the $RTaN_2O$ compounds where nitrogen is the dominant anion species, the nitrogen is disproportionally represented on the 8d site, with the 4c site balanced. These perturbations are not far from a fully disordered system where each site would be $\frac{2}{3} : \frac{1}{3}$. Because x-rays are insensitive to the comparison between oxide and nitride anions, NPD is employed to resolve between the two. In the case of the $RTiNO_2$ (R = Ce, Pr) class studied here, it will be necessary to have the compounds examined by NPD and TEM. Once they are ready, these compounds will undergo that same treatment and allow for a determination of ordering.

1.1.4 Applications and Photocatalysis

Analytical methods for this class of compounds, while still straightforward, are not without their challenges. In fact, difficult property diagnosis is one of the things preventing rapid development in the nitride oxide field. For example, the most common synthetic technique employed for the creation of nitride oxides is a solid state method. This approach suffers from poor sintering, [(41)] charging at grain boundaries,[(42)] and single crystal growth difficulties. [(43)] These problems must be overcome to enable further applications. Until then, bulk characterization will foster an increased understanding of the electronic band structure and material properties of the compounds studied and may provide an impetus to achieve integrated devices and advanced materials. Property characterization for these structures is an ongoing process, with reports including, but not limited to, superconductivity,[(44)] dielectrics,(45, 46) and luminescence.(47) Perhaps the most famous commercial nod towards oxynitrides, and also one that attempts to control the non-constant nitrogen/oxygen stoichiometry by cation doping, has been by Jansen *et al.* [(48)] Non-toxic, chemically inert pigments are made from solid solution $(Ca,La)Ta(O,N)_3$, yielding brilliantly coloured compounds from red to yellow and every shade in between.

Photocatalysis

The first peak oil scare in the 1970s prompted a massive research effort to produce

new renewable and alternative energy generation schemes, water splitting being one of them. To be commercially competitive this process requires proper conduction and valence band placement, efficient charge separation, photostability, high surface area, and low cost. The photocatalytic champion of that first generation of research into photocatalytic water splitting was modified $NaTaO_3$. [(49, 50)] Because this compound was a wide-band-gap semiconductor it did not efficiently utilize the sun's energy (only in the ultraviolet (UV) region, band gap ($E_g >$) 3.0 eV). Additional innovation was necessary. The current generation of water splitting compounds have been centered around exploration and utilization of nitride oxides. A thorough walkthrough of the fundamentals of water splitting and photocatalytic design in nitride oxides is provided in Appendix 4.5. These compounds satisfy many of the above criteria required for a commercially competitive process. They have reduced band gaps ($E_g < 3.0$ eV) which utilize more of the solar spectrum, due to the addition of the less electronegative nitride anion at the valence band maximum. Nitride oxide compounds also have stability in a variety of media, including harsh ones (concentrated acid and alkaline solutions). The compounds used to drive photocatalysis, although not especially common, are not exceedingly rare and, if costly, can be used sparingly. Furthermore the preparation techniques are not overly complicated or drawn out, which should minimize manufacturing costs. The remaining design goals can be engineered: band positions can be controlled by proper selection of elements in the system, charge separation can be controlled by addition of co-catalyts, and surface area can be controlled by preparation technique. $AE\mathrm{TaO_2N}$ has been demonstrated to have the ability to evolve hydrogen, but these nitride oxide compounds do not evolve oxygen. [(51)] To combat this, a process similar to photosynthesis, called a Z-scheme, where the water reduction and oxidation half reactions are achieved by separate catalysts and mediated with a redox couple, has been employed with varied success. [(52)] Recent progress in the water oxidation half reaction for $LaTiNO_2$ with a CoO_x co-catalyst has yielded the best in class results. [(53)] The small band gap (2.0 eV) includes a significant region of the visible spectrum and is an improvement over the band gaps of other common oxide water oxidation photocatalyts, $BiVO_4$ and WO_3, which have band gaps near 2.5 eV. $LaTiNO_2$ also has high carrier lifetimes and good photoconductivity, which provides adequate time for migration of the carriers to the surface of the photocatalyst where chemistry can occur. [(54)] This progress moves the benchmark forward, but still leaves

room for improvement and fundamental understanding. $LaTiNO_2$ is part of a class of nitride oxide perovskites, $RTiNO_2$ ($R = Ln$, where Ln in a lanthanoid). Within this class, Ce – Nd have already been reported as existing, but no reports exist detailing their photocatalytic properties. Given the level of interest in nitride oxide perovskites as photocatalysts and the reported high activity of $LaTiNO_2$ as a water oxidation photocatalyst, these compounds' water oxidation properties should be investigated, accompanied by explanations for their observed properties.

1.1.5 Scope of the Perovskite Nitride Oxide Class, $RTiNO_2$ (R = La – Nd)

The rationale for choosing further study of this class of compounds was that it had been partially characterized in the literature previously, [(55)] and there was speculation that additional compounds may exist, [(30)] and with initial evidence for their existence already presented. [(56)] The nitride oxide class of compounds were first conceived and subsequently synthesized in the late 1970s and early 1980s. They have not yet found widespread use in commercial applications, however. Some of the nitride oxides have been proposed to be good visible light driven photocatalysts (see above). This forms the initial basis for this work, with the additional objective of full characterization of the compounds. The hope is that this may lead to some coveted properties. Diffraction techniques will elucidate the atomic structure, UV-visible diffuse reflectance will reveal the optical properties, X-ray photoelectron spectroscopy (XPS) will deliver electronic information about the valence band, magnetic measurements will provide the spin interactions between the unpaired f-electrons, and the photocatalytic properties will be examined by in situ gas chromatography (GC) measurements. The aim is to provide a wealth of information on the capabilities and properties of these compounds. Because a chemical series is being examined (La $\rightarrow$ Nd), it will also allow for the ability to investigate the changes in the compounds as f-electrons are added to the system. This will drive conclusions on the overall periodic trends that are observed. The results presented in the literature currently afford some questions that will be addressed by this work. $LaTiNO_2$ is the best-in-class water oxidation photocatalyst. The oxidation state of most of the lanthanoids is +3, which means that the La site can be swapped interchangeably for a different cation in that series. The ionic radii for $Z > 57$ (La) decreases gradually and is finely graduated. Is it possible to identify structural tolerance

regions where certain phase modifications dominate? Substitution of other lanthanoids on the La site also opens up the question of what happens to the photocatalytic rates when the f-electrons are added into the system. Furthermore, f-f transitions are spin forbidden, but nevertheless common in similar oxide studies. [(57)] Does this play a role in the photocatalysis rates since a competing process is introduced (radiative decay)? Structurally, some doubt still remains in the literature regarding the ordering of the anions in the nitride oxide systems. While density functional theory (DFT) calculations seem to indicate the existence of short-range order, [(58)] evidence for long-range order has been lacking. This knowledge gap can be filled with a neutron diffraction study paired with experimental TEM and modeling. Also, there are very few magnetic studies on nitride oxide compounds.[(59, 60, 61)] Rare-earth-containing A-site perovskite oxides have been studied, however. They exhibit some interesting structure-magnetism relations. [(62)] Will substitution of nitrogen into the anion lattice have a clear and marked effect on the magnetic interactions? Magnetic studies in tandem with structural studies will aim to address these questions.

1.2 Vanadium (III) Containing Quaternary Phosphates

The ternary phosphate class has a wealth of history, impetus, and relevant applications. Considered separately, vanadium has an abundance of available oxidation states and niche applications for each of them. The majority of work surrounding vanadium has focused on vanadium in its higher oxidation states, four and five, with applications ranging from catalysis, [(63)] to batteries, [(64)] to pigments. [(65)] Nevertheless, the number of quaternary phosphate compounds containing vanadium is a short list, largely involving V-P-O paired with an alkali-metal, alkaline-earth or d^{10} metal cation. More complication is not necessarily better, but here it affords higher functionality in the systems that can be designed. To improve understanding of V^{+3} crystal chemistry and magnetism, we explore the $Fe_7(PO_4)_6$ structure type, and in particular the series, $A_3V_4(PO_4)_6$ where A = Mg, Mn, Fe, Co, and Ni.

1.2.1 $A_3B_4(PO_4)_6$ Structure

This class of compounds has very low structural symmetry, $P\bar{1}$ (Figure 1.8, and is stitched together by phosphate tetrahedra which reside on 3 unique crystallographic

sites. The A cations reside on two distinct crystallographic sites. One makes up a distorted octahedron and is corner-connected to a distorted trigonal bipyramid. The B cations are found in B_2O_{10} units that comprise two edge-sharing octahedra. Multivalent iron (II, III) phosphate, $Fe_7(PO_4)_6$ (or $Fe_3Fe_4(PO_4)_6$ or $Fe_7P_6O_{24}$), is the structure type that this class is based upon. Isostructural analogues can be derived by making substitutions that maintain the valence on a given iron site. This has been done for a variety of vanadates such as: $Mg_3Fe_4(VO_4)_6$ [(66)] and $Mn_3Fe_4(VO_4)_6$. [(67)] Phosphate-containing analogues are less commonly reported, however. In fact, the only quaternary compound containing V^{+3} and another first row transition metal is $Zn_3V_4(PO_4)_6$. [(68)] The challenging task should be under-taken to further evaluate the capability for full substitution at the zinc site. Therefore $A_3V_4(PO_4)_6$, where A = Mg, Mn, Fe, Co, Ni will be investigated and characterized. The structural motifs that direct physical properties in this compound are the polyhedra around the metal centers and their spacing by phosphate tetrahedra.

1.2.1.1 Phosphate Tetrahedron

The most prevalent motif across all phosphorous compounds is a structural subunit, the polyatomic anion phosphate, (PO_4^{-3}). Minerals containing this ion are mined and used in agriculture and industry. Heating and condensation of the phosphate can give pyrophosphates, phosphates connected polymerically. This forms the basis for the existence of phosphorus in natural systems such as adenosine tri- and diphosphate where it is responsible for intracellular energy transfer. The literature is rife with examples of phosphate compounds, natural and synthetic. In 1957 valence shell electron pair respulsion (VSEPR) theory was introduced and reflected the historical belief that atomic polyhedra were more or less rigid and absolute. X-ray diffraction crystallography (discussed in Appendix 4.5), invented around 1910, was well on its way to widespread use, and the number of available crystal structures in the literature was ever increasing. Then in 1974, Werner Baur, in what was no doubt an early example of the power of data mining, combed the literature to produce XRD generated bond parameter data on 211 tetrahedral phosphates. The most general conclusion from this work is that the tetrahedra are actually quite flexible, indicating how stable and versatile this structural arrangement is. The additional results are as follows: 1) The site symmetry of P atoms is found to be 1 in 85% of the cases. 2) Distortions are more pronounced in the P-O

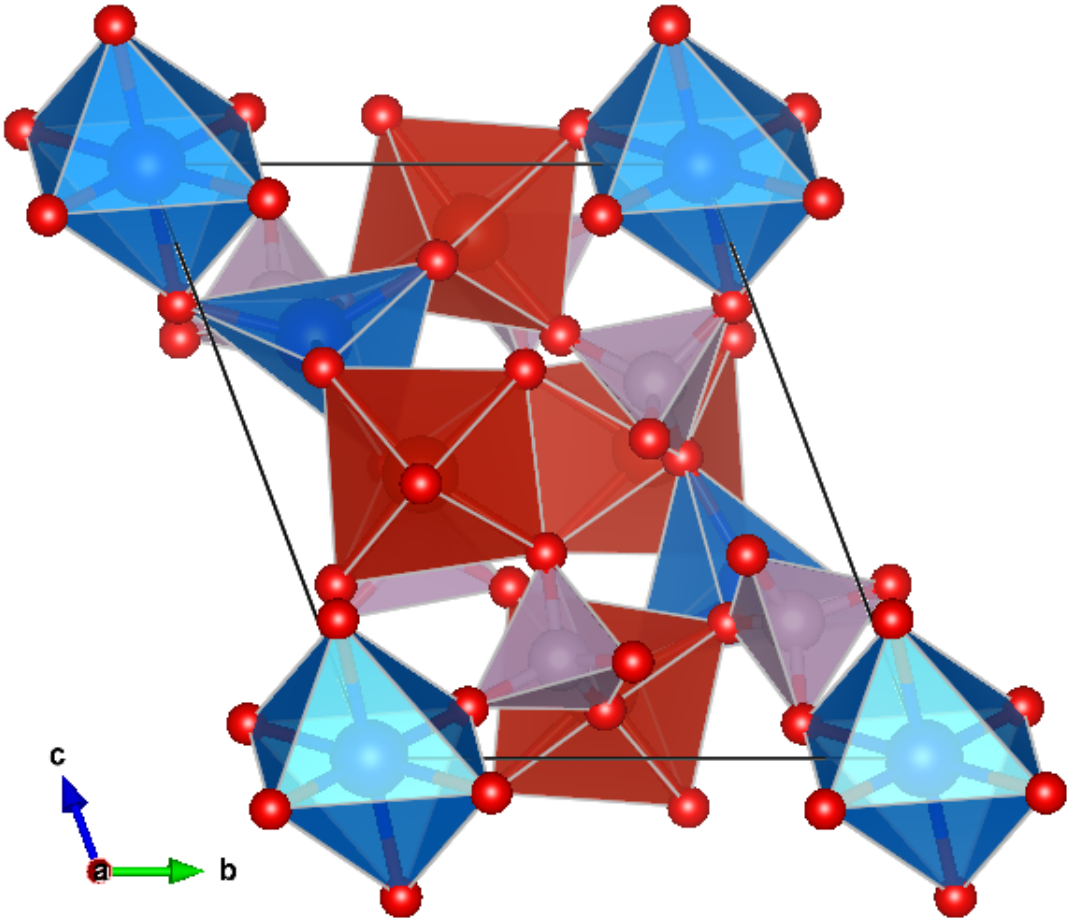

Figure 1.8: $A_3B_4(PO_4)_6$ Structure - *A*-site polyhedra (blue), *B*-site octahedra (red), and phosphate tetrahedra (pink) generate the infinite solid

distances than in the O-O, which means that P atoms can be thought of as displacing relative to a rigid, regular arrangement of O atoms. 3) The mean P-O distances vary from 1.506 to 1.572 $\mathring{A}$. [(14)] The bond parameter ranges provided by Baur's work are expected to extend to the phosphates used in this work. This will serve as a source of comparison and will drive discussion.

1.2.1.2 Transition Metal Polyhedron

The two coordinating geometries in $A_3V_4(PO_4)_6$ are octahedral and trigonal bipyramidal. In $Zn_3V_4(PO_4)_6$, the vanadium is completely ordered on the B_2O_{10} dimer sites, with the zinc residing on the distorted octahedral and trigonal bipyramidal sites. It is unclear if this order would remain if magnetic ions were substituted in place of zinc. The magnetic interactions, orbital filling of the various d-electron counts, and ionic radius changes may drive disorder, partial order, or even a juxtaposition between the cation's preference for the respective sites. Precedents for order and disorder both exist in the literature. Magnetic ions have been shown to order in sarcopside solid solutions as in the case of Ni doped into $Fe_3(PO_4)_2$. [(69)] The driving factor for this phenomena is the inequality of the two available metal sites. In $Mn_3Fe_4(VO_4)_6$, disordering is observed and is driven by the similarity of the ionic Shannon radii (6-coordinate high spin; Mn = 0.97 $\mathring{A}$ vs. Fe = 0.92 $\mathring{A}$). [(67)] The ionic radii of the cations substituted on the A-site in $A_3V_4(PO_4)_6$ spans a wide swath of sizes from 0.97 $\mathring{A}$ (Mn) to 0.83 $\mathring{A}$ (Ni). This will provide a nice probe of the flexibility of the structure. The effects of these substitutions will have a direct impact on the respective bond parameters. These size modulations and the flexibility of the structure may, in turn, have an effect on the distortion indexes (D) of the polyhedral sites. Does having a larger ion in the A-sites increase the bonding interactions between the ligands and force more rigid polyhedra? Does this have an effect on the dimer distortion? Structural insights will help develop their role in physical property outcomes. Lastly, going from VPO_4, to $M_3(PO_4)_2$, to the $A_3V_4(PO_4)_6$ compounds presents a striking contrast in edge-sharing octahedral connectivity. The series goes from infinite edge-sharing one-dimensional (1D) chains to trimeric subunits and is lastly reduced to dimeric subunits. This connectivity may have an systematic effect on the observed physical properties.

1.2.2 Properties of vanadium-phosphate containing compounds

Even though the existing body of literature does not include many quaternary phosphates that contain vanadium, other simple ternary and quaternary phosphate compounds have had significant, far-reaching cultural and technological impacts on how the world functions today. They will be discussed in sequence below with the intent that they will guide research objectives. Additionally, because the compounds in this study are being synthesized for the first time, it is prudent to characterize them. Based on previous applications, they seem suitable for use as batteries or pigments, and may also have interesting magnetic properties. The relevance of this class of compounds will be discussed below.

1.2.2.1 Pigments

Visual representation of images using paint (or some primitive equivalent) has been occurring for millennia. The compounds and elements that give paints their vibrant colors are called pigments. These are then cohesively bound in a suspension (oil, water, polymers, organics, plaster, etc.) and can be selectively applied to a surface to convey information to a viewer in the form of text or images. Therefore, chemistry is providing the medium for art to influence culture. The pigment most relevant to this thesis is (dark) cobalt violet, which corresponds to the chemical compound cobalt (II) phosphate, $Co_3(PO_4)_2$. It resides in an impressive class of cobalt-containing pigments which are obtusely named: cobalt violet, cobalt green, cobalt yellow, and cobalt blue. Fresh off the heels of elemental cobalt's discovery by Georg Brandt in 1735, these pigments cropped up in the late 1780s to the middle of the 1800s. The preparation of cobalt violet has been known since 1859, [(70)] where two varieties of this pigment are known: light and dark. The light variety is anhydrous cobalt arsenate and was developed in Germany in the early nineteenth century. The latter corresponds to anhydrous cobalt phosphate and can be precipitated by wet chemistry techniques and dried at high temperatures to drive off hydrated water. The preparation of the $Co_3(PO_4)_2$ precursor compounds used in this study, 150 years later, are not far varied from this initial report. Some of the criteria that must be considered for a pigment to be viable include stability, compatibility, safety, brilliance, and versatility. Since their introduction, the cobalt violets have been considered to be very stable, but the light variety

could change in oil due to the yellowing effect of linseed oil. [(71)] Their stability has made them more desirable than older organic dye violets, which tended to degrade over time. Compatibility with all painting media is a high priority, and this compound exceeds in this category. Nevertheless, the compound's lack of transparency and weak tinting strength paired with its high cost have given it limited wide-spread commercial use. It is largely limited to niche applications. Vanadium containing compounds have historically also been used as pigments. Their use was in vogue at the turn of the 20th century. Ranging in color from yellow-orange to green-yellow, the most prominent of these compounds occur with vanadium as a polyatomic anion, vanadate (VO_4^{-3}). This list includes the three polymorphs of $BiVO_4$ and the apatite mineral lead vanadate: $Pb_5(VO_4)_3Cl$. In fact, to this day, $BiVO_4$ is a commercially available pigment. This same compound has also found wide application as a photocatalyst. It is in demand and relevant because it is an excellent match for replacing lead based yellow pigments. $VOSO_4$ is a common precursor to other vanadyl dervatives (as in this work, on route to VPO_4). It is used as a textile mordant in the manufacture of colored glass and for blue as well as green ceramic glazes. [(72)] Other vanadium compounds that may have conceivably been tried as pigments include yellow-brown V_2O_5, green-yellow VF_3, and yellow $V_2(SO_4)_3$. [(73)] Vanadium containing compounds as well as the transition metal phosphates have a rich history of use as pigments. This has largely been limited to binary and ternary systems, however. The introduction of a quaternary system adds complexity to the picture, but it also creates new opportunities. Understanding the transition metal contributions in the $A_3V_4(PO_4)_6$ series can be bracketed by comparison to the Mg analogue. This will give a baseline contribution from the V-P-O host framework. Various charge transfer mechanisms can be identified in this way. As Mn, Fe, Co, and Ni become involved, d-d transitions play a heavy role. Cation order and crystal field effects will need to be taken into account. The splittings are different for an octahedron and a trigonal bipyramid (Figure 1.9). This, paired with the possibility of disorder and the d-electron count's effect on the Fermi level, will have an impact on the various excitations that can occur in a given compound. A systemic approach will need to be undertaken to fully understand what is driving the absorption and subsequent excitation phenomena in these compounds.

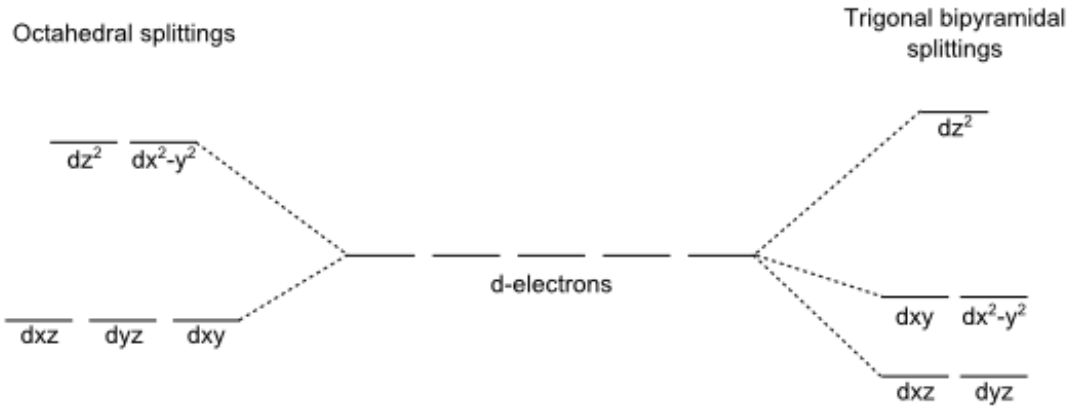

Figure 1.9: Orbtial splittings for the crystal geometries in $A_3V_4(PO_4)_6$ - Octahedra (left) and trigonal bipyramidal (right).

1.2.2.2 Batteries

$LiFePO_4$ is a natural mineral of the olivine family which crystallizes in the orthorhombic *Pbnm* space group with isolated tetrahedra. The atom packing is based on hexagonal, close-packed oxygen. Half of the octahedral sites are occupied by lithium as well as iron, and one-eighth of the tetrahedral sites are occupied by phosphorous. This lays the foundation for the observed properties below. The use of $LiFePO_4$ as a battery electrode was first reported by John Goodenough in 1997.[(74)] It was utilized as a cathode material for rechargeable lithium batteries. The rational design for this compound was based on its low cost, non-toxicity, good thermal stability, good electrochemical performance, safety, and an approximate specific capacity of 170 mA·h/g, or 610 C/g. Due to these merits, it was successful and therefore began its progress down the commercialization pipeline. The outpouring of the canon of research associated with Li-ion batteries has led to other alkali and alkaline-earth battery technologies, such as Mg-ion batteries. As a general rule, the chemical potentials of Mg in the same hosts that are commonly used for Li-ion cathode materials are more negative. There is a lower potential energy of compounds containing divalent cations. [(75)] Advances, though limited, in cathode materials have been made by via Chevrel phases and vandium oxide. [(76)] Intercalation results for Mg doped into V_2O_5 are near theoretical maximum values (589 mA·h/g of V_2O_5), with good stable cycling. [(64)] To get an idea of what the state of the art might be currently, commercial patent applications should be examined. Pellion Technologies Incorporated has a patent "WO2011150093 A1" that indicates that a

broad swath of multinary phosphate materials can be synthesized and prepared as electrode materials. Knowing the productive historical use of these precursor compounds, the success of $LiFePO_4$ as a cathode for Li-ion batteries, and V_2O_5 as a cathode for Mg-ion batteries, as confirmed by the filed patent, seems to indicate a composition of elements that might be ripe for discovery and subsequent general characterization. The main thrust of this work has been to explore ternary/quaternary systems containing vanadium, another similarly sized +2 cation, and phosphate. Using the same criteria as Goodenough used in the design of $LiFePO_4$, it is important to consider if the Mg analog, $Mg_3V_4(PO_4)_6$, might be good for an Mg-ion battery. The compound is low-cost, would be relatively non-toxic, has good thermal stability, and would be safe. One alluring structural feature of these $A_3V_4(PO_4)_6$ compounds is that the polyhedral network is configured in such a way that channels of Mg exist. This may provide good channels for Mg-ion de/intercalation. This then begs the question of whether these compounds have good electrochemical performance and can operate reproducibly at a specific capacity? The currently existing Mg-ion vanadium batteries seem to suggest that V-O containing compounds are compatible with Mg-ion de/intercalation, which further suggests the need to test these compounds as battery cathode materials.

1.2.2.3 Magnetism

The binary transition metal phosphates exhibit a wealth of interesting magnetic interactions. The sarcopside $Fe_3(PO_4)_2$ has two observed magnetic phase transitions, a field-induced ferrimagnetic-antiferromagnetic transition at 38(1) K and an antiferromagnetic-paramagnetic transition at 44(1) K. [(77)] The structure also consists of chains of edge-sharing octahedron, except that every fourth octahedron is missing. Similarly, $Ni_3(PO_4)_2$ has ferromagnetic interactions inside the Ni_3O_{14} trimers which are antiferromagnetically coupled between them, giving rise to a purely antiferromagnetic structure. [(78)] The sarcopside structure is similar to the olivine structure, which is the gateway to magnetic interactions in quarternary phosphate compounds. The $LiMPO_4$ (M = Mn, Fe, Co, Ni) olivine-type class of compounds is comprised of MO_4 layers made up of corner-shared MO_6 octahedra. Three spin exchange interactions were found to be important for $LiMPO_4$, namely, the intralayer superexchange J_1, the intralayer super-superexchange J_b along the b-direction, and the interlayer super-superexchange J_2 along

the b-direction. [(79)] The units associated with J_1 and J_2 are antiferromagnetic individually and then also are coupled antiferromagnetically as a whole. These magnetic interactions form the basis for continued work with phosphates. Interactions in sheets, across trimeric subunits, and in the bulk provide a wealth of information to glean from these systems and their relation to $A_3V_4(PO_4)_6$. This can be assisted by proper manipulation of the system and can be achieved by testing isostructural compounds in a transition metal series (such as Mn, Fe, Co, and Ni). The infinite 1D edge-sharing octahedral chains in VPO_4 have been reported to give weak anti/ferromagnetic interactions. [(80, 81)] As the connectivity is broken up, the long-range magnetic interactions weaken and antiferromagnetic interactions dominate in the olivine-like LiMPO$_4$ class of compounds, which has edge-sharing octahedral trimeric subunits spaced by diamagnetic lithium polyhedra. What happens to the magnetic properties in the $A_3V_4(PO_4)_6$ system where dimeric subunits are present, but the A-site can have a diamagnetic (Mg) or a magnetic (Mn, Fe, Co, Ni) cation in it? Does this facilitate enough magnetic exchange to foster interactions? If so, what kind? The structure of the compound can direct its magnetic properties, but to fully understand this, a general introduction to magnetism and related characterization techniques may be needed (see Appendix 4.5). Careful examination of the bond parameters may be used to give a prediction of the expected magnetic interactions. The Goodenough-Kanamori rules have been devised to help explain and provide guidance for observed magnetic interactions. In these compounds, all the metals have oxygen coordinating ligands, so the dominant magnetic interactions are expected to be driven by superexchange. The strength of the interaction is dependent on how well the orbitals between the bonded atoms overlap. When overlap is low, *e.g.*, when orbitals are orthogonal to each other, the superexchange interaction is weak. Similarly, when the overlap is good so is the superexchange. The $A_3V_4(PO_4)_6$ system has edge-sharing octahedron dimeric subunits as well as a corner-connected octahedron and trigonal bipyramidal dimeric subunits. Both these types of subunits have M-O-M bond angles that vary between $\sim 120 > \theta > 97°$. The overlap is moderate and the strength of the magnetic interactions is therefore predicted to scale in accord with that observation. The rules also indicate that superexchange interactions are antiferromagnetic when (virtual) electron transfer is between orbitals that are each half-filled. Conversely, they are ferromagnetic when electron transfer is from a half-filled to an empty orbital or from a filled to a half-filled orbital. Accounting for both of

these factors results in an expected superexchange interaction (Table 2.2) for a given bond geometry within the crystal structure. Notably: the Goodenough-Kanamori rules predict an equal number of ferromagnetic and antiferromagnetic interactions amongst the various polyhedra for all the compounds in the class. This divide could potentially lead to some interesting magnetic interactions at longer ranges and leaves open the question of: what the net dominant magnetic interaction will be in these compounds.

	Oh-Oh linkage		Oh-TBP linkage	
	V-O-V	V-O-TM	V-O-TM	TM-O-TM
$Mn_3V_4(PO_4)_6$ $Fe_3V_4(PO_4)_6$ $Co_3V_4(PO_4)_6$ $Ni_3V_4(PO_4)_6$	FM	AFM	AFM	FM

Table 1.2: Expected superexchange from the 90° Goodenough-Kanamori rules.

1.2.3 Scope of work for the Quaternary Vanadium (III) Phosphates, $A_3V_4(PO_4)_6$ (A = Mg, Mn, Fe, Co, Ni)

The initial selection criteria for compounds to investigate have been screened based upon prior successful niche applications and the potential for discovery. The result: structural analogues of $Zn_3V_4(PO_4)_6$, which has the $Fe_7(PO_4)_6$ structure-type. This compound will allow substitution of other +2 transition metals on the zinc site, and opens up the possibility of studying trends afforded by incrementally adding d-electrons to the system. The high spin ionic radii for the transition metals in this study (Mn, Fe, Co, Ni) have a broad range of sizes. Can they be used to probe the flexibility of the framework? Hints about the structure can be examined by diffraction studies. Furthermore, might this flexibility translate into favorable ion conduction pathways for Mg-ion batteries? Will the performance of the Mg-ion battery be better catalyzed by a vanadium +3/+5 redox couple? Transition metals in various host lattice systems have traditionally been used to understand the impact on the magnetic properties. What type of magnetic interactions dominate in this structure type? How strong are they, and is it possible to dilute or enhance them enough to change the observed properties? Phosphate systems have been shown to evidence super-super-exchange interactions. [(82)] Is this also the case here? As d-electrons are added to the system

by changing the transition metal, how will this impact the magnetic properties? Are there periodic trends that emerge in ordering temperatures and Weiss constants? The aim is te resolve these questions when magnetization studies are paired with structural data. Consideration should also be given to the compounds as possible pigments. Do these compounds possess the desired properties necessary to compete commercially? Can the colors be made more brilliant or can chemical substitution drive significant red/blue shifts? The optical properties of these compounds can be understood by diffuse reflectance measurements. They will enable a discussion on the relative adsorption energy of each transition metal within the series. Atomic trends within the series when d-electrons are added incrementally is fundamentally enlightening.

1.3 Instrumentation and Characterization

The preparation of never-before synthesized compounds is one feat, but it is not enough to just make new compounds. They should be made with a purpose in mind and/or with the intent to better understand the underlying chemical phenomena within a chemical class or series. Thorough characterization of a material leads to a fundamental understanding of the properties exhibited. In order to achieve this objective for the compounds selected, a variety of techniques must be employed. For characterization, this work will focus on: diffraction (neutron, synchrotron, x-ray), scanning electron microscopy / transmission electron microscopy / electron diffraction, magnetic susceptibility, UV-visible diffuse reflectance, gas chromatography (*in situ* gas formation during photocatalysis), X-ray photoelectron spectroscopy, time resolved infrared spectroscopy, and Brunauer-Emmett-Teller (BET) surface analysis. A strong effort has been made to include all the background information necessary to understand the outcomes of this work, and therefore a brief overview and reference to a more technical review for each technique is given in Appendix A(4.5). The depth of discussion will scale with relevance to this work. Appendix A(4.5) exists to aid in fully understanding the concepts presented later in this thesis. These techniques are often used as individual measurements to aid in characterization or property measurements. In other circumstances, a multitude of techniques are used and summed as a whole to give conclusive results. Basic knowledge of how the data are generated, colleted, and used

are important precursors for understanding and then explaining the observed chemical properties, not to mention optimizing them.

2

Structural and Magnetic Properties of RTiNO$_2$ (R = Ce, Pr, Nd) Perovskite Nitride Oxides

Parts of this chapter have been previously published [(83)] and are reprinted with permission from the publisher.

2.1 Introduction

The magnetic properties of RMX_3 (R = rare earth ion; M = diamagnetic cation; X = anion) are driven by the single ion magnetism of the rare-earth ion and the perovskite structural motif that encapsulates it. There are a relatively limited number of RMX_3 perovskites with diamagnetic MX_3 frameworks containing the earlier magnetic, rare-earth ions, Nd^{3+}, Pr^{3+} and Ce^{3+}. Among them the magnetism of the RAlO$_3$ phases is quite interesting and has been the most extensively studied [(84, 85)]. For PrAlO$_3$, the crystal field effects are important and there is considerable coupling with structural phase transitions [(62, 86)]. The magnetic properties of RGaO$_3$ and RCoO$_3$ are considerably different by comparison [(87, 88)]. A novel comparison is arrived at by examining perovskite nitride oxides, *i.e.*, oxynitrides, where nitrogen replaces some of the oxygen. These compounds have been relatively unexplored with respect to their magnetic prop-

erties. Previous studies on nitride oxide perovskites have revealed colossal magnetoresistance [(59, 61)], paramagnetism [(89)], ferrimagnetism [(90)], and spin glass behavior [(60)]. Structural analysis of ATa(O,N)$_3$ (A = alkaline-earth or rare-earth) has revealed anion distributions ranging from fully ordered [(35)], to partly disordered [(60, 61, 91)], to fully disordered [(42, 55)]. In the RTiNO$_2$ class, LaTiNO$_2$ is reported to adopt an unusual structure of with two inequivalent Ti sites, while NdTiNO$_2$ is reported to possess *Pnma* space group symmetry, which is quite common for perovskites. The structure and anion ordering of the intermediate compounds, CeTiNO$_2$ and PrTiNO$_2$, have not previously been studied. Following our synthetic success at preparing and characterizing RTaN$_2$O (R = Ce, Pr) [(40, 92)], we have prepared the corresponding titanium analogues, RTiNO$_2$ (R = Ce, Pr, and Nd) and present their structural and magnetic properties here.

2.2 Experimental

Samples were prepared by a solid state ammonolysis route from R_2Ti$_2$O$_7$ precursors. Stoichiometric amounts of TiO$_2$ (99.9%, GFS Chemicals) and the appropriate oxide of the rare earth cation (Pr$_6$O$_{11}$: 99.999%, Cerac; CeO$_2$: 99.90%, Acros; Nd$_2$O$_3$: 99.9%, Alfa) were ground using a mortar and pestle for 30 min. Precursors were synthesized in air (Nd) or H$_2$/N$_2$ gas (Pr and Ce) in platinum boats at 1200 °C for 8 hr with 5 °C/min ramp/cool rates. Alumina boats holding the precursors were placed in a tube furnace and gaseous ammonia was passed over the sample during annealing. The furnace was ramped at 10 °C/min to 950 °C, held for 20 hr, and then cooled at 10-20 °C/min to room temperature. This annealing cycle was repeated four times with intermittent grinding. The final CeTiNO$_2$, PrTiNO$_2$, and NdTiNO$_2$ products are colored dark brown, brown-red, and brown, respectively. LECO High Temperature NO Elemental Combustion Analysis was performed to determine the nitrogen to oxygen ratio. The purity of each compound was assessed through Rietveld refinements on powder X-ray diffraction data obtained from a Bruker D8 Advance (Ge monochromator, 15 – 75° 2θ, 0.015° step size, and 1 s dwell time). To obtain constant wavelength neutron powder diffraction (NPD) data, *ca.* 3 g samples of CeTiNO$_2$ and PrTiNO$_2$ were loaded in vanadium sample cans and data were collected at room temperature over a d-space range of 0.8 to 4.8 $\AA$ on the ECHIDNA powder diffractometer at the OPAL research reactor in

Australia. Rietveld refinements were performed using GSAS with the EXPGUI interface [(93)]. Isotropic displacement parameters were used for cations while anions were treated anisotropically. Magnetic measurements were carried out using a 9 T physical properties measurement system (PPMS; Quantum Design). For zero-field cooled magnetization measurements, the sample was cooled down to 5 K without a magnetic field, and measurements were performed during warming in an applied magnetic field of 500 Oe. For the field cooled conditions, the sample was subject to the same cooling and heating in the presence of an applied field of 500 Oe. The morphology and crystallinity of the samples were examined by transmission electron microscopy (TEM, JEOL JEM 2011). TEM samples were prepared by suspending powders in acetone followed by transferring to a holey carbon grid. Electron diffraction patterns were compared to simulation generated by SingleCrystal (CrystalMaker; Oxfordshire, U.K.). Typical settings are: 475 pixels/Åscaling, intensity saturation at 50, and a 0.02 1/Åreflection spot size.

2.3 Results

2.3.1 Structure Determination

The stoichiometry of these compounds can have an effect on the structure of these compounds. Combustion analysis indicates that the presumed O:N ratio of 2:1 is attained, within experimental error. Assuming a 1:1 ratio of rare earth to titanium gives stoichiometries of $CeTiN_{0.99(3)}O_{2.01(3)}$ and $PrTiN_{1.03(3)}O_{1.97(3)}$, respectively. This result implies that Ti has a +4 oxidation state and Ce/Pr maintains a +3 oxidation state.

The effects of tilting and anion ordering can also have a significant impact on the structure of the compounds of study.

2.3.1.1 Tilting

Octahedral tilting in these compounds is identified using the method outlined by Barnes *et al.* [(13)]. The observed superstructure reflections indicate the presence of both in-phase and out-of-phase tilts (see APPENDIX B, 4.5), strongly suggesting the presence of $a^-b^+a^-$ octahedral tilting and Pnma space group symmetry (Figure 1). A Rietveld refinement on XRD data for $CeTiNO_2$ (APPENDIX B, Figure B.1; also, $PrTiNO_2$,

Figure B.2) carried out with *Pnma* symmetry converged to a good fit (R_{wp} = 8.72 %). For the sake of completeness, refinements were carried out in space groups corresponding to other patterns of tilting – $a^+b^+c^-$ (*Pmmn* symmetry, $R_{wp} = 20\%$), $a^+b\,c^-$ ($P2_1/m$ symmetry $R_{wp} = 13.16\%$), $a^0a^0c^-$ ($I4/mcm$ symmetry, $R_{wp} = 9.71\%$), and $a^0a^0a^0$ ($Pm\bar{3}m$ symmetry, $R_{wp} = 10.21\%$) but all other symmetries gave inferior fits and thus can be ruled out.

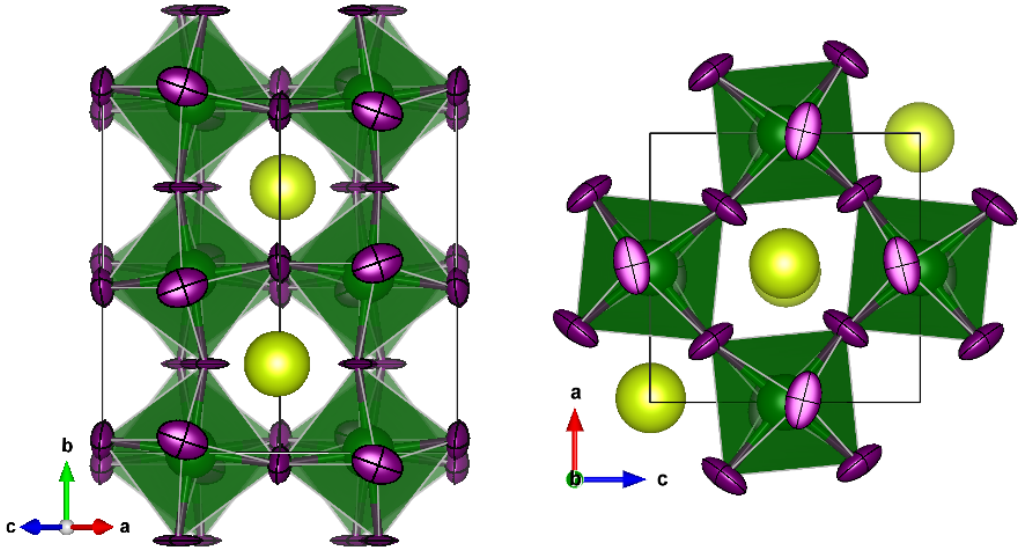

Figure 2.1: Structure of *Pnma* $CeTiNO_2$ viewed down the (101) axis (left), where out-of-phase tilting is evident, and down the (010) axis (right), where in-phase tilting is present - Ce (yellow), Ti octahedra (green) and O/N (purple) are shown.

2.3.1.2 Anion Ordering

Neutron diffraction is an excellent tool to probe long range chemical order of O and N in oxynitrides, due to the differences in scattering lengths of the two elements. Taking inspiration from our prior work on RTaON$_2$, four different anion distributions were considered: **(1)** a random distribution where the occupancies of all anions sites are fixed at 1/3 N and 2/3 O, **(2)** long range trans-ordering of nitride ions, **(3)** long range cis-ordering of nitride ions, and **(4)** a structure where the nitride ions are confined to layers, but with open order and a local cis-configuration within those layers (as found in $SrTaNO_2$ by Yang *et al.*) [(34)] Rietveld refinements using each model (Table 2.1)

reveal that long range ordered models give inferior fits. This is borne out at low angles (high d-spacings), where the discrepancies between the various ordering models and the experimental diffraction patterns are the most obvious (APPENDIX B, Figure B.5 and B.6). In $PrTiNO_2$, the lattice parameters are pseudotetragonal (Table 2.2) which leads to considerable peak overlap which in turn leads to identical fits for models **1** and **4**. When the lattice parameters transition away from pseudo-tetragonal, as is the case for $CeTiNO_2$, it becomes possible to distinguish between the two. Although the difference is still small for $CeTiNO_2$ the random model **(1)** gives a slightly better fit than model **4**. Refinements where the occupancies of the anion sites are allowed to refine freely, while maintaining the $RTiNO_2$ stoichiometry, did not lead to a statistically significant improvement in the fits.

Model	**(1)** Random	**(2a)** *trans*-ordered	**(2b)** *trans*-ordered	**(3a)** *cis*-ordered	**(3b)** *cis*-ordered	**(4)** 2D *cis*-ordered	**(5)** Fixed stoichiometry
Space group	*Pnma*	*Pnma*	$P2_1/m$	$Pmn2_1$	$Pmc2_1$	*Pnma*	*Pnma*
Anion site occupancies	[4e] O = 0.67 N = 0.33 [8g] O = 0.67 N = 0.33	[8g] O = 1 [4e] N = 1	[4f], [2e], [2e] O = 1 [4f] N = 1	[2a], [2a], [4b] O = 1 [4b] N = 1	[2a], [2b], [4c] O = 1 [4c] N = 1	[8g] O = 0.75 N = 0.25 [4e] O = 0.5 N = 0.5	[8g]* O = 0.80(4) N = 0.20(4) [4e] O = 0.60(2) N = 0.40(2)
R_{wp} (%) (R = Ce)	4.07	6.26	6.04	4.63	5.1	4.16	4.05
R_{wp} (%) (R = Pr)	3.92	5.30	5.39	4.53	4.73	3.91	3.91

Table 2.1: Goodness of fit parameters and anion occupancies for different ordering models used to fit neutron powder diffraction patterns of $CeTiNO_2$ and $PrTiNO_2$.

Rietveld refinements in *Pnma* with randomly distributed O and N for $RTiNO_2$ are shown in Figure 2.2. Lattice and goodness of fit parameters are displayed in Table 2.2. The refinements reveal 4.1 and 2.5 wt. % of a TiN secondary phase in $CeTiNO_2$ and $PrTiNO_2$, respectively. Undetected by XRD (APPENDIX B, Figure B.1 and B.2), these minor phase fractions are quantified owing to the superior sensitivity afforded by neutron diffraction technique. Crystallographic parameters are listed in Table 2.3 for $CeTiNO_2$ and Table 2.4 for $PrTiNO_2$.

Compound	$CeTiNO_2$	$PrTiNO_2$	$NdTiNO_2$
Space group	*Pnma*	*Pnma*	*Pnma*
FW (g/mol)	234.0	234.8	238.1
a (Å)	5.5580(5)	5.5468(5)	5.541(1)
b (Å)	7.8369(7)	7.8142(5)	7.796(1)
c (Å)	5.5830(4)	5.5514(5)	5.526(1)
V (Å^3)	243.18(3)	240.62(3)	238.74(5)
Z	4	4	4
# var.	25	25	25
χ^2	2.18	1.70	1.123
R_{wp} (%)	4.07	3.91	9.36
R_p (%)	3.21	3.02	7.37

Table 2.2: Lattice parameters and goodness of fits from Rietveld refinements of room temperature neutron (R = Ce and Pr) and X-ray (R = Nd) powder diffraction data.

Atomic position(s)						
ion	**site**	**x**	**y**	**z**	**occ**	**U_{iso} (Å^2)**
Ti^{+4}	4b	0.5	0	0	1	.0057(8)
Ce^{+3}	4c	.9842(9)	0.25	.988(2)	1	.0086(8)
O/N	4c	.0107(9)	0.25	.5666(6)	.67/.33	.0105*
O/N	8d	.2756(4)	.9649(3)	.7263(6)	.67/.33	.0213*

Anisotropic displacement parameters of the anions						
site	U_{11}	U_{22}	U_{33}	U_{12}	U_{13}	U_{23}
4c	.015(4)	.004(2)	.012(3)	0	−.001(3)	0
8d	.010(1)	.019(1)	.034(2)	−.007(1)	−.002(1)	−.001(2)

Table 2.3: NPD derived coordinates and displacement parameters for $CeTiNO_2$ with *Pnma* symmetry. *Value listed is U_{eqv}.

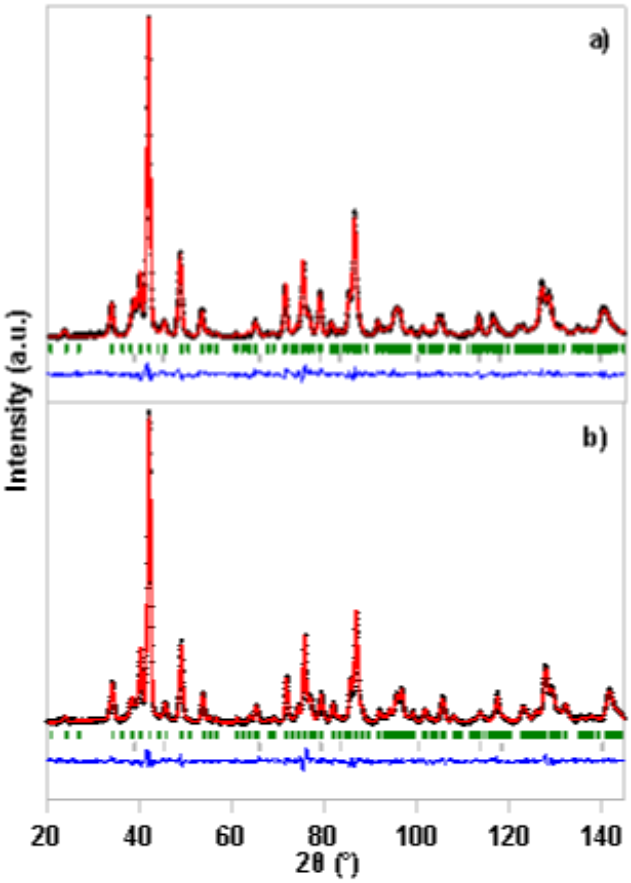

Figure 2.2: NPD patterns for a) $CeTiNO_2$ and b) $PrTiNO_2$ - Black points are experimental data, red and blue lines are the calculated and difference curves, respectively. The upper set of hash marks indicate peak positions for the perovskite phase, while the lower set denote positions of a secondary TiN phase.

Atomic position(s)						
ion	site	x	y	z	occ	U_{iso} (Å^2)
Ti^{+4}	4b	0.5	0	0	1	.0026(8)
Pr^{+3}	4c	.986(1)	0.25	.994(2)	1	.0090(8)
O/N	4c	.012(1)	0.25	.5742(7)	.75/.25(2)	.0111*
O/N	8d	.2796(6)	.9642(3)	.7205(7)	.50/.50(3)	.0157*

Anisotropic displacement parameters of the anions						
site	U_{11}	U_{22}	U_{33}	U_{12}	U_{13}	U_{23}
4c	.015(3)	.007(2)	.012(2)	0	.004(2)	0
8d	.015(2)	.014(1)	.018(2)	.001(1)	−.005(1)	.003(2)

Table 2.4: NPD derived coordinates and displacement parameters for $PrTiNO_2$ with *Pnma* symmetry. *Value listed is U_{eqv}.

2.3.1.3 TEM analysis

The $a^-b^+a^-$ tilting arrangement of the titanium octahedra requires an expansion of the primitive cubic perovskite unit cell ($a_p \sim 4$ Å) to an orthorhombic unit cell ($\sqrt{2}a_p \times 2a_p \times \sqrt{2}a_p$. A superstructure would be induced if a long-range anion ordering exists. Coupled with NPD analysis, TEM/ED was performed to examine the existence of an anion ordered superstructure on a single crystal basis. TEM analysis of $CeTiNO_2$ (Figure 2.3; $PrTiNO_2$, see APPENDIX B, Figure B.7) reveals agglomerated particles consisting of very small grains, which leads to subtle peak broadening in the XRD and NPD patterns (*e.g.* Figure 2.2). Electron diffraction patterns exhibit evidence for crystal twinning ($PrTiNO_2$, Figure 2.4; $CeTiNO_2$, see APPENDIX B, Figure B.8), which is well documented in perovskites [(94)]. This phenomenon is caused by the pseudo-cubic nature of the perovskite where the symmetry is lowered from cubic on cooling, and the effective cell edge lengths remain close to that of a cubic perovskite [(95)].

Selected area electron diffraction (SAED) patterns for both major and minor zone axes give good matches to the simulation ($CeTiNO_2$: APPENDIX B, Figure B.8; $PrTiNO_2$: Figure 2.4 and APPENDIX B, Figure B.9). Reflection conditions and systematic absences expected for *Pnma* are observed for primary reflections and validate the assignment based upon NPD data. The weak $[0kl]$ (k and l = odd) reflections (Figure 2.4, green arrow), can be attributed to orientationally dependent rotational

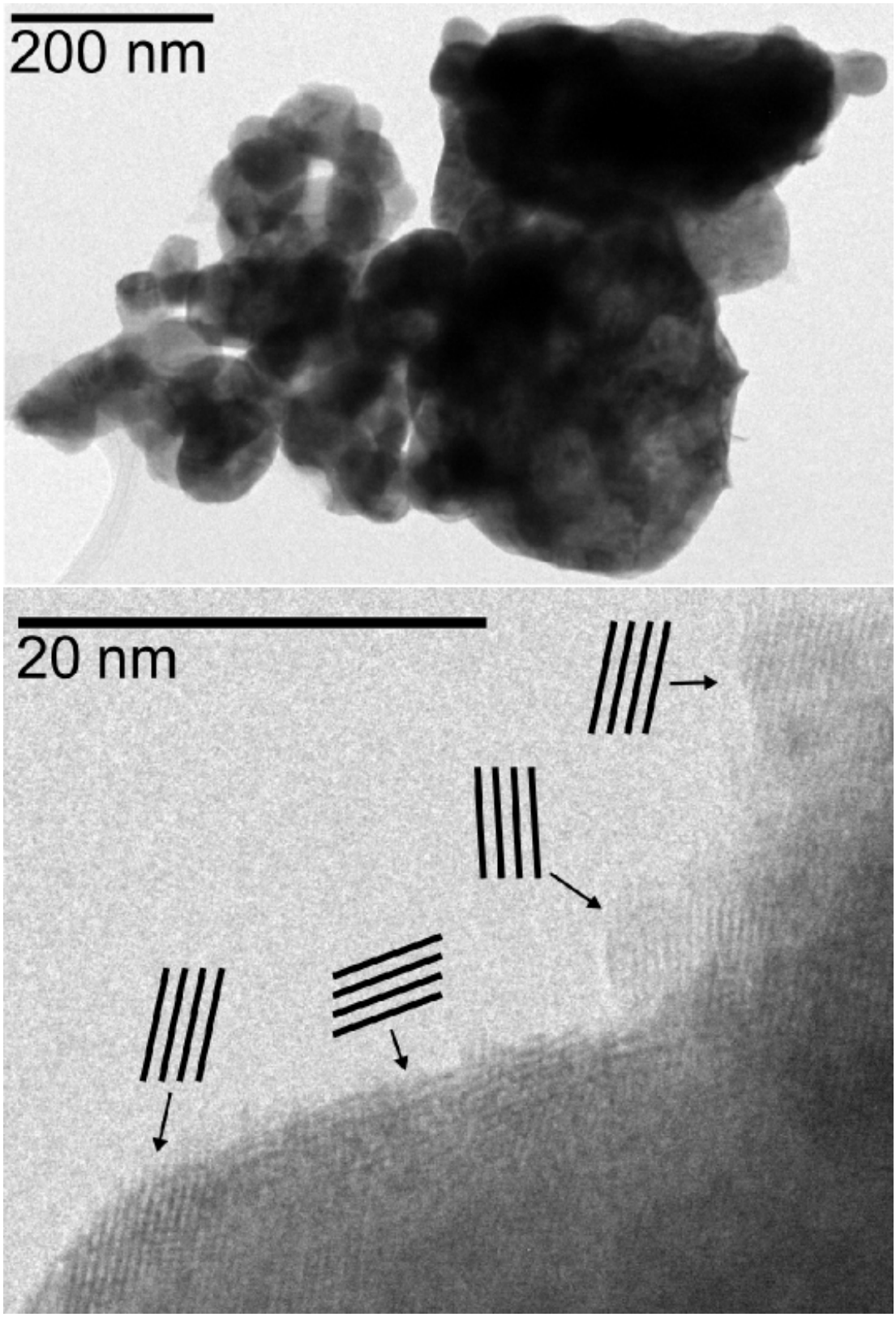

Figure 2.3: TEM images of $CeTiNO_2$ - Agglomeration of particles (top) and polycrystallinity (bottom) are shown.

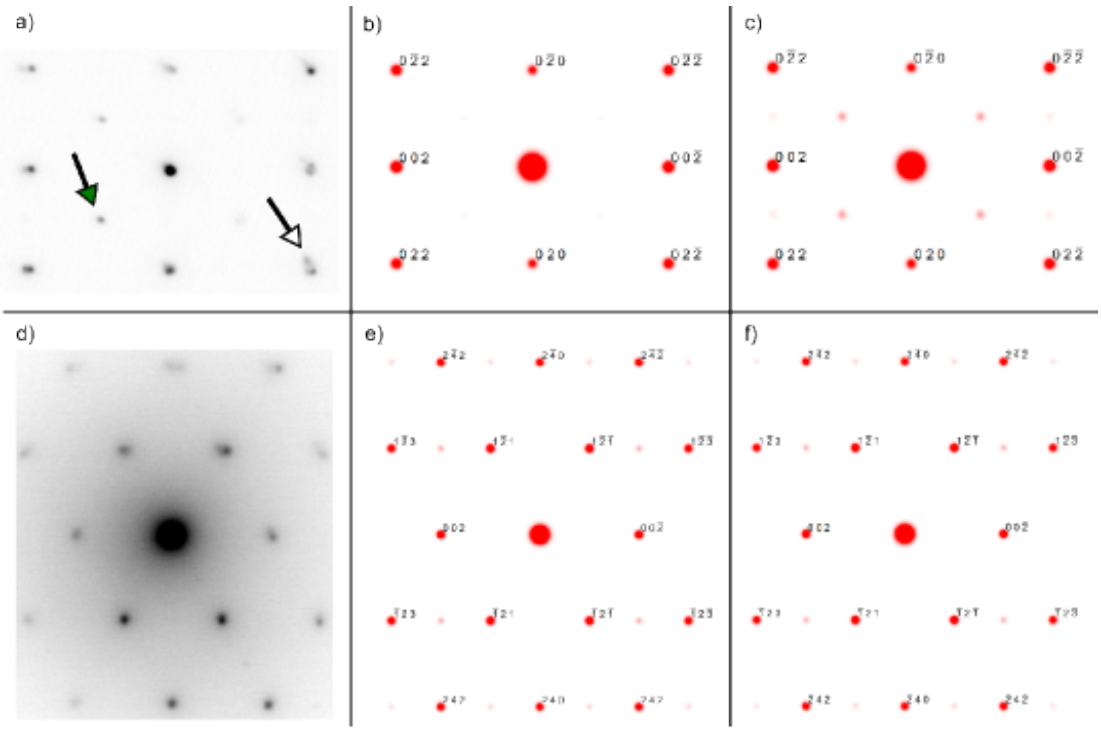

Figure 2.4: TEM (black dots) and simulated (red dots) electron diffraction patterns for $PrTiNO_2$ down a major zone axis (100) (top row) and a minor zone axis (210) (bottom row) - Experimental patterns (a and d) are compared with simulations in *Pnma* (b and e) and $P112_1/m$ (c and f). Electron diffraction patterns suffer from crystal twinning (white arrow). Weak reflections (green arrow) are thought to be due to anion ordering.

order [(34)] driven by a local cis configuration of TiN_2O_4 octahedra [(32)]. This type of short range ordering is expected to lower the symmetry from $Pnma$ to $P112_1/m$ (model **2b**). SAED simulations in this group (APPENDIX B, Figure B.9c) indeed accounts for these $[0kl]$ (k and l = odd) reflections. The presence of supercell reflections gives evidence to support the presence of a 2D arrangement of locally cis-ordered TiO_4N_2 octahedra (model **4**). When the anion occupancies in model **2b** ($P112_1/m$) were allowed to refine they converged to values consistent with a random distribution of O and N (APPENDIX B, Figure B.10; $CeTiNO_2$, $R_{wp} = 4.34\%$; $PrTiNO_2$, $R_{wp} = 4.43\%$). The discrepancies between neutron and electron diffraction results are consistent with the presence of short range order and a lack of long range order. It is noted that these superstructure reflections could also arise due to high energy electron beam induced oxygen loss, which has been observed in maximally valent transition metal oxides [(96)] and evidenced by soot build-up over time as e-beam-ejected oxygen from the nitride oxide reacts with the holey carbon grid. Nonetheless, TEM analysis confirms conclusions typical for nitride oxide systems: local ordering on length scales too short to be seen in neutron or X-ray powder diffraction measurements.

2.3.2 Magnetic Properties

Magnetism in the $RTiNO_2$ class of compounds is derived from f-electrons on the rare-earth ion. The observed differences in magnetism, intra-series, cannot be explained by geometry because changes in the coordination environment of the rare-earth ion are quite subtle, as verified by NPD (above). Instead, magnetic interactions in rare-earth materials are dictated by a combination of LS coupling and crystal field effects [(97)]. Typical for a paramagnet, the zero-field-cooled and field-cooled χ(T) at 500 Oe (APPENDIX B, Figure B.11) overlap in the entire temperature range of study (5 – 300 K). Inverse susceptibility (Figure 2.5) indicates Curie-Weiss behavior over varying ranges for each compound. It is linear for $PrTiNO_2$ at all temperatures probed, with a weak anomaly occurring at 50 K. The origin is likely due to the presence of a minor magnetic impurity in an amount too small to be detected by diffraction techniques. For the other two compounds deviations from ideal Curie-Weiss behavior are observed below 150 K for $CeTiNO_2$ and below 30 K for $NdTiNO_2$. There is no evidence for magnetic ordering down to 5 K, which does not come as a surprise because in related

rare-earth perovskite oxides antiferromagnetic (AFM) ordering is not observed until very low temperatures if at all, for example $T_N = 0.93$ K in $NdAlO_3$ [(98)].

2.4 Discussion

Bond length trends observed in the RTiNO$_2$ series are compared to one another and to analogous RGaO$_3$ and RAlO$_3$ perovskites in Table 2.5. In CeTiNO$_2$ and PrTiNO$_2$, average Ti–X bond distances are similar to those of NdTiNO$_2$, i.e. $\sim$ 2.00 Å. (Table 2.5; also, APPENDIX B, Table B.1). The average Ti–X bond distance in related titanium compounds increases, *e.g.* from 1.95 Åin $CaTiO_3$ [(99)], to 1.992.01 Åin RTiNO$_2$ [(55), this study]. This trend is expected based on the larger ionic radius of the nitride ion (1.46 Å, 4 coordinate) vs. the oxide ion (1.38 Å, 4 coordinate) [(100)].

Compound	Space group	Tilt system	Tolerance factor (τ)	Avg. M-X (Å)	Baur's D	Avg. M-X-M (°)	Ref.
LaTiNO$_2$	$I\bar{1}$	$a^-b^0a^-$	0.96	1.995(4)	0.00317	163.6(4)	*
CeTiNO$_2$	*Pnma*	$a^-b^+a^-$	0.95	1.9955(4)	0.00162	159.8(1)	this work
PrTiNO$_2$	*Pnma*	$a^-b^+a^-$	0.93	1.9935(5)	0.00032	158.1(2)	this work
NdTiNO$_2$	*Pnma*	$a^-b^+a^-$	0.93	1.9991(6)	0.00221	156.08(2)	*
CeGaO$_3$	*Pnma*	$a^-b^+a^-$	0.96	1.97(2)	0.01514	157.9(9)	*
PrGaO$_3$	*Pnma*	$a^-b^+a^-$	0.94	1.9831(4)	0.00291	154.88(7)	*
NdGaO$_3$	*Pnma*	$a^-b^+a^-$	0.93	1.9787(3)	0.00319	153.76(5)	*
CeAlO$_3$	*I*4/*mcm*	$a^0a^0c^-$	1	1.897(9)	0.00023	170.9(4)	*
PrAlO$_3$	$R\bar{3}c$	$a^-a^-a^-$	0.98	1.8957(5)	0	166.2(1)	*
NdAlO$_3$	$R\bar{3}c$	$a^-a^-a^-$	0.97	1.8931(2)	0	164.81(4)	*

Table 2.5: Tolerance factors and bond parameters from NPD data for RTiNO$_2$, RGaO$_3$, RAlO$_3$ (R = Ce, Pr, Nd). $*$ Ref [(55), (101), (102), (103), (104), (105)]

The RTiNO$_2$ and RGaO$_3$ series have many similarities: tolerance factors, M–X bond distances, and *Pnma* symmetry is observed for all three rare-earth ions. The RAlO$_3$ series has slightly larger tolerance factors due to the smaller size of Al^{3+}. This accounts for the relatively shorter MX bond distances and different tilt systems seen in the RAlO$_3$ series. Baurs distortion index, D, gives a measure of the regularity of the bonding about the MX_6 octahedra. An octahedron where all six bonds are of equal length yields a zero value, as observed in PrAlO$_3$ and NdAlO$_3$. RTiNO$_2$ compounds show values that are similar to the gallate perovskites in Table 2.5, all of which take

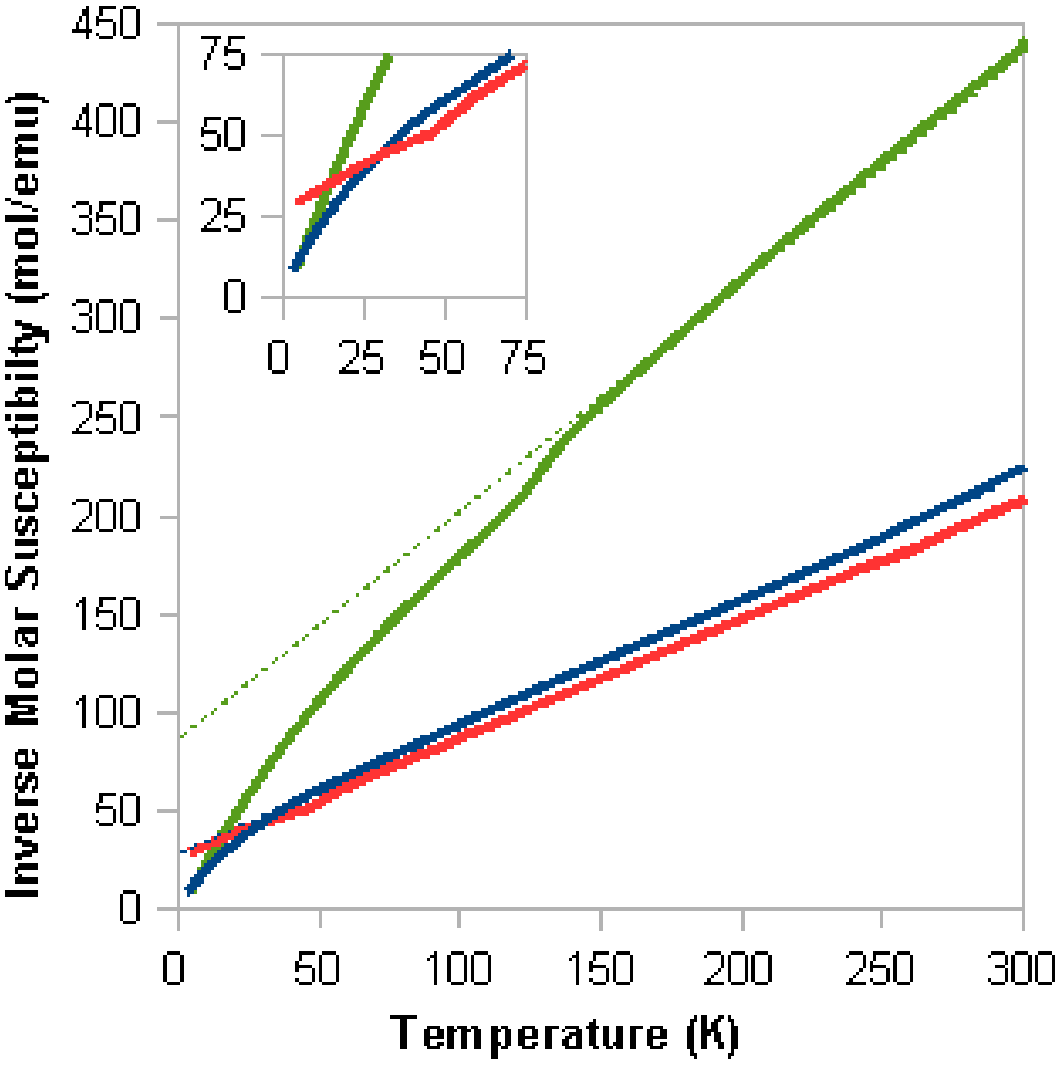

Figure 2.5: Curie-Weiss behavior of RTiNO$_2$ (R = Ce (green), Pr (red), and Nd (blue)) - Dotted lines (blue and green) show the Curie-Weiss fit. Inset shows the anomaly at 50 K in PrTiNO$_2$.

Pnma symmetry. Apparently the presence of two different types of anions does not lead to more distorted octahedra, at least in terms of the average structure. The magnitude of the M–X–M bond angles is directly related to the degree of tilting, more tilting equates to smaller bond angles. As expected the average value of the Ti–X–Ti bond angle decreases as the tolerance factor decreases (Table 2.5). The RGaO$_3$ and RAlO$_3$ oxides exhibit analogous behavior. The isothermal magnetization curves (APPENDIX B, Figure B.12) have no hysteresis, are linear at room temperature, and show weak thermally-induced spin polarization by exhibiting faint curvatures at low temperatures. These indicators are in-line with expectations for a paramagnet [35]. The values derived from fitting data with the Curie-Weiss law in the temperature range 150 – 300 K are presented in Table 2.6. All the compounds studied possess antiferromagnetic interactions ($\theta < 0$), similar to those found in other RMO$_3$ compounds (R = Ce Nd; M = Ga, Al). The Curie constants and effective magnetic moments of the RTiNO$_2$ compounds (Table 2.6) are in agreement with other oxide analogues and in-line with the values calculated for a free R^{3+} ion with Russell Saunders coupling [36]. The CeTiNO$_2$ data matches expectations for a Ce^{3+}, $^2F_{5/2}$ ground state that is split by the crystal field in various J_z states ($\pm 1/2$, $\pm 3/2$, $\pm 5/2$) [37].

Compound	θ (K)	C	μ_{eff} (μ_B)	Theor. μ_{eff} (μ_B)	Ref.
$CeTiNO_2$	−28	0.73	2.43		this work
$CeGaO_3$	--	--	--	2.54	--
$CeAlO_3$	−60	0.72	2.42		*
$PrTiNO_2$	−42	1.66	3.63		this work
$PrGaO_3$	−32	1.68	3.68	3.58	*
$PrAlO_3$	−14	1.5	3.48		*
$NdTiNO_2$	−36	1.49	3.47		this work
$NdGaO_3$	−15	1.61	3.6	3.62	*
$NdAlO_3$	−70	1.6	3.59		*

Table 2.6: Magnetic properties of RTiNO$_2$, RGaO$_3$, and RAlO$_3$ perovskites (R = Ce, Pr, Nd). $*$ Ref (106)(107)(108)

NdTiNO$_2$ deviates from Curie-Weiss behavior below 30 K, which is similar to values reported in studies of Nd$_2$Ti$_2$O$_7$ and NdMO$_3$ (M = Ga, Co), inferring that the Nd^{3+} ion experiences similar anisotropic effects in the nitride oxide perovskite structure as

in other crystalline phases. Single crystal, orientation-dependent magnetization studies of $Nd_2Ti_2O_7$ (a layered perovskite) demonstrated that in-plane magnetization is more than three times as large as the out-of-plane case, suggesting that Nd^{3+} spins prefer to align in the *bc* plane [(109)]. Calculations in the $NdGaO_3$ system reveal that as temperature decreases, crystal field effects begin to dominate over LS coupling [(103)]. $CeTiNO_2$ deviates from Curie-Weiss behavior at a much higher temperature, near 150 K. No magnetic studies of $CeGaO_3$ have been published, but Aruna *et al.* did report a deviation from Curie-Weiss behavior near 100 K in $CeAlO_3$ [(110)]. They attribute the deviation to crystal-field effects, and since the coordination environment in $CeTiNO_2$ will be similar but more distorted than $CeAlO_3$ a slightly higher temperature deviation from Curie-Weiss behavior is not unreasonable. To examine anisotropic magnetism in RTiNO$_2$ in greater detail single crystals are required but their preparation will be nontrivial.

2.5 Conclusion

The RTiNO$_2$ (R = Ce, Pr, Nd) perovskites have been synthesized and their structural and magnetic properties characterized. All three compounds have orthorhombic *Pnma* symmetry due to $a^-b^+a^-$ tilting of the octahedra. No evidence for long range anion order was found in the NPD data; however, superstructure reflections seen in TEM patterns suggest short-range order, similar to that reported in earlier studies of $SrTaNO_2$ [(34)]. The magnetic properties of the RTiNO$_2$ phases are compared with those of analogous RGaO$_3$ and RAlO$_3$ oxide perovskites. The bond distances in the RTiNO$_2$ series are similar to those in the RGaO$_3$ perovskites, which also show paramagnetic behavior down to low temperatures. Low temperature deviations from Curie-Weiss behavior are seen at varying temperatures — Ce (T < 150), Nd (T < 30), Pr (T < 5 K) — and are attributed to a combination of magnetic anisotropy, changes in the LS coupling, and crystal field effects.

3

Electronic structure and photocatalytic water oxidation activity of RTiNO$_2$ (R = Ce, Pr, and Nd) perovskite nitride oxides

Parts of this chapter have been previously published [(111)] and are reprinted with permission from the publisher.

3.1 Introduction

Visible light driven photocatalytic water splitting has attracted considerable attention as an attractive approach to harvesting solar energy. Instead of converting the energy of solar radiation to electrical energy, water splitting produces chemical energy in the form of H_2 and O_2. The photocatalytic process of generating these gases can be broken down into two half reactions – water oxidation by photogenerated holes to produce O_2, and water reduction by photogenerated electrons to produce H_2. Despite four decades of research a photocatalyst that can efficiently split water when irradiated with only visible light remains elusive. A promising way to address this challenging problem is to use separate photocatalysts to drive each half-reaction and couple these two through a redox-active shuttle in the so-called Z-scheme approach. For the water oxidation half of the Z-scheme approach, the most widely studied photocatalysts are

oxides like $BiVO_4$ ($E_g \sim 2.4$ eV)[(112, 113, 114, 115)] and WO_3 ($E_g \sim 2.4$ eV).[(116, 117, 118, 119)] While the band gaps of these oxides are small enough to absorb visible light, they are still large enough that a significant fraction of the visible spectrum is not harvested. In recent years the nitride oxide class of compounds, commonly referred to as oxynitrides, have been identified as promising photocatalysts. Nitride oxides benefit from a reduced band gap with respect to analogous oxides because the valence band maximum (VBM) shifts up in energy due to the presence of nitrogen 2p states which are more electropositive than the oxygen 2p states that comprise the valence band in most oxide photocatalysts.[(41)] TaON ($E_g = 2.4$ eV) was one of the first mixed anion compounds reported for water oxidation.[(120, 121)] Recently $BaNbNO_2$ (Eg = 1.7 eV)[(122)] and $LaTiNO_2$ (Eg = 2.1 eV)[(53)] have been shown to possess excellent O_2 evolution rates, and hence are attractive candidates for the oxygen evolution photocatalyst in a Z-scheme setup. Motivated by the best-in-class performance and high quantum efficiency of $LaTiNO_2$ we have prepared three related nitride oxide perovskites, RTiNO$_2$ (R = Ce, Pr, Nd), and characterized their electronic structures and oxygen evolution photocatalytic activities. The synthesis and structural characterization of these compounds have previously been reported,[(43, 55, 56, 83) but their optical, electronic and photocatalytic properties have not been studied. To put the properties of these three nitride oxide perovskites in context we have also prepared and characterized $LaTiNO_2$ for comparison.

3.2 Experimental

Samples were prepared in an identical manner as reported in the previous chapter.

LECO High Temperature NO Elemental Combustion Analysis was performed to determine the nitrogen to oxygen ratio. The purity of each compound was assessed through Rietveld refinements on powder X-ray diffraction data obtained from a Bruker D8 Advance diffractometer (Ge monochromator, 10 – 110° 2θ, 0.015° step size, and 1 s dwell time). Rietveld refinements were performed using GSAS with the EXPGUI interface.[(93)] Isotropic displacement parameters were used for all ions. The Brunauer–Emmett–Teller (BET) surface area and pore volume of the samples were measured by a Micromeritics Accelerated Surface Area and Porosimetry (ASAP) 2020 instrument,

using nitrogen adsorption/desorption isotherms collected at liquid nitrogen temperature. The desorption branch of the isotherm was used to determine the Barret–Joyner–Halenda (BJH) pore size distribution. Before the measurement, the samples were degassed for 12 hr at 130 °C under a vacuum better than 2 μm Hg. Scanning electron microscopy (SEM), for sample imaging, and electron dispersive X-ray spectroscopy (EDXS), for chemical composition analysis, were performed in a Zeiss Ultra 55 Plus FE-SEM with an electron accelerating voltage of 15 kV. Samples were prepared by dispersing the particles on a conductive carbon tab mounted on a metal substrate holder. X-ray photoelectron spectroscopy (XPS) measurements were performed on powders anchored in carbon tape using a Kratos Axis Ultra XPS instrument. The photoelectron excitation processes were initiated using an Al K_α source (energy 1486.6 eV). The vacuum in the analysis chamber was maintained at 1×10^{-9} Torr. Binding energy reference for all samples was set to the C 1s peak, 284.5 eV. UV-visible diffuse reflectance data were collected using an Ocean Optics USB4000-UV-Vis spectrometer equipped with a standard reflectance probe and a DH-2000-BAL deuterium/tungsten halogen light source. Data were generated using SpectroSuite software, then transformed by the Kubleka-Munk method for subsequent interpretation. The femtosecond time-resolved infrared (TRIR) experiment was performed using a Coherent Ti:sapphire oscillator and regenerative amplifier combination (1 kHz, 50 fs FWHM). The 800 nm output is split and used to generate the mid-IR probe and visible pump beams. For the probe, an OPerA optical parametric amplifier (OPA) with a difference frequency generation (DFG) attachment produces mid-IR energies ranging from 2500 – 800 cm^{-1}. A Ge beamsplitter is used to produce a probe and a reference IR beam that pass through the sample with $\sim$ 5 mm separation. The pump beam is also generated from an OPA with a UV/vis or DFG attachment, after which it passes through a delay stage and is overlapped with the probe at the sample. Probe and reference spectra were collected on a Triax 320 spectrometer equipped with a HgCdTe array (2×32) detector.[(123)] Samples were prepared by uniaxially pressing 2 wt. % $R$$TiNO_2$ in KBr (totaling 400 mg) into a pellet at 100 MPa. The samples were excited at 600 nm, near the band edges (620 to 590 nm), with an energy of 1.0 – 1.5 μJ at the sample. Spectra were background subtracted, plotted, and analyzed using Origin. The kinetic profiles were fit using a triple exponential equation of the form:

$$S(t) = \Sigma_i A_i e^{-t/\tau_i} + C \tag{3.1}$$

where A_i is the amplitude, τ_i is the lifetime, and C is an offset. Errors in the lifetimes are reported as standard errors of the exponential fits. For photocatalytic measurements, the surface of the oxide nitrides was wet impregnated with a CoO_x co-catalyst from 2 wt. % $Co(NO_3)_26H_2O$ (>99.0%, Baker) using a method previously described.[(53)] Water oxidation half reactions were executed in a closed, top-irradiated quartz vessel. 100 mg of co-catalyzed nitride oxide powder and 100 mg La_2O_3 (99.99%, GFS Chemicals) (as a pH buffer) were added to 100 mL of a 0.05 M $AgNO_3$ aqueous solution and suspended using a magnetic stirrer. The $Ag^+_{(aq)}$ ions act as a sacrificial electron acceptor. Reactant solutions were purged of air by bubbling argon through the system until the background GC spectra were featureless. Visible light irradiation was performed using a 150 W Xe lamp equipped with a 400 nm long pass filter and a cold mirror (Newport Oriel, Stratford, CT, USA; optical power: $26\mu W/cm^2$). Gases evolved were separated by a Shimadzu GC-14A gas chromatograph equipped with a 60/80 molecular sieve 5A (Sigma Aldrich, St. Louis, MO, USA) and a thermal conductivity detector. These runs were calibrated against an external standard curve for oxygen. A known oxygen evolving catalyst, $LaTiNO_2$, was used as a benchmark for comparison. To ensure that the system is visible light active only, a UV active perovskite photocatalyst, $SrTiO_3$, was tested for O_2 evolution. The $SrTiO_3$ sample was prepared from TiO_2 (99.9%, GFS Chemicals) and $SrCO_3$ (99.99%, Alfa) by two cycles of heating to 1000 °C, holding for 8 hr each time (with intermittent grinding). Quantum efficiency measurements on $LaTiNO_2$ and $NdTiNO_2$ were carried out using O_2 evolution (same experimental and instrumental set-up) under 450 nm band pass filtered 150 W Xe arc lamp light calibrated by a Si photodiode (Thor labs, Newton, NJ, USA).

3.3 Results and Discussion

3.3.1 Composition and Structure

Combustion analysis is in-line with reports in the previous chapter, while sample purity and structural equivalence to compounds prepared previously was verified by XRD powder patterns (Figure 3.1). Refinements were carried out in their reported space

groups, *Pnma* for RTiNO$_2$ (R = Ce, Pr, Nd) and $I\bar{1}$ for LaTiNO$_2$. Lattice parameters for all four compounds were determined using whole pattern fitting of the XRD powder patterns, and are shown in Table 3.1. The compounds are phase pure and have space group symmetry and lattice parameters that are in agreement with the previously reported values.

	$LaTiNO_2$	$CeTiNO_2$	$PrTiNO_2$	$NdTiNO_2$
Space group	$I\bar{1}$	*Pnma*	*Pnma*	*Pnma*
a (Å)	5.592(8)	5.5563(4)	5.531(1)	5.541(1)
b (Å)	7.870(5)	7.8017(4)	7.7895(5)	7.796(1)
c (Å)	5.582(6)	5.5349(3)	5.5355(9)	5.526(1)
α (Å)	90.1(2)	90	90	90
β (Å)	90.18(5)	90	90	90
γ (Å)	90.3(2)	90	90	90
V (Å^3)	245.69(9)	239.93(3)	238.49(3)	238.74(5)

Table 3.1: Lattice parameters for Rietveld refined RTiNO$_2$ (R = La, Ce, Pr, Nd) perovskites from laboratory X-ray diffraction data.

3.3.2 Surface Properties

A type-II adsorption isotherm has been observed for PrTiNO$_2$ as shown in Figure 3.2 (see APPENDIX C for the iostherms of the other compounds, Figure C.1 – C.3). This isotherm is common for vapor adsorption, *e.g.* water vapor adsorbed on a hydrophobic material. The specific surface areas for RTiNO$_2$ determined by BET at 77 K are 4 – 6 m$^2 g^{-1}$. Capillary condensation driven volume increases in the adsorption branch, occur at relatively high pressure ($\sim$ P/P$_0$ > 0.9), which is indicative of large pore diameter. The pore size distribution (inset in Figure 3.3), determined from the corresponding desorption branch using the BJH method, is broad with pore volume increasing as pore diameter decreases. A wide distribution of pore diameters exists in the range of 20 – 90 nm. These compounds have comparable surface area, pore volume, and pore size (Table 3.2), which is not unexpected given the identical solid state ammonolysis used for the synthesis. The high temperature and long dwell time allow for considerable

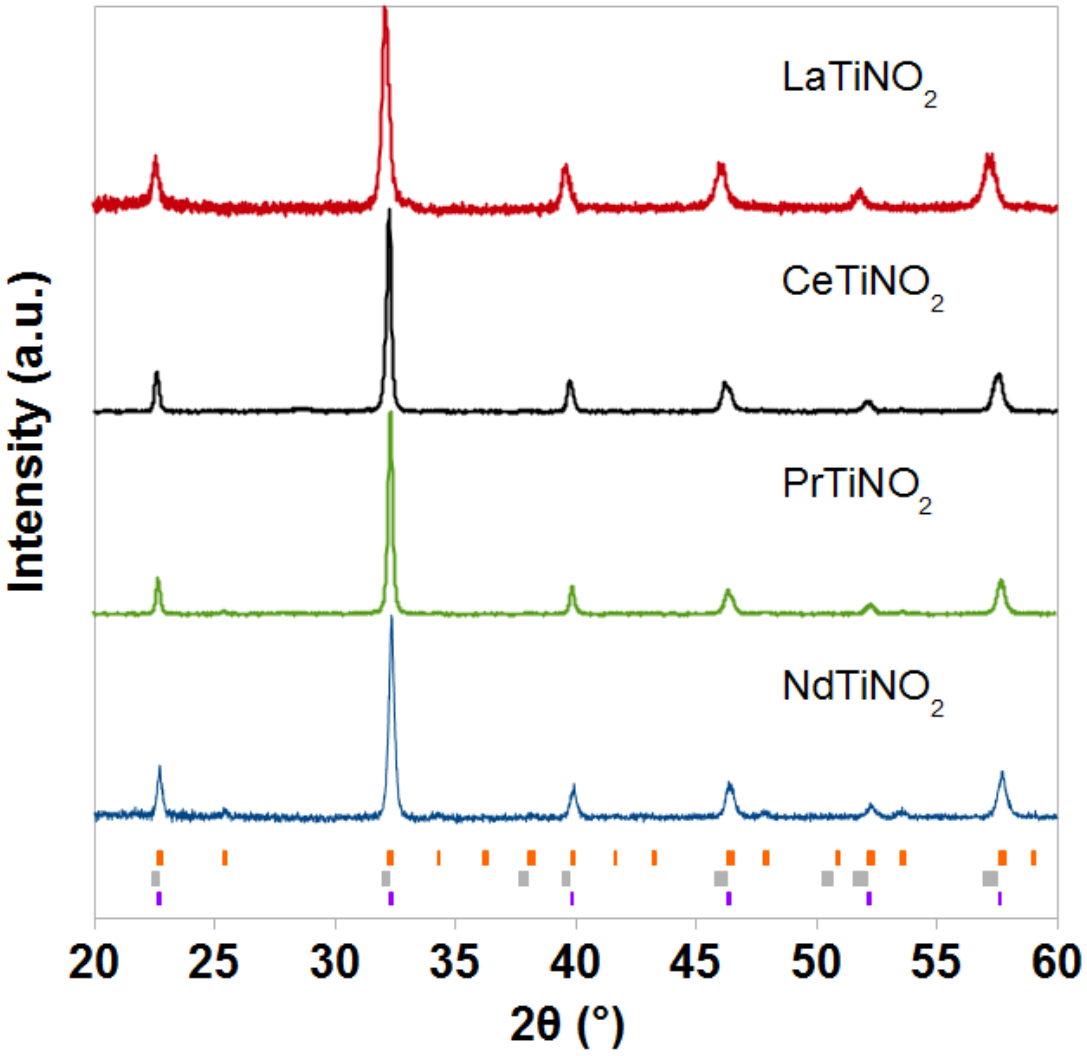

Figure 3.1: Laboratory XRD patterns of RTiNO$_2$ from 20 to 60° 2θ - Reflection positions for a simple cubic perovskite ($Pm\bar{3}m$) with lattice parameter a_p, a triclinic perovskite ($I\bar{1}$) with $\sqrt{2}a_p \times 2a_p \times \sqrt{2}a_p$ lattice parameters, and an orthorhombic perovskite ($Pnma$) with $\sqrt{2}a_p \times 2a_p \times \sqrt{2}a_p$ lattice parameters, are shown with purple (lower), gray (middle), and orange (upper) hash marks, respectively.

grain growth and grain boundary minimization, which lead to small surface area and pore volume.

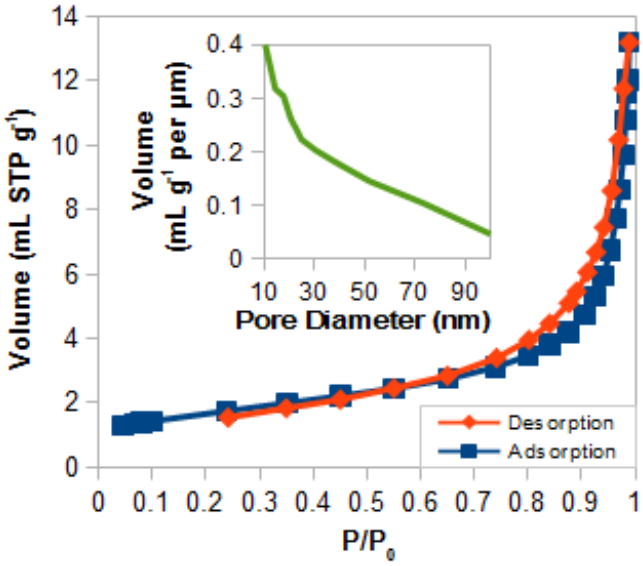

Figure 3.2: N_2 isotherm and pore size distribution (inset) for $PrTiNO_2$ -

Sample:	$LaTiNO_2$	$CeTiNO_2$	$PrTiNO_2$	$NdTiNO_2$
BET Surface area (m^2/g):	6	4	6	5
Pore Volume (cm^3/g):	0.03	0.02	0.02	0.02
Mean Pore Diameter (nm):	20	18	13	17

Table 3.2: Surface features of $R\mathrm{TiNO_2}$ (R = La, Ce, Pr, Nd) powders prepared by solid state ammonolysis.

SEM images ($NdTiNO_2$, Figure 3.3; $R\mathrm{TiNO_2}$ (R = La – Pr), APPENDIX C, Figure C.4 – C.6) reveal that particle size distribution is consistent across all samples. The crystal size in $CeTiNO_2$ (1 – 3 μm) is slightly larger than the other compounds, which is reflected in the BET surface area. Each sample contains both large (50 – 100 μm; not pictured) and small (100 nm 10 μm) particles. The broad distribution of particle sizes is the result of agglomeration during annealing due to sintering. No uniform crystal habit is apparent, with a random orientation of exposed facets for all $R\mathrm{TiNO_2}$. These observations are in-line with the results from our prior work on the same compounds, where TEM analysis shows polycrystallinity even for the smallest particles.[(83)] EDXS

confirms that the CoO_x co-catalyst by has been uniformly distributed on the surface of RTiNO$_2$ particles.

3.3.3 X-ray Photoelectron Spectroscopy

To evaluate the relative positions of the partially filled 4f electron energy levels, XPS measurements in the valence band photoemission region have been performed (Figure 3.4). The spectra of RTiNO$_2$ are characterized by strong, broad peaks spanning from 0 to 8 eV originating largely from the anion 2p orbitals that make up the valence band. A peak originating from occupied f-orbitals, and marked with a purple plus sign, is visible above the valence band edge in CeTiNO$_2$. This same peak appears as a shoulder on the anion 2p valence band edge for PrTiNO$_2$. The peak associated with 4f orbitals cannot clearly be made out in the NdTiNO$_2$ spectrum. This indicates a further shift toward higher binding energy, which implies that the position of the occupied 4f levels lies below the valence band maximum and overlaps with states well within the valence band.

The trend of increasing binding energy of the f-orbital states on going from Ce $\rightarrow$ Pr $\rightarrow$ Nd is consistent with expectations based on effective nuclear charge. Similar XPS trends have been observed in the RTaO$_4$ series.[(57)] Differences in crystal structure that lead to different band dispersions make a direct comparison of the RTaO$_4$ and RTiNO$_2$ XPS spectra difficult, but some qualitative comparisons can be made. In both the RTaO$_4$ and the RTiNO$_2$ series the peak associated with the occupied Ce 4f-states lies at a binding energy that is $\sim$1 eV higher than the peak associated with the Pr 4f-states. A close inspection also reveals that the Pr 4f-states are located closer to the top of the anion 2p valence bands in PrTiNO$_2$ than in PrTaO$_4$, an effect that can be attributed to the contribution of the nitrogen 2p orbitals to the valence band of the former compound.[(41)] The key point is that only the more electropositive rare-earth ions (Ce and Pr) have partially filled 4f states that are at energies higher than or comparable to the valence band maximum. As seen below this feature of the electronic structure has important implications for the photocatalytic activity.

3.3.4 Time-resolved IR Measurements

It has been shown previously that wet-impregnated co-catalysts significantly increase the carrier lifetimes in LaTiNO$_2$.[(53)] To minimize variables and examine intrinsic

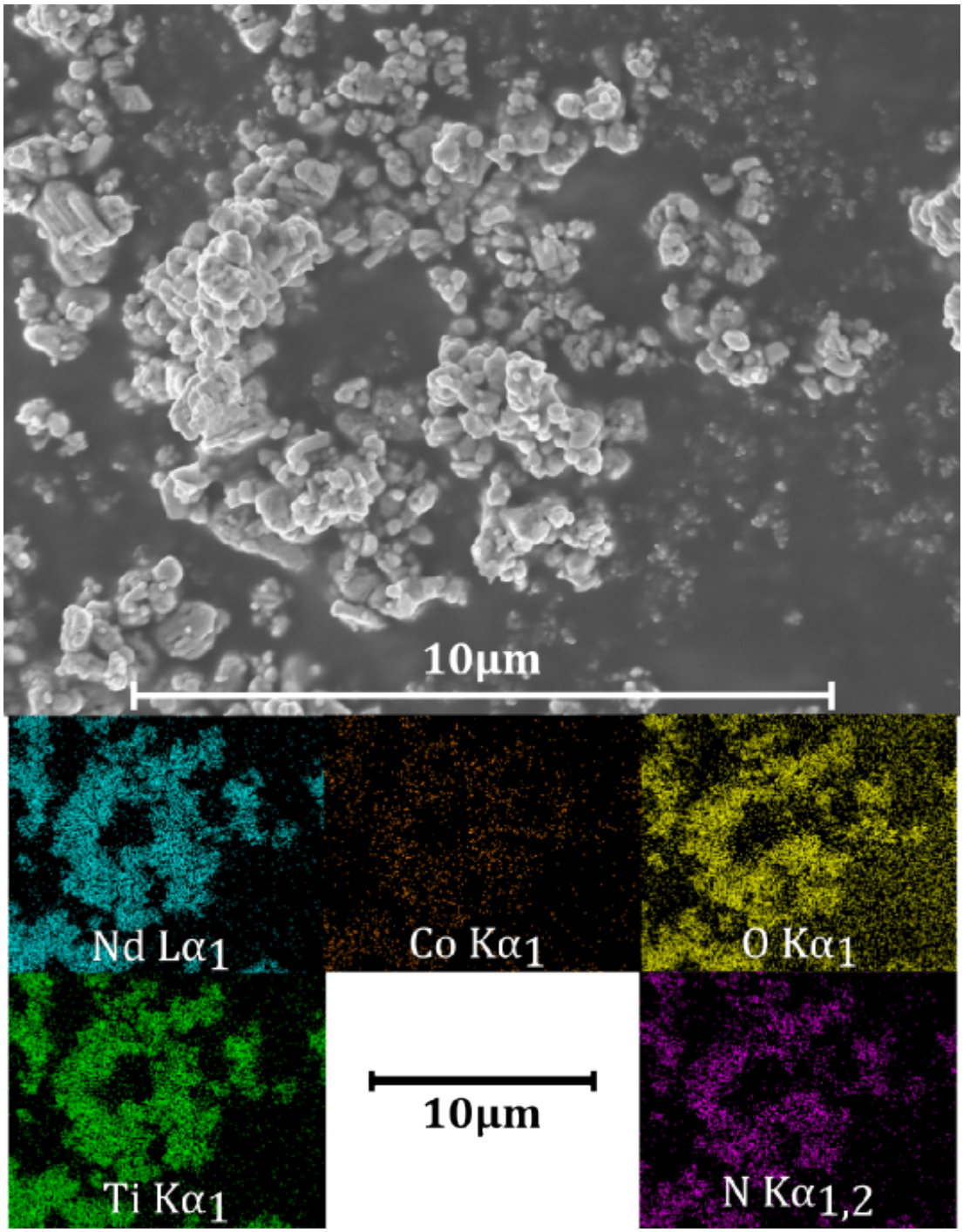

Figure 3.3: SEM image and EDX mapping for $NdTiNO_2$ -

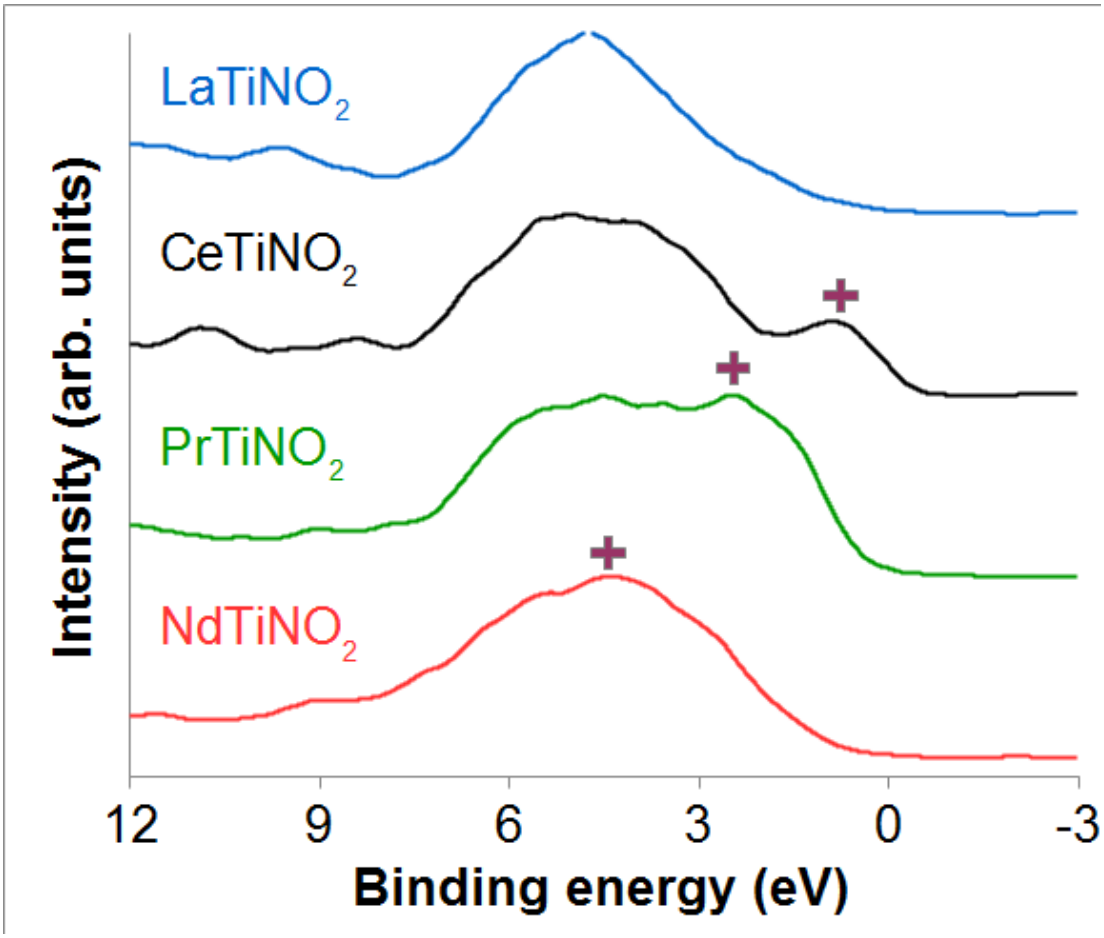

Figure 3.4: XPS of RTiNO$_2$ (R = La, Ce, Pr, Nd) - Crosses mark the positions of the 4f states.

effects, femtosecond TRIR spectra were recorded on bare RTiNO$_2$ (APPENDIX C, Figure C.7 – C.10) to probe the free carriers and lifetimes. In each case, the spectra display an instantaneous rise of a broad mid-IR band, though for LaTiNO$_2$ there is a slower growth component ($\sim$ 2 ps). Kinetic decay for each compound (Figure 3.5) is fit by a triple exponential function (Equation 1.1), revealing free carrier lifetimes that range from 0.59 ps to 1.1 ns (Table 3). For all RTiNO$_2$, residual signal remains at the time limit of the experiment (3 ns) indicating a slow fourth decay component, that in similar studies of TiO$_2$ has been attributed to defects.[(124)] In-line with previous photocurrent and time-resolved diffuse reflectance measurements for LaTiNO$_2$,[(125)] we observe relatively long lifetimes and slow recombination for LaTiNO$_2$.

	$LaTiNO_2$	$CeTiNO_2$	$PrTiNO_2$	$NdTiNO_2$
A_1	0.00607 (46%)	0.00747 (50%)	0.00130 (42%)	0.00837 (91%)
τ_1 (ps)	4.0(2)	0.59(1)	2.2(1)	1.6(1)
A_2	0.00316 (24%)	0.00647 (43%)	0.00138 (45%)	0.00027 (3%)
τ_2 (ps)	96(4)	6.7(6)	21(2)	34(4)
A_3	0.004 (30%)	0.00110 (7%)	0.00039 (13%)	0.00052 (6%)
τ_3 (ps)	1110(60)	170(20)	330(60)	798(53)
ΔOD_{max} (ps)	1.86	0.133	0.387	0.153

Table 3.3: Amplitudes, decay lifetimes and time of ΔOD$_{max}$ from TRIR kinetics for RTiNO$_2$ (R = La-Nd)

The broad mid-IR signals are attributed to absorptions of free carriers within the conduction band of each material. The concentrations in CeTiNO$_2$ and PrTiNO$_2$ diminish rapidly to levels similar to or less than that of NdTiNO$_2$ beyond $\sim$25 ps. These rapid decays are associated with the fast component (τ_1) and are presumed to decay on too short of a time scale to have any significant effect on other processes. In LaTiNO$_2$ the concentrations persist and decay more slowly. The highly localized nature of the 4f orbitals and their location near the VB edge in CeTiNO$_2$ and PrTiNO$_2$ (see previous section), can potentially act as a favorable pathway for carrier recombination. The lifetimes for CeTiNO$_2$ are particularly short. On the other hand, the 4f orbitals in

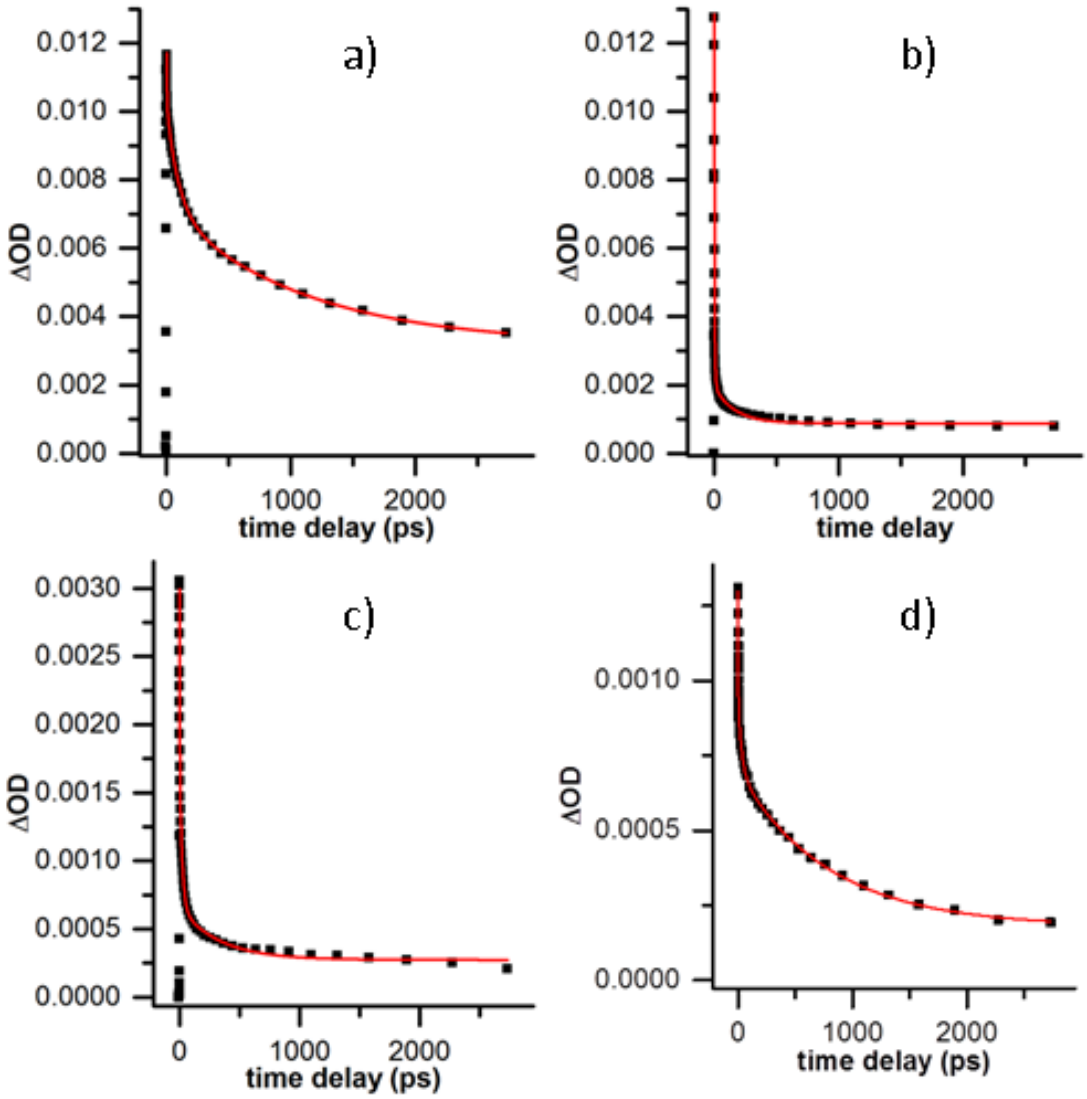

Figure 3.5: Kinetic traces of RTiNO$_2$ (R = a) La, b) Ce, c) Pr, d) Nd) -

$NdTiNO_2$ are located further from the VB edge where the concentration of photogenerated holes is expected to be highest. This difference could lead to reduced rates of electron-hole recombination, longer lifetimes, and allow for carriers to partake in other phenomena (such as water oxidation, see below). The slow components (τ_2 and τ_3) and their associated longer-lived lifetimes are ordered La > Nd > Pr > Ce, validating this hypothesis.

3.3.5 Optical Properties

Diffuse reflectance spectra that enable quantitative comparison of the optical band gaps of $LaTiNO_2$ and the three compounds studied here are shown in Figure 3.6. The band gaps, which were estimated by the linear extrapolation of the adsorption onset (the Shapiro method),[(126)] were found to be 2.1(2), 2.0(2), 2.0(2) and 2.1(2) eV for $LaTiNO_2$, $CeTiNO_2$, $PrTiNO_2$, and $NdTiNO_2$, respectively. The band gap of $LaTiNO_2$ agrees well with previous reports.[(127)] The observed colors for La $\rightarrow$ Nd are red, brown-red, dark brown, and brown. The variations in color are largely due to differences in sub-band gap absorptions. The absorption coefficient for the compounds was not measured but assumed to be unique for each R cation. It is acknowledged that this could have a non-negligible impact on the photocatalytic activity. The difference in the absorption coefficients for the individual $R\mathrm{TiNO}_2$ compounds at energies greater than the band gap should be minimal because they have very similar crystal and electronic structure.

It is well established that the valence to conduction band transitions involve transfer of an electron from crystal orbitals that have predominantly anion character to crystal orbitals derived from the empty titanium 3d orbitals. The optical absorption that occurs at energies below 2.0 eV (λ > 620 nm) does not originate from excitations across the band gap and merits further comment. The shape of $CeTiNO_2$ optical absorption curve between approximately 2.1 and 1.6 eV is qualitatively different than the other three compounds. Given the location of the Ce^{3+} 4f orbitals in the band gap we hypothesize that the unusual shape of the UV-Vis curve in this region is due to transitions from the Ce 4f orbital into the conduction band. This type of transition has been seen in oxides that contain Ce^{3+}, such as $CeVO_4$.[(128)] The upturn seen in absorption spectra of the other three compounds on moving into the infrared region (E < 1.7 eV) is likely of a different origin. The trace amounts of TiN (2 – 4 wt. %, observed

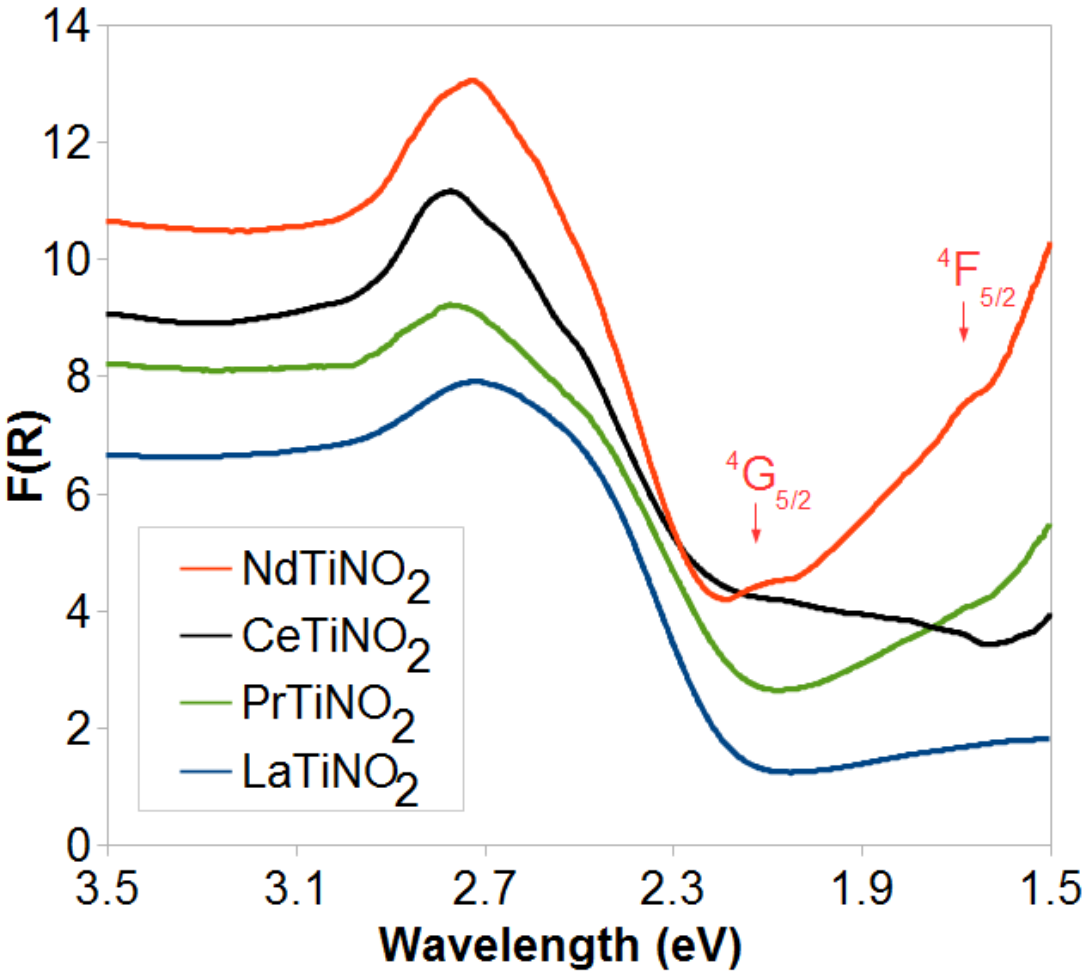

Figure 3.6: Kubleka-Munk transformed UV-visible diffuse reflectance of RTiNO$_2$ - These spectra have not been vertically offset from each other.

in neutron powder diffraction patterns [(83)]) would lead to some absorption in that region, but for the reasons discussed below we feel this is not the main contributor to the sub-band gap absorptions. A more likely cause of this effect is the presence of low levels of Ti^{3+} in the perovskite phase, which could be explained either by anion vacancies, or by $R\mathrm{TiN}_{1+x}\mathrm{O}_{2-x}$ non-stoichiometry. In fact, the slow fourth decay component in the TRIR study hints at such defects. Sub-band gap absorptions, associated with the presence of small amounts of Ti^{3+}, that extend into the mid-IR have been seen in the $\mathrm{TiO}_x\mathrm{N}_y\mathrm{F}_z$, system.[(129)] The upturn of absorbance seen in the low energy side of the absorption spectra increases significantly from LaTiNO_2 to PrTiNO_2 to NdTiNO_2. In addition to the electronic transitions already discussed, weak features associated with f-f transitions are seen in the NdTiNO_2 spectrum. The peaks at 2.1 and 1.6 eV can be assigned to $^4\mathrm{G}_{5/2}$ and $^4\mathrm{F}_{5/2}$ f-f transitions on Nd^{3+}. Because f-f transitions are forbidden, these transitions are very weak.

3.3.6 Photocatalytic Activity for Water Oxidation

The photocatalytic O_2 evolution activity for $R\mathrm{TiNO}_2$ (R = La, Ce, Pr, Nd) and SrTiO_3 samples impregnated with a 2 wt.% CoO_x co-catalyst over a period of eight hours is shown in Figure 3.7. In these experiments a long pass filter as well as a cold mirror were used so that only visible light (800 nm $> \lambda >$ 400 nm) reached the photocatalyst. The results of photocatalytic cycling (3×) experiments can be found in APPENDIX C, Figure C.11. Trace amounts of nitrogen were detected at the initial illumination onset, which is associated with the removal of surface nitrogen, a typical phenomenon in nitride oxides.[(122)] The linear rates of O_2 evolution are found to be 17 μmol/g/hr for LaTiNO_2, 5 μmol/g/hr for CeTiNO_2, 11 μmol/g/hr for PrTiNO_2, 16 μmol/g/hr for NdTiNO_2, and negligible for SrTiO_3.

Prior studies of photocatalytically driven water oxidation by LaTiNO_2, with a CoO_x co-catalyst, report a much higher rate of O_2 evolution (∼600 μmol/hr).[(53)] The decrease in activity is owed in large part to the change in lamp wattage (ref. [(53)] = 300 W; this study = 150 W). For a 300 W Xe arc lamp, power density is typically close to 50 mW/cm^2 (∼ 6 suns). Using a Thor Labs Si photodectector, the measured power density of our 150 W Xe lamp was 26 μW/cm^2 (∼ 0.5 suns). Differences in the intensity of the light source can have a dramatic effect on photocatalytic evolution rates.[(130)] At high light intensity (> 150 W or AM1.5), the photocurrent increases

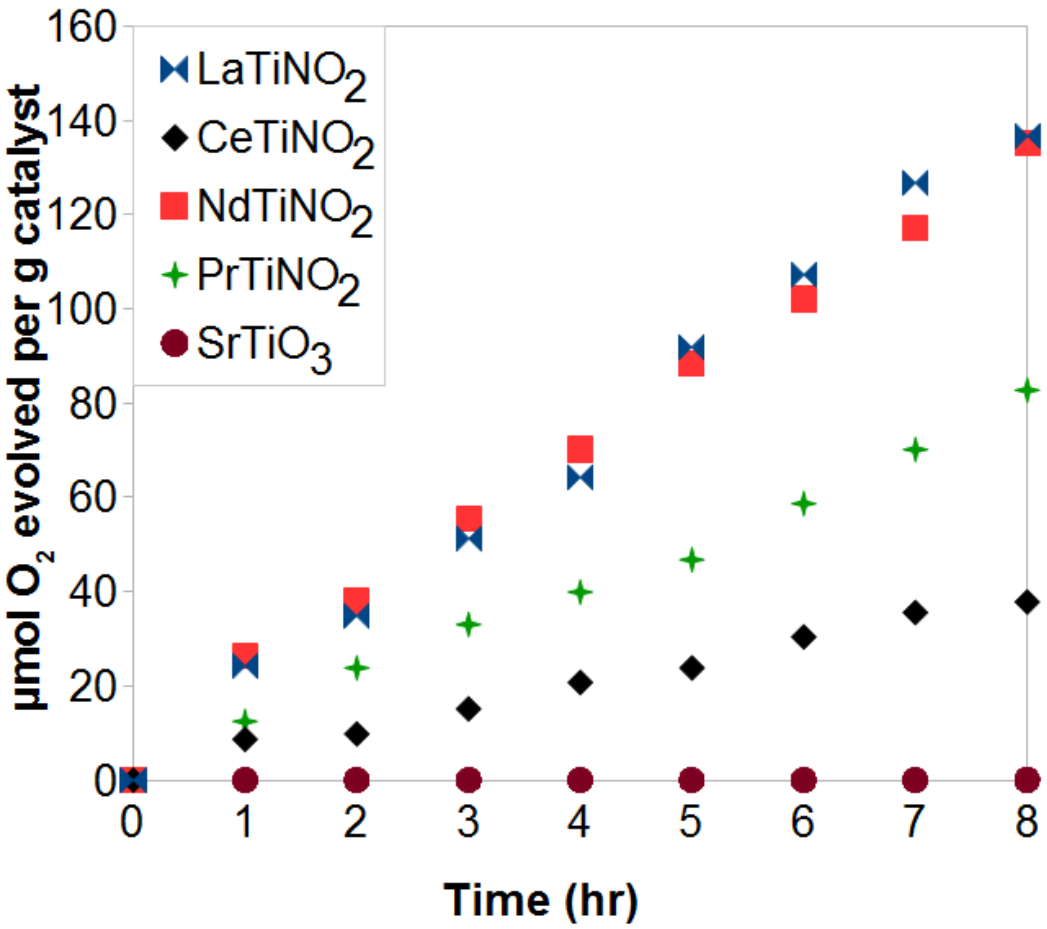

Figure 3.7: Photocatalytic O_2 evolution for 2 wt. % CoO_x co-catalyst modified compounds *R*$TiNO_2$ and $SrTiO_3$ - 100 mg photocatalyst and 100 mg La_2O_3 (pH buffer) were suspended in 100 mL of a 0.05M $AgNO_3$ solution contained within a closed quartz vessel.

are not linear.[(131)] High photocurrents increase the likelihood of charge transfer from semiconductor to co-catalyst before recombination occurs. This charge separation for water splitting is critical as demonstrated in a homojunction $BiVO_4$/a-Si photoelectrochemical cell.[(132)] Accounting for this, $LaTiNO_2$ yields results that are in-line with what should be expected from lower power density light. One must also acknowledge that the sample morphologies indicated by SEM and BET are distinct from those mentioned in the investigation of $LaTiNO_2$ by Zhang *et al.*,[(53)] another factor that makes direct comparison to that work non-trivial. The key finding in this paper is relative rates of O_2 evolution for the four oxide nitride photocatalysts studied. In relative terms, the photocatalytic activity order is $LaTiNO_2 \sim NdTiNO_2 > PrTiNO_2 > CeTiNO_2$. Given the already established behavior of $LaTiNO_2$ as an effective photocatalyst for the oxygen evolution half-reaction, this result shows that $NdTiNO_2$ is equally promising, whereas $PrTiNO_2$ and particularly $CeTiNO_2$ are inferior. For the most part the variability in the photocatalytic rates of the RTiNO$_2$ compounds studied here is not due to differences in particle size and/or shape, as these compounds have similar surface areas, pore volumes, pore sizes, distributions, and morphologies. Neither is it due to the band gap or the position of the conduction or valence band edges, which are also quite similar across the entire series. Although there may be slight variations in absorption coefficient for each compound, those differences alone cannot explain the differences in photocatalytic activity. The differences in photocatalytic rates appear to be linked to the presence of partially filled f-orbitals either in the band gap or near the top of the valence band. Because both Ce and Pr have occupied and highly localized 4f states (flat bands) that are energetically accessible to the photogenerated holes this leads to unwanted recombination of the free carriers. In contrast, the 4f orbitals of La^{3+} must lie well above the valence band, and the occupied 4f-orbitals on $NdTiNO_2$ are positioned well below the valence band edge, as shown in Figure 3.8. Consequently, these two compounds have comparable activities for the oxidation of water.

The recombination of carriers is evidenced by the slow component of the carrier lifetimes in $NdTiNO_2$ (798 ps) and $LaTiNO_2$ (1110 ps), values that are considerably longer than in $PrTiNO_2$ (330 ps) and $CeTiNO_2$ (170 ps). The relatively long carrier lifetime allows carriers enough time to be transferred from the bulk to the surface deposited cobalt co-catalyst, where it then undergoes the cascade of processes that must occur for water oxidation. By proxy, the $PrTiNO_2$ and $CeTiNO_2$ suffer from higher

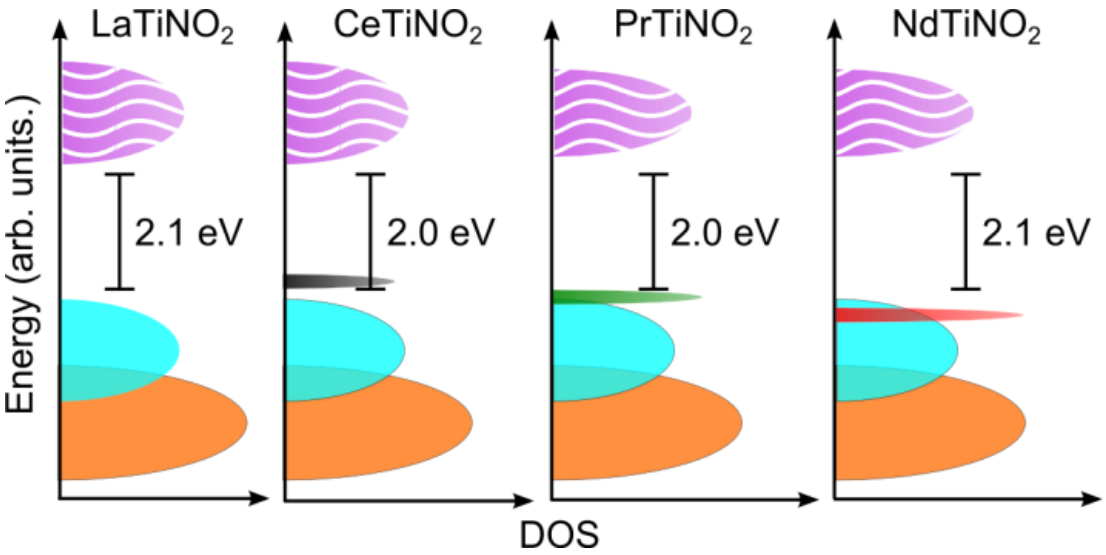

Figure 3.8: Schematic diagrams for the DOS in RTiNO$_2$ perovskites - Orbitals are split into a filled oxygen 2p (orange)/nitrogen 2p (cyan) valence band and an unfilled Ti 3d (wavy violet) conduction band. The localized f-orbital states decrease in energy sequentially for Ce (black), Pr (green), and Nd (red).

rates of carrier recombination before efficient transfer can occur, directly yielding lower rates of water oxidation. These results show that prediction or measurement the f-orbital states with respect to the valence band maximum should be part of the process of designing new lanthanoid-containing perovskite nitride oxide photocatalysts. Good candidate compounds should yield f-orbitals that do not fall close to the band edge positions. Many of the heavier rare-earth ions have f-orbital positions known to be more negative than Nd^{3+}.[(133)] Therefore, compositions such as RTi(N,O)$_x$ (R = Sm, Gd, Ho – Lu) may provide interesting or superior photocatalytic activities because the f-orbitals would reside below the valence band maximum. It is pertinent to note that LaTiNO$_2$ and NdTiNO$_2$ have similar photocatalytic activities, despite the fact that the latter appears to have a larger concentration of Ti^{3+}. This observation would seem to suggest that while the presence of Ti^{3+} states leads to increased absorption of visible light it does not have a significant impact on the photocatalytic activity. A systematic study on water reduction by the RTiNO$_2$ (R = Ce – Nd) compounds was not undertaken in this work. However, the electronic data presented here suggests that water reduction results for NdTiNO$_2$ would be similar to those of LaTiNO$_2$, with CeTiNO$_2$ and PrTiNO$_2$ results inferior due to rapid carrier recombination rates.

3.4 Conclusion

The photocatalytic properties of the $R\mathrm{TiNO_2}$ (R = Ce – Nd) perovskites have characterized for the first time. The band gaps of all four compounds lie between 2.0 – 2.1 eV, which allow them to absorb a significant fraction of the visible spectrum. When powders of these compounds are impregnated with 2 wt. % cobalt co-catalyst they are capable of photocatalytic water oxidation. The oxygen evolution rates are 5 – 17 μmol/hour/g under illumination from a 150 W Xe arc lamp ($400 < \lambda < 800$ nm), with the activities following the trend: La $\sim$ Nd $>$ Pr $>$ Ce. XPS measurements show that the 4f-orbitals play a critical role in photocatalytic activity. When they lie near the top of the valence band, as is the case for Ce and Pr, photocatalytic activities decrease because the partially filled 4f orbitals act as recombination centers. TRIR kinetic decays reveal that the Ce and Pr compounds have much shorter carrier lifetimes. The O_2 evolution rates in $\mathrm{NdTiNO_2}$ are comparable to $\mathrm{LaTiNO_2}$, which makes this compound a candidate for further optimization as a water oxidation photocatalyst and demonstrates the viability of other possible $R\mathrm{TiNO_2}$ photocatalysts.

4

Structural, Magnetic, and Optical Properties of $A_3V_4(PO_4)_6$ (A = Mg, Mn, Fe, Co, Ni)

4.1 Introduction

Transition metal containing phosphate compounds have a wealth of interesting magnetic and exchange interactions. For instance, $Fe_3(PO_4)_2$ has two observed magnetic phase transitions, a field-induced ferrimagnetic-antiferromagnetic transition at 38(1) K and an antiferromagnetic-paramagnetic transition at 44(1) K. [(77)] $Ni_3(PO_4)_2$ has ferromagnetic interactions inside Ni_3O_{14} trimeric subunits which are antiferromagnetically coupled, giving rise to a purely antiferromagnetic structure. [(78)]

The number of studies examining magnetism in the V^{+3}-O-P system, however, is limited and even conflicting. For instance, reports on VPO_4 show antiferromagnetic behavior below 15 K, [(81)] while a later report suggests ferromagnetic behavior below 15 K. [(80)]. This discrepancy is compounded by a general lack of quaternary phosphate compounds containing V^{+3}. To bolster the number of compounds in this class, the $Fe_7(PO_4)_6$ structure type has been utilized to prepare compounds of the type $A_3V_4(PO_4)_6$ where A = Mg, Mn, Fe, Co, and Ni.

$A_3V_4(PO_4)_6$ is structurally comprised of two kinds of subunits (A_2O_{10} and V_2O_{10}) that are connected in a corrugated fashion. On the other hand, VPO_4 consists of edge shared octahedral 1D chains isolated by phosphate tetrahedra. These two contrasting

structural moieties, with reduced linearity of the vanadium polyhedral connectivity in going from VPO_4 to $A_3V_4(PO_4)_6$, raises questions pertaining to structural effects and the length of exchange interactions. Furthermore, the impact of nonmagnetic (Mg) or magnetic (Mn, Fe, Co, Ni) A_2O_{10} subunits on the exchange interactions can be studied.

Beyond magnetism, d-d transitions are expected in $A_3V_4(PO_4)_6$ and a thorough investigation of the optical properties driving the observed colors is warranted.

4.2 Experimental

$A_3(PO_4)_2$ (A = Mg, Mn, Fe, Co) precursors were prepared by solution methods involving stoichiometric dropwise addition of aqueous (0.1 – 0.3 M) $Na_3PO_4{\cdot}12H_2O$ (99.7%; Fischer Scientific) to (0.1 – 0.3 M) $Mg(NO_3)_2{\cdot}6H_2O$ (98%; Flynn Sci.),$(NH_4)_2Fe(SO_4)_2{\cdot}6H_2O$ (99.9%; Mallinkrodt), $CoSO_4$ (98%; Damon-Guide), or $MnCl_2{\cdot}4H_2O$ (99.7%; Mallinkrodt), resulting in precipitation. These powders were collected and dried overnight at 100 °C in air. The Mg and Mn containing powders were subsequently heated to 700 °C to drive off the remaining coordinated water and to achieve crystallization. To prevent oxidation, $Fe_3(PO_4)_2$ was heated under flowing H_2/N_2 (5/95%) at 900 °C for 15 h with a 2.5 °C/min ramp rate.[(77)] The $Ni_3(PO_4)_2$ precursor was prepared by solid state heat treatment, where $Ni(NO_3)_2{\cdot}6H_2O$ (99.8%; Mallinkrodt) and $(NH_4)H_2PO_4$ (98%+; Sigma Aldrich) were ground together using a mortar and pestle for 30 min first, and then heated in air at 300 °C for 1 h with 5°C/min ramp/cool rates and with a follow-up treatment at 800 °C for 10 h with 2.5/15 °C/min ramp/cool rates. VPO_4 was prepared by a similar approach, where $VO(SO_4){\cdot}3H_2O$ (99.9%; Alfa Aesar) and$(NH_4)H_2PO_4$ were ground together and then heated under flowing H_2/N_2 (5/95%) to 900 °C for 5 h with 5 °C/min ramp/cool rates. Heating and intermittent grinding were repeated until phase pure VPO_4 was obtained. All precursors were checked and verified by X-ray diffraction (XRD) for purity. Stoichiometric amounts of $A_3(PO_4)_2$ and VPO_4 precursors were mixed together using a mortar and pestle, uniaxially pressed into pellets at 104 MPa, and sealed in an evacuated quartz tube. This tube was heated to 1050 °C for 10 h with a 2.5 °C/min ramp and a 10°C/min cool rate to achieve phase pure products.

The purity of each compound was assessed through Rietveld refinements on powder X-ray diffraction data obtained from a Bruker D8 Advance (Ge monochromator, Cu

Kα_1, 10 – 65° 2θ, 0.015° step size, and 1 s dwell time; Appendix D, Figure D.1 – D.5). Constant wavelength ($\lambda = 2.4395$ $\AA$) neutron powder diffraction (NPD) data were obtained at room temperature over a d-space range of 1.25 to 20 $\AA$ on the ECHIDNA powder diffractometer at the OPAL research reactor in Australia. For synchrotron X-ray diffraction (SXRD) analysis, samples were packed into 1.5 mm diameter Kapton capillaries, and data were collected at room temperature over 1 – 50° 2θ (scan parameters, $\lambda \approx 0.4133$ $\AA$) on the 11-BM [(134)] at Argonne National Laboratory. Combined NPD and SXRD Rietveld refinements were performed using GSAS with the EXPGUI interface [(93)]. Isotropic displacement parameters for the oxygen about a phosphorous tetrahedron were constrained to refine together. Cation displacement parameters (except vanadium) were refined together. Due to high V transparency to neutrons, V displacement parameters were constrained to match the A-site cation parameters, in each compound, respectively. To account for order/disorder on the cation sites, occupancies of the transition metals were allowed to refine freely. Sites that deviated from unity were accounted for, and constraints were implemented to maintain stoichiometry.

DC magnetic measurements were carried out using a Quantum Design MPMS SQUID magnetometer. Less than 50 mg of powder sample was encapsulated in a gel capsule and mounted at the center of a straw for insertion into the instrument. The susceptibility was measured in the range of 2.5 – 400 K in an applied magnetic field of 1000 Oe under both zero-field-cooled (ZFC) and field-cooled (FC) conditions. For ZFC measurements, the sample was cooled from 300 K in the absence of an applied field, and the susceptibility was measured during warming in a field of 1000 Oe. For FC measurements, the sample was subject to the same cooling and heating in the presence of an applied field of 1000 Oe. Isothermal magnetization was measured between –7 T and 7 T at 5 K and 300 K, respectively.

UV-visible diffuse reflectance data were collected using an Ocean Optics USB4000-UV-Vis spectrometer equipped with a standard reflectance probe and a DH-2000-BAL deuterium/tungsten halogen light source. Data were generated using SpectroSuite software and then transformed by the Kubelka-Munk method [(135)] for subsequent interpretation.

4.3 Results

4.3.1 Crystal Structure

It was found that this class of compounds crystallizes with $P\bar{1}$ symmetry. The A cations reside in a distorted octahedral site and a distorted trigonal bipyramidal site. The two polyhedra are connected through a common corner and form an A_2O_{10} unit. On the other hand, the V^{3+} cations reside in a V_2O_{10} unit comprising two edge-sharing octahedra. These two kinds of subunits (A_2O_{10} and V_2O_{10}) are connected in a corrugated fashion by sharing edges (VO_6 and AO_5) and corners (VO_6 and AO_6) (Figure 4.1). The structure is then connected together by three kinds of crystallographically distinct PO_4 tetrahedra (Figure 4.2). The structure resembles another known quaternary V^{3+} containing phosphate compound, $Zn_3V_4(PO_4)_6$. [(68)]

Synchrotron X-ray diffraction was further utilized to accurately determine the positions of the atoms, while neutron diffraction was conducted to refine oxygen positions and cation site occupancies. Determination of thermal parameters is benefited by using both data sets. Also, in a low symmetry space group such as $P\bar{1}$ in this case, simultaneous refinements increase the number of degrees of freedom available in the refinement and lessen the chance of confounded results.

Combined Rietveld refinements on the room temperature synchrotron X-ray and neutron diffraction data for $A_3V_4(PO_4)_6$ result in R_{wp} = 5.32 – 6.73% for the NPD data and R_{wp} = 10.60 – 17.52% for SXRD data, with the poor fits of the latter due to the presence of unfitted peaks associated with a secondary phase. The peaks were identified (Appendix D, Table D.1), but could not be matched to any known compounds in the Inorganic Crystal Structure Database (ICSD). The secondary phases observed in each compound is unique. It should be noted that these secondary phases, if active, may contribute to the magnetic properties. These will contribute random error in the examined system. Nonetheless, R_F^2 values for the $A_3V_4(PO_4)_6$ series are in general low and indicate good fits of the experimental data.

The refined lattice parameters and cell volumes for $A_3V_4(PO_4)_6$ (Table 4.1) are similar to those of $Zn_3V_4(PO_4)_6$. The refined SXRD and NPD patterns for $Mn_3V_4(PO_4)_6$ are shown in Figure 4.3 (others: Appendix D, Figures D.6 – D.9), and atomic positions as well as thermal parameters are presented in Table 4.2 (others: Appendix D, Table D.2 – D.5).

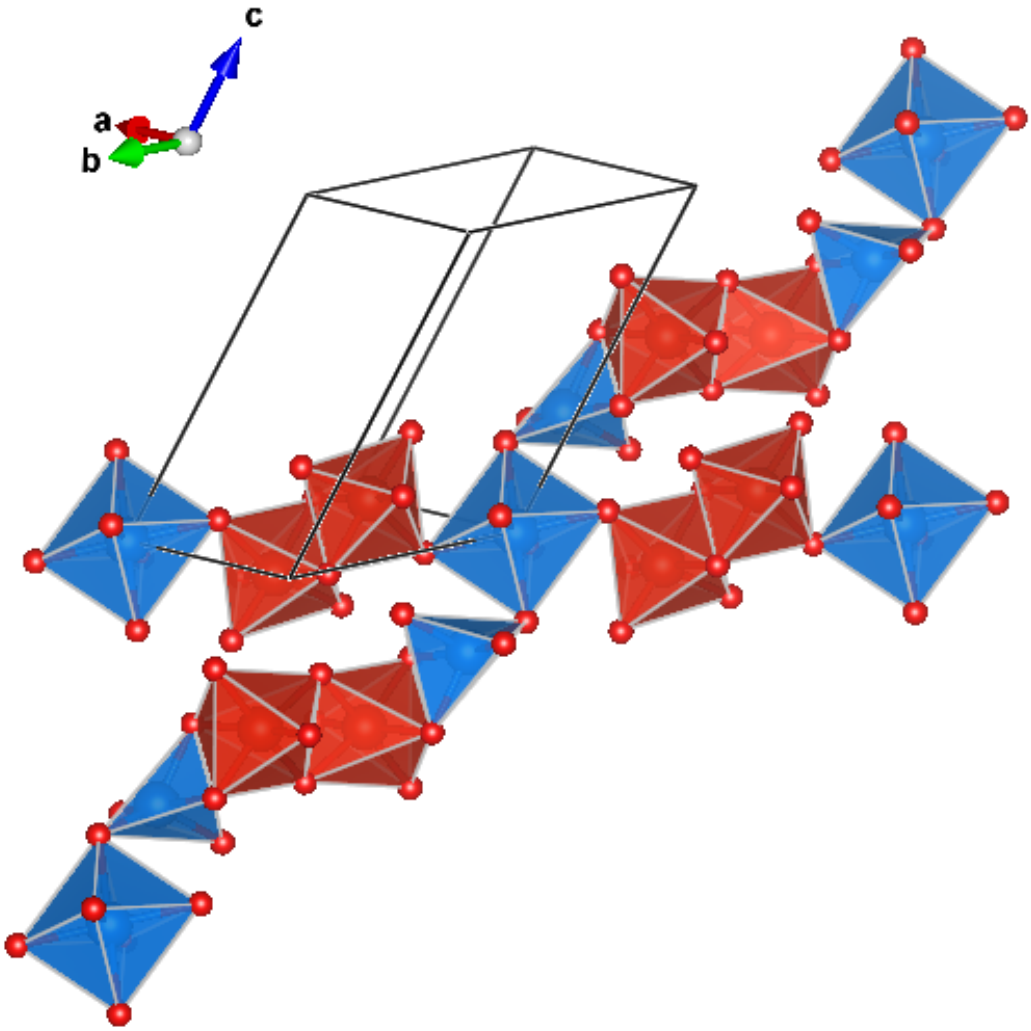

Figure 4.1: $A_3V_4(PO_4)_6$ crystal structure viewed along the canted (1-10) direction, showing polyhedral connectivity - PO_4 tetrahedra are not shown to enhance clarity of the *A*- (blue) and *B*-site (red) polyhedra.

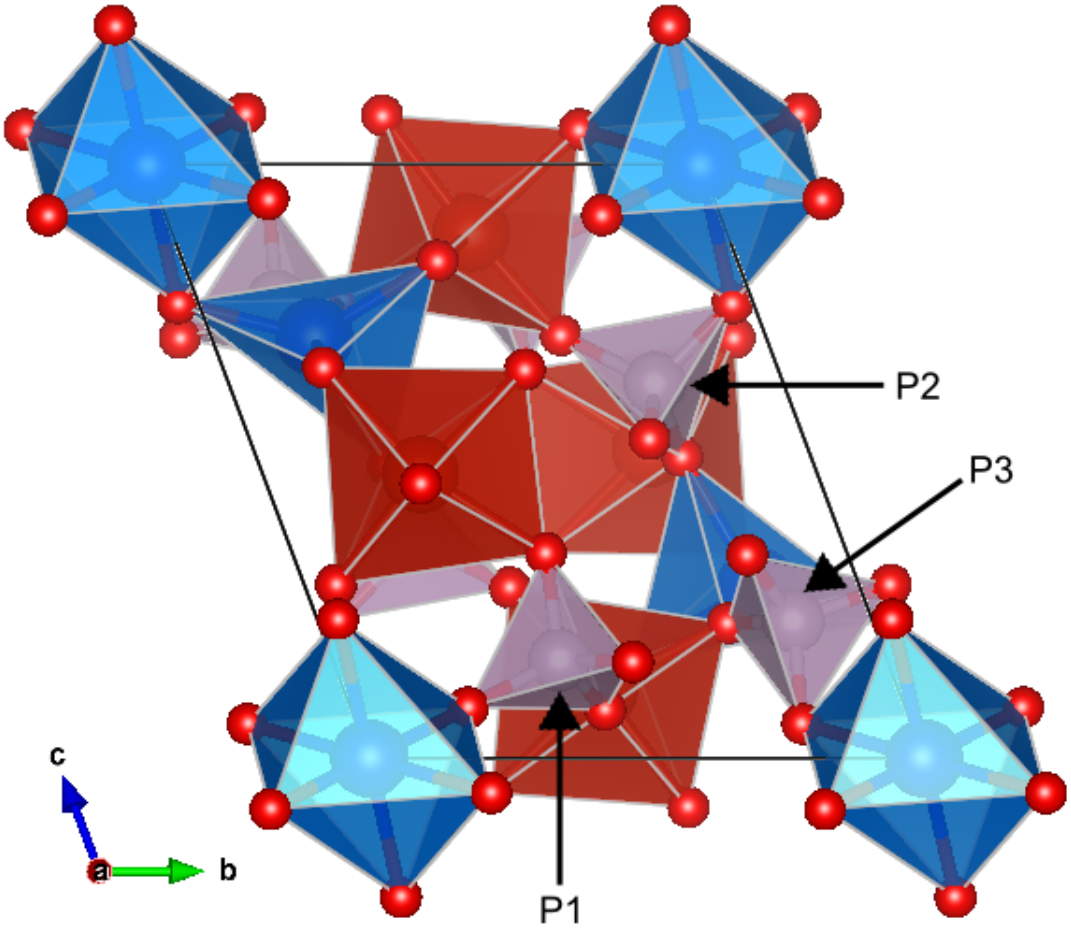

Figure 4.2: $A_3V_4(PO_4)_6$ crystal structure viewed down (100) - crystallographically unique PO_4 tetrahedra are labeled relative to the A- (blue) and B-site (red) polyhedra.

Compound	$Mg_3V_4(PO_4)_6$	$Mn_3V_4(PO_4)_6$	$Fe_3V_4(PO_4)_6$	$Co_3V_4(PO_4)_6$	$Ni_3V_4(PO_4)_6$
Space group			$P\bar{1}$		
a (Å)	6.32597(3)	6.38063(1)	6.37023(2)	6.34839(2)	6.31394(3)
b (Å)	7.89686(4)	8.09194(1)	7.97114(2)	7.89159(2)	7.88683(4)
c (Å)	9.28860(4)	9.36507(1)	9.35541(3)	9.31907(2)	9.25525(5)
α (Å)	105.25(2)	106.15(2)	106.04(2)	105.31(2)	105.32(2)
β (Å)	108.61(2)	108.18(2)	108.39(2)	108.68(2)	108.70(2)
γ (Å)	101.28(2)	102.02(2)	101.57(2)	101.48(2)	101.22(2)
V (Å^3)	403.945(4)	417.591(1)	411.136(2)	405.501(2)	400.894(4)
# var.			94		
χ^2	6.64	10.78	26.08	17.99	22.22
$R_{wp,\ TOTAL}$ (%)	9.87	10.83	16.84	14.3	15.90
$R_{p,\ TOTAL}$ (%)	7.41	8.13	9.61	8.58	9.79
$R_{wp,\ NPD}$ (%)	5.98	5.32	6.53	5.93	6.73
$R_{p,\ NPD}$ (%)	4.88	4.29	5.09	4.65	5.26
$R_{F^2,\ NPD}$ (%)	5.33	5.16	6.37	7.78	10.20
$R_{wp,\ sXRD}$ (%)	10.60	11.27	17.52	14.86	16.49
$R_{p,\ sXRD}$ (%)	8.15	9.13	10.78	9.55	10.81
$R_{F^2,\ sXRD}$ (%)	3.52	7.39	6.30	4.83	6.41

Table 4.1: Lattice parameters and goodness of fit for $A_3V_4(PO_4)_6$, where A = Mg, Mn, Fe, Co, and Ni.

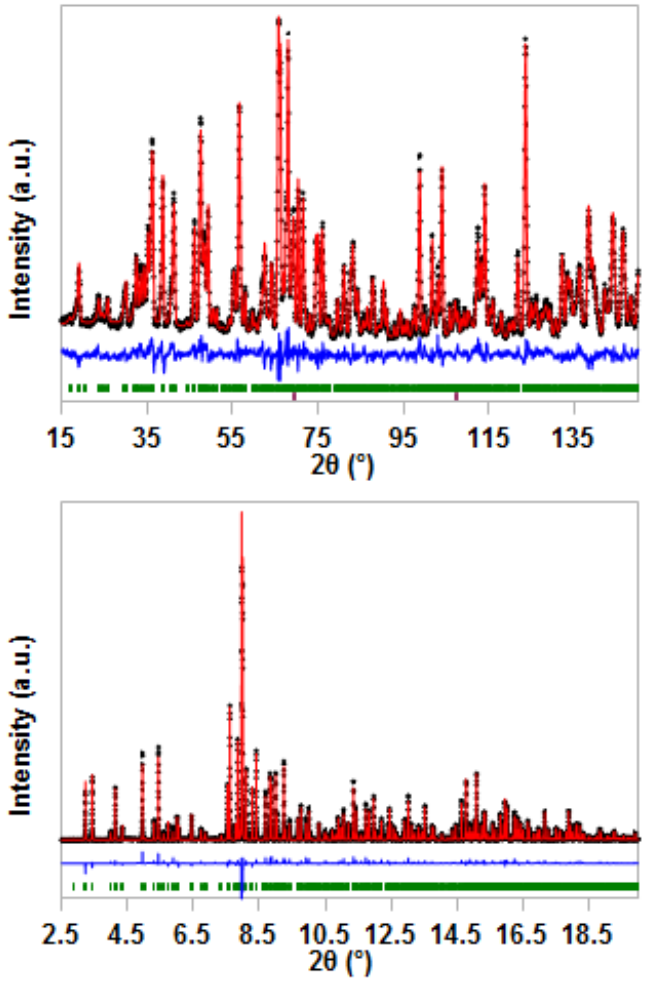

Figure 4.3: Combined room temperature NPD (top) and SXRD (bottom) Rietveld refinements of $Mn_3V_4(PO_4)_6$. - Observed (black dots), calculated (red), difference (blue), indexed peaks (green vertical bars), and vanadium sample can (purple vertical bars) are compared.

Atomic position(s)						
ion	site	x	y	z	occ	U_{iso} (Å^2)
Mn1	1a	0	0	0	1	0.0044(3)
Mn2/V1	2i	0.2852(2)	0.8175(1)	0.2898(1)	0.87/0.13	0.0044(3)
V2/Mn3	2i	0.3851(2)	0.4619(1)	0.1129(1)	0.87/0.13	0.0044(3)
V3	2i	0.9546(2)	0.2861(1)	0.4740(1)	1	0.0044(3)
P1	2i	0.2213(3)	0.1484(2)	0.7630(2)	1	0.0049(3)
P2	2i	0.0966(3)	0.5927(2)	0.8347(2)	1	0.0006(4)
P3	2i	0.6034(3)	0.7623(2)	0.6350(2)	1	0.0058(5)
O1	2i	0.2181(5)	0.2086(4)	0.9378(3)	1	0.0044(5)
O2	2i	0.0118(5)	0.1832(4)	0.6488(3)	1	0.0044(5)
O3	2i	0.4561(5)	0.2728(4)	0.7710(3)	1	0.0044(5)
O4	2i	0.2074(5)	0.9493(4)	0.7037(3)	1	0.0044(5)
O5	2i	0.8791(5)	0.4611(4)	0.8371(3)	1	0.0075(5)
O6	2i	0.0640(5)	0.5371(4)	0.6494(3)	1	0.0075(5)
O7	2i	0.3097(5)	0.5380(4)	0.9216(3)	1	0.0075(5)
O8	2i	0.1267(5)	0.7881(4)	0.9183(3)	1	0.0075(5)
O9	2i	0.5517(5)	0.6328(4)	0.7218(3)	1	0.0068(5)
O10	2i	0.7279(5)	0.9525(4)	0.7622(3)	1	0.0068(5)
O11	2i	0.3655(5)	0.7580(4)	0.5104(3)	1	0.0068(5)
O12	2i	0.7518(5)	0.7073(4)	0.5366(3)	1	0.0068(5)

Table 4.2: Atomic positions, site occupation, and thermal parameters of room temperature $Mn_3V_4(PO_4)_6$.

4.3.2 Magnetic Properties

For all $A_3V_4(PO_4)_6$ samples, DC magnetic susceptibility measured under ZFC and FC conditions overlap over the entire studied temperature range (2.5 – 400 K). A cusp is present at 15 K for A = Fe, Co and 12.5 K for A = Mn, Ni, indicating an antiferromagnetic type transition ($Co_3V_4(PO_4)_6$: Figure 4.4, left y-axis; others: Appendix D, Figure D.10 – D.13). The inverse susceptibility in the paramagnetic region (100 – 400 K for A = Mn, Fe, Co, Ni and 150 – 400 K for Mg) follows the Curie-Weiss law, and the extracted effective moments and Weiss constants are summarized in the table below. The experimentally obtained effective moments are in good agreements with the ones calculated using the formula:

$$\mu_{eff} = (3 \cdot \mu_{spin}(A^{2+})^2 + 4 \cdot \mu_{spin}(V^{3+})^2)^{1/2} \tag{4.1}$$

and assuming high spin A^{2+}(Table 4.3). Differences can be accounted for by the combined effect of a negative orbital contribution from V^{3+} and a positive orbital contribution from Fe^{2+}, Ni^{2+}, and Co^{2+}. The absolute values of the Weiss constants for $A_3V_4(PO_4)_6$ with A = Mn, Fe, Co, and Ni are larger than the observed T_N, and the most negative θ_W is found in $Mg_3V_4(PO_4)_6$ with nonmagnetic Mg^{2+}. This indicates that vanadium spins couple in an antiferromagnetic way, whereas magnetic A^{2+} introduces ferromagnetic interactions. The isothermal magnetization at 5 K agrees with the χ(T) measurement and supports antiferromagnetic ground states ($Co_3V_4(PO_4)_6$: Figure 4.5; others: Appendix D, Figure D.14 – D.16). The irreversibility displayed by $Fe_3V_4(PO_4)_6$ is attributed to tiny amount of unknown magnetic secondary phase.

Compound	Magnetic type	T_N (K)	θ_W (K)	Exp. μ_{eff} (μB)	Calc. μ_{eff} (μB)
$Mg_3V_4(PO_4)_6$	Paramagnetic	N/A	–66.6	5.20	5.66
$Mn_3V_4(PO_4)_6$	Antiferromagnetic	12.5	–37.5	11.00	11.70
$Fe_3V_4(PO_4)_6$	Antiferromagnetic	15	–36.2	10.10	10.20
$Co_3V_4(PO_4)_6$	Antiferromagnetic	15	–29.3	9.83	8.77
$Ni_3V_4(PO_4)_6$	Antiferromagnetic	12.5	–50.1	8.14	7.48

Table 4.3: Magnetic properties of $A_3V_4(PO_4)_6$ where A is Mg, Mn, Fe, Co, Ni.

Neutron diffraction data at low temperature were obtained to shine light on the magnetic structures in the ordered state for $A_3V_4(PO_4)_6$ with A = Mn, Fe, Co, and

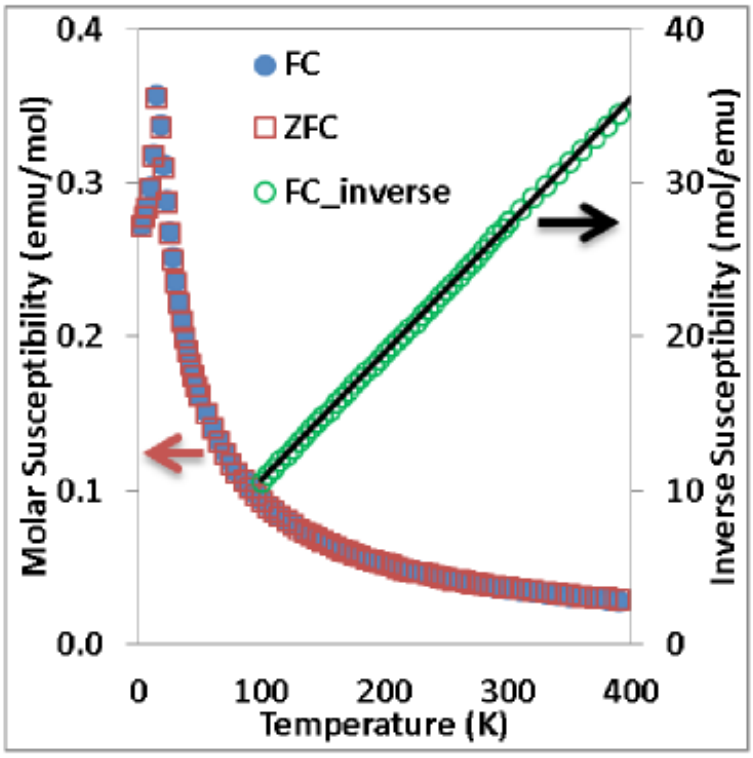

Figure 4.4: χ**(T) (left y-axis) and** χ^{-1}**(T) (right y-axis) for** $Co_3V_4(PO_4)_6$**.** - arrows indicate which axis sample data pertains to.

Ni. Extra reflection peaks due to a magnetic contribution are found. Attempts to index these peaks failed, however, to yield simple propagation vectors to describe the magnetic structures. Considering that the nuclear structure is already complicated by low symmetry, solving the magnetic structure from scratch does not seem feasible in the short term and will not be covered in this work.

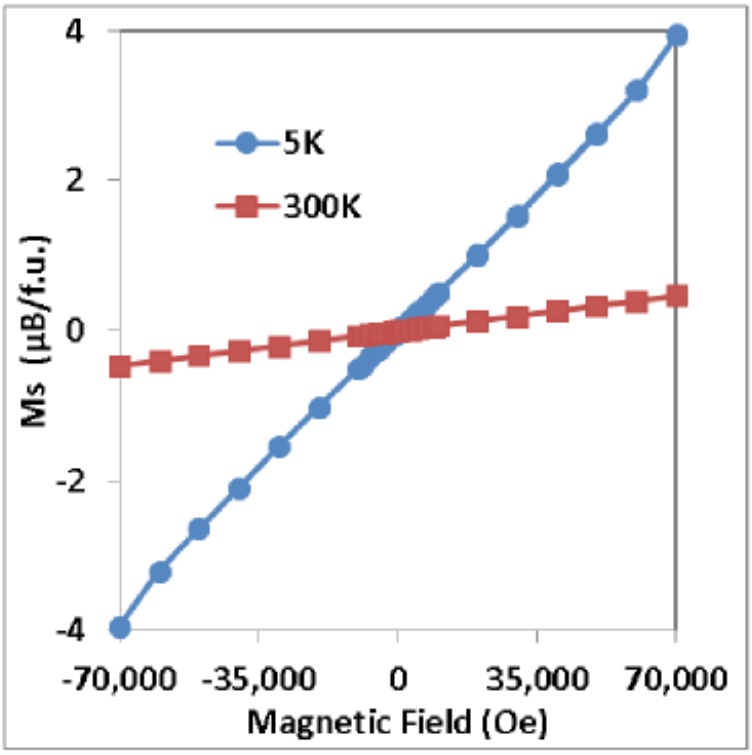

Figure 4.5: Isothermal magnetization of $Co_3V_4(PO_4)_6$ - remanent magnetization is not observed

4.3.3 UV-Visible Diffuse Reflectance

Diffuse reflectance spectra enable the quantitative comparison of optical properties of the $A_3V_4(PO_4)_6$ compounds (Figure 4.6). The observed colors for Mg, Mn $\rightarrow$ Ni are light lime green, brown, brown, green, and tan (Figure 4.7). The variations in color are due to differences in sub-band gap absorptions caused by d-d transitions (when allowed). The absorption coefficient for the compounds was not measured. Differences in the absorption coefficients for the individual $A_3V_4(PO_4)_6$ compounds, however, at

energies greater than the band gap should be minimal because they have very similar crystal and thus electronic structures.

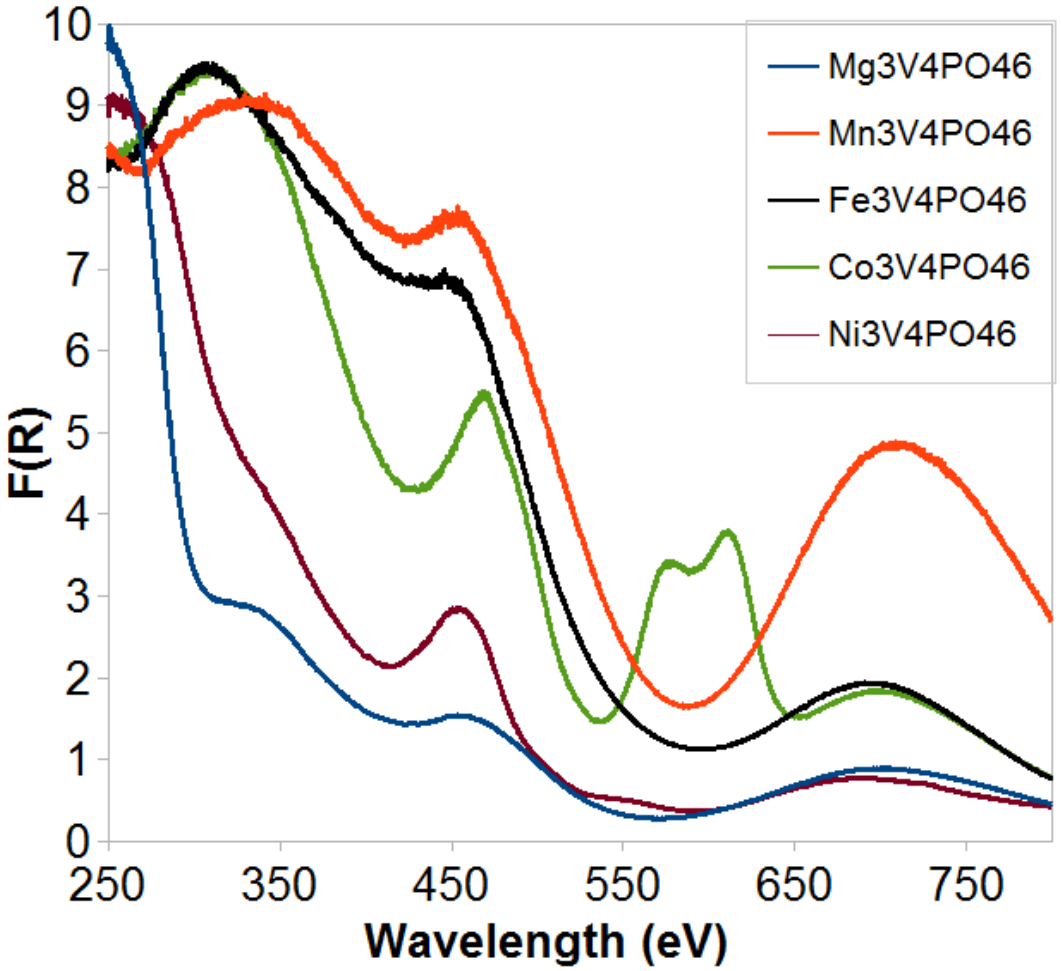

Figure 4.6: Kubelka-Munk transformed UV-visible diffuse reflectance for $A_3V_4(PO_4)_6$ compounds - See chart key for sample identification.

There are 3 transitions associated with V^{3+} which are systematically present in all of the $A_3V_4(PO_4)_6$ series and are most obvious in the Mg analog with peaks at 330, 460, and 700 nm. These peaks correspond to the $^3T_{1g}(F) \rightarrow {}^3T_{2g}$, $^3T_{1g}(F) \rightarrow {}^3T_{1g}(P)$, and $^3T_{1g}(F) \rightarrow {}^3A_{2g}$ transitions, respectively. In the $Mn_3V_4(PO_4)_6$ and $Fe_3V_4(PO_4)_6$ compounds, the only observable transitions are those relating to V^{3+}. In the Mn analogue the d-d transitions are spin and Laporte forbidden and therefore weak. In $Fe_3V_4(PO_4)_6$, the transitions are also weak and washed out by the V^{3+} transitions.

Figure 4.7: Photographs of $A_3V_4(PO_4)_6$ powder samples - Captured via a 10 MP camera under direct fluorescent light.

The d-d transitions in A = Co [580 nm, $^4T_1(F) \rightarrow {}^4A_2$; 610 nm, $^4T_1(F) \rightarrow {}^4T_1(B)$] and Ni [550 nm, $3A_{2g} \rightarrow {}^3T_{1g}(P)$] are observed, though weaker in the latter case. Relative F(R) values within the $A_3V_4(PO_4)_6$ series increase where Mg > Ni > Co > Fe > Mn and is the result of increased fluorescence due to unpaired electrons.

4.4 Discussion

Average bond distances of the A-O, V-O, and P-O bonds are listed in Table 4.4. The P-O distances of the PO_4 within the $A_3V_4(PO4)_6$ framework are very close, with the values falling into Baur's initial survey results of 1.506 to 1.572 $\mathring{A}$ [(14)] The average metal-oxygen bond distances are also in-line with expectations for both octahedral and trigonal bipyramidal configurations. Bond-valence-sum (BVS) values suggest that oxidation states for the cations are within 5% of expected values.

	$Mg_3V_4(PO_4)_6$	$Mn_3V_4(PO_4)_6$	$Fe_3V_4(PO_4)_6$	$Co_3V_4(PO_4)_6$	$Ni_3V_4(PO_4)_6$
A1-O	2.108(3)	2.207(3)	2.179(5)	2.128(4)	2.100(5)
A2-O	2.037(4)	2.118(3)	2.084(5)	2.043(4)	2.020(6)
V1-O	2.012(3)	2.007(3)	1.997(5)	1.993(4)	2.016(6)
V2-O	1.991(3)	2.007(3)	2.000(5)	2.006(4)	2.000(6)
P1-O	1.556(3)	1.558(3)	1.553(5)	1.560(4)	1.553(6)
P2-O	1.554(3)	1.555(3)	1.555(5)	1.561(5)	1.549(6)
P3-O	1.555(3)	1.549(3)	1.555(5)	1.552(4)	1.560(6)

Table 4.4: Average bond distances ($\mathring{A}$) in $A_3V_4(PO_4)_6$.

The A cation in an octahedron is the only special site (1a) in the low symmetry space group ($P\bar{1}$), and the positions of the remaining cations and anions are allowed to refine freely. Given this freedom, the coordination polyhedra are prone to distortion. Although the average bond distances result in reasonable BVS values, the Baur's distortion values (D, Table 4.5) for different polyhedra suggest variable local geometries. For example, in an octahedron where all six bonds are equal in length, the D is zero, while in a typical perovskite with corner-connected octahedral, the D is about 0.00##, where # is an integer. The level of distortion in $A_3V_4(PO_4)_6$, though elevated, matches compounds with similar edge-sharing octahedral geometries such as $Fe_2(PO_4)_2$ (D = 0.0168 – 0.0415), VPO_4 (D = 0.0333), and $Fe_7(PO_4)_6$ (D = 0.0310 – 0.0490). Individual bond distances (Appendix D, Table D.6) show varied distances for each polyhedral

M-O bond.

	$Mg_3V_4(PO_4)_6$	$Mn_3V_4(PO_4)_6$	$Fe_3V_4(PO_4)_6$	$Co_3V_4(PO_4)_6$	$Ni_3V_4(PO_4)_6$
A1-O	0.0415	0.0301	0.0473	0.0411	0.0234
A2-O	0.0140	0.0170	0.0231	0.0202	0.0127
V1-O	0.0232	0.0248	0.0239	0.0212	0.0217
V2-O	0.0298	0.0272	0.0305	0.0278	0.0419
P1-O	0.0110	0.0141	0.0102	0.0247	0.0168
P2-O	0.0134	0.0215	0.0130	0.0131	0.0193
P3-O	0.0082	0.0160	0.0171	0.0133	0.0191

Table 4.5: $A_3V_4(PO_4)_6$ polyhedral distortion indices (Baur's D).

Magnetic cations have been shown to order in sarcopside solid solutions as Ni is doped into $Fe_3(PO_4)_2$. [(69)] The driving factor for this phenomenon is the inequality of the two available cation sites. In $Mn_3Fe_4(VO_4)_6$, however, disordering of cations is observed and driven by the similarity of the ionic Shannon radii (6-coordinate high spin; Mn = 0.97 $\mathring{A}$ vs. Fe = 0.92 $\mathring{A}$). [(67)] The ionic radii of the A cations in $A_3V_4(PO_4)_6$ spans a range from 0.97 $\mathring{A}$ (Mn) to 0.83 $\mathring{A}$ (Ni). Each cation site is crystallographically distinct, suggesting inequalities between the various sites. Similar to the above outcomes, ordering of the cations in $A_3V_4(PO_4)_6$ is governed by their relative sizes. The amount of disorder observed in the compounds can be sorted by proximity to the V^{+3} ionic radii (0.72 $\mathring{A}$) where Ni > Mg > Co > Fe. Disordering occurs between the adjacent AO_6 octahedra and VO_6 octahedra which share corners. $Mn_3V_4(PO_4)_6$, with the largest size disparity between the two cations, favors disordering between the edge-sharing AO_5 trigonal bipyramid and VO_6 octahedron. This is driven by V^{3+} with d^2 configuration gaining stability via half-filling of the degenerate d_{xz} and d_{yz} orbitals on the trigonal bipyramidal site (high spin Mn^{2+} is half-filled regardless of configuration).

Magnetic properties within the $A_3V_4(PO_4)_6$ series are very similar. To understand the full system, individual M_2O_{10} subunits, where $M = A$ or V, must be examined. The V-V coupling in the edge-sharing octahedral V_2O_{10} subunits must be antiferromagnetic, as indicated by the negative Weiss constant in $Mg_3V_4(PO_4)_6$. This is consistent with the reported antiferromagnetic V-V coupling in the edge-sharing VO_6 octahedral chains in VPO_4. [(81)] Since the Goodenough-Kanomori rule predicts a ferromagnetic superexchange interaction within the V_2O_{10} subunit, direct exchange is more likely to dominate and yield the observed antiferromagnetic coupling. These V_2O_{10} subunits

are bridged by A_2O_{10} units, which make long range magnetic order difficult when A is nonmagnetic, as in the case of $A = Mg^{2+}$. On the other hand, for A = Mn, Fe, Co, and Ni, the magnetic transition metal ions facilitate the propagation of magnetic interactions throughout the crystal, leading to the observed long range magnetic order at low temperature. A-O-A and A-O-V bond angles are also bent (between $120° > \theta > 95°$; Appendix D, Table D.7), which leads to ferromagnetic superexchange within the A_2O_{10} units and antiferromagnetic superexchange between A_2O_{10} and V_2O_{10}. The former is likely to be the reason for the reduction in Néel temperature compared to what might be expected from Curie-Weiss behavior alone. These results are not common, given that ferrimagnetism might be expected from a system where the two subunits present have differing moments, and yet antiferromagnetism is observed. A similar ordering behavior as in these compounds is observed in the isostructural compound $Mg_{2.88}Fe_{4.12}(PO_4)_6$ (θ_W = –82 K, T_N = 43 K), where the presence of ordering is driven by a small proportion of Fe^{2+} ions in MO_6 octahedra that connect the chains, as well as the strong tendency for Fe^{3+} spins to order. [(136)]

These compounds have similar electronic and crystal structures, and the absorption bands are similar. The starting materials, VPO_4 and $A_3(PO_4)_2$, where A = Mg, Mn, Fe, Co, Ni, are used as a benchmark for identifying these transitions (Appendix D, Figure D.17). In d-d transitions for Co and Ni, red shifts are observed in going from the hexaaqua metals to the ternary phosphates (Table 4.6). These red shifts are partially responsible for the color changes in going from $Co_3(PO_4)_2$ (purple) to $Co_3V_4(PO_4)_6$ (green). These two compounds have identical cobalt coordination geometries: both edge- and corner-sharing octahedra (Oh) and trigonal bipyramids (TBP). Therefore, bond length changes about these polyhedra are the motivation for the red shifts. In $Co_3(PO_4)_2$ the trigonal bipyramid is severely distorted with a distortion index of 0.03599, while the octahedron is comparatively less distorted (distortion index of 0.0209). In $Co_3V_4(PO_4)_6$, these distortions are juxtaposed, with the distortion index being 0.0202 for TBP and 0.0411 for Oh. This has an impact on the orbital overlap between the Co-O and hence the energy separations between the transitions. Specifically, in $Co_3V_4(PO_4)_6$, the apical oxygen(s) on the TBP and the Oh are contracted versus its $Co_3(PO_4)_2$ counterpart. The polyhedral Jahn-Teller distortions about the octahedron are elongated equatorially and compressed axially, which simultaneously lowers the triply degenerate energy levels of the t_{2g} state (lower energy antibonding

interaction) at the cost of increasing the energy of the doubly degenerate e_g (higher energy antibonding interaction). The net result is a less energy separation between the e_g and the t_{2g}, which leads to a red shift in the d-d transition.

		Compound		
Metal	**Transition (nm)**	$[A(H_2O)_6]^{2+}$	$A_3(PO_4)_2$	$A_3V_4(PO_4)_6$
Co	$^4T_1(F) \rightarrow {}^4A_2$	480	480	580
	$^4T_1(F) \rightarrow {}^4T_1(B)$	500	580	610
Ni	$^3A_{2g} \rightarrow {}^3T_{1g}(P)$	340	430*/480*	550*
	$^3A_{2g} \rightarrow {}^1E_g$	670	710	&
	$^3A_{2g} \rightarrow {}^3T_{1g}(F)$	700	800	&

Table 4.6: d-d transitions for hexaaqua and phosphate-related Co and Ni compounds. Very weak transitions (asterisk) and washed out peaks (ampersand) are indicated.

The compounds have Earth-tone colors such as the deep green in Co, the light lime green in Mg, or the browns in Mn and Fe. The purple to green color change going from $Co_3(PO_4)_2$ to $Co_3V_4(PO_4)_6$ is driven by the Co^{+2} red shift as well as the V^{+3} red shift, which is presumed to result from similar arguments to the one above (coordinated polyhedral distortions). This shift results in a small energy gap (lack of absorption) from 2.3 – 2.4 eV in $Co_3V_4(PO_4)_6$, bracketed by the V(III) and Co(II) transitions, and generates the intense green color that is observed. In contrast, $Mg_3V_4(PO_4)_6$ has a broad window with a minimum near these energies, but with less total peripheral absorption, which results in a (much) brighter and lighter green color.

4.5 Conclusion

$A_3V_4(PO_4)_6$ (A = Mg, Mn, Fe, Co, Ni) compounds are synthesized for the first time. Rietveld refinements of combined synchrotron and neutron powder diffraction data reflect changes in the crystal structure associated with differences in the ionic radii in the series: unit cell volume, cation order/disorder, bond parameters. The low symmetry of the assigned space group, $P\bar{1}$, yields varied individual bond lengths within the distorted polyhedra. The dilution of edge-sharing magnetic ion octahedra in going from infinite chains (VPO_4) to trimer ($LiMPO_4$) to dimer ($A_3V_4(PO_4)_6$) transitions from weakly ferromagnetic to antiferromagnetic is driven by diluting the edge-sharing connectivity with diamagnetic cations to weaken the long range magnetic exchange interactions.

This dilution also drives the relations observed in the Weiss constants (-60 to -25 K) as well as the Néel temperatures (< 3 to 15 K). The effective magnetic moments for $A_3V_4(PO_4)_6$ (A = Mg, Mn, Fe, Co, Ni) are 5.16 μ_B, 11.04 μ_B, 10.08 μ_B, 9.76 μ_B, and 7.96 μ_B, respectively. Deviations from the calculated values are explained as half to full filling of the t_{2g} orbitals occurs in going from A = Mn $\rightarrow$ Ni. The colors of the compounds are light lime green, brown, brown, green, and tan, which are dictated by the d-d transitions of the Co and Ni, nestled among the absorptions contributed by V^{+3} in their common V-P-O framework.

APPENDIX A: WALKTHROUGH OF INSTRUMENTATION AND CONCEPTS

Photocatalysis and Water Splitting Walkthrough

Visible Light Driven Overall Water Splitting by Semiconductor Photocatalysts

A large impetus for the work presented in this thesis has been driven by research in materials for water splitting. The replacement of terminal resource power generating technologies with renewable and regenerative ones is achieved when the latter technologies are developed enough to out compete and supplant existing technologies. To achieve these goals with water splitting in mind, a thorough understanding of all the factors at play are necessary.

Need and Fundamentals

With persistent increases in global population and the rise of the Brazil, Russia, India, and China (or the BRIC countries) the demands for energy sources has kept pace. This demand has been met primarily through increases in petroleum processes and though coal operations. [(137)] The turn of the 21st century saw a peak oil scare [(138)] and a subsequent surge in the interest and subsequent drive in research for alternative, clean, and renewable energy production that was competitive versus conventional sources. This was enhanced by increasingly alarming evidence for anthropogenic based climate change. [(139)] One of the proposed methods for supplanting current energy ecosystems is to harvest solar energy. It is estimated that 4 TW of energy from the sun hits the Earth every day. Light harvesting can be harnessed through physical (e.g. heat-

ing), electrical (photovoltaics), or chemical methods. Using the latter technique, the proposed method is to use photons to drive chemical reactions that produce fuel in a renewable or energy efficient manner. One of the most simple and elegant, but difficult approaches to employing this technique is to use sunlight to break down water into its constituent atoms, hydrogen and oxygen. Once generated, these gases can be stored or recombined to generate energy. The thermodynamics of water are such that the decomposition process is very energy intensive (Gibbs free energy (ΔG) large and positive). The energy necessary for water splitting requires 237 kJ/mol and is an endothermic reaction (Hess' law). Furthermore, the decomposition process is entropy driven. 1 mole equivalent of water becomes 1.5 mole equivalents of gas, and requires a phase change under ambient conditions. This is a tall order. Lastly, for proper decomposition to occur, both an oxidation and a reduction half reaction must occur: hydrogen reduced and oxygen oxidized. Their half reactions, at pH = 0 (standard conditions), are as follows:

$$2H_2O_{(l)} \rightarrow O_{2(g)} + 4H^+_{(aq)} + 4eE^o_ox = 1.23V(E^o_red = 1.23V) \quad (2)$$

$$2H^+_{(aq)} + 2e \rightarrow H_{2(g)}E^o_red = 0.00V \quad (3)$$

To find out how the actual potential in a given solution differs from the standard potential, Gibbs free energies are integrated and the Nernst equation is employed to give:

$$E = E^0(RT/nF) \cdot ln(Q) \quad (4)$$

This can be simplified to find the redox potentials for the given half reaction at any pH:

$$(4)E = E^00.059 \cdot pH \quad (5)$$

These are the minimum potentials required if the aim is electrolysis of water. To promote this reaction using the energy provided by the sun, a catalytic approach is necessary. To achieve this a compound must be able to achieve a metastable state that can bind or interact with water strongly enough to weaken the O-H bonds or at least facilitate efficient charge transfer from the compound to water, but that is still stable enough to not react with itself or the products. Equations 2 and 3 show that the sum of these reactions requires 4 holes and 2 electrons. The desired photocatalytic system would inject both holes and electrons constantly during illumination from the sun, satiating those demands. By examining a standard reduction potential table, it becomes

apparent that water has been well studied. There are many reactions involving H_2O, ^{-}OH, or H^{+} that can change the equilibrium of the system (Le Chatelier effects). This complicates the system and therefore pH changes in an aqueous photocatalytic system must be monitored or controlled carefully.

Proof of Concept for Photocatalysis

Semiconductors have been identified as possible candidates for the generation of holes and electrons necessary to facilitate the decomposition of water. This is enabled by the photonic excitation of an electron from a ground state, the valence band (VB) to an excited state, the conduction band(CB). In the 1970s, Fujishima and Honda were the first researchers to demonstrate that water splitting is possible using a semiconductor photocatalyist (TiO_2) to drive the reaction photoelectrochemically [(140)]. This research was embarked upon during the first peak oil shortage, when concerns for the premature termination of petroleum as a fuel source were high, resulting in the first big governmental funding push to discover alternative energy sources. While the TiO_2 example is not a true photocatalytic one it represents a historic landmark none the less. A fever pitch existed in the global research community then. Since then, many examples of pure photocatalysts have been reported. Most of the examples dating from that time employ the use of wide-band-gap semiconductors and insulators. [(141)] In order for a catalyst to be functional the conduction band must reside at energies greater (more positive) than the water reduction potential, and the valence band needs to be at an energy less (more negative) than the water oxidation potential. No straightforward way exists to compare the energy of the absolute band positions of a compound with the redox potentials of water, but an approximation does exist. It is based upon the idea of an absolute electrode potential. [(142)] This potential is the difference in energy between the Fermi level of a given electrode and a point outside of the system (E_{vac}). This can be bracketed to the standard hydrogen electrode where:

$$E_a^M bs = E_S^M HE + (4.44 + / - 0.02)V \tag{6}$$

A given catalyst can have its absolute band positions determined using a suite of instrumental techniques (Kelvin probe force microscopy, UV-Visible diffuse reflectance, and X-ray photoelectron spectroscopy at a minimum), which, in turn, can then be

evaluated and understood with respect to its ability to effectively split water into hydrogen and oxygen. Recall that for a photocatalyst to split water, the VB and the CB must straddle the respective redox potentials. The first generation of photocatalysts for water splitting were effective because they had wide band gaps. The separation between the conduction band of the catalyst and the water reduction potential is large; likewise for the separation between the valence band and the water oxidation potential. This provides an over potential that can drive the photocatalytic water decomposition reaction forward. Very efficient and highly active wide-gap photocatalyts have been identified and widely studied. [(143)] The drive for next-generation photocatalysts is to better utilize the solar spectrum. The sun at the center of our solar system emits black body radiation. The solar spectrum (Figure A.1) has a maximum photon flux centered near 0.8 eV and decreases in either direction. To fully utilize the sunlight reaching earth the perfect photocatalyst would have a minimum band gap (energy separation between VB and CB) of 1.23 eV, limited by the minimum required energy to split water. A significant over-potential (0.4 V per half reaction) in often required, however, to decompose water. [(144)] An ideal, efficient next-generation photocatalyst would have a band gap just greater than 1.23 V. An approach in this work to achieve a reduced semiconductor band gap is through the aliovalent substitution of oxides to form nitride oxides (Section 1.1.2).

Co-catalyst

The number of requisites necessary for a photocatalyst to be exceptional is high, but some of the dilemmas encountered can be skirted by modification of a catalyst that meets many of the requirements. The addition of a co-catalyst is designed to compartmentalize and streamline the photocatalytic process. The choice of the proper photocatalyst should reflect the desire to have it act as an excited carrier sink (hole or electron), passivate the catalyst surface against unwanted side reactions, be well band-matched with the catalyst, and prevent back reaction of products. Noble metals used previously as selective catalysts are a natural choice because they satisfy the majority of the above stipulated requirements. In fact, co-catalysts have been readily employed that utilize noble metal derivatives, and it is common to screen catalysts with a suite of them to test and optimize them for activity. [(145)] Co-catalyst design and attachment to the photocatalyst evokes the use of core-shell moieties to achieve the desired properties. Wet impregnation [(146)], dry impregnation [(147)], or photodeposition

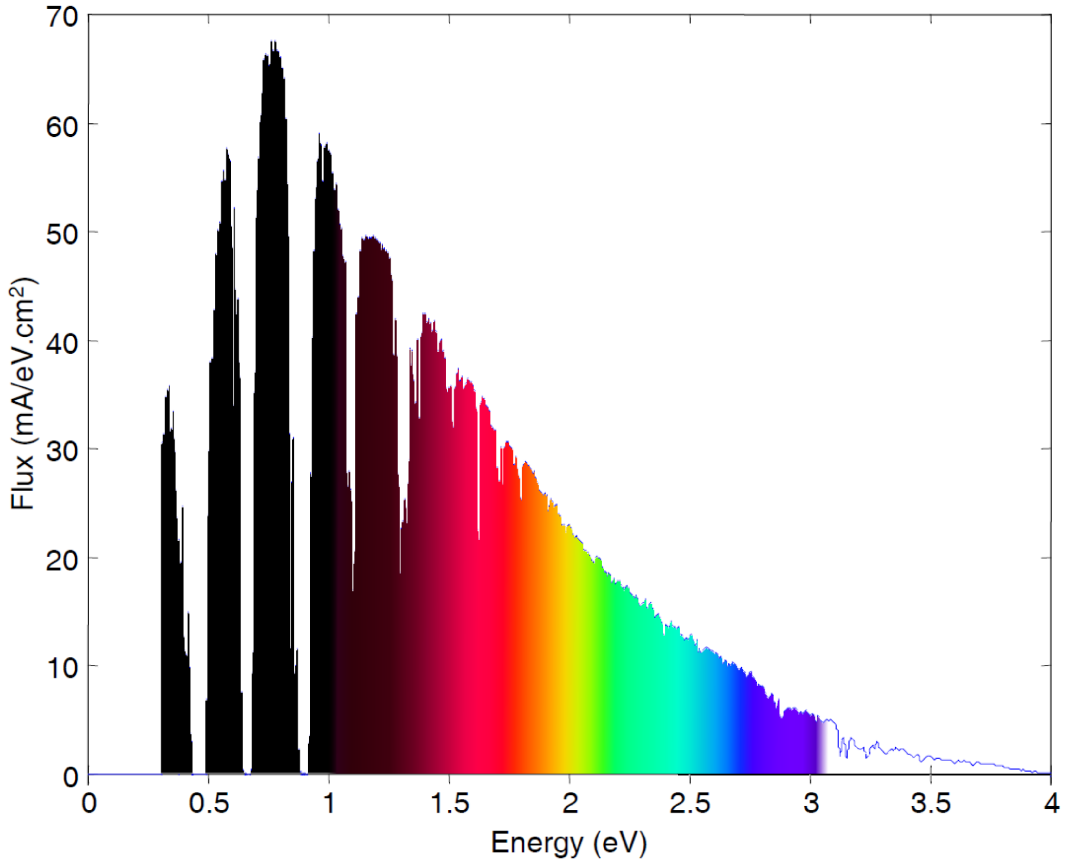

Figure A.1: Incident solar spectrum photon flux -

[(148)] techniques uniformly deposit a target metal onto the surface of the photocatalyst. Heat treatment can then oxidize the outer layer of the co-catalyst, yielding a core-shell moiety. There are a variety of different configurations of this approach, all with the same end goal. The completed manifold (Figure A.2) should allow for excited carriers to be favourably transferred from the catalyst to the co-catalyst and lastly to water. The chosen catalyst should have a Fermi level that is energetically appropriate for the desired half reaction, lying in-between the redox potential for water and the band position of the catalyst. This energetically favors forward transfer of the carriers, acts to promote charge separation, and can help prevent back transfer. Charge transfer from the catalyst to the co-catalyst is favourable when executed in this way. Because the co-catalyst core is a metal, it allows relatively free movement (high mobility) of the carriers within the medium. The shell is oxidized to prevent back reaction of the photogenerated products. To facilitate charge injection through the outer shell and on into the electrolyte (water), it needs to be thin enough prevent inhibition of carrier transfer (no drastic changes in electronic structure or Fermi level) but must be thick enough to prevent back reaction to water from the products (passivation layer).

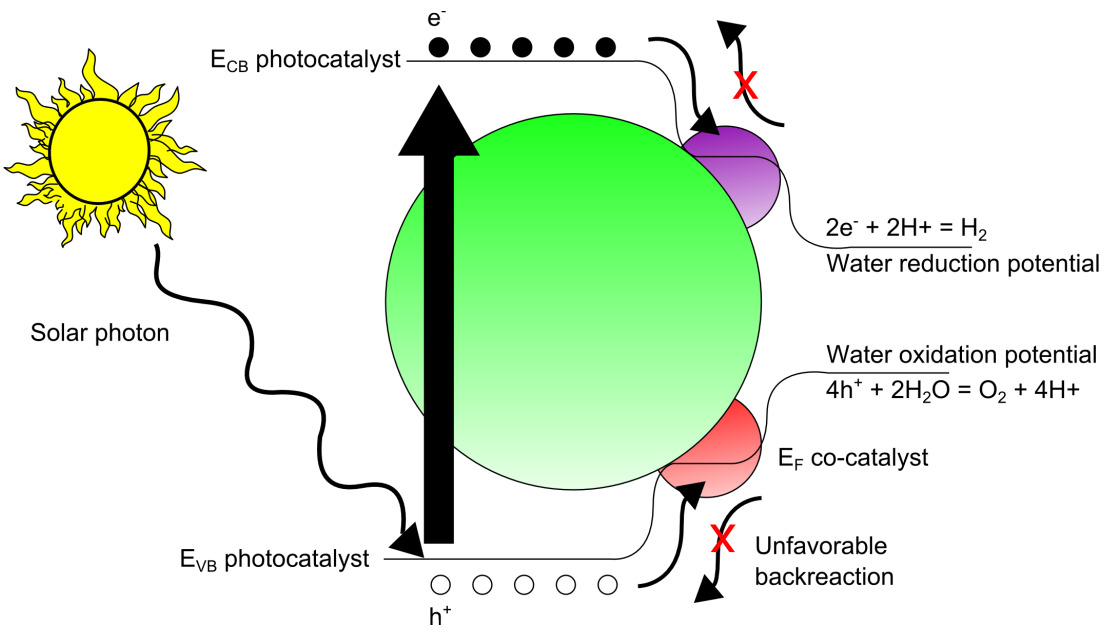

Figure A.2: Proper selection of semiconductor (green), oxygen co-catalyst (red), and hydrogen co-catalyst (purple) will result in efficient charge transfer to water - Holes travel up in energy while electrons travel down in energy.

Common co-catalysts for these systems use Pt [(149)] and Ir [(150)] derivatives for H_2 generation, while Co [(151)], Ru [(152)], and again, Ir derivatives are used to promote the O_2 half reaction. NiO [(148)] and Rh-Cr [(153)] blends have been used for simultaneous generation of both gases. Interfaces and exposed facets of a photocatalyst can also play a significant role in the activity of the catalyst. Special care should be taken to ensure that this is accounted for in experiments. It has been shown that the photocatalyst $BiVO_4$ shows activity towards each half reaction on different facets. [(154)] Furthermore, the overall structure and nanostructure of the compound can also have a profound impact on the observed properties. In the $NaTaO_3$ photocatalyst, a terrace like surface structure was observed and correlated with the high overall activity of the compound [(143)].

Sacrificial Donors and Acceptors:

The overall complexity of the photocatalytically assisted water decomposition can be simplified by examining each half reaction individually. An experiment can then be designed to examine the ability of a compound to reduce water, or to oxidize water. This can be helpful when the exact band positions of a catalyst are not yet determined, are in question, or are not favorable for overall water splitting. This technique is exceedingly important for the latter point. If the band positions are favourable for one but not both of the half reactions, the water splitting system as a whole will not proceed, because it is effectively short circuited by the immediate build-up of left-over carriers (and subsequent band bending) in the semiconductor, which prevents further charge migration and transfer. To coax out water reduction activity (requiring photogenerated electrons), a foreign species can be added to the reaction vessel that will serve as a hole scavenger. Small chain alcohols (methanol and ethanol) serve this purpose quite well. These electron donors have a single hole, multiple step degradation process. Methanol degrades to formaldehyde, formic acid, bicarbonate, and finally CO_2. [(155)] Choice of a sacrificial reagent is not limited to these molecules, but should be chosen on the basis that it is more easily oxidized (has a more favourable oxidation potential) than water. This ensures that the photocatalytic reduction of water is not impeded by its reciprocal half reaction, water oxidation. On the other hand, to evaluate the water oxidation activity of a compound, the added agent needs to be an electron scavenger. Silver nitrate ($AgNO_3$) is typically used as the sacrificial reagent in these photocatalytic reactions. As the Ag^+ is photoreduced on the surface of the compound, it accepts an

electron. When a photocatalyst has adequate band positions to oxidize water, but does not have the correct positioning for reduction of water, a sacrificial reagent should be chosen that has more energetically favorable redox potential than the reduction of water (Figure A.3). This will kick-start the process by now preventing the build-up of electrons on the surface of the catalyst and allow them to be transferred to the sacrificial reagent where they react. This occurs in support of the main objective: to observe the water oxidation rates that would otherwise not be possible to observe.

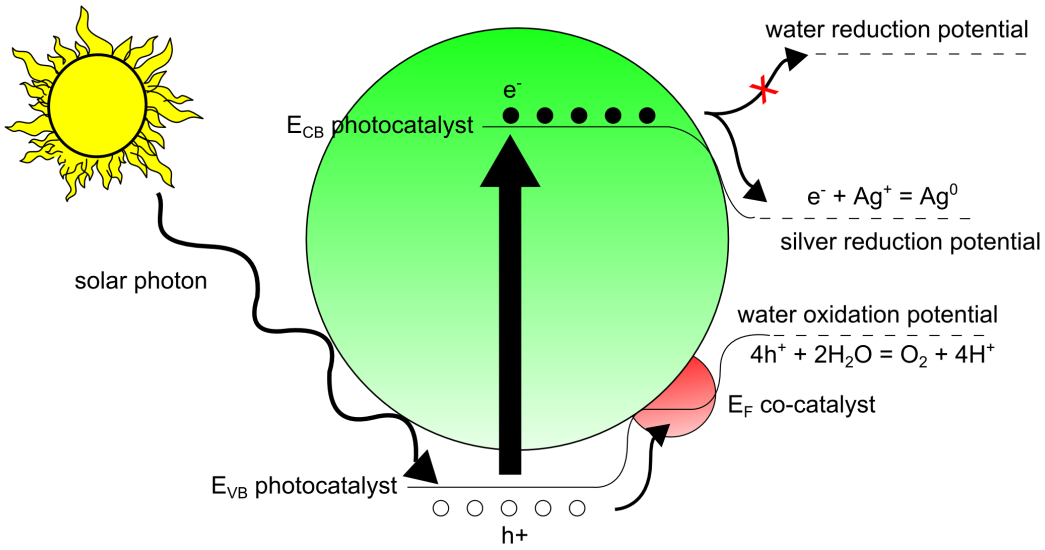

Figure A.3: Choosing a correct sacrificial donor relies on favourable band position placement. -

Occasionally, other sacrificial donors are used for/in specialized situations. Methylene blue, methyl orange, and rhodamine are industrial organic dyes that are often found as persistent contaminants in water systems where they are present. For the concerned reader: modern, advanced water treatment processes using ozone and UV have no problems in removing these contaminants. Nonetheless, they are often used in drinking and waste water test systems as an indicator of the efficacy of a given treatment method. So it goes for testing photocatalytic compounds as well. If a sample can successfully degrade these compounds, the logic is that it may be possible to successfully apply this technique to current water treatment processes. Other additives to a given system can assist in remedying the shortcomings of a photocatalyst. I^-/I_3^- [(156)] and Fe^{2+}/Fe^{3+} [(157)] are used as redox shuttles. Dye sensitized solar cells

often employ these electrolytes. [(158)] These molecules reside in solution and react at the surface of the photocatalyst, to be either reduced or oxidized by a targeted redox catalyst, and can then be carried off into solution, to go and be regenerated in the reverse redox direction at an adjacent reactive site that is designed for that.

Considerations in Photocatalyst Design

All of the above conditions (experimental, physical, or otherwise) need to be planned and accounted for in order to permit an efficient photocatalytic system for overall water splitting. The most urgent aspects of the design of a good catalyst are: conduction and valence band placement, susceptibility to electrochemical bias, efficient charge separation, photostability, surface area, and cost. Valence band placement has been thoroughly discussed for the substitution of nitrogen into an oxide lattice. There are other substitutions that are possible, incorporating other elements, notably fluoride or sulfide. Incorporation of fluoride into an oxide lattice increases the breadth of the valence band, or if a fluoride is used out-right, it would push down the position (lower the energy) of the valence band. Tantalum compounds provide an excellent example, demonstrating how the band (gap) picture changes on going from a fluoride oxide (TaO_2F) to an oxide (Ta_2O_5) to a nitride oxide (TaON) [(31)]. The incorporation of sulfide into an oxide lattice should yield similar results to a nitride oxide. The valence band is moved up (higher in energy) on account of having similar electronegativity to nitrogen. They differ by their relative stability on illumination in water. Oxide sulfides tend to have issues with decomposition via photo-oxidation [(159)]. On the other hand, the (solid state) physical properties are superior, with high conductivity and mobility. The choice elements for the placement of the conduction band has been largely simplified by compilation of the data available in the literature. Schoonen *et al.* have given the absolute band positions of all the usual semiconductors [(160)], and if a more blank slate is preferred Keszler *et al.* have taken the time to compile the average band positions occupied by a given ion (with both cations and anions presented). [(161)] These two combined works provide an excellent template to design derivatives or new photocatalysts. If the designed compounds are intended to be perovskites, the *A*-site cation choice is also important. This is not entirely intuitive, because the *A*-site ion does not make any orbital contributions to the conduction band minimum. As mentioned previously (Section 1.1.1.3), tilting of the *B*-site octahedra are influenced by the size of the

A-site cation. This same tilting has a strong influence on the orbital overlap between the *B*-site d cation - p anion anti-bonding interaction that makes up the conduction band minimum [(162)]. Systems that are more tilted result in less dispersion of the bands due to less overlap in general, while less tilted octahedra have wide bands due to better overlap. This undulation from narrow to wide band widths, going from tilted to not tilted octahedra, is what causes the drastic, systematic change in band gap on going from $CaTaNO_2$ (3.0 eV) $\rightarrow$ $SrTaNO_2$ (2.5 eV) $\rightarrow$ $BaTaNO_2$ (2.0 eV). [(42)] Designing a compound that can be processed easily into an electrode has the benefit that the band positions can be manipulated. A straightforward, simple synthesis procedure tends to lend itself to the ability to fabricate an electrode from a target compound, and, in turn, facilitates the making of a photoelectrochemical cell. Now, instead of the system being completely reliant on photo-processes for operation, electrical processes can help supplement and drive a reaction forward that would otherwise not be possible. We refer to the classic example by Honda *et al.* [(140)] on TiO_2. Using linear sweep voltammetry and with the electrode illuminated, the potential at which the photocurrent is initialized can be monitored. The observed photocurrent indicates the mobility of the carriers upon illumination, which are necessary for the water redox reaction to occur. Experiments can then be designed to determine the flat band potential, where the electronic bands at the solid-electrolyte interface are perfectly horizontal [(163)]. Band manipulation can then occur to engineer the outcomes of the photoelectrochemical reactions. For example, a forward or reverse bias can be applied to facilitate (enhance) water decomposition rates. The idea is that photo-assisted water splitting will occur at a lower voltage than the electrolysis of water ($<$1.23 V), translating into higher efficiencies and cost savings. Effective charge separation requires the excitons to be decoupled into its respective parts, an electron and hole. This can be achieved by a variety of the above discussed approaches: band-structure control, enabling charge transfer at interfaces, and preventing the re-combination of carriers. Bands with high dispersion at the conduction band minimum and valence band maximum provides the excited electron and/or hole with mobility to traverse the crystal and ideally react to produce the target products. Proper choice of coupling agents is important, such as with good pairing of the Fermi levels of the catalyst and co-catalyst. This induces mobility at an interface, allowing electrons to be shuttled away by moving down in energy (and conversely, the holes to be shuttled away by moving up in energy). This also

assists with preventing the recombination of carriers. Photostability can be ensured by selection of structures, facets, or compounds that are expected to have good resilience with respect to the reaction conditions of the water splitting system. Because of the thermodynamics and the electronegativity of oxygen, the main culprit for the degradation of a catalyst is photo-oxidation. This, however, doesn't exclude the danger of photoreduction occurring in the sample. During water splitting experiments for one of the most successful systems (10% solar to hydrogen efficiency), the thin film catalyst compound, $InGaP_2$, experienced pitting due to photo-oxidative degradation. [(164)] This, in turn, can have both an adverse and a beneficial effect on the catalyst. In the previous example, the effect is adverse, slowly reducing the turn-over number of the process and causing a gradual loss of function. The solution proposed for this problem is to separate the components responsible for each half reaction and enable cathodic protection in one case and anodic protection in the other. In nitride oxides, photooxidation at the onset of photocatalysis has been reported to experience the liberation of a minute amount of nitrogen gas. [(122)] This is attributed to surface passivation of the catalyst. Oxide or hydroxide replaces terminal or surface adsorbed nitrogen species, but does so in a nondestructive, predictable manner, allowing photocatalysis to continue unimpeded thereafter. The field of nanotechnology has been steadily emerging over the last two decades, with serious inroads made into crystal engineering. Hydrothermal techniques have paved the way and offered strong control of the facets that grow and persist during a heat treatment. High surface area, single crystal products with active facets exposed are the desired product. In systems where a comparison is to be made between two compounds, it is important to control and account for differences in the surface area and crystal morphology. Ideally, the two compounds need to be identical to eliminate these effects as contributing factors to the photocatalytic properties of these compounds. Conversely, for any one compound, a series of compounds in terms of surface areas, crystal sizes and exposed facets can be grown to optimize the conditions for the highest active catalytic rate. A comprehensive review on these topics has been prepared elsewhere [(165)].

Set-up

The photocatalytic products evident from water splitting in nitride oxides are ideally hydrogen and oxygen. Nitrogen is commonly observed due to surface degradation of

the nitride oxides (discussed above), and if methanol is used as a sacrificial reagent, then carbon oxides (mainly, CO and CO_2) are also formed. A gas chromatograph is used to quantify the amount of these products (integrated peak area) generated per unit time. Detection can be provided by a variety of methods: thermal conductivity, flame ionization, catalytic combustion, electron capture, infrared spectroscopy, mass spectroscopy, etc. [(166)] Thermal conductivity is robust and provides adequate sensitivity for most photocatalytic work. This technique measures conductivity changes in the flowing gas as it passes over a filament with a current passing through it. The carrier gas keeps this filament cool, uniformly resistive, and electrically efficient. As the sample is eluted over this piece, a response in the voltage is measured, and can be (internally or externally) standardized to give individual sample data results. The correct column choice must provide suitable resolution between each product (reactant, and side product). In photocatalysis, columns packed with compounds within the aluminum silicate zeolite class often give adequate separation between analytes. A chosen vessel must be penetrable by the desired wavelengths of light. For this reason, it is quite common to use quartz as the vessel medium. It has high transparency to UV and visible radiation regimes. Other more common glasses (borosilicate) more readily adsorb UV light. The choice of light source is dependent on the type of experiment intended to be carried out. For instance, proof-of-concept compounds that have not yet been optimized require more input to yield measurable results. There are five common light sources: W, Hg, Xe arc, lasers, and light emitting diodes (LEDs). Of those listed, the Xe arc lamps have an emission spectrum most similar to the solar spectrum. The photon flux can be adjusted by lamp wattage (directly correlated), and also by manipulating the light power through optical concentration (spot size adjustment). For reference, the sun has an incident power rating near 100 mW/cm^2, and this should be used as a benchmark. [(167)] Lastly, it must be confirmed that the vessel is gas-tight and not prone to leaks. Once these three criteria are judiciously considered the vessel is filled with water (sacrificial reagent, pH buffers,) and the photocatalyst. This mixture is illuminated and suspended by stirring. The head space can then be collected and injected (inline sampling port or by syringe) to the GC. The entire instrumental schematic (Figure A.4) works simultaneously to produce experimental data at regularly times intervals.

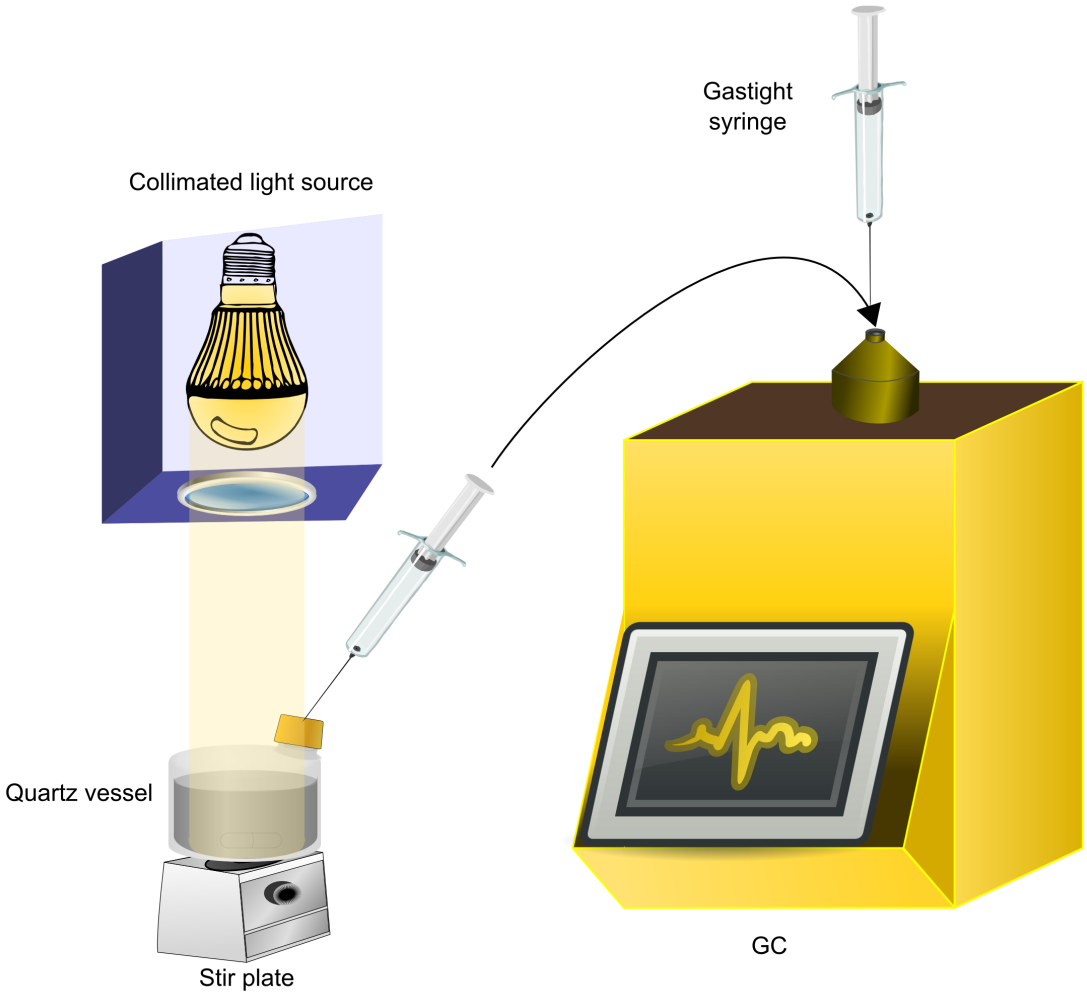

Figure A.4: Tandem photocatalytic-GC schematic -

A recent review contains a wealth of information regarding the experimental set-up, current state of the art, techniques, and strategies. [(168)]

Magnetism Walkthrough

Magnetic behaviour makes up a fairly large aspect of the compounds studied in this work. Therefore it is necessary to present a more expansive walkthrough of the guiding principles, magnetic properties, characterization, and instrumentation.

History

Scholars and academics have contributed to the body of work relating to magnetism over the last few millennia, but the science of magnetism did not start until science, logic, and rational thought caught on during the Renaissance era. In 1550, Girolamo Cardano's work entitled *De Subtilitate Rerum* distinguished between magnetic and electrical forces. Some 50 years later, William Gilbert published his work *On the Magnet and Magnetic bodies, and on that Great Magnet the Earth* which was a literature and spoken word review presenting the then state-of-the-art knowledge on magnetism in Europe. Much has happened since then, all events notable and tremendous, but not included here. A history of magnetism in its full form has been beautifully told by Brian Scott Baigrie [(169)]. More recently, but still a little over 100 years ago, Hieke Kamerlingh Onnes discovered superconductivity. Using liquid helium to cool mercury, the scientist observed that the resistivity of the sample dropped to zero at temperatures below 4.2 K. This introduces the current era of magnetism that is still in full force today. The ability to cool substances to very low temperatures has opened up the field of low temperature physics. It is in this realm that most magnetic systems, inclusive of the ones contained herein, are studied.

Fundamentals

There are two main contributors in magnetism: electron and nuclear magnetic moments. The latter contributor is much smaller in magnitude than the former, and therefore, will not be thoroughly discussed here. Electron magnetic moments are made up of spin and orbital derived contributions. The orbital moments can be arrived at by considering (Figure A.5) where an electron revolves about an atom's nucleus with a radius, r, and an angular velocity, ω. The magnetic moment (μ_l) contributed by orbital motion is then calculated by:

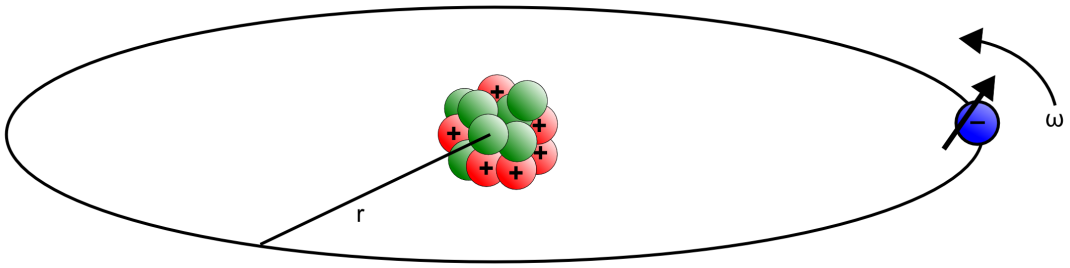

Figure A.5: Electron orbiting about a nucleus -

$$\mu_l = \mu_0 \dot{A} \cdot i \tag{7}$$

where A is the area of a circle, μ_0 is the vacuum permeability, and i is current. By inserting $A = \pi \mathrm{r}^2$ and $i = -\mathrm{e}\omega/2\pi$ into Equation 7, we obtain:

$$\mu_l = \mu_0 \pi r^2 (-e\omega/2\pi) = -e\mu_0 \omega r^2/2 \tag{8}$$

This can be further reduced by noting that the angular momentum of an electron is given by $\mathrm{P}_l = \mathrm{mr}^2\omega$. Thus, magnetic moment by an electron's orbital motion is:

$$\mu_l = -(\mu_0 e/2m) P_l \tag{9}$$

Quantum mechanics states that electron orbital motion about an atomic nucleus is quantized. Orbital angular momentum can therefore be given by using the orbital angular momentum number, l.

$$P_l = \hbar l \tag{10}$$

where $\hbar$ is Planck's constant. The magnetic moment due to orbital motion of an electron can now be reduced to:

$$\mu_l = \mu_0(-e\hbar/2m)l = -\mu_B l \tag{11}$$

where μB is a Bohr magneton. On the other hand, magnetic moment originating from an electron's spin (μ_s) is given using the spin angular momentum number, s, from the Dirac equation:

$$\mu_s = -(\mu_0 e/m) P_s = -({}_0 e/m)\hbar s = -2\mu_B s \tag{12}$$

where $\mathrm{P}_s = \hbar \mathrm{s}$, $\mathrm{s} = \pm\frac{1}{2}$. Total magnetic moment (μ) contributed by an electron can be arrived at by combination of Equations 11 and 12:

$$\mu = \mu_l \mu_s = -(l2s)\mu_B = -g_j \mu_B \tag{13}$$

where $j = l + s$ (total angular momentum) and g is the g-factor (note: $g = 2$ for $l = 0$).

The above example is for a single electron system. As electrons are added, the Pauli Exclusion Principle comes into effect. It states that it is impossible for two electrons to have quantum numbers (n, l, m_l, and m_s) where values would be identical to each other. It is for this reason that electrons spontaneously pair within a given subshell with spins anti-parallel, exactly opposite to each other and with m_s corresponding to $\frac{1}{2}$ and $-\frac{1}{2}$. This pairing occurs under ambient conditions for all core electrons. Full pairing occurs in the outer shell when it is completely empty or filled (s^0, p^0, d^0, f^0, *etc.*). When this occurs throughout an entire electronic system, it is not eligible for electron driven magnetism and is said to be diamagnetic (Figure A.6a; compared to other magnet types). Side note: There is still a very small magnetic moment associated with the movement of an electron about the nucleus.

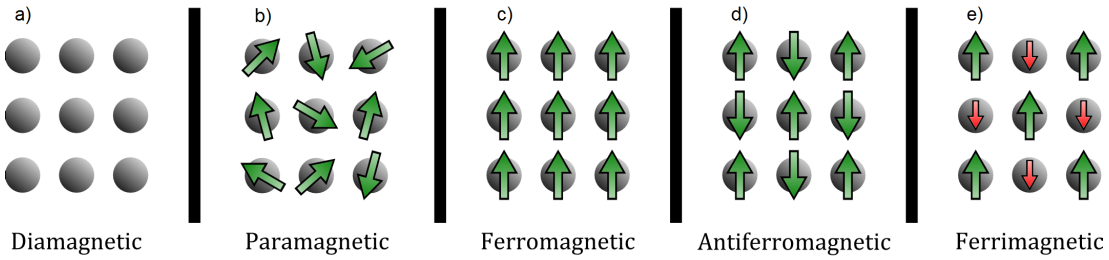

Figure A.6: Types of magnetism - Arrows denote orientation of unpaired electron spin. Colors indicate magnitude of moment.

The vast majority of magnetic properties comes from outer-shell electrons and their associated interactions (locally and globally). How multiple electrons are arranged for a given configuration is governed by Hund's rules:
For the lowest energy state to be achieved...

1. The multiplicity $(2S + 1)$, where S is total spin angular momentum, must be maximized.

2. The largest possible choice for the total orbital angular momentum quantum number, L, must be chosen

3. When the outer shell is less than or equal to half filled, the total angular momentum quantum number (J) must be the lowest value possible. On the other hand, a more than half filled outer shell must have a maximized J.

These rules assume L-S (Russel-Saunders) coupling in, which the total spin-momentum quantum number (S) and the total orbital-momentum quantum number (L) are summed and then combined to yield the total angular-momentum quantum number (J). This is because the interactions between the orbital angular momenta of individual electrons is stronger than the spin-orbital coupling between spin and orbital angular momenta. It is commonly evoked for situations where low (middle, and high) Z atoms are involved. In fact, this approach still works well for compounds containing lanthanoids. As Z becomes quite large, so does the nuclear charge, driving the need to adopt a different method instead, j-j coupling. The j for each electron is calculated from l and s, and then summed to achieve J. This approach becomes necessary when the spin-orbit interactions become as strong as the interactions between individual spins or orbital angular momenta. In multi-electron systems the amount of magnetic cooperation depends on the choice of the elements in a compound, the structural arrangement, temperature, external magnetic field, *etc.* For determining the factors that drive the magnetic interactions of a system it is often easiest to start with the simplest calculations and add in more complex components as they are needed. Initially, the experimentally determined magnetic moment of a sample should be compared to the calculated effective magnetic moment (μ_{eff}) with spin only considerations:

$$\mu_{eff} = 2(S(S+1))^{\frac{1}{2}} \cdot \mu_B \tag{14}$$

When the two values are not in agreement, however, then the spin and orbital momentum contributions can be calculated (neglecting spin-orbit coupling):

$$\mu_{eff} = (4S(S+1) + L(L+1))^{\frac{1}{2}} \cdot \mu_B \tag{15}$$

If better agreement is still warranted, full treatment of the system for (L-S) coupling may be necessary:

$$\mu_{eff} = g_J(J(J+1))^{\frac{1}{2}} \cdot \mu_B \tag{16}$$

Otherwise, it will be necessary to carry out calculations of the moment with *j-j* coupling in mind:

$$J = \Sigma j_i = \Sigma(l_i + s_i) \tag{17}$$

where i is the number of electrons in the system. J is then inserted into the previous equation (above) and computed.

Systems with unpaired electrons that do not order and have random orientation are called paramagnetic (Figure A.6b). Transition metal or f-block ions consistently contribute unpaired electrons to a compound. The magnetic moment of a compound is often in good agreement with the spin-only calculated moment. [(40)] This occurs because ligands, routinely the diamagnetic anions in a compound, quench the orbital angular momentum. Deviation from the spin-only value occurs when the orbital contribution is large or if spin-orbit coupling occurs. The former can occur in partially filled t_{2g} orbitals (barring the half-full case). Spin-orbit contributions increase (decrease) the moment for greater (less) than half-filled orbitals. In the remaining bulk of cases, a permanent atomic moment can exist with either cooperative or non-cooperative (paramagnetic) behavior. There are three main groupings of cooperative, spontaneous permanent atomic moments: ferromagnetism, antiferromagnetism, and ferrimagnetism. Ferromagnetism (FM) occurs when unpaired electrons spontaneously orient themselves in the same direction (Figure A.6c). Antiferromagnetism (AFM) occurs in a system where two spins align antiparallel to each other, canceling out the effective moment [Figure A.6d]. Ferrimagnetism (FiM) has the same configuration as antiferromagnetism, but often occurs in a heterogeneous system (*e.g.*, ternary compound with two different magnetic ions exist with different magnetic moments) where the spins do not cancel each other out [Figure A.6e]. A net magnetic moment then is able to persist. In order for cooperative ordering to occur, the spins on one magnetic ion must be interacting with the spins on another magnetic ion. This can occur between adjacent atoms in a metal, for example, and is called magnetic (direct) exchange. If the coupling is strong, interactions will persist even when diluted by inserting a chemically bonded (diamagnetic) ligand between the two atoms, *e.g.* an MXM bond where M is a magnetic cation and X is a non-magnetic anion [Figure A.7]. This is called a superexchange interaction. It is semi-covalent and is typically observed in oxides, nitrides, halides, and other hybrid motif compounds (such as nitride oxides). The interaction is formed from two

direct exchange interactions, MX and XM, where the anion is an intermediary. The up or down orientation of the unpaired electron's spin is influenced by preservation of the Pauli principle across the bonding orbitals.

Determination of magnetic properties

External magnetic field and temperature are the two most prominent variables that have a significant effect on determining if the magnetic properties of a given compound or solid are readily observable by experiment. The magnetic properties of a material determine how it interacts with an applied external magnetic field (H), and this is how most magnetic measurements are carried out. A diamagnet will have repulsive effect towards H, while a paramagnet will have an attractive effect. The magnetic induction (or internal field strength; B) depends on H and the magnetization intensity (or field derived from the sample; I) where:

$$B = H + 4\pi I \tag{18}$$

It follows then that the permeability (P), the ability to support the formation of a magnetic field within itself is B/H. This can then be worked back into the above equation to find that:

$$P = 1 + 4\pi\chi \tag{19}$$

where χ is the volume susceptibility but is an extrinsic property that is most directly related in this case to the amount of sample present. To account for this effect, and find the intrinsic susceptibility, the molar susceptibility (χ_m) is needed:

$$\chi_m = (\chi \cdot M_w)/\rho \tag{20}$$

where M_w is the molar mass and ρ is density.

During the initial characterization of a compound, this is the most commonly measured magnetic property. Magnetic susceptibility can be measured with respect to external applied field (H). From this plot, the coercivity, a gauge of the field strength required to flip the polarity of the spins within a sample, can be understood. Typically, this measurement is carried out via a hysteresis loop. Though most useful for probing a ferromagnetic material, the data from all types of magnetic materials can be

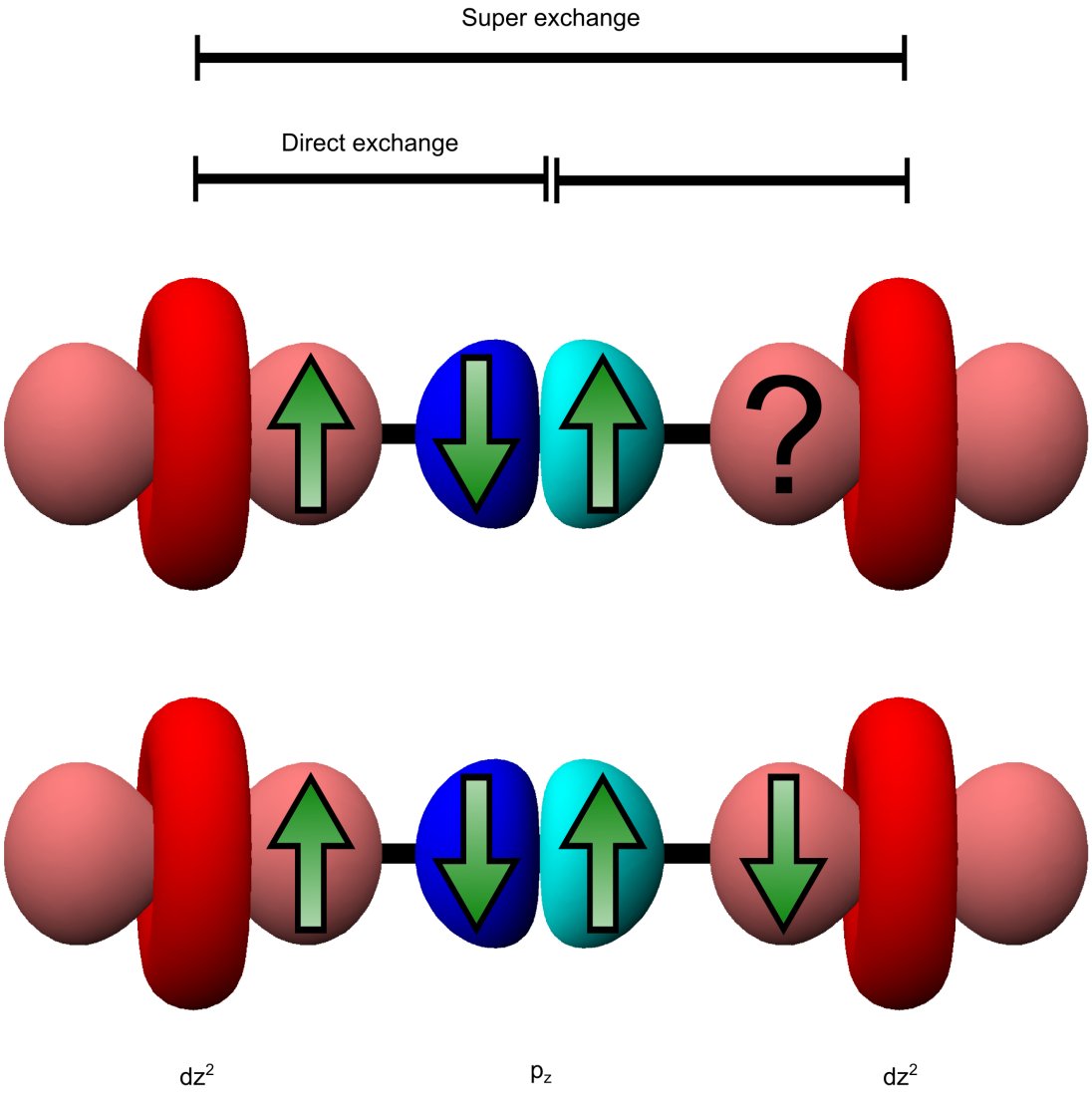

Figure A.7: Magnetic direct and super exchange between dz^2 and p_z orbitals in an *M-X-M* bonded solid - In the hypothetical system (top) an electron would be driven by super exchange to orient spin down (bottom)

informative (Figure A.8) and provide confirmation of conclusions from other magnetic tests.

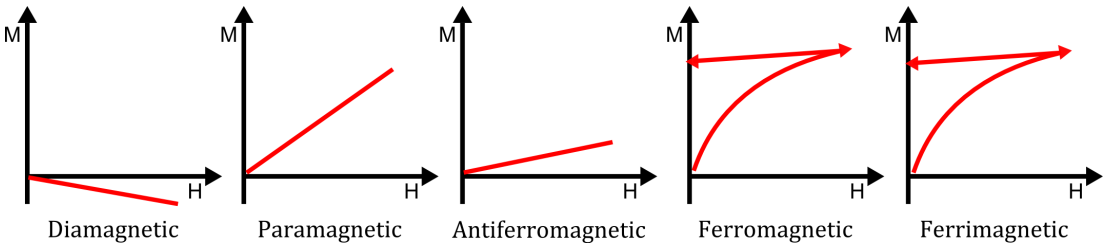

Figure A.8: Magnetic hysteresis loops (*M* v *H* curves) for different types of magnets -

Magnetic susceptibility serves as a pivot into other magnetic studies, *e.g.*, the changes in the magnetic susceptibility with respect to temperature. As temperature increases, so does thermal motion which decouples the magnetic interactions. When the temperature exceeds the coupled spin alignment energy throughout the lattice, this causes the spins to no longer hold a specific orientation (random, fluxional arrangement; similar to thermal smearing of atomic positions), and paramagnetism dominates. At temperatures below this point, the converse is true, magnetic order dominates, and an organized arrangement of the spins occurs or is induced by an applied magnetic field. The temperature at which this ordering occurs in a ferromagnet is called the Curie temperature (T_C), while for an antiferromagnet, it is called the Nel temperature (T_N). While varying the temperature, the magnetic susceptibility for a magnetic compound class can be significantly altered during a transition from magnetic disorder to order (Figure A.9). In a diamagnetic or a paramagnetic system, however, no ordering event occurs and susceptibility trends are preserved.

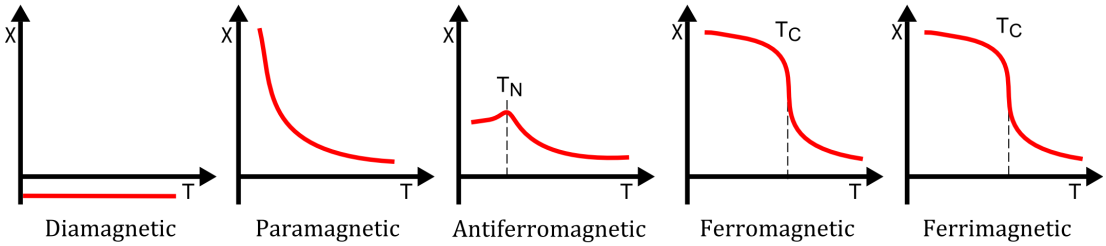

Figure A.9: Temperature dependent magnetic susceptibility plots for various types of magnets -

In a solid, the temperature at which ordering of magnetic moments occurs varies greatly. For strongly correlated systems, the highest temperature at which magnetism has been reported to exist, 1400 K, is found in metallic cobalt. [(170)] Industrial applications often require oxides, which tend to be more stable and inert during fabrication or device processing. Some examples of compounds with high ordering temperatures are Fe_2O_3 at 948 K and CrO_2 at 386 K [(171)]. Very strong magnetic interactions with high ordering temperatures have a good figure of merit, but there are not many examples ranked near the best-of-class. In reality, a majority of the magnetic compounds reported in the literature have weak magnetic interactions, which only become evident below ambient temperatures, and typically < 100 K. Temperature regimes where disordered arrangements dominate and thus paramagnetism is observed can also provide valuable information about the general magnetic properties of a compound. Molar magnetic susceptibility with respect to temperature is driven by the relation:

$$\chi_m = C/(T + \theta_w) \tag{21}$$

where C is the Curie constant and θ_w is the Weiss constant An ideal paramagnet should yield a straight line in a plot of inverse susceptibility (χ_m^{-1}) versus temperature when the magnetic interactions are localized and weakly interacting. When this occurs, a material is said to obey the Curie-Weiss law. Deviations from this indicate more complex interactions. C and θ_w can be extracted from this plot as the slope and x-intercept, respectively. The Curie constant indicates the size of the magnetic moment per formula unit, while the Weiss constant evidences short range magnetic interactions. For antiferromagnetic (AFM) interactions a negative Weiss constant is observed, and will be positive for a ferromagnetic(FM) one (Figure A.10; Also, the ordinary plots of other magnetic types).

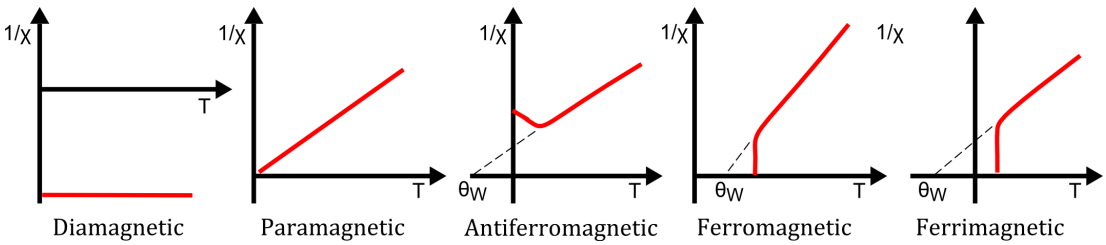

Figure A.10: Weiss constants for a variety of magnet types derived from temperature dependent inverse susceptibility plots -

Below the ordering temperature of a magnetic material, the arrangement of spins throughout a solid can help to explain how spins interact and sort. For instance, the distances between spins on nearby atoms can illuminate competing interactions and define which coupling dominates. It can also determine the orientation of spins with respect to one another. Largely, this can all be achieved through the use of neutron powder diffraction (NPD). This technique is typically used for nuclear refinement of compounds containing low Z, but it is also a powerful technique relative to magnetic characterization. The neutrons have a non-zero spin and are therefore able to interact with the unpaired electrons, which gives rise to cooperative (ordered) magnetic structures. When the neutrons are scattered by unpaired electrons, a magnetic diffraction event occurs, which, like nuclear diffraction, can be solved to yield a magnetic structure. The advantages of NPD are that the big picture is obtained, the propagation vector can be determined, and extinction issues are minimized. Conversely, the disadvantages include difficulty in indexing, information is lost due to powder averaging, phase determination can be difficult, and no domain or multi-k information is gained.

Set-up

The effects resulting in a material's inherent magnetism have been thoroughly discussed (see above). The importance of obtaining this information helps in the determination of the physical properties of a given material or device. How and what is used to measure these properties has not been covered. When an instrument is designed to measure the magnetization (magnetic moment) of a material, it should ideally do so as a vector, accounting for direction and strength (relative to the spatial orientation of the device). A laboratory magnetometer achieves this, and to do so requires a sample to be placed inside of the instrument where the temperature and magnetic field can be controlled and insulated against external factors. A general schematic illustration for a (vector) magnetometer is provided in Figure A.11.

There are many types of magnetometer instrumentation but the two types normally found in laboratories are a vibrating sample magnetometer (VSM) and a superconducting quantum interference device (SQUID). The former detects magnetization by mechanically oscillating a sample inside of an inductive pick up coil. The resulting change in flux or induced current is correspondingly measured. This technique is approximately one order of magnitude less sensitive than for a SQUID, which has its

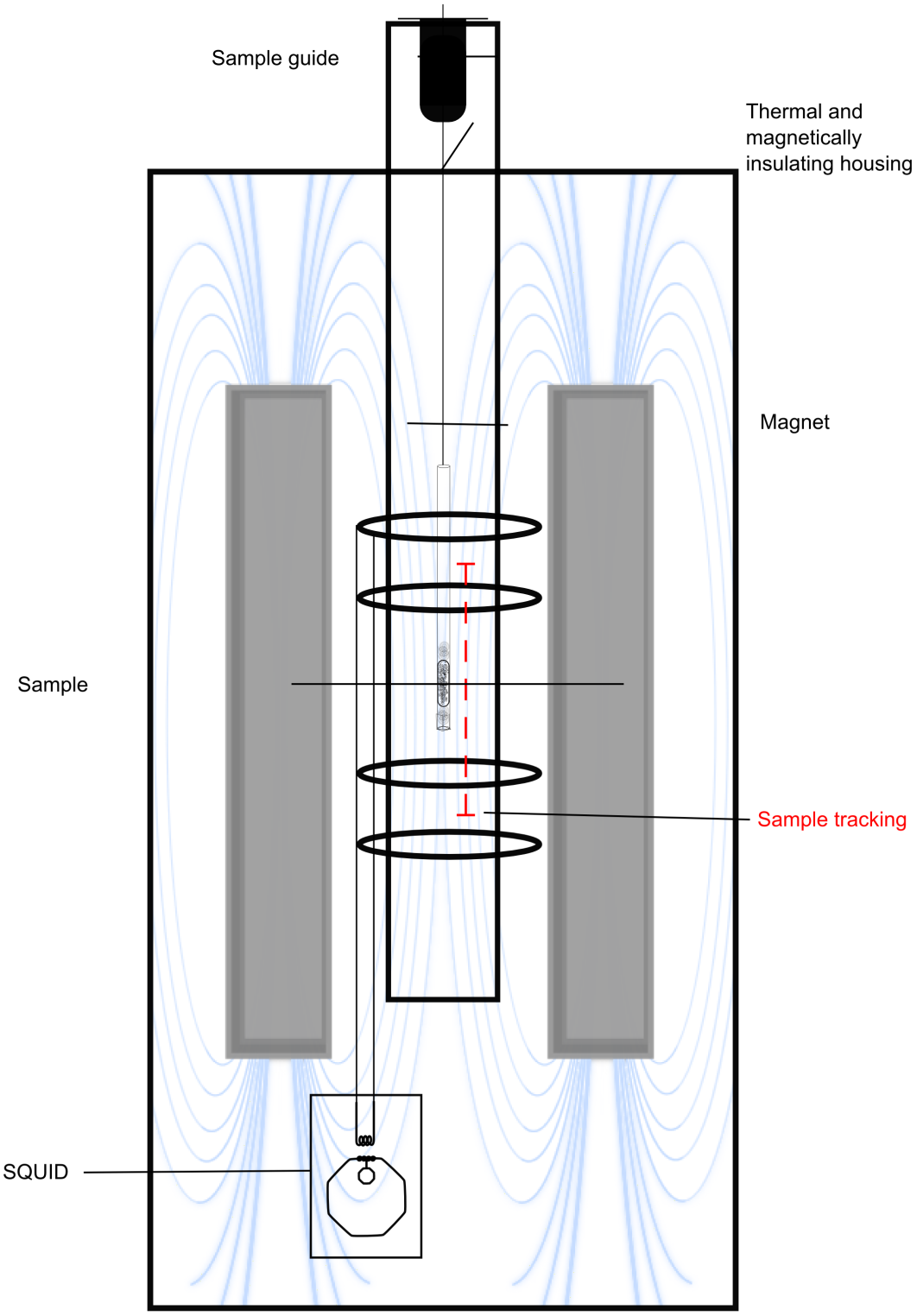

Figure A.11: SQUID magnetometer schematic -

sensitivity enhanced by the use of Josephson junction(s). Although a more technical description and discussion exist, [(172)] a gross over-simplification would be to say that the SQUID device operates by measuring a sample induced voltage change against a biased current looped about said sample. Proper sample preparation is important. The correct amount of sample must be selected to give a proper response within the detection range for the instrument, and it must be mounted in a manner that does not allow for it to move. Small displacements of the sample can affect measurement outcomes. A sample holder that has minimum mass and magnetic moment with stability at low temperatures is also necessary. The types of measurements these instruments are capable of are (partially) covered in the introduction to magnetism (above). The disadvantages to magnetic measurements is that they often require large amounts of helium, are prone to breakage (magnet can be quenched), and require advanced training to properly operate.

Instrumentation and Characterization

A brief overview and reference to a more technical review for each technique used in this work is given below. The depth of discussion will scale with relevance to this work.

Diffraction

This phenomena occurs whenever a wave (photon, neutron, etc.) interacts with an obstacle or slit that is comparable to its wavelength. Three common diffraction techniques exist that are useful to a scientist, each in their own way: X-ray, synchrotron, and neutron diffraction. The invention of a way to harness X-ray radiation by Wilhelm Rontgen in 1895 paved the way for X-ray diffraction (XRD). The X-rays had wavelengths on the same order as the spacings typical for crystal lattices. The technique was fleshed out first by the Bragg family, starting in 1912, and they went on to define and develop much of the physics necessary for the mentioned diffraction techniques. The geometrical relation between the atomic layer spacing in a crystal and the wavelength used to probe it with diffraction resulted in Bragg's law:

$$2d(sin(\theta)) = n\lambda \tag{22}$$

where d is the d-spacing, θ is the angle of incident radiation relative to the crystal plane, n is an integer, and λ is the wavelength of the radiation used.

Ideal samples are randomly arranged polycrystalline powders with zero preferred orientation. The typical experimental set-up for an X-ray diffractometer (Figure A.12)

has a source, sample, and detector. To systematically check for d-spacings in a given crystalline powder, the X-ray source is scanned about an arc (θ) relative to the sample. At different values of θ, constructive interference of X-rays due to the ordered arrangement of atoms in the solid (diffraction event) results in a observed signal at the detector. In a given full scan, each signal corresponds to a different crystal orientation (Miller indices). The difference between these d-spacings can then be used to deduce information about a sample's type (cubic, tetragonal, orthorhombic, monoclinic, etc.) and intrinsic lattice parameters (a, b, c, α, β, and γ).

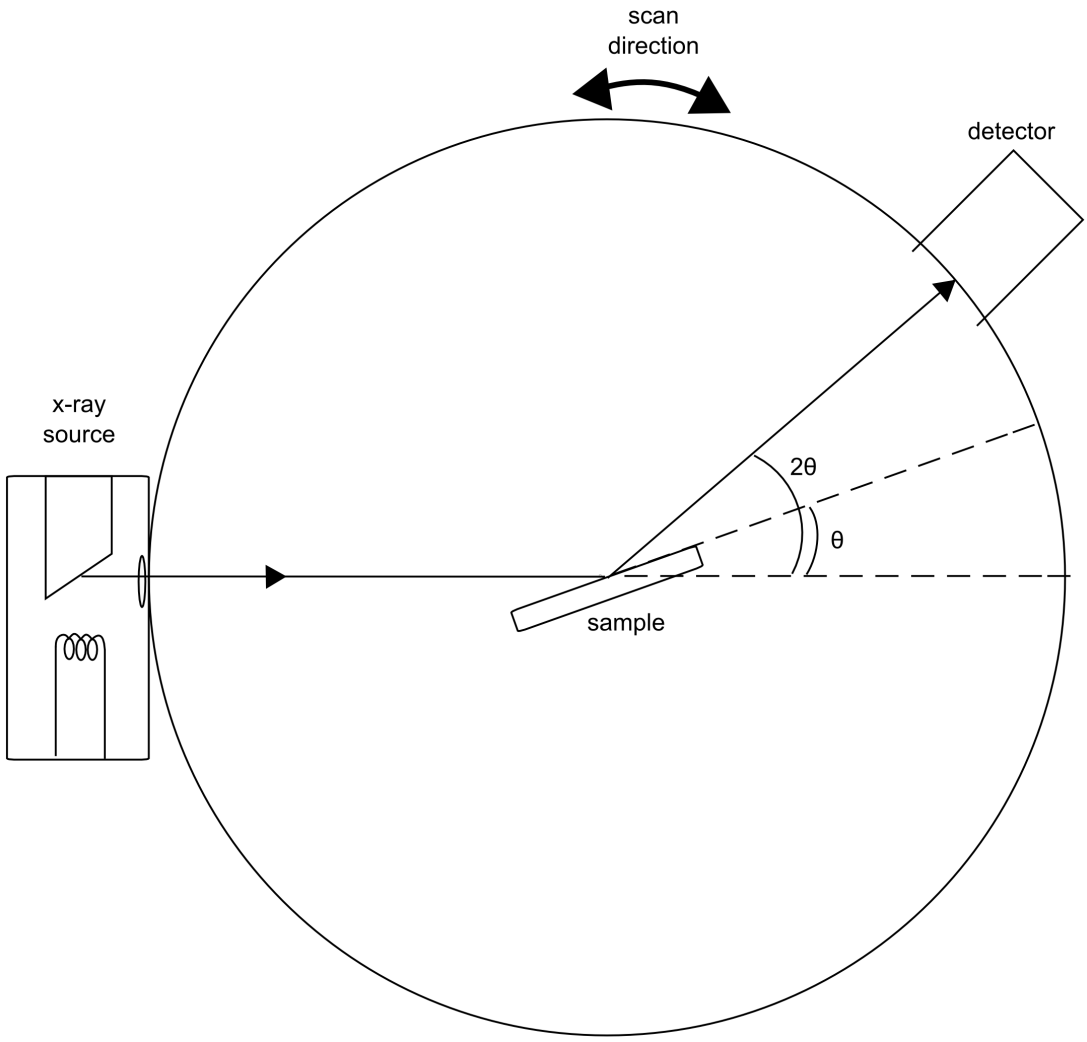

Figure A.12: X-ray Diffractometer schematic -

X-ray diffraction occurs because the light interacts with the electrons about an

atom. Higher Z atoms have more electrons present, scatter X-rays more frequently, and therefore give more counts at the detector. This can, in turn, be used to provide additional information about a given crystal, such as ion type and position within a unit cell. For additional concepts and technique with respect to XRD techniques, the reader should see Cullity and Stock. [(173)] In the case of laboratory XRD, the X-rays are generated using a process similar to how light is generated from a light bulb, except instead of using tungsten as the filament, where visible light is observed, other metals that emit x-rays are used. Metal sources arranged from more common as a source to less common are as follows: Cu ($\lambda = 1.54$ $\mathring{A}$) >> Mo ($\lambda = 0.71$ $\mathring{A}$) >> Co ($\lambda = 1.78$ $\mathring{A}$) > Cr ($\lambda = 2.28$ $\mathring{A}$). [(174)] The reason to choose one over the other is that the emitted x-ray wavelengths of a given source can be more or less prone to matching the energy needed to cause some elements to fluoresce. This phenomenon needs be suppressed to keep background intensity low in the data set. A prescient choice of source can prevent this issue from occurring. X-rays are also used in synchrotron diffraction (SXRD), but they are generated using a different mechanism. Electrons are accelerated to nearly the speed of light about a (circular) path, guided by large magnets. At each guide, the interaction of the electrons being bent with the magnetic field results in a burst of high energy X-rays, ($\lambda \sim 0.4\mathring{A}$). These X-rays are then used to effect diffraction. The benefits to this technique are: high brightness, high energy, and high intensity. These things combine to give the highest resolution and penetration depth with the smallest sample size. Additionally, SXRD also enables time resolved studies and Laue experiments (one shot, instead of a full scan) to occur. The result is more precise and accurate information about the chemical system being probed. Further inquiry regarding the applications of synchrotron light on diffraction in materials should be sought elsewhere. [(175)] A coherent source of neutrons can also be used to execute a diffraction experiment, dubbed neutron powder diffraction (NPD). This necessitates a nuclear reactor or spallation source, which limits the number of facilities that offers this technique. Filters can be used to achieve a single wavelength of neutrons or a time of flight can also be used to sort the energies of the incident neutrons. Supplementary information regarding this technique and its applications are provided by Bacon. [(176)] The benefits from the use of neutrons as an experimental technique, in addition to the resolution of the magnetic structure discussed below, are: sensitivity to low Z atoms, the ability to resolve different isotopes of the same atom, and the absence of

radiation damage. [(177)] On the other hand, the technique is not well suited to small single crystal work, is difficult to access, and depending on the sample's composition, can result in prolonged levels of radioactivity in the sample.

Transmission Electron Microscopy/ Electron Diffraction/ Scanning Electron Microscopy

Diffraction and microscopy are combined in a single instrument, a transmission electron microscope (TEM), whereby the user is able to interchangeably switch between the two techniques. To achieve this feat a technique that harnesses a very small De Broglie wavelength is required and satisfied by the use of electrons. They are generated at a source (high voltage W filament or LaB_6 single crystals), focused/collimated, exposed to a sample, and then the output recorded or observed (Figure A.13). The sample must be thin, transparent enough for some of the electrons to travel through the object unimpeded ($\sim<$ 100 nm), and vacuum stable (the best medium for unimpeded electron movement).

When microscopy of a sample is desired, an image is generated based upon the observed intensity contrasts of electrons being adsorbed by the sample. These imaged particles are helpful for resolving particle size and morphology. In high resolution TEM, enough magnification can be achieved to image individual atoms in a crystal lattice, where dislocations and defects can be examined, amongst other things. Additionally, electron diffraction (ED) can be conducted. Differing from the above diffraction techniques, the spot size of the incident electron beam is small, allowing for focus on a region of a polycrystalline particle that is uniform, coherent, and often singly crystalline. The patterns generated are a projection of the reciprocal lattice (spots corresponding to lattice reflections). This can be used to solve crystal structures (or provide supporting conclusions in tandem with other techniques), evaluate twinning, ordering, and superstructures, and examine defects (See Section 2.3.1.3). An authoritative text by Williams on this subject provides deeper insight on TEM than that provided here. [(178)] TEM is a versatile technique that yields powerful information about a sample. Notable within this instrumental suite, electron energy loss spectroscopy (EELS) can be used to determine atom type. It is not without its drawbacks, however. Some disadvantages to the use of TEM are: high upfront expense, nontrivial sample preparation, expert technical

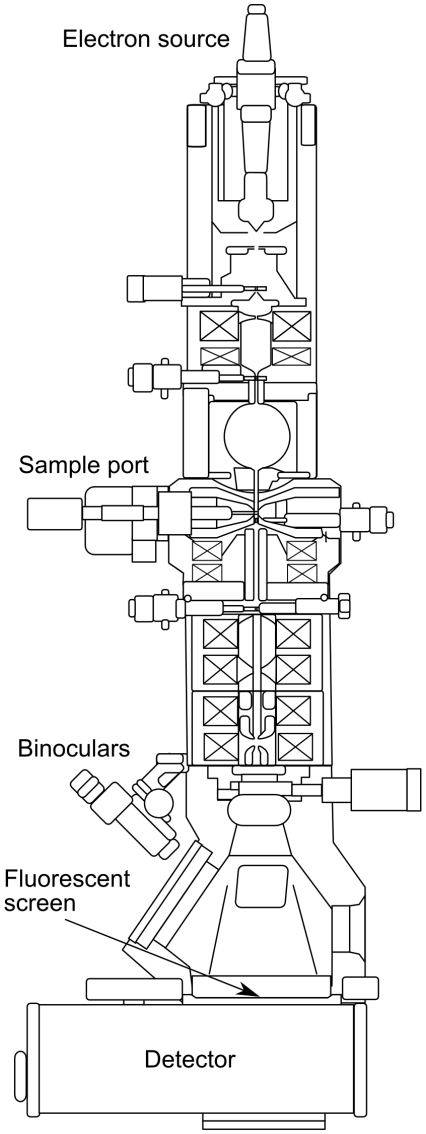

Figure A.13: TEM schematic -

training required for use, sample size constraints, and the instruments are high maintenance. Scanning electron microscopy (SEM) is similar to TEM in that electrons are used to probe a medium, but differs by imaging the material using scattered electrons (instead of transmitted ones). A benefit of the former is that the electron generation and focusing optics of the two techniques are basically identical. Consequently, the sample platform and the detector type as well as configuration are different. Less stringent sample size constraints exist in SEM, because samples are no longer limited by the need to be thin. SEM resolution is lower. SEM yields information about the surface and morphology of a sample, whereas TEM is optimized for atomic level attributes. A useful add-on technique to SEM is called energy dispersive x-ray spectroscopy (EDXS), which enables identification of the elemental make up on the sample's surface. SEM and X-ray microprobe analysis are thoroughly covered elsewhere by Goldstein. [(179)]

UV-visible Diffuse Reflectance

Just as SEM uses the back-scatter of electrons from a material to produce data, diffuse reflectance instead uses electromagnetic radiation with energies near the visible (200 – 800 nm) to illuminate the surface of a material. A detector is used to detect reflected light or the absence of reflected (absorbed) light. There are two types of reflected light: specular and diffuse. The former glances off the incident surface with a mirror-like interaction, such that the angle of incidence is equal to the angle of reflection. Diffusely reflected light on the other hand is indicated by a luminous distribution of reflected light at the spot of incident radiation, i.e. the diffuse light is reflected in a multitude of directions. The mechanism driving the diffuse reflectance phenomenon is sub-surface scattering centers/interfaces. [(180)] Light reaches a randomly arranged interface particle or otherwise, that has features on the same order of magnitude as the wavelength of light. Some of the incident light undergoes reflection, some is transmitted, and the process repeats enough times that a randomly oriented luminal distribution of light is reflected back. In addition to reflection, if the energy of an incident photon is greater in energy than the band gap (E_g) of the compound, adsorption can occur. The band gap is the energy separation between the conduction band of a material and the valence band:

$$E_g = E_{CB} - E_{VB} \tag{23}$$

Other adsorption events can occur as well that don't involve the band gap but are the result of light induced charge transfer. The important information obtained from a typical UV-visible diffuse reflectance measurement then is the energy separation between the selected electronic states within a compound. This is also the minimum energy needed to facilitate photon driven charge transfer. Transition metal compounds often have octahedral e_g and t_{2g} splitting energies that are resolved in the energy range probed. Absorption(s) due to these electronic states are what gives a given compound its apparent color (reflected color sans absorbed wavelengths of photons). The instrumental set up is straightforward (Figure A.14) and has been streamlined by the invention of fiber optics, which supplant the need for an integrating sphere. Recent progress in this technique is presented by Schoonheydt. [(181)]

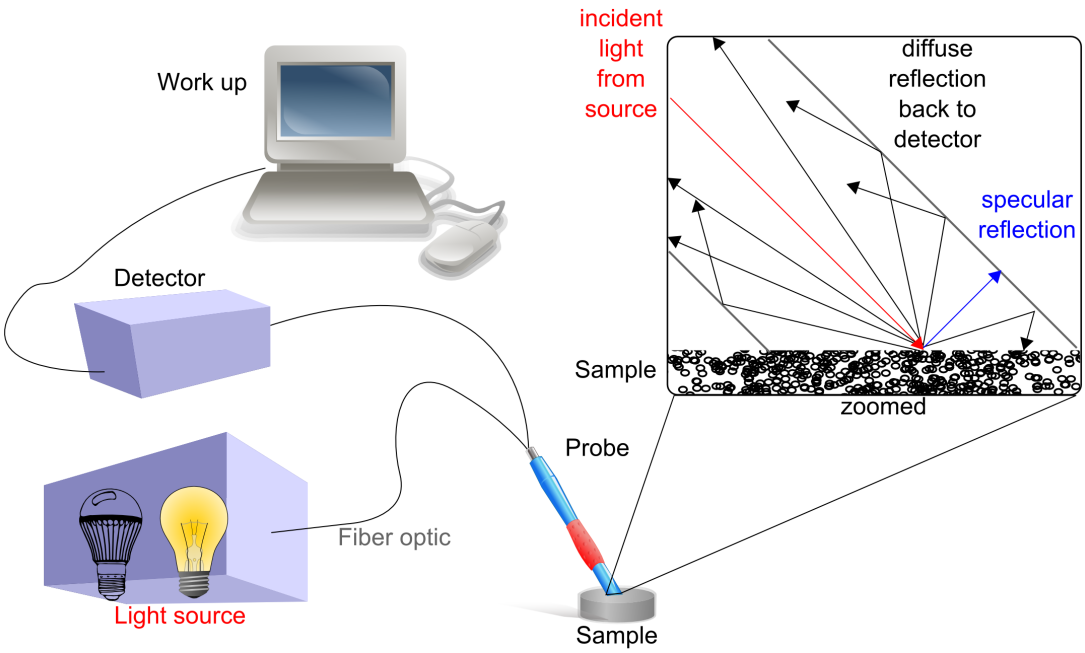

Figure A.14: UV-visible diffuse reflectance schematic - There are many fates for reflected light (inset)

X-ray photoelectron spectroscopy (XPS)

Dr. Kai Siegbahn is credited with the invention of this instrument in the 1960s. Owing to the versatility of the technique and the relative ease of operation, the instruments became ubiquitous. A Nobel Prize (Physics) acknowledging this contribution was awarded in 1981. XPS is a non-destructive surface technique that is capable of measuring the

composition, empirical formula, chemical and; electronic states, and uniformity of a given compound or film. Both insulating and conducting samples can be probed. The instrumental set up requires a high vacuum, sample stage, directed high energy X-rays, and an ejected electron capture detector (Figure A.15). In order for a detection event to occur, an electron must be ejected from the sample. This can be achieved if a high energy X-ray (Al K_α) collides with a core electron and the X-ray is of greater energy than the binding energy of the given core electron. This event must occur near the surface of the compound, so that the electron can traverse through the vacuum, be collected, sorted by energy, and then detected. A composite profile yielding the binding energies of each element contained within the sample can be ascertained.

The energies of the ejected, sorted electrons can probe electronic states up to the valence band of the material. In this capacity, it can be used to gauge the energy separation between the valence band (featured in XPS spectra) and the Fermi level (zero binding energy). Moreover, this can help to identify comparative differences near the valence band within a series of related compounds. There are many caveats to this experimental technique. The front runner is that it is very surface sensitive, surfaces are usually dirty, so results can be adversely affected by this. Adventitious carbon is almost unavoidable in sample analysis, but on the other hand, it is well documented as a result of this. The binding energy of the C 1s electron at 284.6 eV is then used to normalize the rest of the data obtained. Other difficulties associated with XPS are that valence band fine structure cannot be obtained (so ultraviolet photeelectno spectroscopy (UPS) should be used), it requires the bulk to be similar to the surface for accurate results, and is limited by the probe area (10 μm minimum). For a more thorough analysis of this technique, Watts has authored a review. [(182)]

Time-resolved Infrared Spectroscopy (TRIR)

The emergence of this technique is predicated on the addition of time resolution, a relatively new innovative technique, to an older technology, spectroscopy. This was driven by the invention of devices that are capable of operating under very fast and short time constraints, which has also been aided by lasers that have binary-like on-off responses. Additionally, with rapid advances in the computing (transistor) industry, limitations associated with response time for a given device have been increasingly

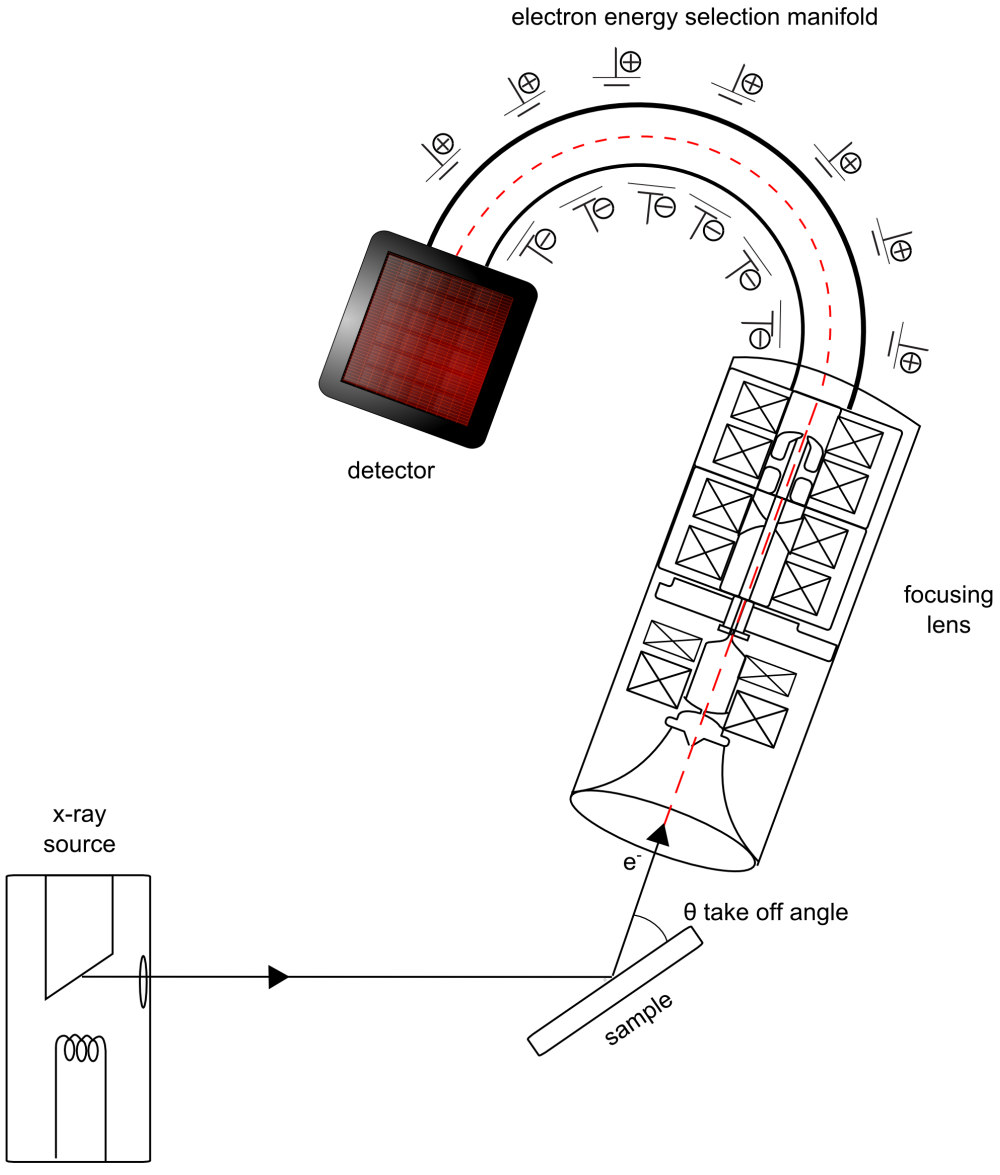

Figure A.15: XPS schematic -

repealed. The time intervals available for analysis have decreased from micro- to nano-, pico-, and even into the femtosecond regime. To understand how this technique works, it should be broken down into its 3 respective parts: pump, probe, and time resolution. There are a variety of different pump (laser, LED, lamp, *etc.*) and probe (UV, visible, IR, *etc.*) combinations that can be chosen to understand different dynamic effects that occur when light interacts with a sample. In the case of time-resolved infrared spectroscopy, the technique provides structural information on the excited-state kinetics. Both dark and emissive states can be understood in this way. For this work, the decay time of photogenerated carriers is employed. The time regime at which these effects are measured is in the picoseconds. In a typical run sequence, the sample is pulsed with an intense, usually coherent light (pump) for a duration of time. The wavelength of light should be chosen such that it is of suitable energy to facilitate the adsorption of said light by the sample. Often times, this corresponds to laser energy that is equivalent to or slightly greater than the band gap of the material. Simultaneously, the sample will also be exposed to a pulse of infrared light (probe). The pump is sequentially turned off, and the infrared light remains. Changes in adsorption of the compound in the infrared ($\sim$ 1700 cm^{-1}) are recorded per unit time. Usually the investigated spectroscopic features grow in intensity or decay away. Schematically (Figure A.16), the technique is straightforward, but experimentally complicated. The reader is urged to consult the literature for additional information as it continues to evolve and develop. [(183)]

Electronically, the explanation of what is occurring during the time resolved infrared spectroscopy process is that the pump excites a carrier (electron) from the valence band maximum to the conduction band minimum. The probe is then utilized to further excite that carrier in higher energy states within the conduction band. As the probe is shut off, no new carriers are generated. What happens to the already excited population of carriers is observed. A variety of processes can occur with the excited carriers such as being transferred to a defect or carrier recombination. These effects occur on different time scales, with the relevant latter instance occurring on very short time scales (tens of picoseconds).

BET Surface Area The year 1938 saw what would go on to be a very successful analytical technique for the determination of the total exposed surface existing on a given

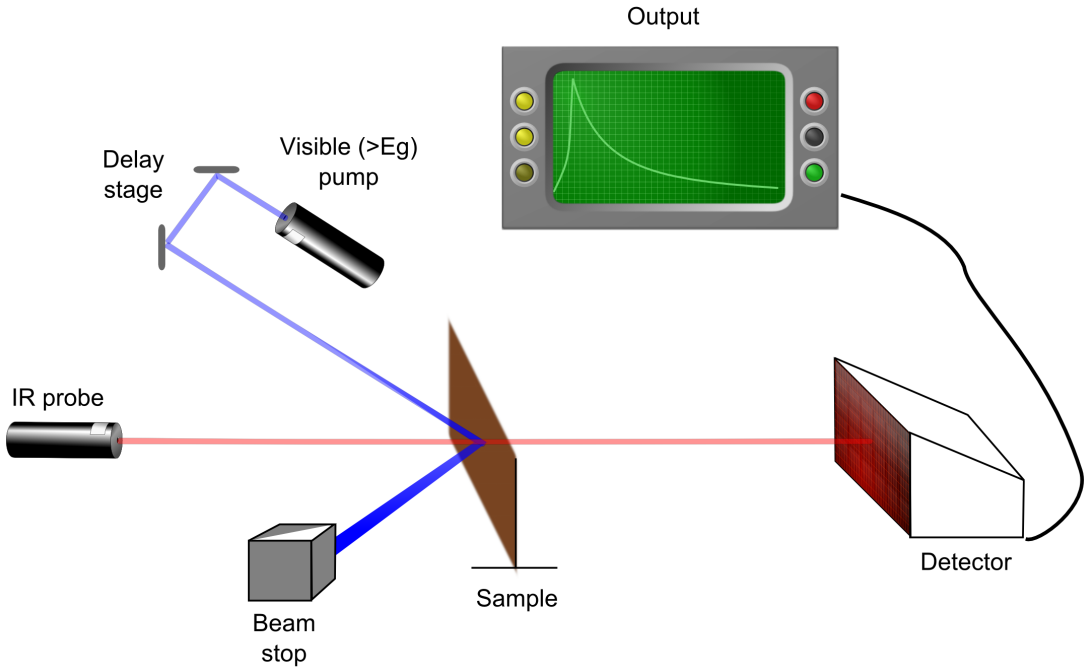

Figure A.16: Time-resolved infrared spectroscopy schematic -

solid. It was presented by Brunauer, Emmett, and Teller (BET), and they showed that determination of specific surface area can be achieved by examining the multi-layer adsorption of non-corrosive gases (N_2, CO_2, Ar) on a sample surface. In addition to the surface area, the pore volume, area, and diameter can be obtained from this technique. These data are helpful in characterizing the effects of sample surface porosity and particle size. In turn, these can aid in the design of catalytic, filtration, and adsorbent systems, as well as in sintering and reactivity studies. Enough sample should be provided for a given measurement such that at least 1 m^2 of total surface is exposed. A standard is often used in tandem to confirm results. To execute a measurement, the sample is placed in a vessel (Figure A.17). It is heated to desorb any residual surface species and then proceeds to lower the pressure to a set point, usually near 5 Pa. The dead volume of the vessel is determined, and the temperature of the vessel is cooled to 77 K. A sufficient amount of N_2 gas should be allowed into the vessel to yield the lowest desired relative pressure. By adjusting the P/P_0 values, the volume of adsorbed gas can be monitored and converted to the surface areas. An additional reference is available by Shields and Lowell. [(184)]

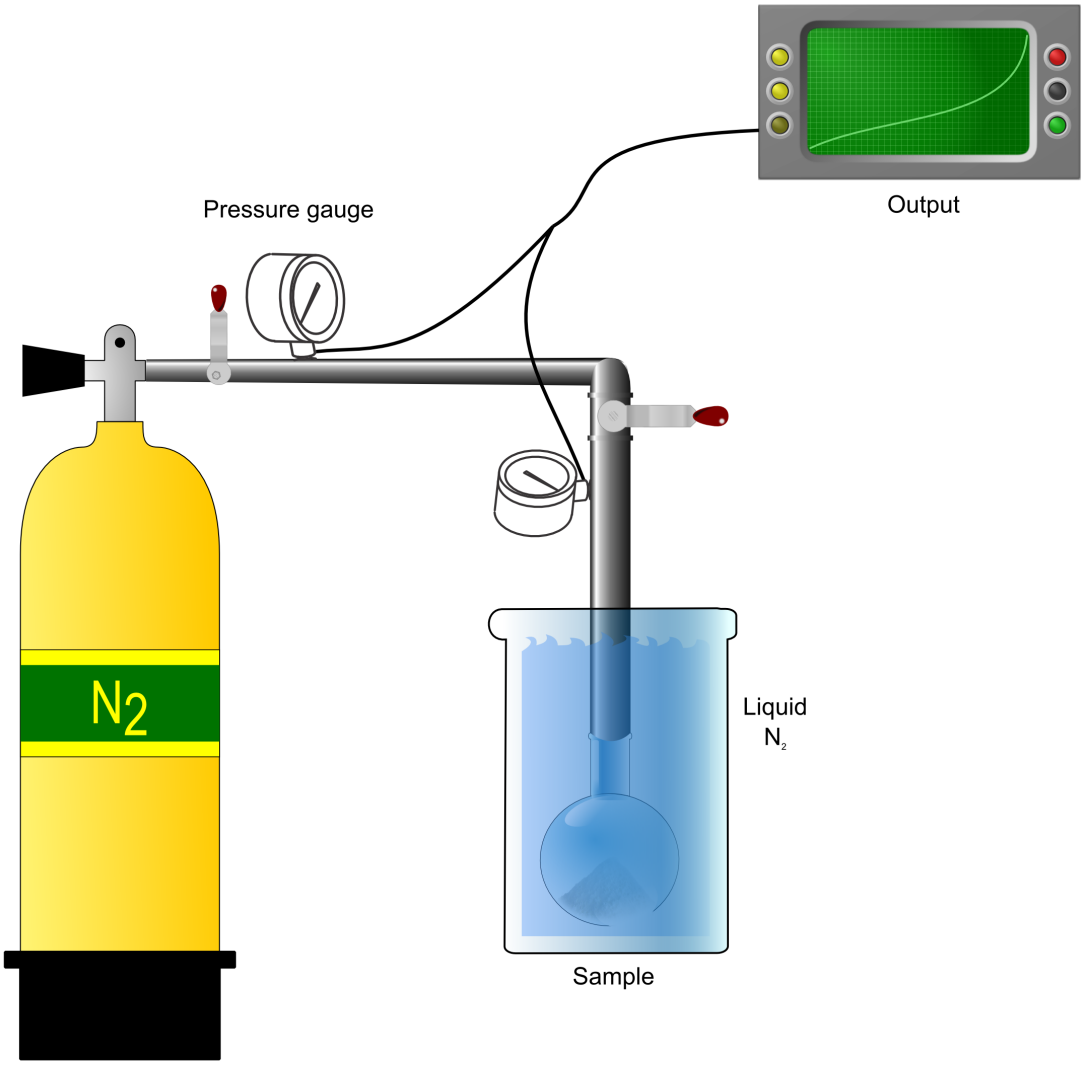

Figure A.17: BET surface area schematic -

Note on the Instrumentation

The above sections exist to aid in fully understanding the concepts presented later in this thesis. They are used as individual measurements to aid in characterization or property measurements. In other circumstances, a multitude of techniques are used and summed as a whole to give conclusive results. Basic knowledge of how the data are generated, collected, and used are important precursors for understanding and then explaining the observed chemical properties, not to mention for optimizing them.

APPENDIX B: SUPPORTING INFORMATION FOR THE STRUCTURAL AND MAGNETIC PROPERTIES OF RTiNO$_2$ (R = Ce, Pr, Nd) PEROVSKITE NITRIDE OXIDES

Structure refinements for XRD data

Final XRD Rietveld refinements for $CeTiNO_2$ and $PrTiNO_2$ (Figure B.1 and B.2) leads to a *Pnma* space group assignment. For RTiNO$_2$, refinement of the 8d Wyckoff position results in divergence as a result of the poor sensitivity of the XRD to weak peak splittings typically found in pseudocubic structures [(34)]. It was accounted for by weighting Ti-N bond distances to values similar to those reported by Clarke *et. al.* for $NdTiNO_2$, with which our prepared Nd sample is in agreement [(55)]. The *Pnma*-indicating <*eeo*> indice are more distinct in the $PrTiNO_2$. The $CeTiNO_2$ may be near a transition from *Pnma* to $I\bar{1}$, the space group observed for $LaTiNO_2$ (refinements still yield the best fit in *Pnma*). The anomaly in the difference curve at *ca.* 28 °2θ for $CeTiNO_2$ is due to a small amount (< 1 %) of starting material, $Ce_2Ti_2O_7$.

A Rietveld refinement on XRD data for $PrTiNO_2$ carried out with *Pnma* symmetry converged to a good fit (R_{wp} = 8.19 %). For the sake of completeness, refinements were

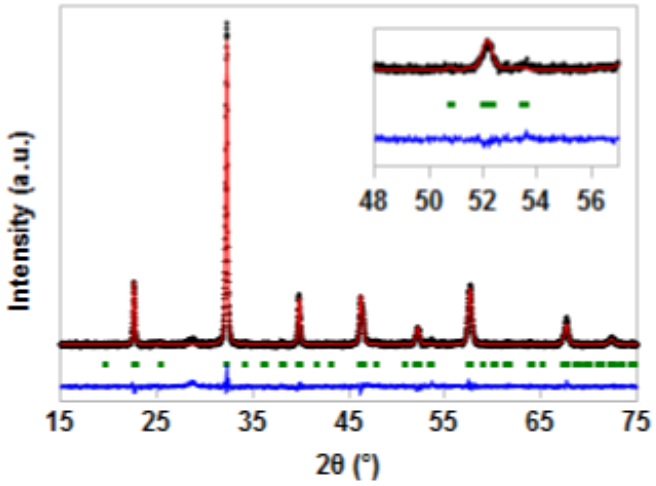

Figure B.1: Rietveld refinement of XRD data of $CeTiNO_2$ - Black = observed, red = calculated, blue = difference, green hashes = indexed reflections. Inset shows the $<eoo>$ peak at *ca.* 53 °2θ.

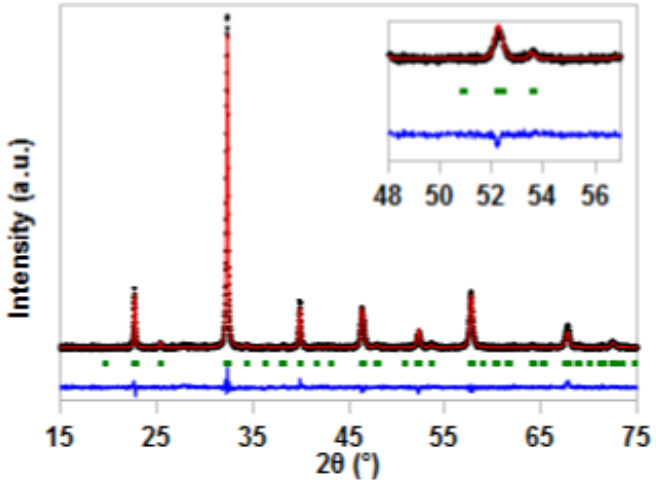

Figure B.2: Rietveld refinement of XRD data of $PrTiNO_2$ - Black = observed, red = calculated, blue = difference, green hashes = indexed reflections. Inset shows the $<eoo>$ peak at *ca.* 53 °2θ.

carried out in space groups corresponding to other patterns of tilting—$a^+b^+c^-$($Pmmn$ symmetry, $R_{wp} = 21\%$), $a^+b^-c^-$($P2_1/m$ symmetry $R_{wp} = 13.53\%$), $a^0a^0c^-$ ($I4/mcm$ symmetry, $R_{wp} = 9.39\%$), and $a^0a^0a^0$ ($Pm\bar{3}m$ symmetry, $R_{wp} = 9.55\%$)— but all other symmetries gave inferior fits and thus can be ruled out.

Anion order

Different ordering models for a perovskite with an $a^-b^+a^-$ tilting arrangement and –XY_2 anion stoichiometry have been worked out previously [(40)] and are applied here. The models can be broken into three groups: random (**1**: *Pnma* disordered), trans (**2a**: *Pnma* and **2b**: $P2_1/m$), and cis (**3a**: $Pmn2_1$, **3b**: $Pmc2_1$, and **4**: cis 2D-chains *Pnma*). Triclinic ordering models are also possible, but were excluded due to a lack of experimental evidence for their existence.

To analyze $CeTiNO_2$ and $PrTiNO_2$, each of the ordering models (**1** – **4**) was used to refine the NPD data. The goodness of fit was then compared to each other (Table 1). Similar conclusions to previous work were arrived at [(40)]. The best fits per ordering model are trans < cis disorder. $CeTiNO_2$ was best fit by model **1** and **4**, with anion occupancies set to 33% N / 67% O at all anion Wyckoff positions and occupancies allowed to refine stoichiometrically, respectively. Similarly, model **1** and **4** were found to be equivalent for $PrTiNO_2$. When anion occupancies for this compound were allowed to refine freely they arrived at similar anion occupancies to model **4**, in which partial anion order exists as 2D-cis chains comprised of – N – Ti – N – Ti – linkages. XRD derived lattice parameters of our $NdTiNO_2$ are in agreement with a previous NPD study [(55), which suggests that RTiNO$_2$ (R = La and Nd) favors a disordered anion arrangement (model **1**).

There is a pitfall in the refinement process that explains different ordering conclusions for these compounds: the insensitivity of refined occupancies in a pseudo-tetragonal system. While a more pronounced orthorhombic system ($NdTiNO_2$ or $CeTiNO_2$) has adequate peak splittings that allow for refinement of occupancy dependent reflections for an array of nitrogen/oxygen ratios (Figure B.3), the pseudo-tetragonal system ($PrTiNO_2$) has overlapping reflections that lead to identical intensities regardless of occupancy distribution, preventing accurate refinement. By comparing a and c lattice parameters, the proximity of these *Pnma* systems to a pseudo-tetragonal unit cell is ascertained. For $a/c = 1$, no distortion occurs and the system

is tetragonal. In RTiNO$_2$, the a/c values increase from 0.9951 (Ce), to 0.9990 (Pr), to 1.0027 (Nd), passing through a pseudo-tetragonal phase near PrTiNO$_2$. Simulated NPD patterns have shown that changes in occupancy are nuanced when $a/c = 1$(comparisons of simulated NPD for lattice and occupancy changes in PrTiNO$_2$, Figure B.4), in agreement with previous findings [(34)]. In pseudo-tetragonal PrTiNO$_2$, freely refined occupancies drift to what best fits a fully tetragonal nitride oxide perovskite, i.e. occupancies matching $I4/mcm$ SrTaNO$_2$ (2D-cis ordered; model **4**). Conversely, the Nd and Ce analogues have adequate orthorhombic distortions and the anion occupancies for N and O bear weight in the refinement. This explains why model **4** fits PrTiNO$_2$ well but provides a less adequate fit versus model **1** in CeTiNO$_2$.

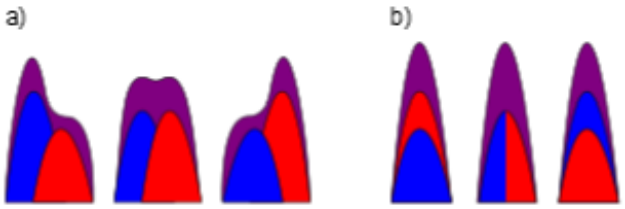

Figure B.3: Simulated NPD intensity outcomes based on various anion occupancies in a generic a) orthorhombic and b) pseudo-tetragonal perovskite nitride oxide - The simulated pattern (purple) is derived from the summed contributions of oxygen (red) and nitrogen (blue).

Simulated neutron powder diffraction patterns

The .cif files from the final NPD Rietveld refinement for PrTiNO$_2$ were imported into Diamond 3.0 (Crystal Impact; Bonn, Germany). Lattice parameters as well as the occupancies were adjusted accordingly to assess changes in the NPD patterns (Figure B.4).

Rietveld Refinements of NPD patterns at low angles

Fitting of the peaks at low angles gave a good finger printing approach to properly identifying the correct space group. This region had reflections that were sensitive to the various ordering models. Each of the various models were refined against the NPD data for PrTiNO$_2$ (Figure B.5) and CeTiNO$_2$ (Figure B.6).

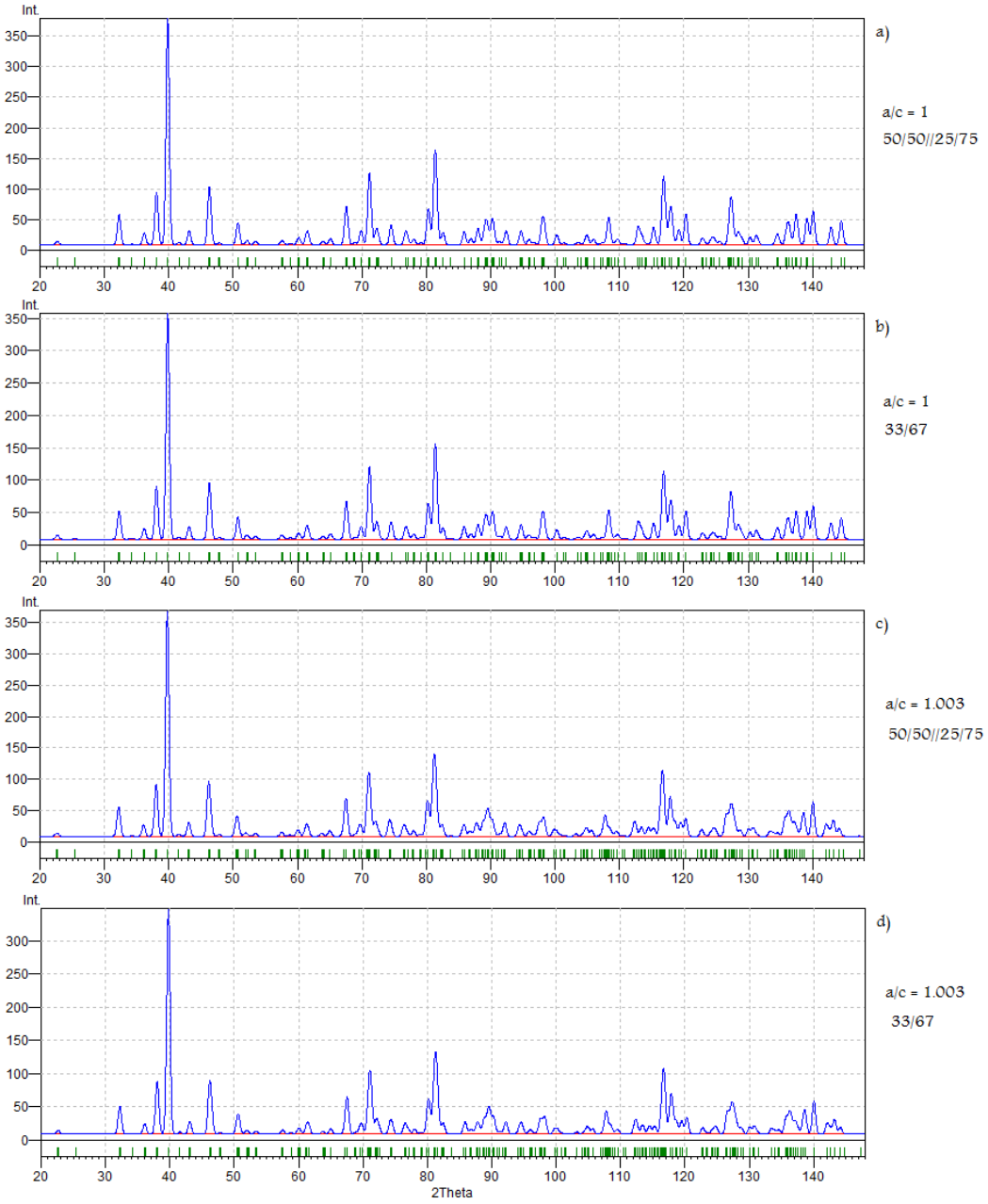

Figure B.4: Investigating anion order by simulated NPD patterns for $PrTiNO_2$ of varying a/c and anion occupancy. - Pseudo-tetragonal ($a/c = 1$) simulations with anion ordering model a) **4** and b) **1** are compared to orthorhombic distortions ($a/c = 1.003$) with anion model c) **4** and d) **1**.

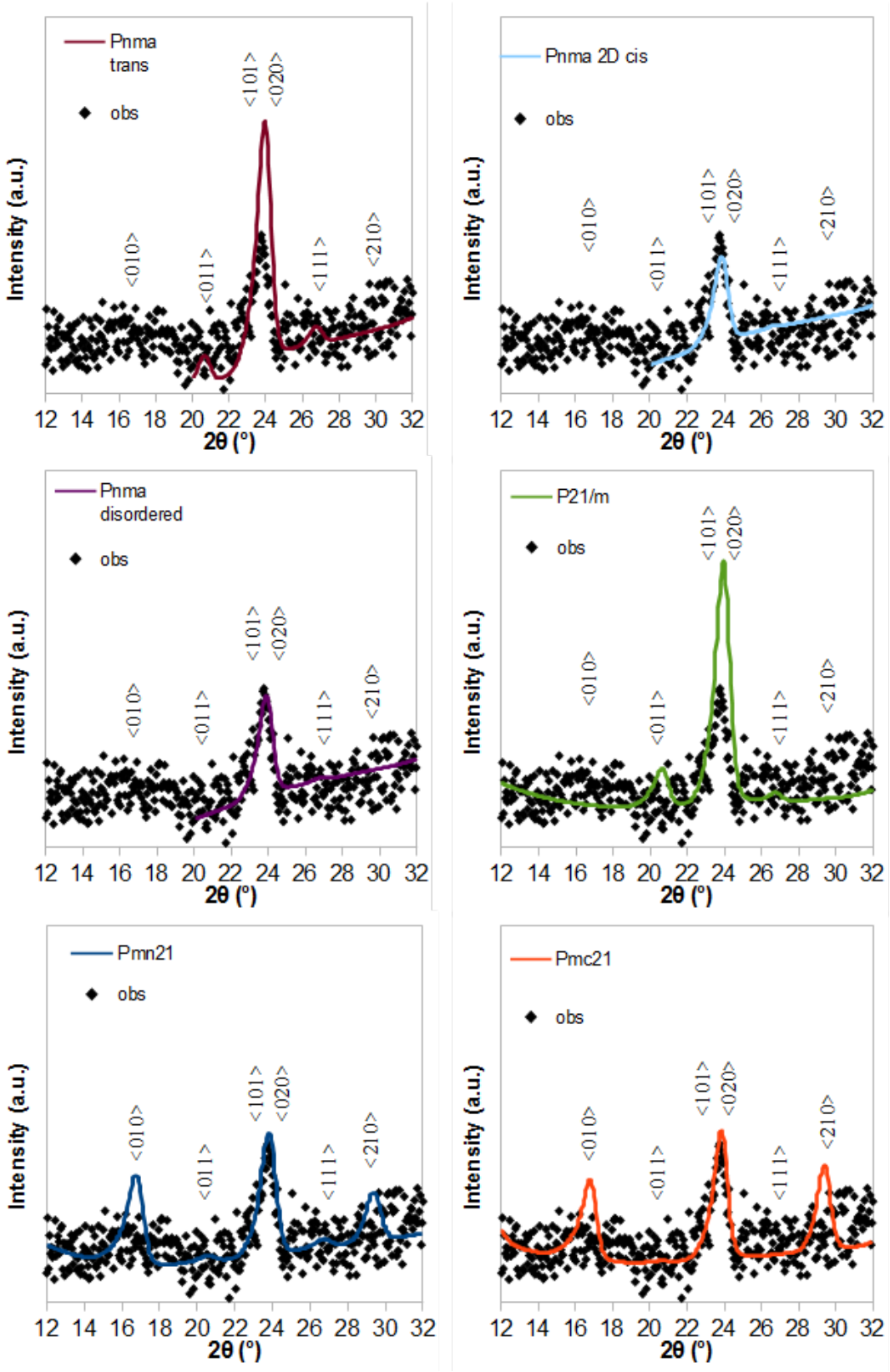

Figure B.5: NPD Rietveld refinement fits for anion ordering models at low angles in $PrTiNO_2$. - Experimental (back dots) and calculated colored line are shown

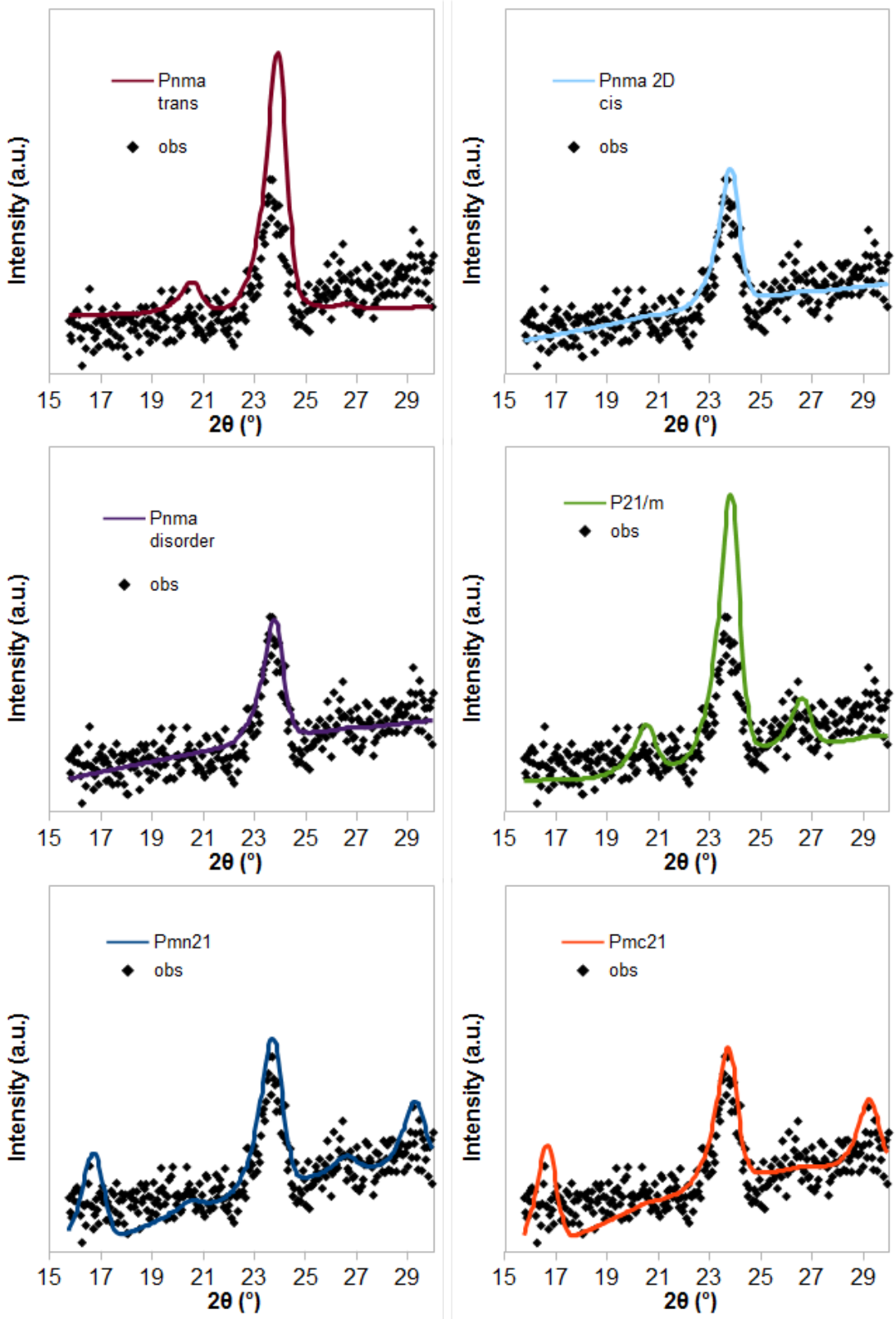

Figure B.6: NPD Rietveld refinement fits for anion ordering models at low angles in $CeTiNO_2$. - Experimental (back dots) and calculated colored line are shown

TEM supporting data

TEM images of the $PrTiNO_2$ samples (Figure B.7) indicate the morphology and size distribution of the as synthesized particles. Long range anion ordering was evaluated by comparison of experimental electron diffraction patterns to simulated patterns for both the $CeTiNO_2$ (Figure B.8) and $PrTiNO_2$ (Figure B.9). Evidence from the ED data suggests long range order, however the Rietveld refinements of $CeTiNO_2$ (Figure B.10, top) and $PrTiNO_2$ (bottom) in the specified system do not provide a better fit versus the disordered *Pnma* model.

Magnetic measurements of RTiNO$_2$

The temperature dependent magnetic susceptibility of the RTiNO$_2$ compounds under field cooled and zero field cooled conditions (Figure B.11) yields paramagentic behaviour. In support of these findings the isothermal magnetization curves (Figure B.12 also confirm paramagnetic behaviour.

Additional bond parameters

Individual bond distances and angles are provided (Table B.1) as a supplement to the averaged distances provided in the main text.

Compound	M-X (Å)			M-X-M (°)	
$CeTiNO_2$	2x 1.991(3)	2x 1.9950(6)	2x 2.005(3)	158.241(2)	160.6(1)
$PrTiNO_2$	2x 1.995(4)	2x 1.995(4)	2x 1.9976(8)	156.6(2)	158.9(1)
$NdTiNO_2$	2x 1.9951(7)	2x 1.9963(2)	2x 2.0060(7)	155.40(1)	156.42(3)
$CeGaO_3$	2x 1.93(2)	2x 1.998(3)	2x 2.00(2)	151.475(3)	161.2(9)
$PrGaO_3$	2x 1.977(2)	2x 1.9798(7)	2x 1.992(2)	154.58(9)	155.029(1)
$NdGaO_3$	2x 1.9729(5)	2x 1.975(1)	2x 1.988(1)	153.59(6)	153.854(2)
$CeAlO_3$	2x 1.897(9)	4x 1.898(5)		166.4(3)	
$PrAlO_3$	6x 1.8957(5)			166.2(1)	
$NdAlO_3$	6x 1.8931(2)			164.81(4)	

Table B.1: Bond parameters for RTiNO$_2$ and analogous oxide compounds

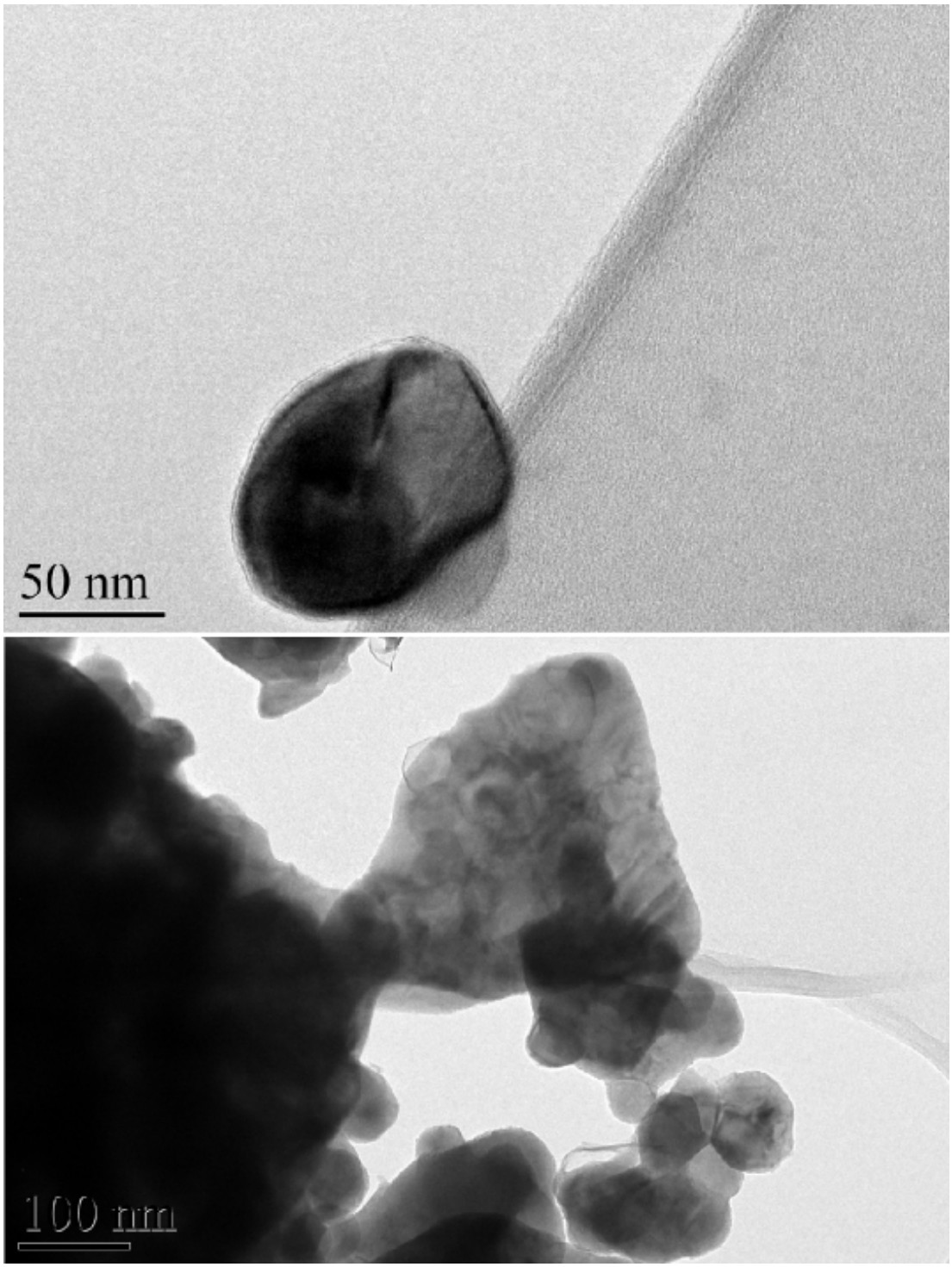

Figure B.7: TEM images of agglomerated particles of $PrTiNO_2$. -

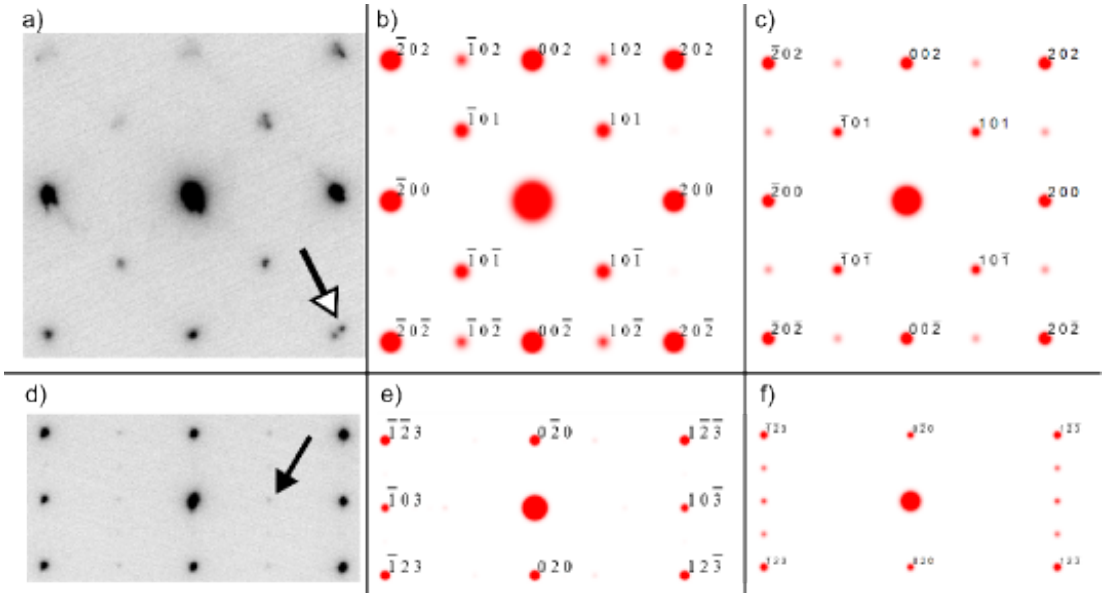

Figure B.8: Experimental (black dots) and simulated (red dots) electron diffraction patterns for $CeTiNO_2$. - A major zone axis [010] (top row) is complemented by a minor zone axis [301] (bottom row). Experimental patterns (a and d) are matched to simulations in *Pnma* (b and e) and $P112_1/m$ (c and f). Electron diffraction patterns suffer from crystal twinning (white arrow). Weak reflections (black arrow) are thought to be due to anion ordering.

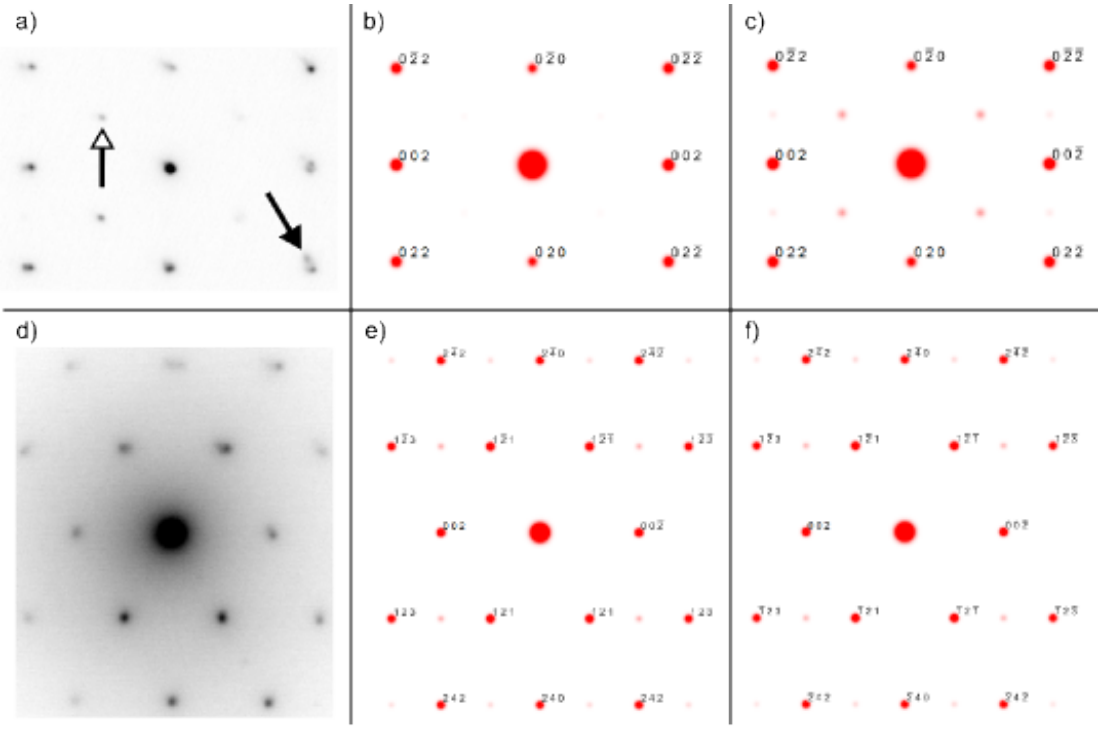

Figure B.9: TEM (black dots) and simulated (red dots) electron diffraction patterns for $PrTiNO_2$ - A major zone axis [100] (top row) is complemented by a minor zone axis [210] (bottom row). Experimental patterns (a and d) are matched to simulations in *Pnma* (b and e) and $P112_1/m$ (c and f). Electron diffraction patterns suffer from crystal twinning (black arrow). Weak reflections (white arrow) are thought to be due to anion ordering.

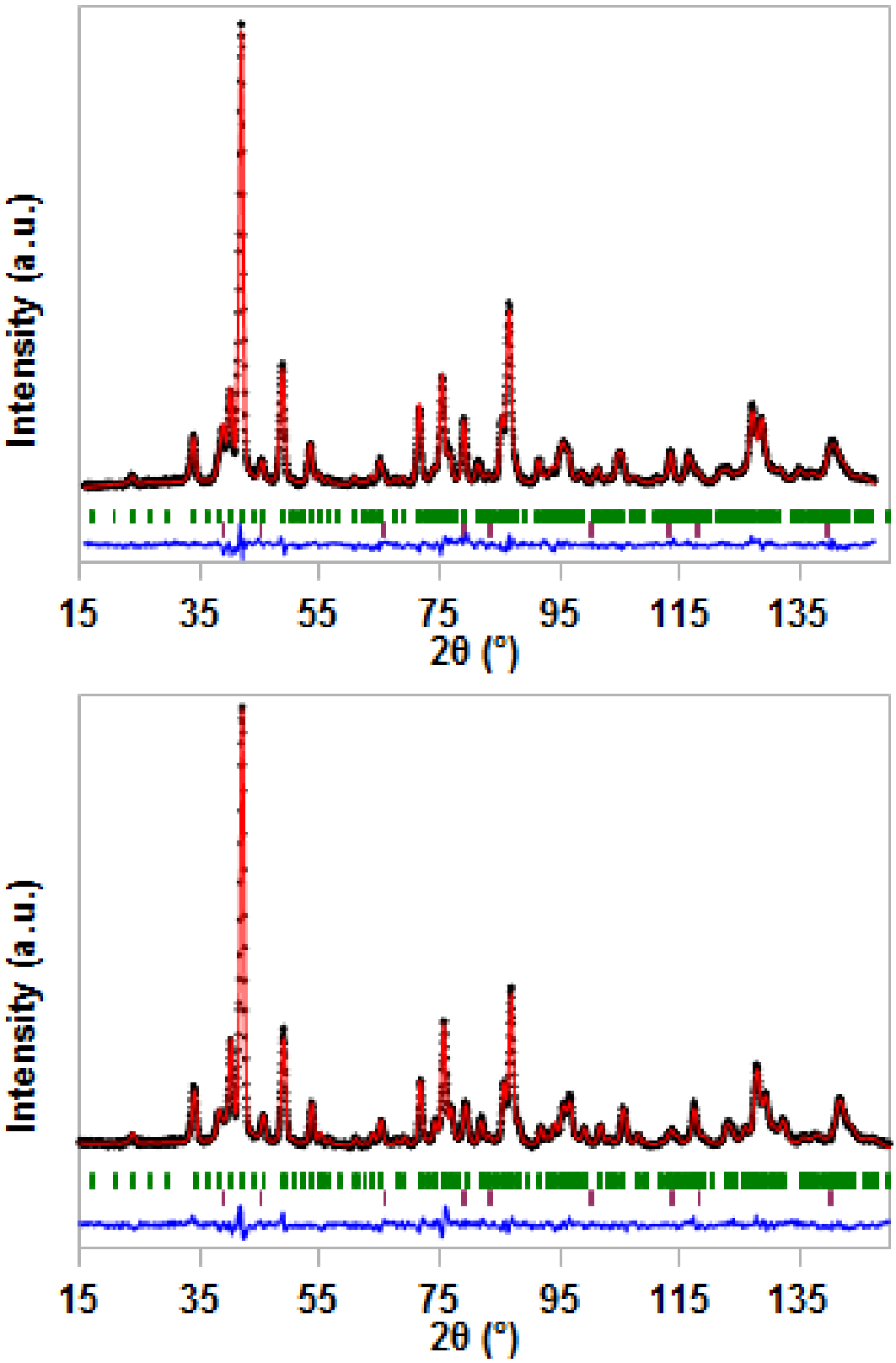

Figure B.10: Rietveld refinements of NPD data for $CeTiNO_2$ (top) and $PrTiNO_2$ (bottom) in $P112_1/m$. -

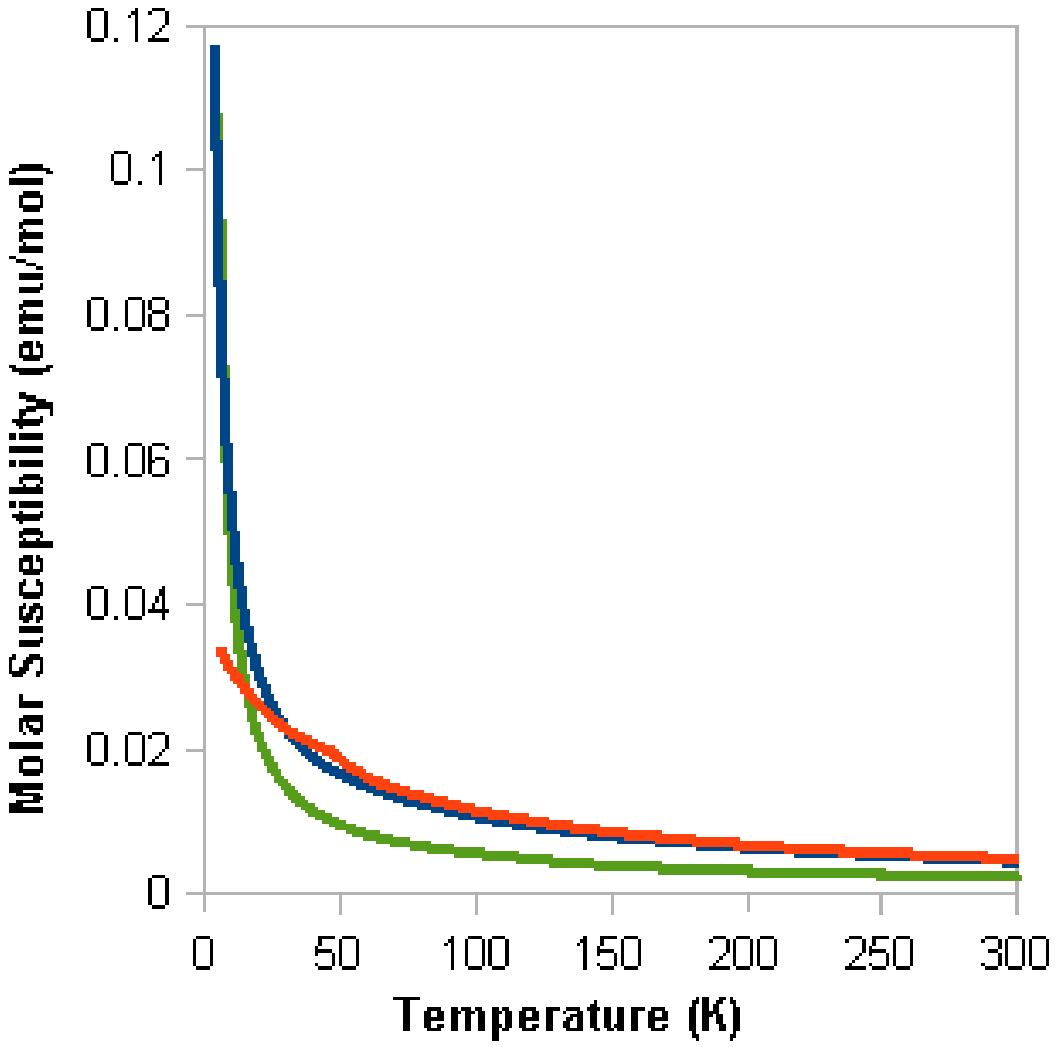

Figure B.11: ZFC cooled paramagnetic behaviour down to 5 K in RTiNO$_2$ where R = Ce (green), Pr (red), and Nd (blue) - FC data yield identical plots (not shown here).

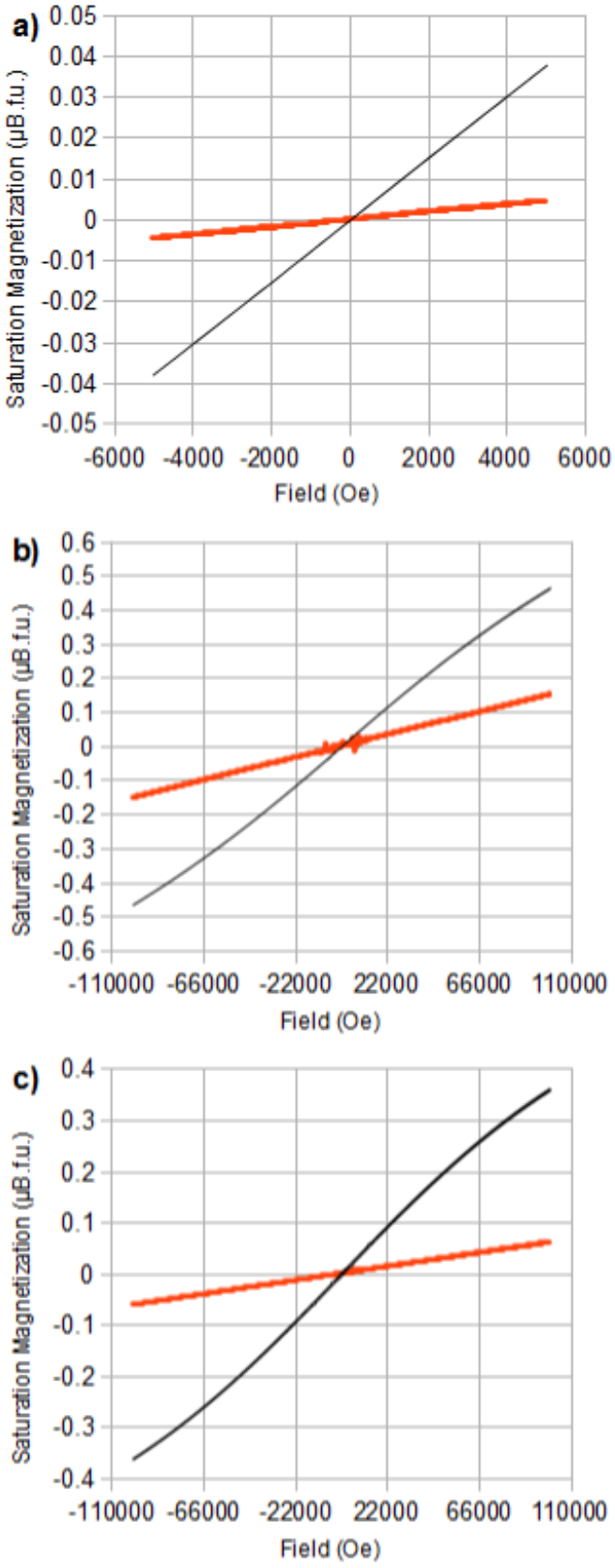

Figure B.12: Isothermal magnetization curves at 10 (black) and 300 K (red) for RTiNO$_2$ where R is a) Ce, b) Pr, and c) Nd. -

APPENDIX C: SUPPORTING INFORMATION FOR ELECTRONIC STRUCTURE AND PHOTOCATALYTIC WATER OXIDATION BY RTiNO$_2$ (R = Ce, Pr and Nd) PEROVSKITE NITRIDE OXIDES

BET measurements

N_2 isotherms for RTiNO$_2$ (R = La [Figure C.1], Ce [C.2], Nd [C.3]) show Type IV behavior. Pore size distribution (inset) is comparable between these samples. As pore diameter decreases pore volume increases. CeTiNO$_2$ has a slight deviation from this trend, with a pore diameter weighting more heavily about 55 nm.

SEM/EDXS measurements

SEM/EDXS analysis on RTiNO$_2$ (R = La [Figure C.4], Ce [C.5], Pr [C.6]) shows that particle size distribution is consistent between all samples and each contains both large (50 100 μm) and small (100 nm 10 μm) particles. There is an even distribution of each constituent element, including the wet-impregnated CoO$_x$ co-catalyst.

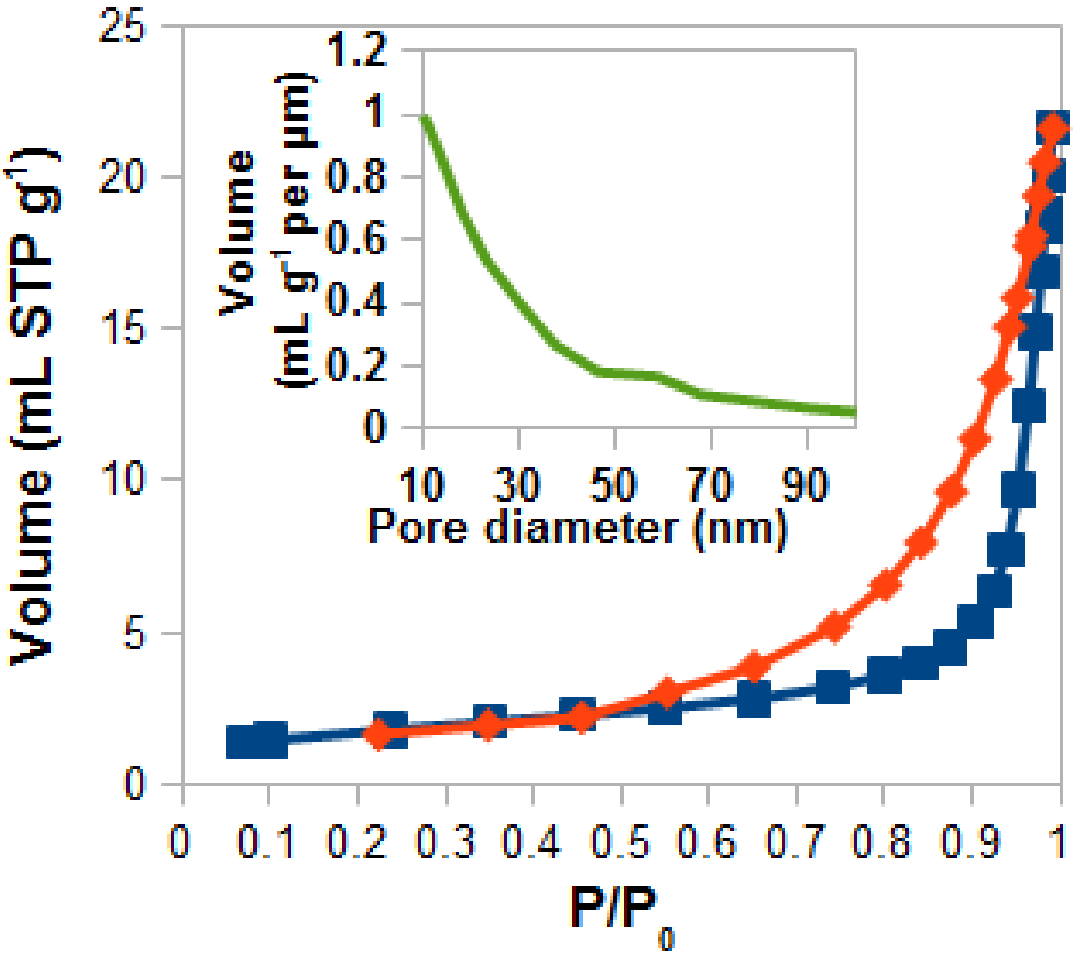

Figure C.1: N_2 isotherm and pore size distribution (inset) for $LaTiNO_2$ -

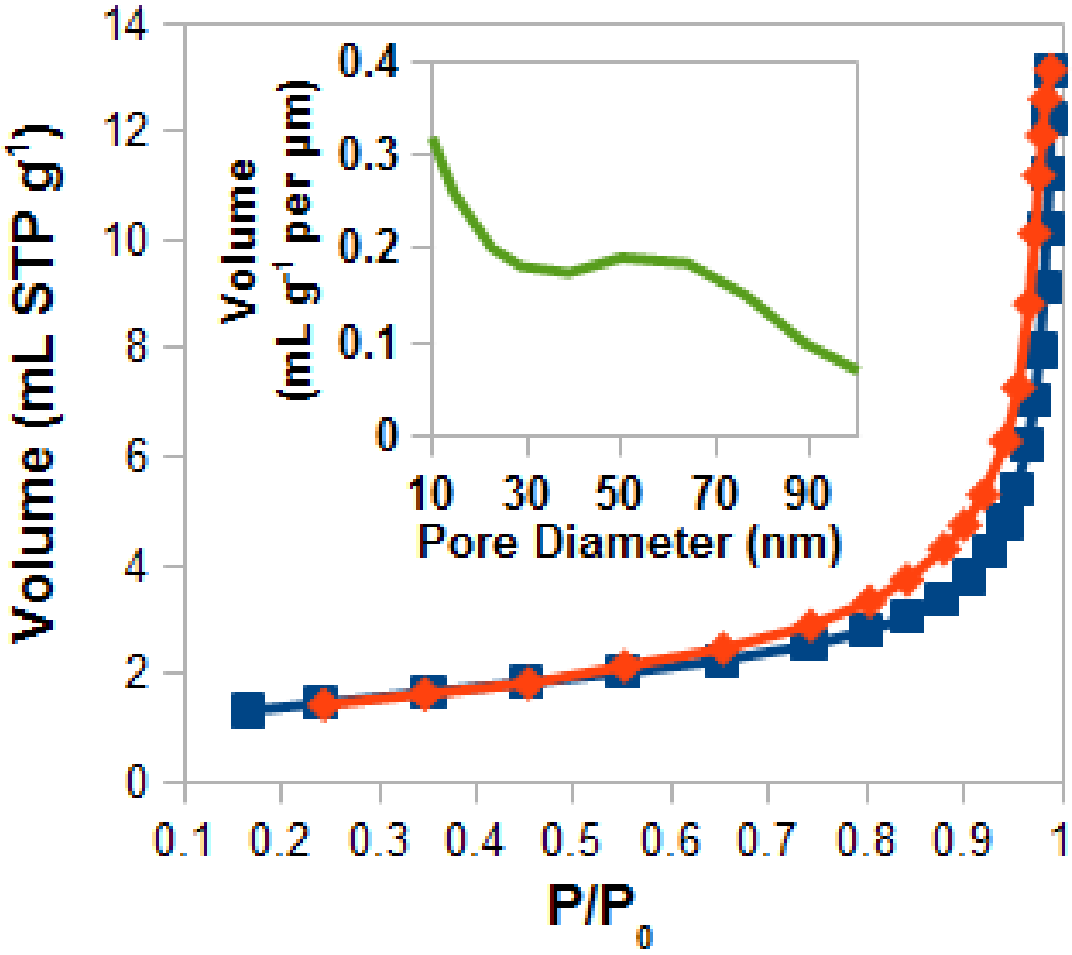

Figure C.2: N_2 **isotherm and pore size distribution (inset) for** $CeTiNO_2$ -

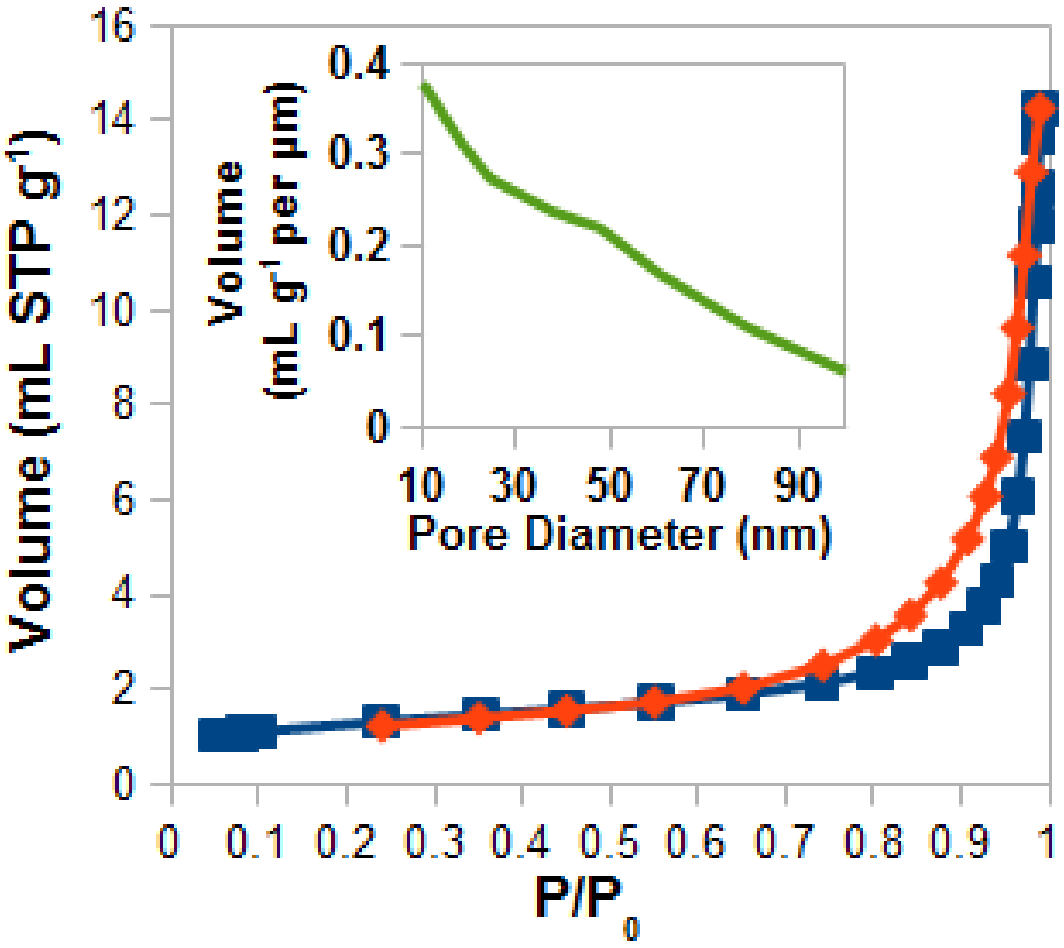

Figure C.3: N_2 isotherm and pore size distribution (inset) for $NdTiNO_2$ -

Time resolved IR transient adsorption

The mid-IR absorption in $R\mathrm{TiNO}_2$ (Figures C.7 – C.10) is attributed to free electrons in the conduction band or intra-band gap trap states.

Photocatalysis

Continuous photocatalytic activity measurement for the $R\mathrm{TiNO}_2$ compounds over three cycles (Figure C.11) demonstrates the samples are catalytic. XRD patterns of the samples before and after the reaction remain the same. Rates reported for each $R\mathrm{TiNO}_2$ compound are an average of the rates determined for each of the three continuous cycles. Before the start of each illumination session, the samples were held in the dark for 2 hours to test for any reactions (gas formation); no gas was observed for all cases. After samples illuminated for 8 hours the sample system was vented. Prior to the next cycle, solutions were bubbled with Ar gas, and the vessel was purged until GC spectrum yields an ambient background.

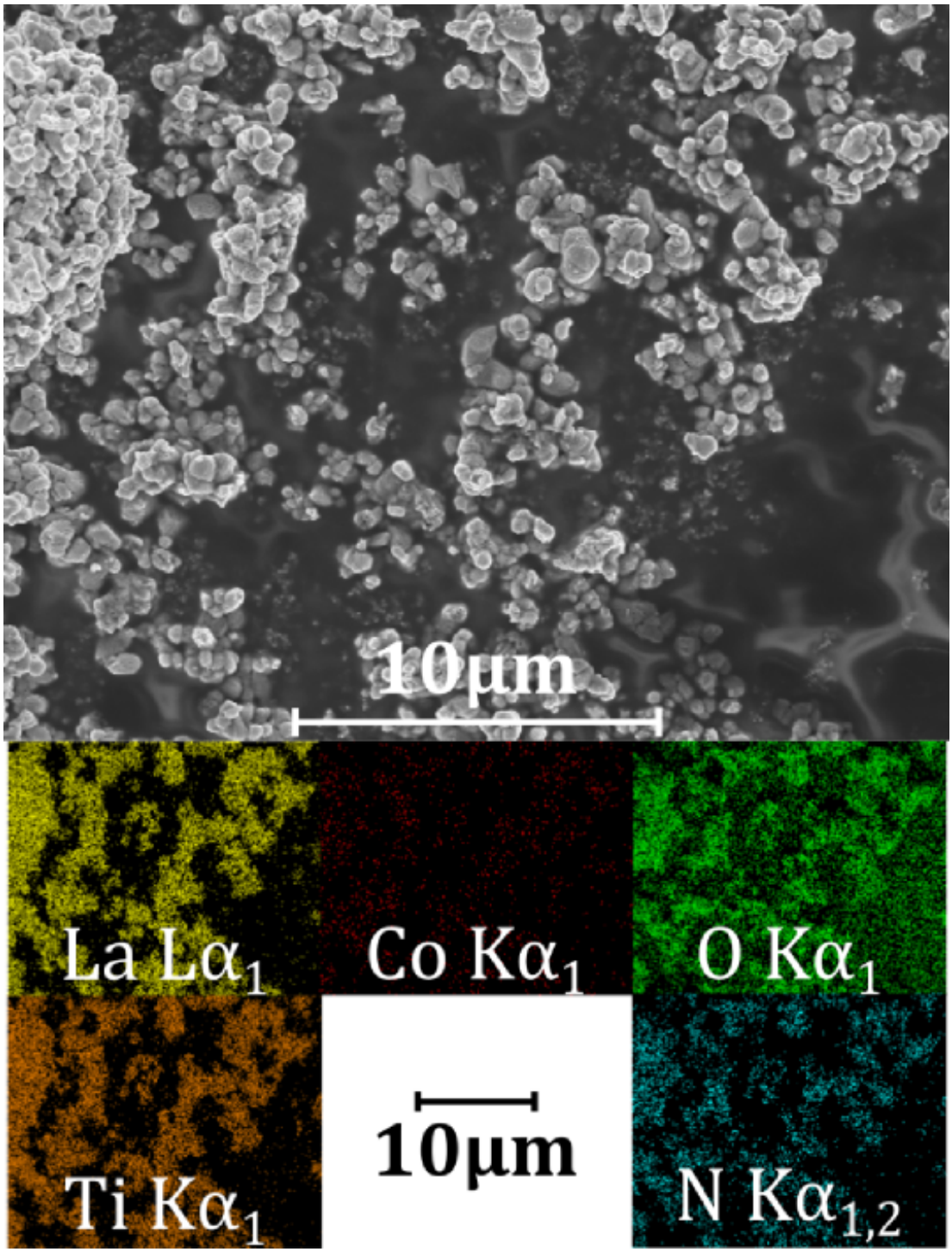

Figure C.4: SEM image and EDX mapping for $LaTiNO_2$ -

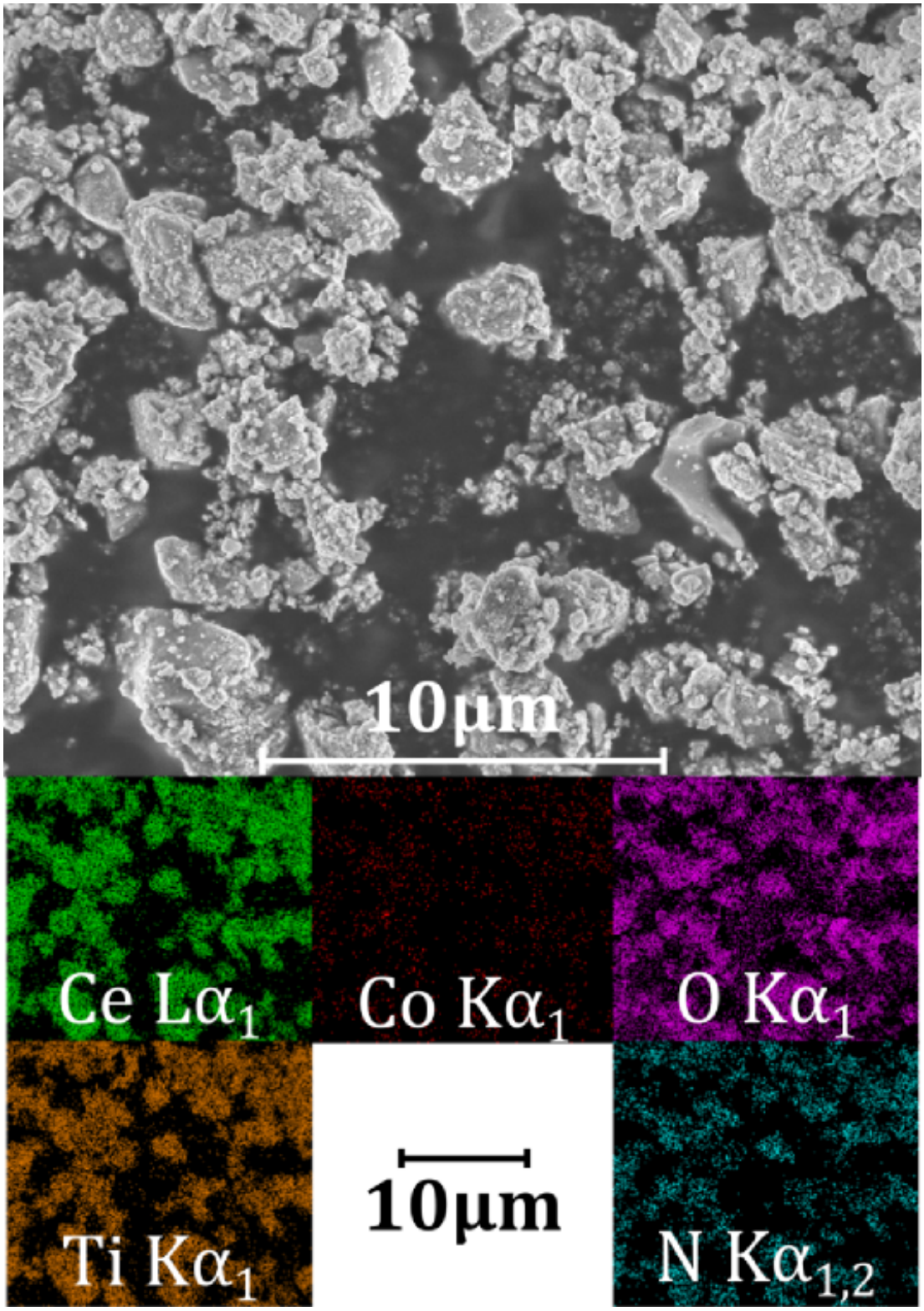

Figure C.5: SEM image and EDX mapping for $CeTiNO_2$ -

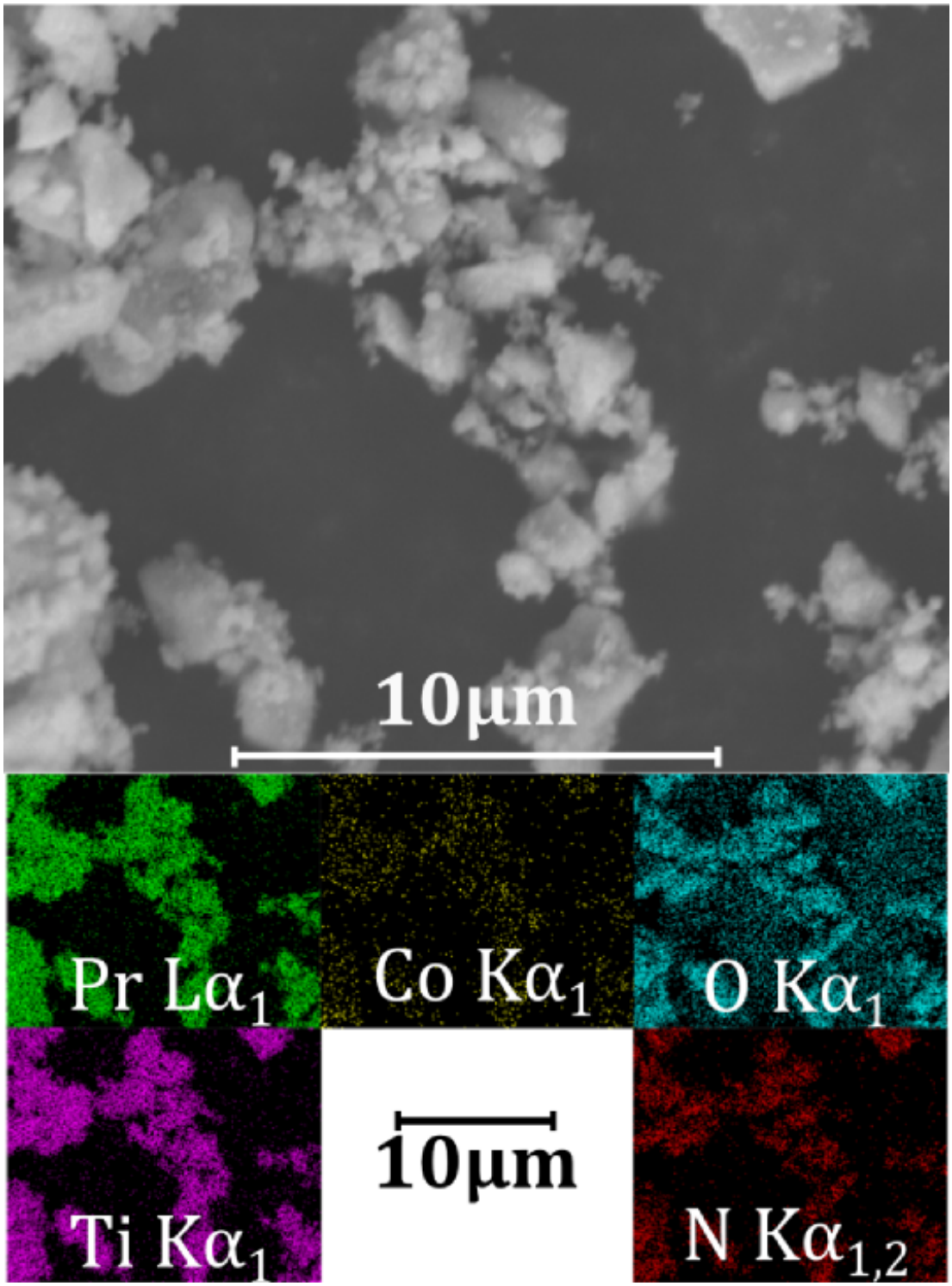

Figure C.6: SEM image and EDX mapping for $PrTiNO_2$ -

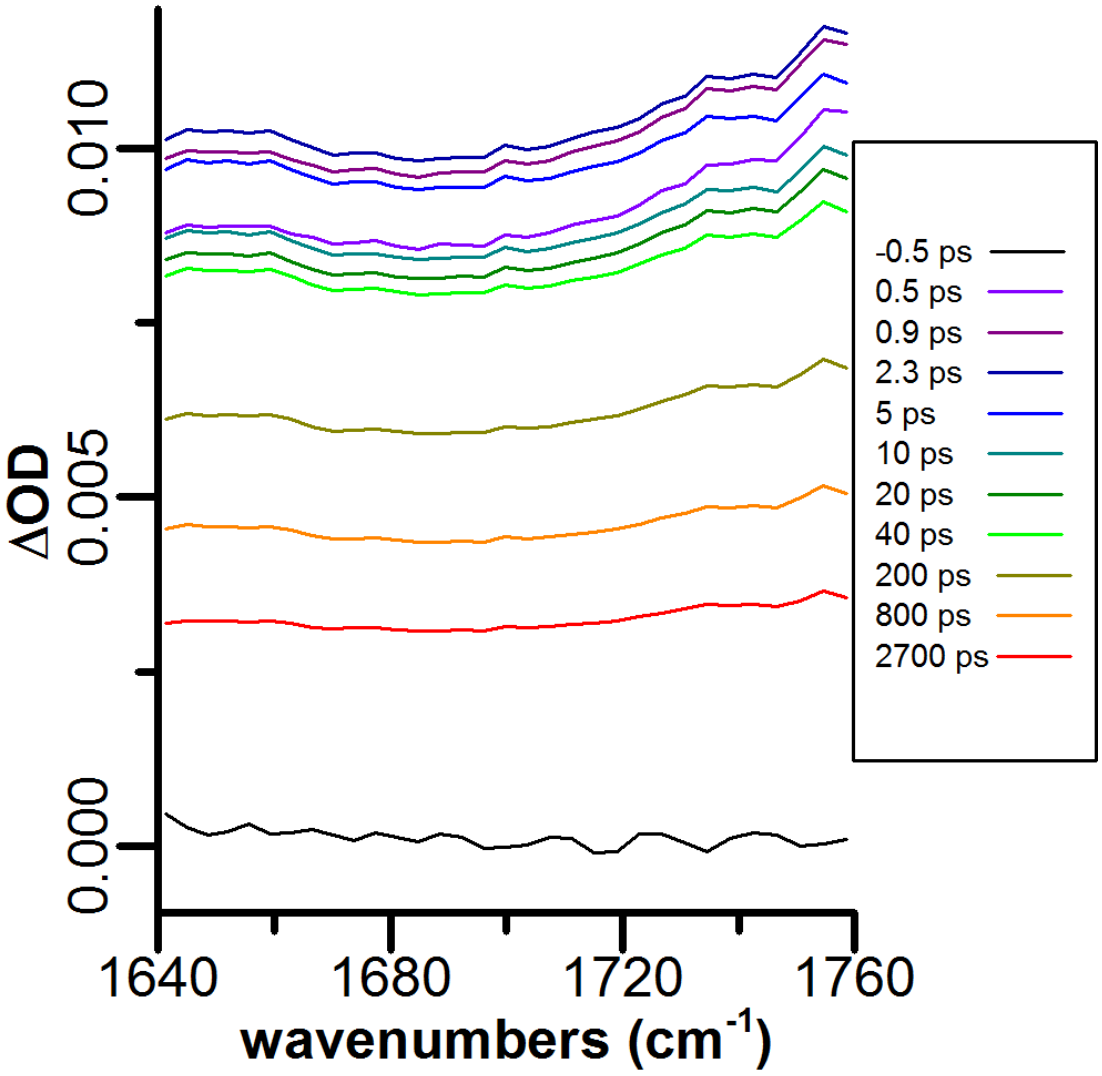

Figure C.7: Femtosecond TRIR spectra of $LaTiNO_2$ collected at room temperature, λ_{ex} = 600 nm -

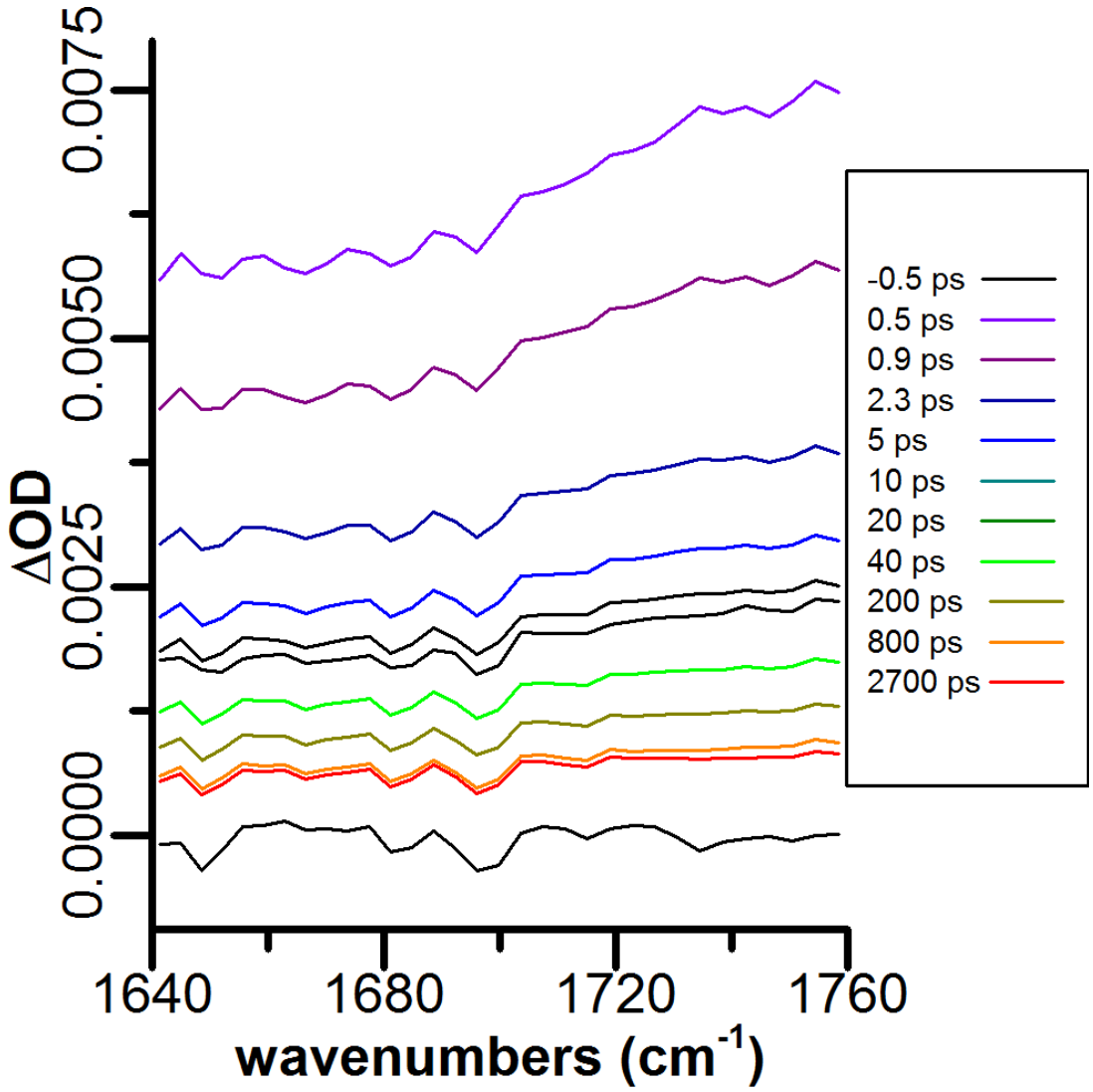

Figure C.8: Femtosecond TRIR spectra of $CeTiNO_2$ collected at room temperature, λ_{ex} = 600 nm -

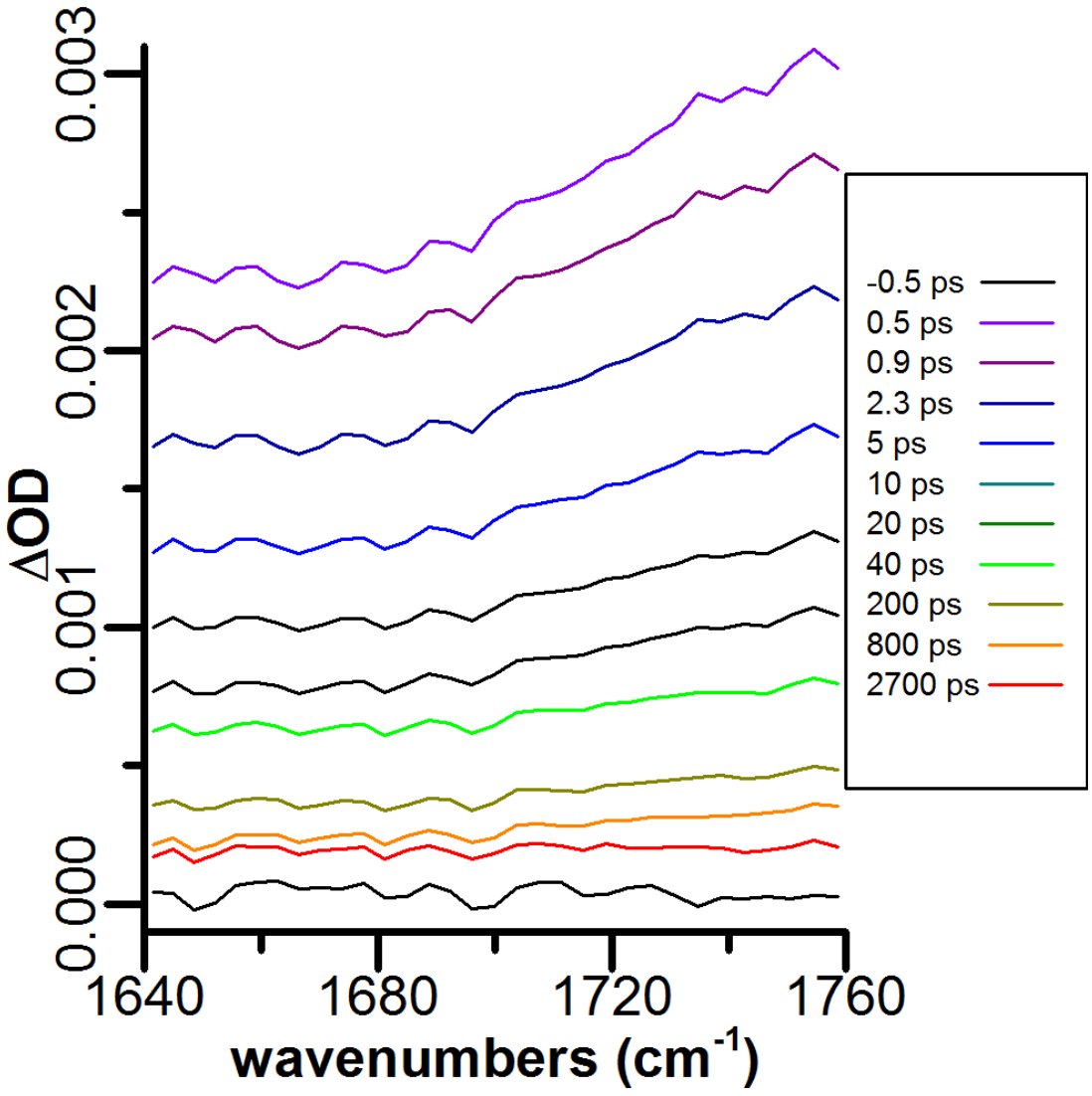

Figure C.9: Femtosecond TRIR spectra of $PrTiNO_2$ collected at room temperature, λ_{ex} = 600 nm -

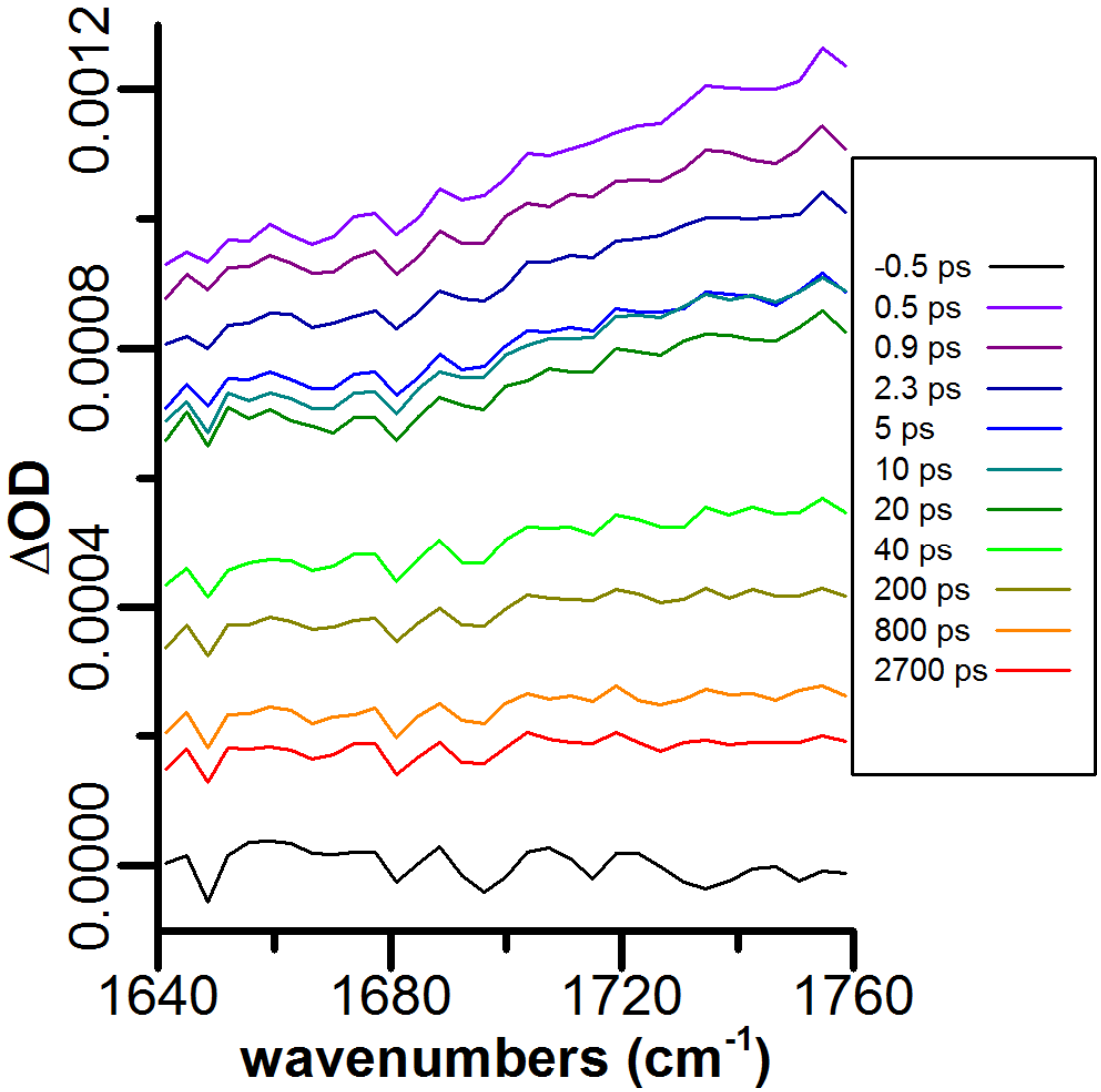

Figure C.10: Femtosecond TRIR spectra of $NdTiNO_2$ collected at room temperature, λ_{ex} = 600 nm -

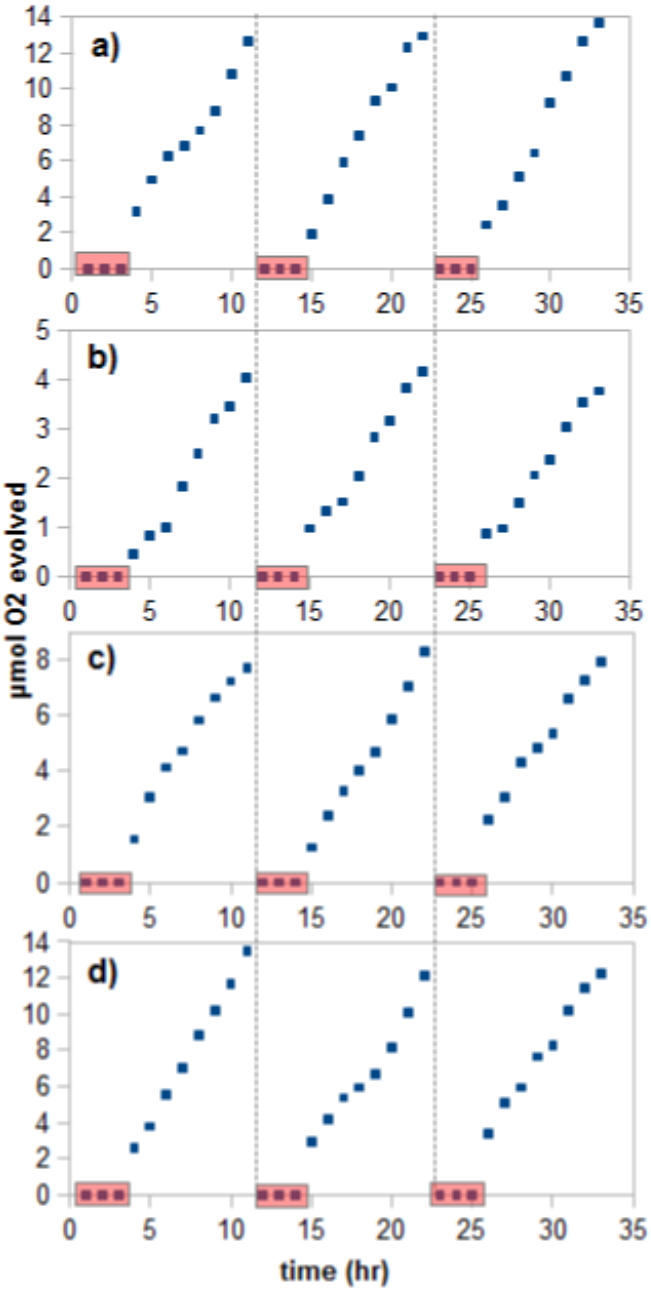

Figure C.11: Cycled photocatalysis of RTiNO$_2$ (R = a) La, b) Ce, c) Pr, d) Nd) - 150 W Xe arc lamp illuminating 100 mg CoO$_x$:RTiNO$_2$ and La$_2$O$_3$ suspended in 100 mL of 0.05M AgNO$_3$. Dashed vertical lines indicate a purge. Data points contained within the red boxes are taken in the dark.

APPENDIX D: SUPPORTING INFORMATION FOR THE STRUCTURAL, MAGNETIC, AND OPTICAL PROPERTIES OF $A_3V_4(PO_4)_6$ (A = Mg, Mn, Fe, Co, and Ni)

Rietveld Refinement of XRD data

Final XRD Rietveld refinements for $A_3V_4(PO_4)_6$, where A is Mg (Figure D.1), Mn (Figure D.2), Fe (Figure D.3), Co (Figure D.4), and Ni (Figure D.5), leads to a $P\bar{1}$ space group assignment. To maximize the degrees of freedom, rigid body PO_4 tetrahedra were used. Thermal parameters were not refined and were instead set to reasonable values. Rietveld refinement on XRD data for $A_3V_4(PO_4)_6$ where A is Mg, Mn, Fe, Co, and Ni resulted in respective 1.07 (R_{wp} = 14.5), 1.14 (11.5), 1.25 (3.5), 1.05 (6.5), 1.09 (14.7) goodness of fit values. Incident X-rays generate background fluorescence, resulting in elevated noise and making adequate fits challenging.

Combined sXRD and NPD refinements

Combined Rietveld refinements of synchrotron and neutron powder diffraction data have been carried out for $A_3V_4(PO_4)_6$ where A is Mn (Figure D.6), Fe (Figure D.7), Co (Figure D.8), and Ni (Figure D.9). Unidentified peaks were investigated and indexed during Rietveld refinement of synchrotron data (Table D.1). In $Mg_3V_4(PO_4)_6$, they are attributed to V_2O_3, however, in the remaining $A_3V_4(PO_4)_6$ compounds, the peaks

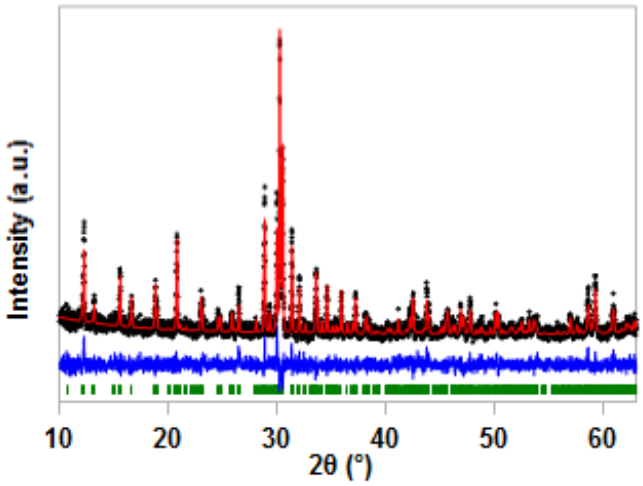

Figure D.1: Rietveld refinement of laboratory XRD data for $Mg_3V_4(PO_4)_6$ - Observed (black dots), calculated (red), difference (blue), and indexed peaks (green vertical bars) are compared.

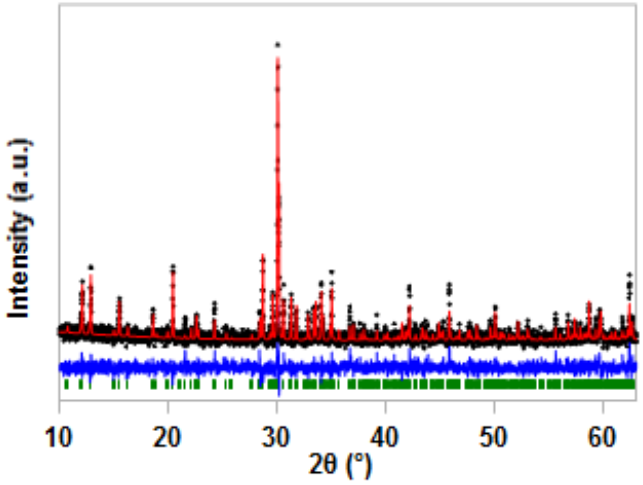

Figure D.2: Rietveld refinement of laboratory XRD data for $Mn_3V_4(PO_4)_6$ - Observed (black dots), calculated (red), difference (blue), and indexed peaks (green vertical bars) are compared.

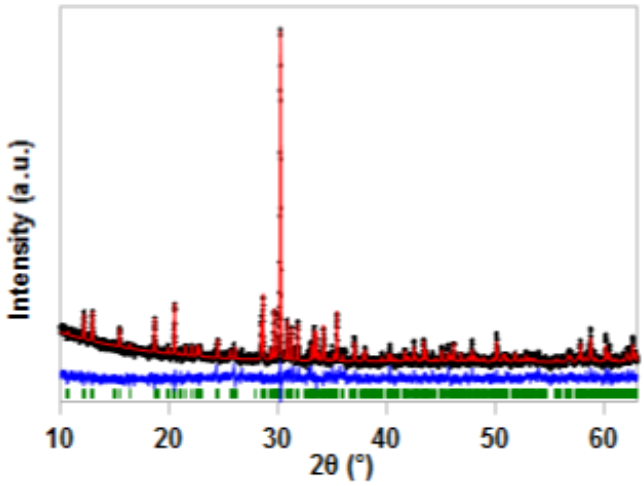

Figure D.3: Rietveld refinement of laboratory XRD data for $Fe_3V_4(PO_4)_6$ - Observed (black dots), calculated (red), difference (blue), and indexed peaks (green vertical bars) are compared.

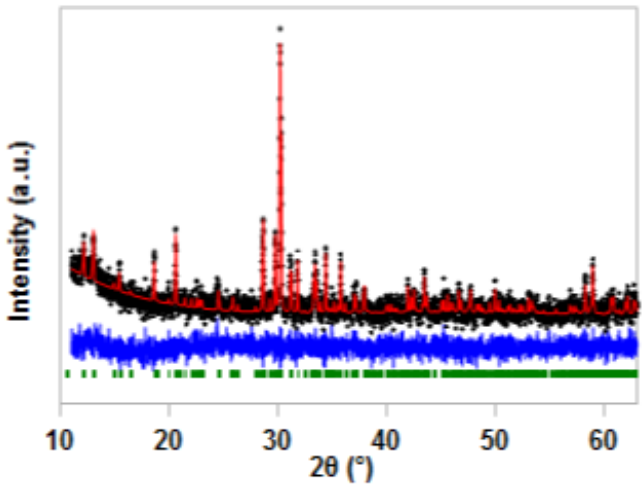

Figure D.4: Rietveld refinement of laboratory XRD data for $Co_3V_4(PO_4)_6$ - Observed (black dots), calculated (red), difference (blue), and indexed peaks (green vertical bars) are compared.

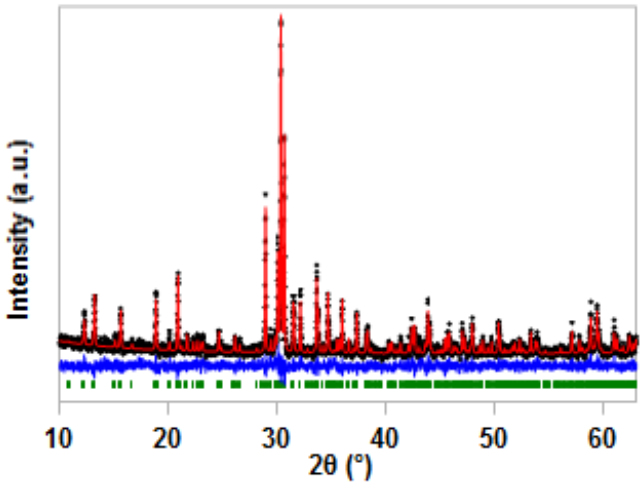

Figure D.5: Rietveld refinement of laboratory XRD data for $Ni_3V_4(PO_4)_6$ - Observed (black dots), calculated (red), difference (blue), and indexed peaks (green vertical bars) are compared.

did not produce matches to any known compounds in the ICSD. The NPD fit for $Ni_3V_4(PO_4)_6$ has unaccounted peaks at 2θ = 64°, 120.5°, and 145° 2θ, but these are presumed to be from secondary phase contributions as well. Atomic positions resulting from those refinements for $A_3V_4(PO_4)_6$, where A is Mn (Table D.2), Fe (Table D.3), Co (Table D.4), and Ni (Table D.5) are reported.

Magnetization measurements

χ(T) (left vertical axis) and $\chi^{-}1$(T) (right vertical axis) for $A_3V_4(PO_4)_6$, where A is Mg (Figure D.10), Mn (Figure D.11), Fe (Figure D.12), and Ni (Figure D.13) convey adherence to Curie-Weiss behavior, indicating the ordering temperature and magnetic character. Coercivity of this series of compounds was also probed for $A_3V_4(PO_4)_6$, where A is Mn (Figure D.14), Fe (Figure D.15), and Ni (Figure D.16).

Individual bond parameters of $A_3V_4(PO_4)_6$

Rietveld refined data allowed the extraction of bond parameters (Table D.6) and bond angles (Table D.7) for the series.

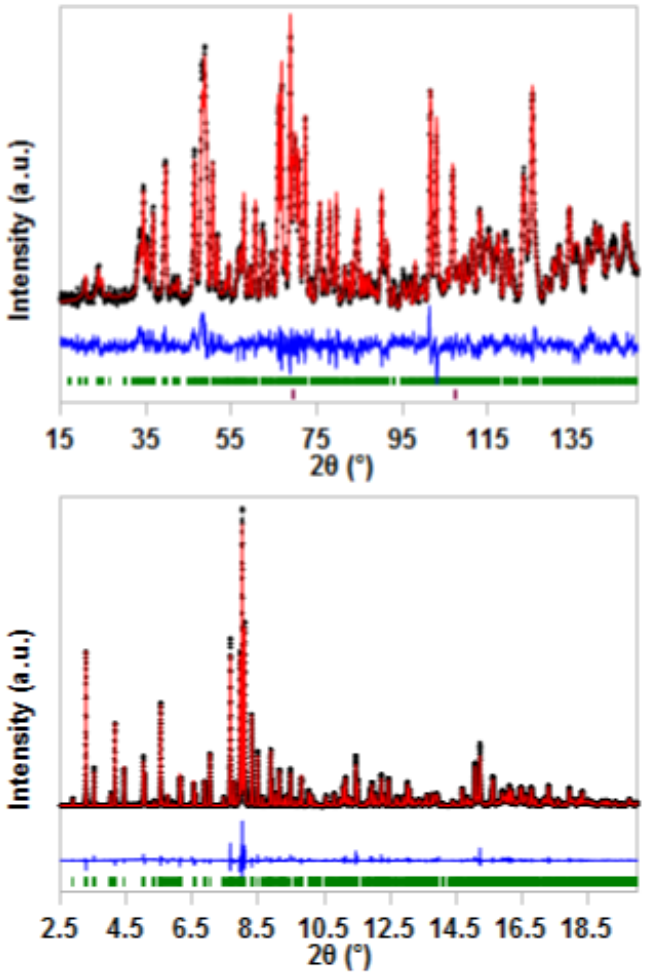

Figure D.6: Combined room temperature NPD (top) and SXRD (bottom) Rietveld refinements of $Mg_3V_4(PO_4)_6$ - Observed (black dots), calculated (red), difference (blue), indexed peaks (green vertical bars), and vanadium can (purple vertical bars) are compared.

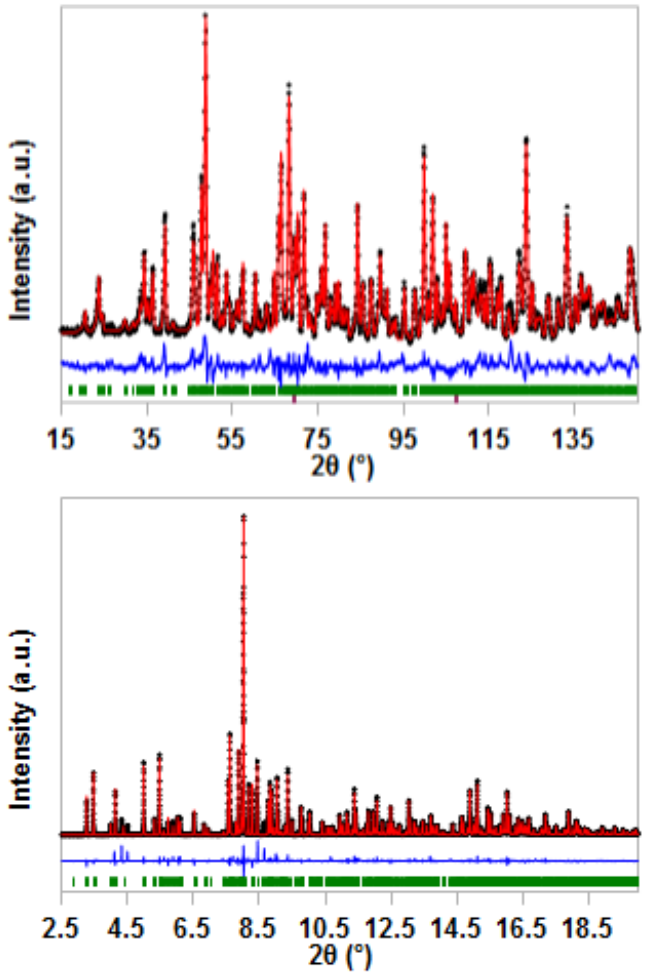

Figure D.7: Combined room temperature NPD (top) and SXRD (bottom) Rietveld refinements of $Fe_3V_4(PO_4)_6$ - Observed (black dots), calculated (red), difference (blue), indexed peaks (green vertical bars), and vanadium can (purple vertical bars) are compared.

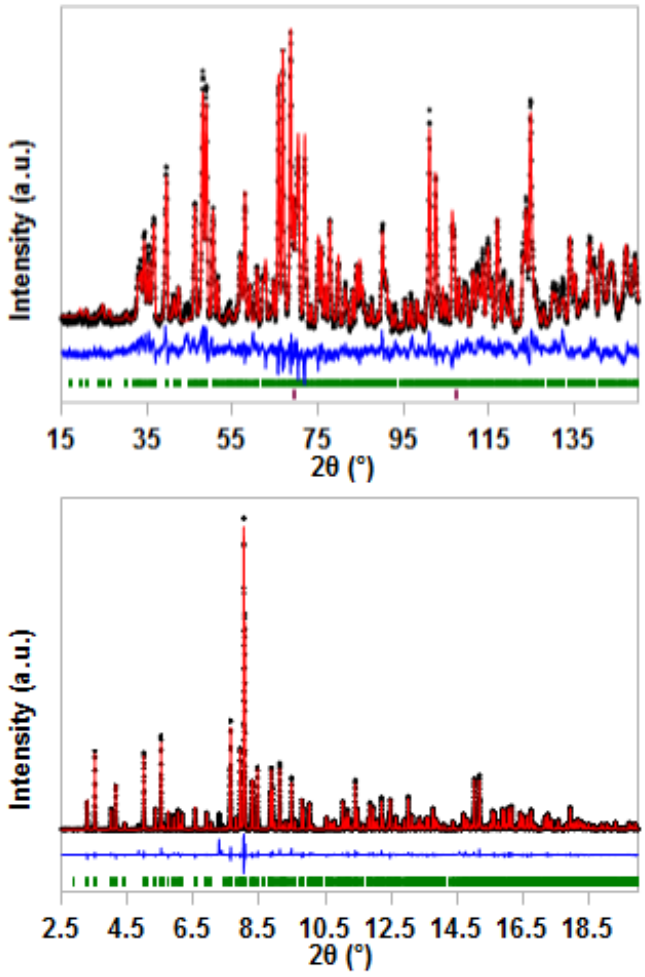

Figure D.8: Combined room temperature NPD (top) and SXRD (bottom) Rietveld refinements of $Co_3V_4(PO_4)_6$ - Observed (black dots), calculated (red), difference (blue), indexed peaks (green vertical bars), and vanadium can (purple vertical bars) are compared.

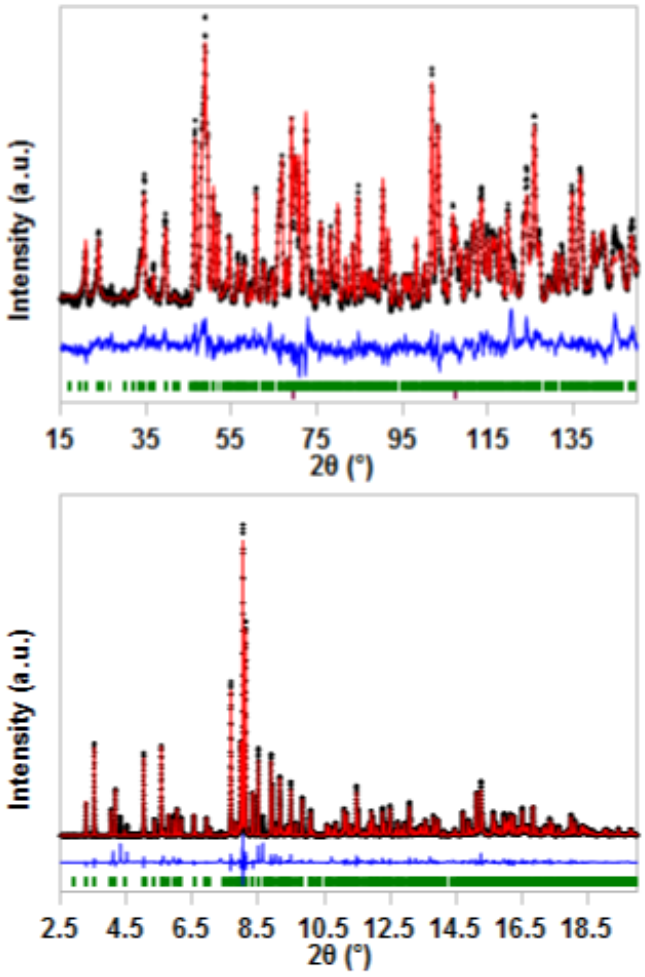

Figure D.9: Combined room temperature NPD (top) and SXRD (bottom) Rietveld refinements of $Ni_3V_4(PO_4)_6$ - Observed (black dots), calculated (red), difference (blue), indexed peaks (green vertical bars), and vanadium can (purple vertical bars) are compared.

$Mg_3V_4(PO_4)_6$	$Mn_3V_4(PO_4)_6$	$Fe_3V_4(PO_4)_6$	$Co_3V_4(PO_4)_6$	$Ni_3V_4(PO_4)_6$
D-spacing (Å)				
3.66	3.83	6.635	4.9	5.79
2.715*	3.31*	6.18	3.26*	5.49*
2.475	3.065	5.78	3.22	5.25
		5.485*	3.08	4.22
		5.27	2.45	2.75
		4.225	1.61	2.21
		3.92		
		3.665		
		3.57		
		3.525		
		3.4		
		3.21		
		3.08		
		3.025		
		2.84		
		2.745		
		2.635		

Table D.1: Secondary phase peaks indexed in SXRD patterns. The most intense peak (*) is noted.

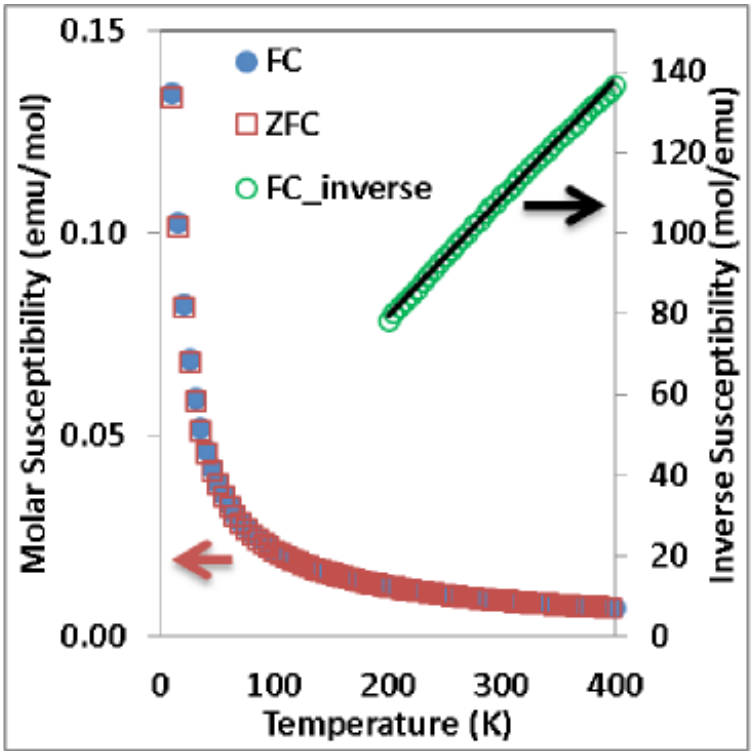

Figure D.10: χ(T) (left y-axis) and $\chi^{-}1$(T) (right y-axis) for $Mg_3V_4(PO_4)_6$ -

Atomic position(s)						
ion	site	x	y	z	occ	U_{iso} (Å^2)
Mg1/V1	1a	0	0	0	0.74/0.26	0.0027(6)
Mg2	2i	0.2835(4)	0.8138(3)	0.2896(3)	1	0.0027(6)
V2/Mg3	2i	0.3885(2)	0.4627(2)	0.1157(2)	0.87/0.13	0.0027(6)
V3	2i	0.9526(2)	0.2848(2)	0.4784(1)	1	0.0027(6)
P1	2i	0.2243(3)	0.1422(3)	0.7694(2)	1	0.0055(4)
P2	2i	0.0877(3)	0.5892(2)	0.8344(2)	1	0.0015(6)
P3	2i	0.6085(3)	0.7695(3)	0.6330(2)	1	0.0043(4)
O1	2i	0.2250(5)	0.1983(4)	0.9447(4)	1	0.010(4)
O2	2i	0.0135(6)	0.1859(4)	0.6590(4)	1	0.010(4)
O3	2i	0.4567(6)	0.2596(4)	0.7707(4)	1	0.010(4)
O4	2i	0.2096(6)	0.9400(4)	0.7063(4)	1	0.010(4)
O5	2i	0.1049(6)	0.7879(4)	0.9186(4)	1	0.0092(6)
O6	2i	0.0573(5)	0.5432(4)	0.6497(4)	1	0.0092(6)
O7	2i	0.8733(6)	0.4575(4)	0.8368(4)	1	0.0092(6)
O8	2i	0.3090(6)	0.5399(4)	0.9184(4)	1	0.0092(6)
O9	2i	0.546(6)	0.6309(4)	0.7152(4)	1	0.0083(6)
O10	2i	0.7340(5)	0.9630(4)	0.7692(4)	1	0.0083(6)
O11	2i	0.3733(5)	0.7733(4)	0.5091(4)	1	0.0083(6)
O12	2i	0.7605(6)	0.7226(4)	0.5376(4)	1	0.0083(6)

Table D.2: Room temperature combined SXRD and NPD derived atomic parameters for $Mg_3V_4(PO_4)_6$.

Atomic position(s)						
ion	site	x	y	z	occ	U_{iso} (Å^2)
Fe1/V1	1a	0	0	0	0.94/0.06	0.0033(4)
Fe2	2i	0.2823(2)	0.8156(2)	0.2917(2)	1	0.0033(4)
V2/Fe3	2i	0.3875(3)	0.4612(2)	0.1142(2)	0.97/0.03	0.0033(4)
V3	2i	0.9554(3)	0.2861(2)	0.4751(2)	1	0.0033(4)
P1	2i	0.6012(5)	0.7642(4)	0.6326(3)	1	0.0044(9)
P2	2i	0.0950(5)	0.5925(4)	0.8362(3)	1	0.0065(9)
P3	2i	0.2263(5)	0.1446(4)	0.7642(3)	1	0.0050(9)
O1	2i	0.3609(9)	0.7539(6)	0.5071(6)	1	0.0079(9)
O2	2i	0.5526(9)	0.6362(7)	0.7224(6)	1	0.0079(9)
O3	2i	0.7548(9)	0.7131(7)	0.5401(6)	1	0.0079(9)
O4	2i	0.7249(8)	0.9633(7)	0.7613(6)	1	0.0079(9)
O5	2i	0.1238(8)	0.7935(7)	0.9206(6)	1	0.011(1)
O6	2i	0.8746(9)	0.4669(7)	0.8381(6)	1	0.011(1)
O7	2i	0.3110(9)	0.5414(7)	0.9192(6)	1	0.011(1)
O8	2i	0.0626(9)	0.5429(7)	0.6522(6)	1	0.011(1)
O9	2i	0.2093(8)	0.9443(7)	0.7036(6)	1	0.0045(9)
O10	2i	0.455(9)	0.2705(7)	0.7703(6)	1	0.0045(9)
O11	2i	0.2226(8)	0.2054(7)	0.9404(6)	1	0.0045(9)
O12	2i	0.0155(8)	0.1803(6)	0.6534(6)	1	0.0045(9)

Table D.3: Room temperature combined SXRD and NPD derived atomic parameters for $Fe_3V_4(PO_4)_6$.

Atomic position(s)						
ion	site	x	y	z	occ	U_{iso} (Å^2)
Co1/V1	1a	0	0	0	0.76/0.24	0.0009(4)
Co2	2i	0.2916(2)	0.8146(2)	0.2923(1)	1	0.0009(4)
V2/Co3	2i	0.3887(3)	0.4626(2)	0.1148(2)	0.94/0.06	0.0009(4)
V3/Co4	2i	0.9544(3)	0.2847(2)	0.4789(2)	0.94/0.06	0.0009(4)
P1	2i	0.2209(4)	0.1411(3)	0.7678(3)	1	0.0059(8)
P2	2i	0.0906(4)	0.5891(3)	0.8319(3)	1	0.0080(8)
P3	2i	0.6112(4)	0.7695(3)	0.6352(3)	1	0.0099(8)
O1	2i	0.2274(7)	0.2015(6)	0.9478(5)	1	0.0107(9)
O2	2i	0.0123(8)	0.1814(6)	0.6582(5)	1	0.0107(9)
O3	2i	0.4567(8)	0.2658(6)	0.7740(5)	1	0.0107(9)
O4	2i	0.2121(7)	0.9421(6)	0.7091(5)	1	0.0107(9)
O5	2i	0.8713(8)	0.4561(6)	0.8348(5)	1	0.0127(8)
O6	2i	0.0649(7)	0.5436(6)	0.6520(5)	1	0.0127(8)
O7	2i	0.3141(8)	0.5416(6)	0.9240(5)	1	0.0127(8)
O8	2i	0.1077(7)	0.7866(6)	0.9196(5)	1	0.0127(8)
O9	2i	0.5505(7)	0.6299(6)	0.7154(5)	1	0.0060(8)
O10	2i	0.7343(7)	0.9647(6)	0.7656(5)	1	0.0060(8)
O11	2i	0.372(8)	0.7678(5)	0.5082(5)	1	0.0060(8)
O12	2i	0.7562(8)	0.7202(6)	0.5366(5)	1	0.0060(8)

Table D.4: Room temperature combined SXRD and NPD derived atomic parameters for $Co_3V_4(PO_4)_6$.

Atomic position(s)						
ion	site	x	y	z	occ	U_{iso} (Å^2)
Ni1/V1	1a	0	0	0	0.52/0.48	0.0026(4)
Ni2	2i	0.2765(2)	0.8100(2)	0.2854(2)	1	0.0026(4)
V2/Ni3	2i	0.3930(5)	0.4632(4)	0.1183(3)	0.76/0.24	0.0026(4)
V3	2i	0.9556(3)	0.2831(3)	0.4786(3)	1	0.0026(4)
P1	2i	0.2269(5)	0.1395(4)	0.7715(4)	1	0.008(1)
P2	2i	0.0873(6)	0.5913(4)	0.8349(4)	1	0.005(1)
P3	2i	0.6018(6)	0.7694(4)	0.6322(4)	1	0.010(1)
O1	2i	0.2265(9)	0.1932(7)	0.9512(7)	1	0.007(1)
O2	2i	0.012(1)	0.1786(7)	0.6647(7)	1	0.007(1)
O3	2i	0.454(1)	0.2579(7)	0.7730(7)	1	0.007(1)
O4	2i	0.2173(9)	0.9393(8)	0.7072(7)	1	0.007(1)
O5	2i	0.122(1)	0.7895(8)	0.9197(7)	1	0.014(1)
O6	2i	0.054(1)	0.5447(8)	0.6516(7)	1	0.014(1)
O7	2i	0.869(1)	0.4558(8)	0.8362(7)	1	0.014(1)
O8	2i	0.305(1)	0.5362(7)	0.9203(7)	1	0.014(1)
O9	2i	0.539(1)	0.6278(7)	0.7067(7)	1	0.001(1)
O10	2i	0.7320(9)	0.9601(7)	0.7696(7)	1	0.001(1)
O11	2i	0.366(1)	0.7660(7)	0.5008(7)	1	0.001(1)
O12	2i	0.762(1)	0.7210(7)	0.5341(7)	1	0.001(1)

Table D.5: Room temperature combined SXRD and NPD derived atomic parameters for $Ni_3V_4(PO_4)_6$.

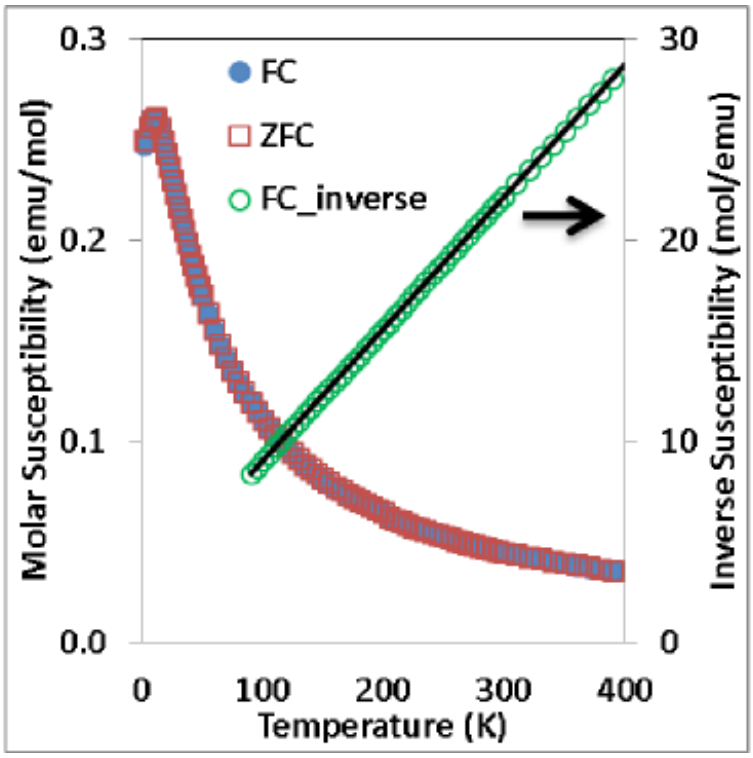

Figure D.11: χ(T) (left y-axis) and $\chi^{-}1$(T) (right y-axis) for $Mn_3V_4(PO_4)_6$ -

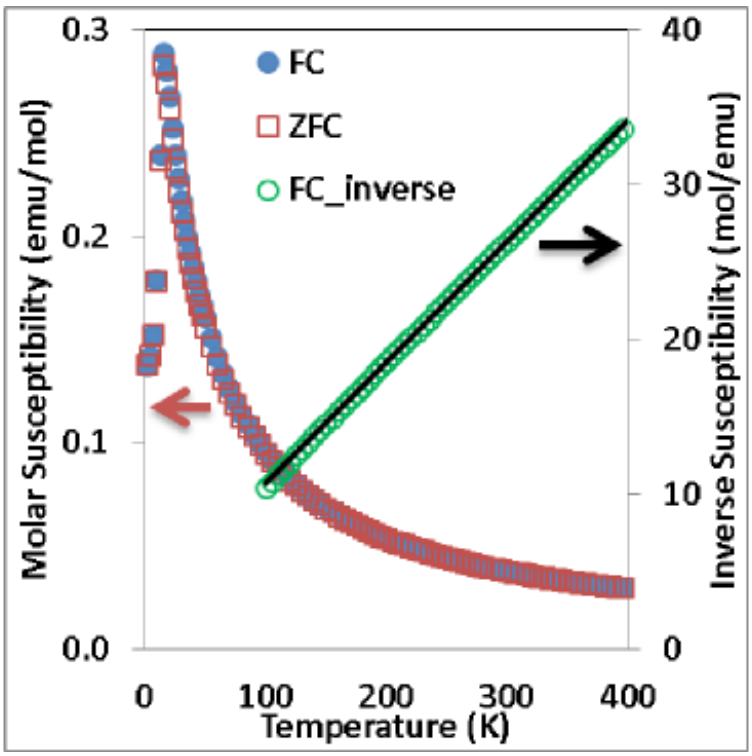

Figure D.12: χ(T) (left y-axis) and $\chi^{-}1$(T) (right y-axis) for $Fe_3V_4(PO_4)_6$ -

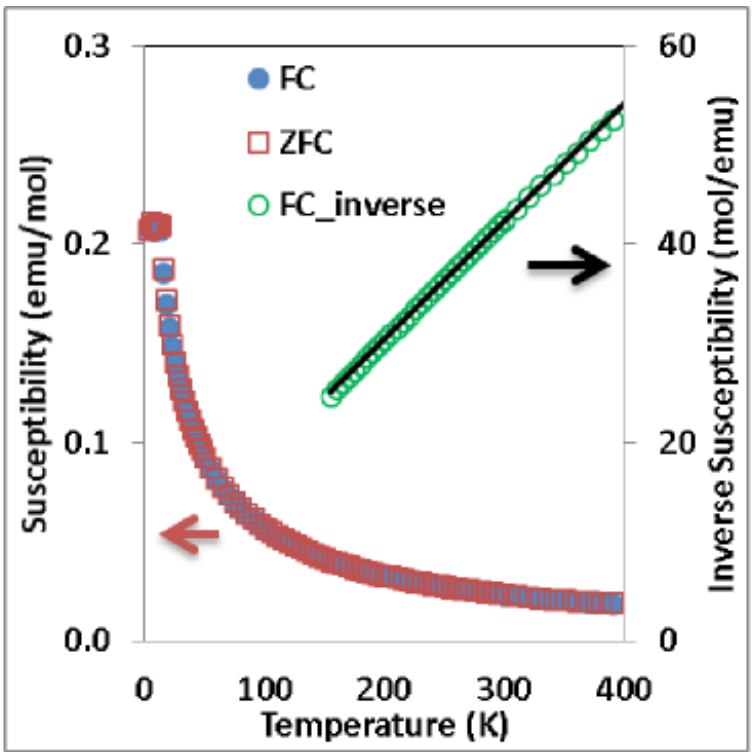

Figure D.13: χ(T) (left y-axis) and $\chi^{-}1$(T) (right y-axis) for $Ni_3V_4(PO_4)_6$ -

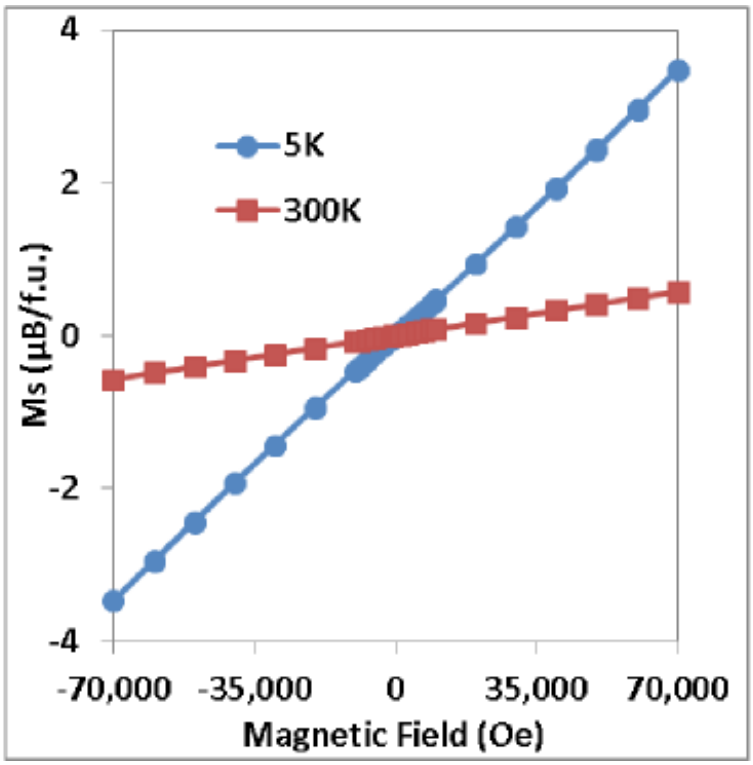

Figure D.14: Isothermal magnetization of $Mn_3V_4(PO_4)_6$ -

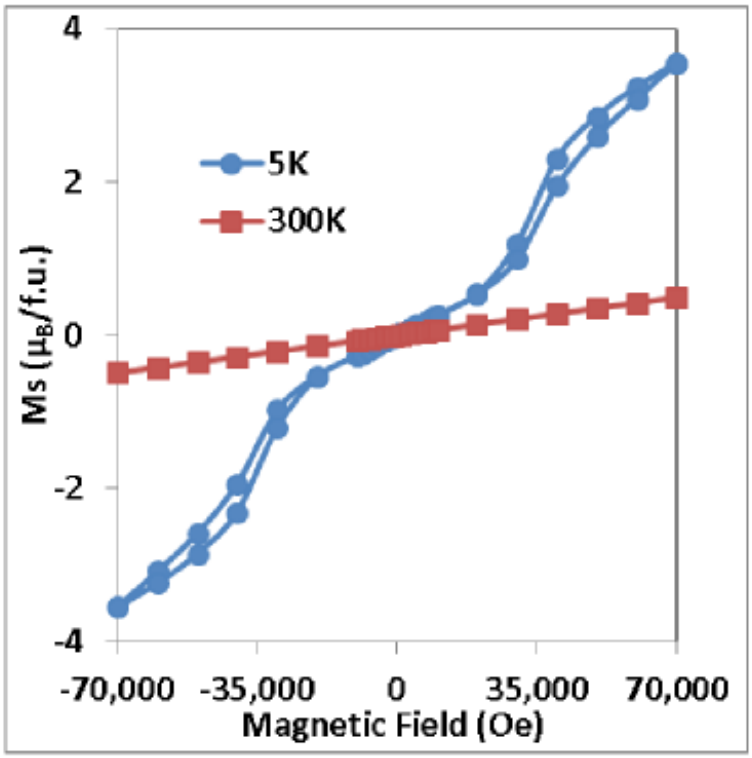

Figure D.15: Isothermal magnetization of $Fe_3V_4(PO_4)_6$ -

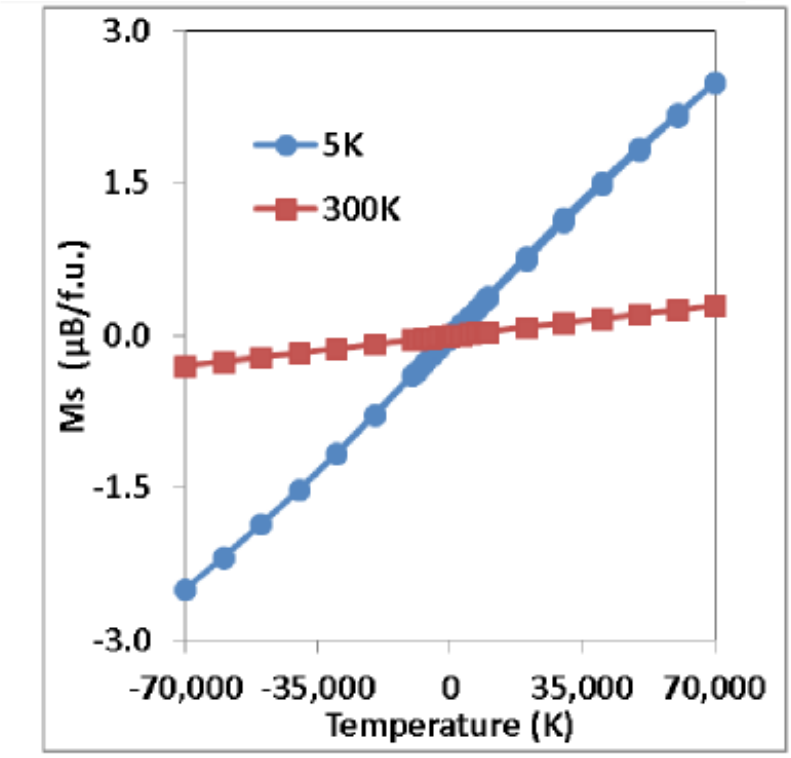

Figure D.16: Isothermal magnetization of $Ni_3V_4(PO_4)_6$ -

	$Mg_3V_4(PO_4)_6$	$Mn_3V_4(PO_4)_6$	$Fe_3V_4(PO_4)_6$	$Co_3V_4(PO_4)_6$	$Ni_3V_4(PO_4)_6$
Polyhedra	**M-X (Å)**				
***A*1-O**	2x 2.182(3)	2x 2.281(3)	2x 2.024(5)	2x 2.189(4)	2x 2.121(5)
	2x 1.977(3)	2x 2.226(3)	2x 2.253(5)	2x 2.197(4)	2x 2.027(5)
	2x 2.165(3)	2x 2.101(3)	2x 2.260(5)	2x 1.996(4)	2x 2.153(5)
***A*2-O**	2.081(4)	2.145(3)	2.136(5)	2.126(4)	2.027(6)
	1.991(4)	2.084(3)	2.112(5)	2.009(4)	2.014(5)
	2.064(4)	2.062(3)	2.089(5)	1.976(4)	2.033(6)
	2.035(4)	2.181(3)	2.120(5)	2.063(4)	2.063(5)
	2.013(4)	2.107(3)	1.964(5)	2.041(4)	1.961(6)
V1-O	2.077(3)	2.039(3)	1.869(5)	2.040(4)	2.092(6)
	1.872(3)	1.883(3)	1.981(5)	1.875(4)	1.900(6)
	2.040(3)	2.053(3)	2.034(5)	2.029(4)	2.041(6)
	2.016(3)	1.982(3)	2.007(5)	1.992(4)	2.010(6)
	2.025(3)	2.005(3)	2.045(5)	1.984(4)	2.006(6)
	2.040(3)	2.071(3)	2.044(5)	2.036(4)	2.046(6)
V2-O	1.992(3)	2.005(3)	2.042(5)	2.009(4)	2.060(6)
	2.070(3)	2.057(3)	1.922(5)	2.079(4)	2.073(5)
	2.055(3)	2.037(3)	1.895(5)	2.057(4)	2.080(6)
	2.025(3)	2.074(3)	2.035(5)	2.045(4)	2.037(6)
	1.878(3)	1.897(3)	2.062(5)	1.896(4)	1.828(6)
	1.926(3)	1.952(3)	2.041(5)	1.948(4)	1.919(6)
P1-O	1.569(3)	1.580(3)	1.579(5)	1.603(4)	1.605(6)
	1.562(4)	1.563(3)	1.535(5)	1.539(4)	1.544(6)
	1.572(3)	1.589(3)	1.540(5)	1.594(5)	1.547(6)
	1.522(3)	1.524(3)	1.559(5)	1.503(4)	1.515(6)
P2-O	1.523(3)	1.574(3)	1.521(5)	1.581(5)	1.489(6)
	1.596(3)	1.600(3)	1.561(5)	1.565(4)	1.571(6)
	1.550(3)	1.571(3)	1.545(5)	1.579(5)	1.577(6)
	1.548(3)	1.497(3)	1.590(5)	1.520(4)	1.558(6)
P3-O	1.549(3)	1.538(3)	1.508(5)	1.540(4)	1.513(6)
	1.560(3)	1.517(3)	1.569(5)	1.544(4)	1.547(6)
	1.576(3)	1.587(3)	1.594(5)	1.593(4)	1.581(6)
	1.536(3)	1.561(3)	1.549(5)	1.529(4)	1.598(5)

Table D.6: Combined SXRD and NPD derived bond parameters for $A_3V_4(PO_4)_6$ where A is Mg, Mn, Fe, Co, and Ni.

	Octahedral-Octahedral		Octahedral-Trigonal Bipyramidal	
	V-O-V (°)	V-O-TM (°)	V-O-TM (°)	TM-O-TM (°)
$Mn_3V_4(PO_4)_6$	96.78(13) 104.79(13)	116.01(13)	102.95(13) 101.07(13) 100.00(13) 102.70(13)	115.26(13)
$Fe_3V_4(PO_4)_6$	96.53(24) 103.27(22)	116.34(23)	100.19(22) 101.49(23) 101.43(22) 100.95(22)	117.22(23)
$Co_3V_4(PO_4)_6$	97.88(21) 103.65(20)	118.52(20)	100.57(19) 100.40(20) 101.25(20) 101.38(20)	119.02(20)
$Ni_3V_4(PO_4)_6$	96.82(27) 104.18(27)	120.22(26)	100.93(26) 98.81(26) 103.05(26) 99.97(25)	115.62(24)

Table D.7: Combined SXRD and NPD derived bond angles for $A_3V_4(PO_4)_6$ where A is Mg, Mn, Fe, Co, and Ni.

Kubelka-Munk UV-visible diffuse reflectance

To help elucidate the contributions of individual d-d transitions, the Kubelka-Munk UV-visible diffuse reflectance was collected for the starting materials (Figure D17). The charge transfer between the non-bonding 2p oxygen atoms and the phosphorous 3p is the most prominent feature for all compounds at energies greater than 3.7 eV. At lower energies the d-d transitions, if present, are observed and closely resemble the adsorption spectra of the 2+ transition metals in aqueous media (e.g. $V(H_2O)_6^{+3}$, $Mn(H_2O)_6^{+2}$, $Fe(H_2O)_6^{+2}$, *etc.*). d-d transitions associated with cobalt and nickel make up the two doublets that are observed at 2.25 and 2.6 eV as well as at 2.65 and 2.9 eV, respectively.

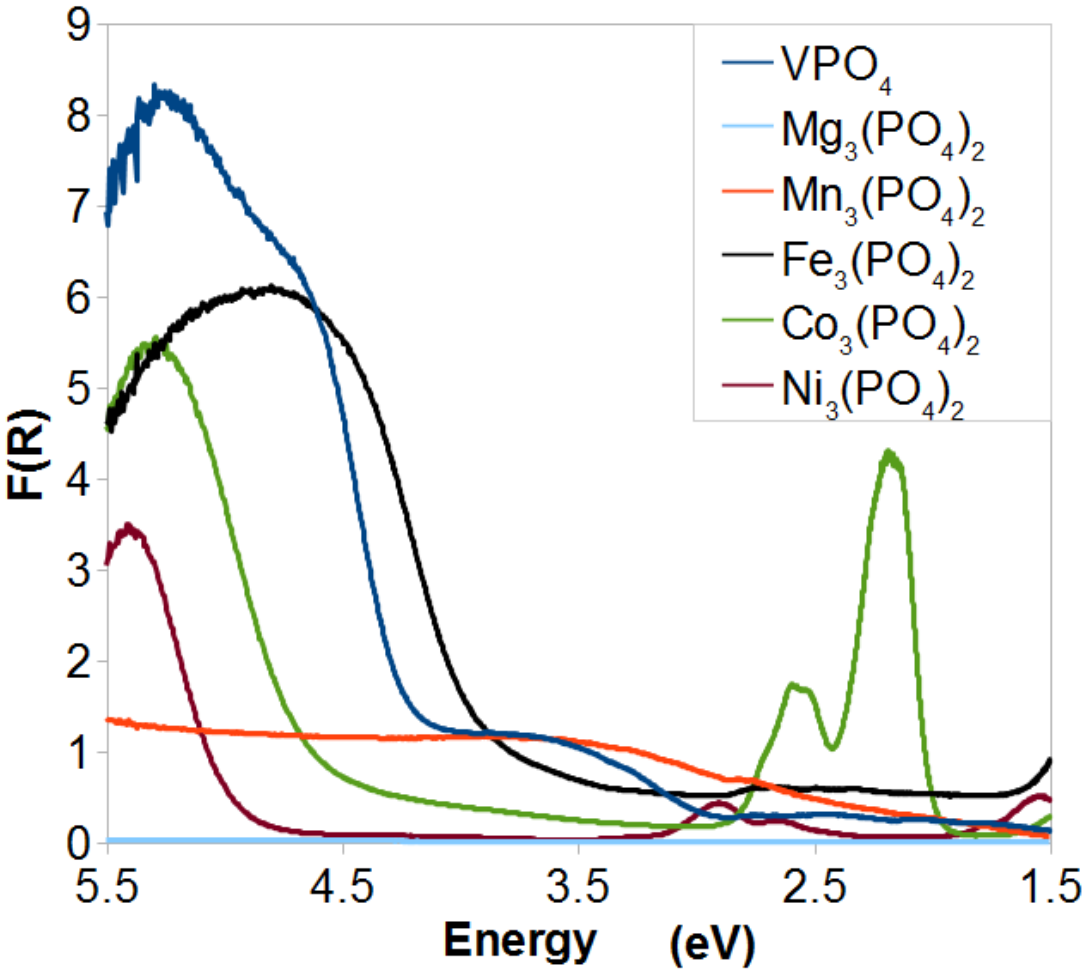

Figure D.17: Kubelka-Munk UV-visible diffuse reflectance of VPO_4 and $A_3(PO_4)_2$, where *A* is Mg, Mn, Fe, Co, and Ni - See chart key for sample identification.

References

[1] A.S. Bhalla, R. Guo, and R. Roy. **The perovskite structure–a review of its role in ceramic science and technology**. *Material Research Innovations*, **4**(1):3–26, 2000. 3

[2] R.H. Mitchell. *Perovskites: Modern and Ancient*. Almaz Press, 2002. 3

[3] S. Royer, D. Duprez, F. Can, X. Courtois, C. Batiot-Dupeyrat, S. Laassiri, and H. Alamdari. **Perovskites as substitutes of noble metals for heterogeneous catalysis: dream or reality**. *Chemical Reviews*, **114**(20):10292–10368, 2014. 3

[4] J.B Goodenough. **Electronic and ionic transport properties and other physical aspects of perovskites**. *Reports on Progress in Physics*, **67**(11):1915, 2004. 3

[5] V.M. Goldschmidt. **Die Gesetze der Krystallochemie**. *Naturwissenschaften*, **14**(21):477–485, 1926. 3

[6] M. W. Lufaso and P. M. Woodward. **Prediction of the crystal structures of perovskites using the software program SPuDS**. *Acta Crystallographica Section B: Structural Crystallography and Crystal Chemistry*, **57**(6):725–738, 2001. 3

[7] A. M. Glazer. **The classification of tilted octahedra in perovskites**. *Acta Crystallographica Section B*, **28**(11):3384–3392, 1972. 4

[8] P. M. Woodward. **Octahedral Tilting in Perovskites. I. Geometrical Considerations**. *Acta Crystallographica Section B*, **53**(1):32–43, 1997. 4

[9] C. J. Howard and H. T. Stokes. **Group-Theoretical Analysis of Octahedral Tilting in Perovskites**. *Acta Crystallographica Section B: Structural Science*, **54**(6):782–789, 1998. 4

[10] C. J. Howard, B. J. Kennedy, and P. M. Woodward. **Ordered double perovskites a group-theoretical analysis**. *Acta Crystallographica Section B Structural Science*, **59**(4):463–471, 2003. 4

[11] H. T. Stokes, E. H. Kisi, D. M. Hatch, and C. J. Howard. **Group-theoretical analysis of octahedral tilting in ferroelectric perovskites**. *Acta Crystallographica Section B Structural Science*, **58**(6):934–938, 2002. 4

[12] S Porter. *Perovskite and Pyrochlore Tantalum Oxide Nitrides: Synthesis and Characterization*. Ohio State University Dissertation, 2012. 4, 11

[13] P. W. Barnes, M. W. Lufaso, and P. M. Woodward. **Structure determination of A_2M^3+$\mathbf{TaO_6}$ and A_2M^3+$\mathbf{NbO_6}$ ordered perovskites: octahedral tilting and pseudosymmetry**. *Acta Crystallographica Section B*, **62**(3):384–396, 2006. 5, 30

[14] W H. Baur. **Bond length variation and distorted coordination polyhedra in inorganic crystals**. *Transactions of the American Crystallographic Association*, **6**:129, 1970. 7, 19, 76

[15] M.W. Lufaso and P.M. Woodward. **Jahn–Teller distortions, cation ordering and octahedral tilting in perovskites**. *Acta Crystallographica Section B: Structural Science*, **60**(1):10–20, 2004. 7

[16] L. Liu, R.-J. Xie, N. Hirosaki, T. Takeda, C.-n. Zhang, J. Li, and X. Sun. **Photoluminescence properties of β-SiAlON:$\mathbf{Yb^{2+}}$, a novel green-emitting phosphor for white light-emitting diodes**. *Science and Technology of Advanced Materials*, **12**(3):034404–+, 2011. 7

[17] P. Velasco, J.A. Alonso, M.J. Martinez-Lope, M.T. Casais, J.L. Martinez, and M.T. Fernandez-Diaz. **Synthesis and properties of $\mathbf{Tl_2Mn_{2-x}Ti_xO_7}$ pyrochlores with colossal magnetoresistance**. *Journal of Physics Condensed Matter*, **131**:10991–11000, 2001. 7

[18] T. Ishihara, H. Nishiguchi, K. Fukamachi, and Y. Takita. **Effects of acceptor doping to $\mathbf{KTaO_3}$ on photocatalytic decomposition of pure $\mathbf{H_2O}$**. *The Journal of Physical Chemistry B*, **103**(1):1–3, 1999. 7

[19] J. Fergus. **Perovskite oxides for semiconductor-based gas sensors**. *Sensors and Actuators B: Chemical*, **123**(2):1169 – 1179, 2007. 7

[20] P. Song, H. Qin, L. Zhang, K. An, Z. Lin, J. Hu, and M. Jian. **The structure, electrical and ethanol-sensing properties of $La_{1x}Pb_xFeO_3$ perovskite ceramics with x≤0.3**. *Sensors and Actuators B: Chemical*, **104**(2):312 – 316, 2005. 7

[21] D.A. Landinez Tellez and J. Albino Aguiar. **Effect of Cu-site Co, Ni, and Ga substitution on the superconductivity of tetragonal $LaCaBaCu_3O_{7y}$ system**. *Journal of Magnetism and Magnetic Materials*, **226-230, Part 1**(0):318 – 320, 2001. ¡ce:title¿Proceedings of the International Conference on Magnetism (ICM 2000)¡/ce:title¿. 7

[22] I. Bretos, T. Schneller, R. Waser, D. F. Hennings, S. Halder, and F. Thomas. **Compositional substitutions and aliovalent doping of $BaTiO_3$-based thin films on nickel foils prepared by chemical solution deposition**. *Journal of the American Ceramic Society*, **93**(2):506–515, 2010. 7

[23] J.H. Hwang and Y.H. Han. **Dielectric properties of $(Ba_{1-x}Ce_x)TiO_3$**. *Japanese Journal of Applied Physics*, **39**:2701–+, 2000. 7

[24] T. Takata and K. Domen. **Defect engineering of photocatalysts by doping of aliovalent metal cations for efficient water splitting**. *The Journal of Physical Chemistry C*, **113**(45):19386–19388, 2009. 7

[25] R. Marchand. **Nitrogen and oxygen-nitrogen compounds of silicon**. *Revue de Chimie Minerale*, **7**(1):87–119, 1970. 8

[26] R. Marchand. **Oxynitrides with potassium nickel(II) tetrafluoride structure. Ln_2AlO_3N compounds (Ln = lanthanum, neodymium, samarium)**. *Comptes Rendus des Seances de l'Academie des Sciences, Serie C: Sciences Chimiques*, **282**(7):329–3, 1976. 8

[27] R. Marchand, F. Pors, and Y. Laurent. **Preparation and characterization of new oxynitrides with a perovskite structure**. *Revue Internationale des Hautes Temperatures et des Refractaires*, **23**(1):11–15, 1986. 8

[28] S. G. Ebbinghaus, H.-P. Abicht, R. Dronskowski, T. Mller, A. Reller, and A. Weidenkaff. **Perovskite-related oxynitrides Recent developments in synthesis, characterisation and investigations of physical properties**. *Progress in Solid State Chemistry*, **37**(2-3):173–205, 2009. 8

[29] N. Kumar, A. Sundaresan, and C.N.R. Rao. **Rare earth niobium oxynitrides, $LnNbON_{2-\delta}$ (Ln = Y, La, Pr, Nd, Gd, Dy): Synthesis, structure and properties**. *Materials Research Bulletin*, **46**(11):2021–2024, 2011. 8

[30] W. Li, E. Ionescu, R. Riedel, and A. Gurlo. **Can we predict the formability of perovskite oxynitrides from tolerance and octahedral factors?** *Journal of Materials Chemistry A*, **1**(39):12239–12245, 2013. 8, 15

[31] Y.-I. Kim. *Syntheses, crystal structures, and dielectric property of oxynitride perovskites*. Ohio State University Dissertation, 2005. 8, 89

[32] K. Page, M. W. Stoltzfus, Y. I. Kim, T. Proffen, P. M. Woodward, A. K. Cheetham, and R. Seshadri. **Local atomic ordering in $BaTaO_2N$ studied by neutron pair distribution function analysis and density functional theory**. *Chemistry of Materials*, **19**(16):4037–4042, 2007. 10, 12, 38

[33] C.M. Fang, G.A. de Wijs, E. Orhan, G. de With, R.A. de Groot, H.T. Hintzen, and R. Marchand. **Local structure and electronic properties of $BaTaO_2N$ with perovskite-type structure**. *Journal of Physics and Chemistry of Solids*, **64**:281–286, 2003. 11

[34] M. Yang, J. Oro-Sole, J. A. Rodgers, A. B. Jorge, A. Fuertes, and J. P. Attfield. **Anion order in perovskite oxynitrides**. *Nature Chemistry*, **3**(1):47–52, 2011. 11, 12, 31, 38, 42, 117, 120

[35] E. Gunther, R. Hagenmayer, and M. Jansen. **Structural investigations on the oxidenitrides $SrTaO_2N$, $CaTaO_2N$ and $LaTaN_2O$ by neutron and X-ray powder diffraction**. *Zeitschrift fur Anorganische und Allgemeine Chemie.*, **626**:1519–25, 2000. 12, 29

[36] S. J. Clarke, K. A. Hardstone, C. W. Michie, and M. J. Rosseinsky. **High-temperature synthesis and structures of perovskite and n = 1 RuddlesdenPopper tantalum oxynitrides**. *Chemistry of Materials*, **14**(6):2664–2669, 2002. 12

[37] T. Motohashi, Y. Hamade, Y. Masubuchi, T. Takeda, K. Murai, A. Yoshiasa, and S. Kikkawa. **Structural phase transition in the perovskite-type tantalum oxynitrides, $Ca_{1x}Eu_xTa(O,N)_3$**. *Materials Research Bulletin*, **44**(9):1899 – 1905, 2009. 12

[38] F. Pors, R. Marchand, Y. Laurent, P. Bacher, and G. Roult. **Etude structurale des perovskites oxyazotees $BaTaO_2N$ et $BaNbO_2N$: Structural study of $BaTaO_2N$ and $BaNbO_2N$ oxynitrided perovskites**. *Materials Research Bulletin*, **23**(10):1447 – 1450, 1988. 12

[39] N. Diot, R. Marchand, J. Haines, J.M. Leger, P. Macaudiere, and S. Hull. **Crystal structure determination of the oxynitride Sr_2TaO_3N**. *Journal of Solid State Chemistry*, **146**(2):390–393, 1999. 12

[40] S.H. Porter, Z. Huang, and P.M. Woodward. **Study of anion order/disorder in RTaN$_2$O (R = La, Ce, Pr) perovskite nitride oxides**. *Crystal Growth & Design*, **14**(1):117–125, 2014. 12, 29, 98, 119

[41] W.-J. Chun, A. Ishikawa, H. Fujisawa, T. Takata, J. N. Kondo, M. Hara, M. Kawai, Y. Matsumoto, and K. Domen. **Conduction and valence band positions of Ta$_2$O$_5$, TaON, and Ta$_3$N$_5$ by UPS and electrochemical methods**. *The Journal of Physical Chemistry B*, **107**(8):1798–1803, 2003. 13, 44, 50

[42] Y.-I. Kim, P. M. Woodward, K. Z. Baba-Kishi, and C. W. Tai. **Characterization of the structural, optical, and dielectric properties of oxynitride perovskites AMO$_2$N (A = Ba, Sr, Ca; M = Ta, Nb)**. *Chemistry of Materials*, **16**(7):1267–1276, 2004. 13, 29, 90

[43] S. G. Ebbinghaus, R. Aguiar, A. Weidenkaff, S. Gsell, and A. Reller. **Topotactical growth of thick perovskite oxynitride layers by nitridation of single crystalline oxides**. *Solid State Sciences*, **10**(6):709–716, 2008. 13, 44

[44] G. Tobias, J. Oro-Sole, D. Beltran-Porter, and A. Fuertes. **New family of Ruddlesden-Popper strontium niobium oxynitrides: (SrO)(SrNbO$_{(2-x)}$N)$_{(n)}$ (n = 1, 2)**. *Inorganic Chemistry*, **40**(27):6867–9, 2001. 13

[45] Y.-I. Kim and P. M. Woodward. **Dielectric property of oxynitride perovskites containing Ta^{5+}**. *Ceramic Transactions 169. Synthesis Properties and Crystal Chemistry of Perovskite-Based Materials*, pages 179–186, 2005. 13

[46] R. Marchand, F. Pors, Y. Laurent, O. Regreny, J. Lostec, and J. M. Haussonne. **Perovskites oxynitrurees utilisees en tant que materiaux dielectriques**. *Journal de Physique Colloques*, **47**(C1):C1–901–C1–905, 1986. 13

[47] Y. Q. Li, A. C. A. Delsing, G. de With, and H. T. Hintzen. **Luminescence properties of Eu^{2+}–activated alkaline-earth silicon-oxynitride MSi$_2$O$_{2-\delta}$N$_{2+2/3\delta}$ (M = Ca, Sr, Ba): A promising class of novel LED conversion phosphors**. *Chemistry of Materials*, **17**(12):3242–3248, 2005. 13

[48] M. Jansen and H. P. Letschert. **Inorganic yellow-red pigments without toxic metals**. *Nature*, **404**(6781):980–982, 2000. 13

[49] H. Kato and A. Kudo. **Highly efficient decomposition of pure water into H$_2$ and O$_2$ over NaTaO$_3$ photocatalysts**. *Catalysis Letters*, **58**(2-3):153–155, 1999. 14

[50] A. Kudo and H. Kato. **Effect of lanthanide-doping into NaTaO$_3$ photocatalysts for efficient water splitting**. *Chemical Physics Letters*, **331**(5):373–377, 2000. 14

[51] K. Maeda and K. Domen. **New non-oxide photocatalysts designed for overall water splitting under visible light**. *The Journal of Physical Chemistry C*, **111**(22):7851–7861, 2007. 14

[52] K. Maeda, D. Lu, and K. Domen. **Solar-driven Z-scheme water splitting using modified BaZrO$_3$–BaTaO$_2$N solid solutions as photocatalysts**. *ACS Catalysis*, **3**(5):1026–1033, 2013. 14

[53] F. Zhang, A. Yamakata, K. Maeda, Y. Moriya, T. Takata, J. Kubota, K. Teshima, S. Oishi, and K. Domen. **Cobalt-modified porous single-crystalline LaTiO$_2$N for highly efficient water oxidation under visible light**. *Journal of the American Chemical Society*, **134**(20):8348–8351, 2012. 14, 44, 46, 50, 57, 59

[54] T. Minegishi, N. Nishimura, J. Kubota, and K. Domen. **Photoelectrochemical properties of LaTiO$_2$N electrodes prepared by particle transfer for sunlight-driven water splitting**. *Chemical Science*, **4**(3):1120–1124, 2013. 14

[55] S. J. Clarke, B. P. Guinot, C. W. Michie, M. J. C. Calmont, and M. J. Rosseinsky. **Oxynitride perovskites: synthesis and structures of LaZrO$_2$N, NdTiO$_2$N, and LaTiO$_2$N and comparison with oxide perovskites**. *Chemistry of Materials*, **14**(1):288–294, 2002. xv, 15, 29, 39, 44, 117, 119

[56] F. Tessier, L. Le Gendre, F. Chevir, R. Marchand, and A. Navrotsky. **Thermochemistry of a new class of materials containing dinitrogen pairs in an oxide matrix**. *Chemistry of Materials*, **17**(13):3570–3574, 2005. 15, 44

[57] M. Machida, S. Murakami, T. Kijima, S. Matsushima, and M. Arai. **Photocatalytic property and electronic structure of lanthanide tantalates, LnTaO$_4$ (Ln = La, Ce, Pr, Nd, and Sm)**. *The Journal of Physical Chemistry B*, **105**(16):3289–3294, 2001. 16, 50

[58] H. Wolff and R. Dronskowski. **First-principles and molecular-dynamics study of structure and bonding in perovskite-type oxynitrides ABO$_2$N (A = Ca, Sr, Ba; B = Ta, Nb)**. *Journal of Computational Chemistry*, **29**(13):2260–2267, 2008. 16

[59] A.B. Jorge, J. Or-Sol, A.M. Bea, N. Mufti, T.T. M. Palstra, J.A. Rodgers, J.P. Attfield, and A. Fuertes. **Large coupled magnetoresponses in EuNbO$_2$N**. *Journal of the American Chemical Society*, **130**(38):12572–12573, 2008. 16, 29

[60] J. Oro-Sole, L. Clark, N. Kumar, W. Bonin, A. Sundaresan, J.P. Attfield, C. N. R. Rao, and A. Fuertes. **Synthesis, anion order, and magnetic properties of RVO$_{3-x}$N$_x$ perovskites (R = La, Pr, Nd; 0 < x < 1)**. *Journal of Materials Chemistry C*, **2**:2212–2220, 2014. 16, 29

[61] M. Yang, J. Or-Sol, A. Kusmartseva, A. Fuertes, and J.P. Attfield. **Electronic tuning of two metals and colossal magnetoresistances in $EuWO_{1+x}N_{2x}$ perovskites**. *Journal of the American Chemical Society*, **132**(13):4822–4829, 2010. 16, 29

[62] M. Wencka, S. Vrtnik, M. Jagodič, Z. Jagličić, S. Turczynski, D. A. Pawlak, and J. Dolinšek. **Observation of anomalous magnetism in the low-temperature monoclinic phase of single-crystalline $PrAlO_3$ perovskite**. *Physical Review B*, **80**:224410, Dec 2009. 16, 28

[63] R. Glaum, E. Benser, and H. Hibst. **Novell ternary and polynary vanadium (IV) phosphates as catalysts for selective oxidations of light hydrocarbons**. *Chemie Ingenieur Technik*, **79**(6):843–850, 2007. 16

[64] D. Imamura, M. Miyayama, M. Hibino, and T. Kudo. **Mg intercalation properties into V_2O_5 gel/carbon composites under high-rate condition**. *Journal of the Electrochemical Society*, **150**(6):A753–A758, 2003. 16, 22

[65] G. Buxbaum. *Industrial Inorganic Pigments*. Wiley, 2008. 16

[66] N. Guskos, V. Likodimos, S. Glenis, G. Zolnierkiewicz, J. Typek, R. Szymczak, and A. Blonska-Tabero. **Magnetic frustration in the site ordered $Mg_3Fe_4(VO_4)_6$ vanadate**. *Journal of Applied Physics*, **101**(10):103922–103922, 2007. 17

[67] X. Wang, D.A. Vander Griend, C.L. Stern, and K.R. Poeppelmeier. **Site-specific vanadates $Co_4Fe_{3.33}(VO_4)_6$ and $Mn_3Fe_4(VO_4)_6$**. *Inorganic Chemistry*, **39**(1):136–140, 2000. 17, 19, 77

[68] S. Boudin, A. Grandin, A. Leclaire, M.M. Borel, and B. Raveau. **The Original Structure of $Zn_3V_4(PO_4)_6$ Involving Bioctahedral V_2O_{10} Units and ZnO_5 Trigonal Bipyramids**. *Journal of Solid State Chemistry*, **115**(1):140 – 145, 1995. 17, 65

[69] A.G. Nord. **Crystallographic studies of olivine-related sarcopside-type solid solutions**. *Zeitschrift fur Kristallographie-Crystalline Materials*, **166**(1-4):159–176, 1984. 19, 77

[70] M. Salvetat. **Matieres minerales colorantes vertes et violettes.** *Comptes Rendus des Seances de l'Academie des Sciences XLVIII*, page 295, 1859. 20

[71] J. Mallegol, J. Lemaire, and J. Gardette. **Yellowing of oil-based paints**. *Studies in Conservation*, pages 121–131, 2001. 21

[72] S. Budavari. *The Merck Index*. Chapman & Hall, 1996. 21

[73] N. Eastaugh. *The pigment compendium: a dictionary of historical pigments*, **1**. Routledge, 2004. 21

[74] A.K. Padhi, K.S. Nanjundaswamy, and J.B.D. Goodenough. **Phospho-olivines as positive-electrode materials for rechargeable lithium batteries**. *Journal of the Electrochemical Society*, **144**(4):1188–1194, 1997. 22

[75] E. Levi, Y. Gofer, and D. Aurbach. **On the way to rechargeable Mg batteries: the challenge of new cathode materials**. *Chemistry of Materials*, **22**(3):860–868, 2009. 22

[76] D. Aurbach, Z. Lu, A. Schechter, Y. Gofer, H. Gizbar, R. Turgeman, Y. Cohen, M. Moshkovich, and E.l. Levi. **Prototype systems for rechargeable magnesium batteries**. *Nature*, **407**(6805):724–727, 2000. 22

[77] J.K. Warner, A.K. Cheetham, A.G. Nord, R.B. Von Dreele, and M. Yethiraj. **Magnetic structure of iron(II) phosphate sarcopside $Fe_3(PO_4)_2$**. *Journal of Materials Chemistry*, **2**:191–196, 1992. 23, 62, 63

[78] J. Escobal, J.L. Pizarro, J.L. Mesa, J.M. Rojo, B. Bazan, M.I. Arriortua, and T. Rojo. **Neutron diffraction, specific heat and magnetic susceptibility of $Ni_3(PO_4)_2$**. *Journal of Solid State Chemistry*, **178**(9):2626 – 2634, 2005. 23, 62

[79] D. Dai, M.-H. Whangbo, H.-J. Koo, X. Rocquefelte, S. Jobic, and A. Villesuzanne. **Analysis of the spin exchange interactions and the ordered magnetic structures of lithium transition metal phosphates $LiMPO_4$ (M = Mn, Fe, Co, Ni) with the olivine structure**. *Inorganic Chemistry*, **44**(7):2407–2413, 2005. 24

[80] T. Yamauchi and Y. Ueda. **Isostructural transition metal ortho-phosphates with linear chain of S= 1/2, 1, and 3/2**. *Journal of Magnetism and Magnetic Materials*, **177**:705–706, 1998. 24, 62

[81] R. Glaum, M. Reehuis, N. Stusser, U. Kaiser, and F. Reinauer. **Neutron diffraction study of the nuclear and magnetic structure of the $CrVO_4$ type phosphates $TiPO_4$ and VPO_4**. *Journal of Solid State Chemistry*, **126**(1):15–21, 1996. 24, 62, 77

[82] M. Avdeev, C.D. Ling, T.T. Tan, S. Li, G. Oyama, A. Yamada, and P. Barpanda. **Magnetic structure and properties of the rechargeable battery insertion compound Na_2FePO_4F**. *Inorganic Chemistry*, **53**(2):682–684, 2013. 25

[83] S.H. Porter, Z. Huang, Z. Cheng, M. Avdeev, Z. Chen, S. Dou, and P.M. Woodward. **Structural and magnetic properties of RTiNO$_2$ (R = Ce, Pr, Nd) perovskite nitride oxides**. *Journal of Solid State Chemistry*, **226**:279 – 285, 2015. 28, 44, 49, 57

[84] L. Vasylechko, A. Senyshyn, D. Trots, R. Niewa, W. Schnelle, and M. Knapp. **CeAlO$_3$ and Ce$_{1x}R_x$AlO$_3$ (R = La, Nd) solid solutions: Crystal structure, thermal expansion and phase transitions**. *Journal of Solid State Chemistry*, **180**(4):1277 – 1290, 2007. 28

[85] T. Shishido, M. Tanaka, H. Horiuchi, H. Iwasaki, N. Toyota, D. Shindo, and T. Fukuda. **Growth of rare earth aluminate crystals from molten solutions**. *Journal of Alloys and Compounds*, **192**(12):84 – 86, 1993. 28

[86] S.M. Moussa, B.J. Kennedy, B.A. Hunter, C.J. Howard, and T. Vogt. **Low temperature structural studies on PrAlO$_3$**. *Journal of Physics Condensed Matter*, **13**(9):L203–L209, 2001. 28

[87] A. Senyshyn, D.M. Trots, J.M. Engel, L. Vasylechko, H. Ehrenberg, T. Hansen, M. Berkowski, and H. Fuess. **Anomalous thermal expansion in rare-earth gallium perovskites: a comprehensive powder diffraction study**. *Journal of Physics: Condensed Matter*, **21**(14):145405, 2009. 28

[88] P. Novk, K. Knek, M. Maryko, Z. Jirk, and J. Kune. **Crystal field and magnetism of Pr^{3+} and Nd^{3+} ions in orthorhombic perovskites**. *Journal of Physics: Condensed Matter*, **25**(44):446001, 2013. 28

[89] D. Logvinovich, J. Hejtmnek, K. Kniek, M. Maryko, N. Homazava, P. Tome, R. Aguiar, S. G. Ebbinghaus, A. Reller, and A. Weidenkaff. **On the magnetism, thermal- and electrical transport of SrMoO$_2$N**. *Journal of Applied Physics*, **105**(2), 2009. 29

[90] M. Retuerto, C. de la Calle, M.J. Martnez-Lope, F. Porcher, K. Krezhov, N. Menndez, and J.A. Alonso. **Double perovskite Sr$_2$FeMoO$_{6x}$N$_x$ (x=0.3, 1.0) oxynitrides with anionic ordering**. *Journal of Solid State Chemistry*, **185**:18 – 24, 2012. 29

[91] S. G. Ebbinghaus, A. Weidenkaff, A. Rachel, and A. Reller. **Powder neutron diffraction of SrNbO$_2$N at room temperature and 1.5K**. *Acta Crystallographica Section C*, **60**(9):i91–i93, 200. 29

[92] S. Balaz, S.H. Porter, P.M. Woodward, and L.J. Brillson. **Electronic structure of tantalum oxynitride perovskite photocatalysts**. *Chemistry of Materials*, **25**(16):3337–3343, 2013. 29

[93] B. H. Toby. *EXPGUI, a graphical user interface for GSAS. Journal of Applied Crystallography*, **34**(2):210–213, 2001. 30, 44, 64

[94] S.B. Ubizskii, L.O. Vasylechko, D.I. Savytskii, A.O. Matkovskii, and I.M. Syvorotka. **The crystal structure and twinning of neodymium gallium perovskite single crystals**. *Superconductor Science and Technology*, **7**(10):766, 1994. 35

[95] W.L. Wang and H.Y. Lu. **Twinning induced by the rhombohedral to orthorhombic phase transition in lanthanum gallate (LaGaO$_3$)**. *Physics and Chemistry of Minerals*, **33**(7):435–444, 2006. 35

[96] D.J. Smith, M.R. McCartney, and L.A. Bursill. **The electron-beam-induced reduction of transition metal oxide surfaces to metallic lower oxides**. *Ultramicroscopy*, **23**(34):299 – 303, 1987. 38

[97] KH Jürgen Buschow and Frank R de Boer. *Physics of Magnetism and Magnetic Materials*. Springer, 2003. 38

[98] F. Bartolom, J. Bartolom, and J. Blasco. **Magnetic order of Nd^{3+} in NdAlO$_3$**. *Journal of Magnetism and Magnetic Materials*, **157158**(0):491 – 492, 1996. 39

[99] S. Sasaki, C. T. Prewitt, J. D. Bass, and W. A. Schulze. **Orthorhombic perovskite CaTiO$_3$ and CdTiO$_3$: structure and space group**. *Acta Crystallographica Section C*, **43**(9):1668–1674, Sep 1987. 39

[100] RD t Shannon and C Tfc Prewitt. **Effective ionic radii in oxides and fluorides**. *Acta Crystallographica Section B: Structural Crystallography and Crystal Chemistry*, **25**(5):925–946, 1969. 39

[101] M. Stan, T.J. Armstrong, D.P. Butt, T.C. Wallace, Y.S. Park, C.L. Haertling, T. Hartmann, and R.J. Jr. Hanrahan. **Stability of the perovskite compounds in the Ce-Ga-O and Pu-Ga-O systems**. *Journal of the American Ceramic Society*, **85**(11):2811–2816, 2002. xv, 39

[102] W. Marti, P. Fischer, F. Altorfer, H.J. Scheel, and M. Tadin. **Crystal structures and phase transitions of orthorhombic and rhombohedral RGaO$_3$ (R = La, Pr, Nd) investigated by neutron powder diffraction**. *Journal of Physics: Condensed Matter*, **6**(1):127, 1994. xv, 39

[103] L. Vasylechko, L. Akselrud, W. Morgenroth, U. Bismayer, A. Matkovskii, and D. Savytskii. **The crystal structure of NdGaO$_3$ at 100 K and 293 K based on synchrotron data**. *Journal of Alloys and Compounds*, **297**(12):46 – 52, 2000. xv, 39, 42

[104] B.J. Kennedy, T. Vogt, C.D. Martin, J.B. Parise, and J.A. Hriljac. **Pressure-induced phase transition in $PrAlO_3$**. *Chemistry of Materials*, **14**(6):2644–2648, 2002. xv, 39

[105] C. J. Howard, B. J. Kennedy, and B. C. Chakoumakos. **Neutron powder diffraction study of rhombohedral rare-earth aluminates and the rhombohedral to cubic phase transition**. *Journal of Physics: Condensed Matter*, **12**(4):349, 2000. xv, 39

[106] S. Turczynski, K. Orlinski, D.A. Pawlak, R. Diduszko, J. Mucha, M. Pekala, J. Fagnard, P.H. Vanderbemden, and M.A. Carpenter. **Czochralski crystal growth, thermal conductivity, and magnetic properties of Pr_x $La_{1-x}AlO_3$, where x = 1, 0.75, 0.55, 0.40, 0**. *Crystal Growth and Design*, **11**(4):1091–1097, 2011. xv, 41

[107] A. Podlesnyak, S. Rosenkranz, F. Fauth, W. Marti, A. Furrer, A. Mirmelstein, and H.J. Scheel. **Crystal-field and magnetic properties of the distorted perovskite $NdGaO_3$**. *Journal of Physics: Condensed Matter*, **5**(48):8973, 1993. xv, 41

[108] E. Antic-Fidancev, M. Lemaitre-Blaise, L. Beaury, G. Teste de Sagey, and P. Caro. **Interpretation of the optical absorption spectrum and of the paramagnetic susceptibility of $NdAlO_3$**. *The Journal of Chemical Physics*, **73**(9):4613–4618, 1980. xv, 41

[109] H. Xing, G. Long, H. Guo, Y. Zou, C. Feng, G. Cao, H. Zeng, and Z.-A. Xu. **Anisotropic paramagnetism of monoclinic $Nd_2Ti_2O_7$ single crystals**. *Journal of Physics: Condensed Matter*, **23**(21):216005, 2011. 42

[110] S.T. Aruna, N.S. Kini, S. Shetty, and K.S. Rajam. **Synthesis of nanocrystalline $CeAlO_3$ by solution-combustion route**. *Materials Chemistry and Physics*, **119**(3):485 – 489, 2010. 42

[111] S.H. Porter, Z. Huang, S. Dou, S. Brown-Xu, A.T.M. Golam Sarwar, R.C. Myers, and P.M. Woodward. **Electronic structure and photocatalytic water oxidation activity of RTiNO$_2$ (R = Ce, Pr, and Nd) perovskite nitride oxides**. *Chemistry of Materials*, **27**(7):2414–2420, 2015. 43

[112] A. Kudo, K. Ueda, H. Kato, and I. Mikami. **Photocatalytic O_2 evolution under visible light irradiation on $BiVO_4$ in aqueous $AgNO_3$ solution**. *Catalysis Letters*, **53**(3-4):229–230, 1998. 44

[113] A. Kudo, K. Omori, and H. Kato. **A Novel Aqueous Process for Preparation of Crystal Form-Controlled and Highly Crystalline $BiVO_4$ Powder from Layered Vanadates at Room Temperature and Its Photocatalytic and Photophysical Properties**. *Journal of the American Chemical Society*, **121**(49):11459–11467, 1999. 44

[114] S. Tokunaga, H. Kato, and A. Kudo. **Selective Preparation of Monoclinic and Tetragonal $BiVO_4$ with Scheelite Structure and Their Photocatalytic Properties**. *Chemistry of Materials*, **13**(12):4624–4628, 2001. 44

[115] J. Yu and A. Kudo. **Effects of structural variation on the photocatalytic performance of hydrothermally synthesized $BiVO_4$**. *Advanced Functional Materials*, **16**(16):2163–2169, 2006. 44

[116] M. Grätzel. *Energy resources through photochemistry and catalysis*. Academic Press, 1983. 44

[117] N. Serpone and E. Pelizzetti. *Photocatalysis: fundamentals and applications*. A Wiley Interscience publication. Wiley, 1989. 44

[118] A. A. Krasnovskii and G. P. Brin. **Inorganic models of Hill's reaction**. *Doklady Akademii Nauk SSSR*, **147**:656, 1962. 44

[119] J.R. Darwent and A. Mills. **Photo-oxidation of water sensitized by WO_3 powder**. *Journal of the Chemical Society, Faraday Transactions 2*, **78**:359–367, 1982. 44

[120] G. Hitoki. **(Oxy)nitrides as new photocatalysts for water splitting under visible light irradiation**. *Electrochemistry (Tokyo, Japan)*, **70**(6):463, 2002. 44

[121] M. Hara, J. Nunoshige, T. Takata, J.N. Kondo, and K. Domen. **Unusual enhancement of H_2 evolution by Ru on TaON photocatalyst under visible light irradiation**. *Chem. Commun.*, pages 3000–3001, 2003. 44

[122] T. Hisatomi, C. Katayama, Y. Moriya, T. Minegishi, M. Katayama, H. Nishiyama, T. Yamada, and K. Domen. **Photocatalytic oxygen evolution using $BaNbO_2N$ modified with cobalt oxide under photoexcitation up to 740 nm**. *Energy & Environmental Science*, **6**:3595–3599, 2013. 44, 57, 91

[123] J. Wang, G. Burdzinski, J. Kubicki, and M.S. Platz. **Ultrafast UVvis and IR studies of p-biphenylyl acetyl and carbomethoxy garbenes**. *Journal of the American Chemical Society*, **130**(33):11195–11209, 2008. 45

[124] M.J. Llansola-Portoles, J.J. Bergkamp, D. Finkelstein-Shapiro, B.D. Sherman, G. Kodis, N.M. Dimitrijevic, D. Gust, T.A. Moore, and A.L. Moore. **Controlling Surface Defects and Photophysics in TiO_2 Nanoparticles**. *The Journal of Physical Chemistry A*, **118**(45):10631–10638, 2014. 53

[125] C. Le Paven-Thivet, A. Ishikawa, A. Ziani, L. Le Gendre, M. Yoshida, J. Kubota, F. Tessier, and K. Domen. **Photoelectrochemical properties of crystalline perovskite lanthanum titanium oxynitride films under visible light**. *The Journal of Physical Chemistry C*, **113**(15):6156–6162, 2009. 53

[126] I. P. Shapiro. **Determination of the forbidden-zone width from diffuse-reflection spectra**. *Optika i Spektroskopiya*, **4**:256–60, 1958. 55

[127] A. Kasahara, K. Nukumizu, T. Takata, J.N. Kondo, M. Hara, H. Kobayashi, and K. Domen. **$LaTiO_2N$ as a visible-light (600 nm)-driven photocatalyst**. *The Journal of Physical Chemistry B*, **107**(3):791–797, 2003. 55

[128] M.R. Dolgos, A.M. Paraskos, M.W. Stoltzfus, S.C. Yarnell, and P.M. Woodward. **The electronic structures of vanadate salts: Cation substitution as a tool for band gap manipulation**. *Journal of Solid State Chemistry*, **182**(7):1964 – 1971, 2009. 55

[129] H.A. Seibel II, P. Karen, T.R. Wagner, and P.M. Woodward. **Synthesis and characterization of color variants of nitrogen- and fluorine-substituted TiO_2**. *Journal of Materials Chemistry*, **19**:471–477, 2009. 57

[130] T. Hisatomi, K. Miyazaki, K. Takanabe, K. Maeda, J. Kubota, Y. Sakata, and K. Domen. **Isotopic and kinetic assessment of photocatalytic water splitting on Zn-added Ga_2O_3 photocatalyst loaded with $Rh_{2y}Cr_yO_3$ cocatalyst**. *Chemical Physics Letters*, **486**(46):144 – 146, 2010. 57

[131] C. Ruan, M. Paulose, O.K. Varghese, and C.A. Grimes. **Enhanced photoelectrochemical-response in highly ordered TiO_2 nanotube-arrays anodized in boric acid containing electrolyte**. *Solar Energy Materials and Solar Cells*, **90**(9):1283 – 1295, 2006. 59

[132] F.F. Abdi, L. Han, A.H.M. Smets, M. Zeman, B. Dam, and R. van de Krol. **Efficient solar water splitting by enhanced charge separation in a bismuth vanadate-silicon tandem photoelectrode**. *Nature communications*, **4**, 2013. 59

[133] C. W. Thiel, H. Cruguel, H. Wu, Y. Sun, G. J. Lapeyre, R. L. Cone, R. W. Equall, and R. M. Macfarlane. **Systematics of 4f electron energies relative to host bands by resonant photoemission of rare-earth ions in aluminum garnets**. *Physical Review B*, **64**:085107, Aug 2001. 60

[134] J. Wang, B.H. Toby, P.L. Lee, L. Ribaud, S.M. Antao, C. Kurtz, M. Ramanathan, R.B. Von Dreele, and M.A. Beno. **A dedicated powder diffraction beamline at the Advanced Photon Source: Commissioning and early operational results**. *Review of Scientific Instruments*, **79**(8), 2008. 64

[135] Gustav Kortüm and James E Lohr. *Reflectance spectroscopy: Principles, methods, applications*. Springer New York, 1969. 64

[136] Y. Saad, M. Hidouri, I. lvarez Serrano, M.L. Veiga, A. Wattiaux, and M.B. Amara. **Crystal structure and Mssbauer spectroscopy of a new iron phosphate $Mg_{2.88}Fe_{4.12}(PO_4)_6$**. *Journal of Alloys and Compounds*, **584**(0):625 – 630, 2014. 78

[137] V. Sinha and B.K. Karmakar. *Proceedings of the International Symposium and Exposition on Automotive Electronics and Alternate Energy Vehicles, November 19-21,1999*. Allied Publishers Limited, 1999. 81

[138] S.M. Gorelick. *Oil Panic and the Global Crisis: Predictions and Myths*. Wiley, 2011. 81

[139] C. Rosenzweig, D. Karoly, M. Vicarelli, P. Neofotis, Q. Wu, A. Casassa, G.and Menzel, T.L. Root, N. Estrella, and B. Seguin. **Attributing physical and biological impacts to anthropogenic climate change**. *Nature*, **453**(7193):353–357, 2008. 81

[140] A. Fujishima and K. Honda. **Electrochemical photolysis of water at a semiconductor electrode.** *nature*, (238):37–8, 1972. 83, 90

[141] X. Chen, S. Shen, L. Guo, and S.S. Mao. **Semiconductor-based photocatalytic hydrogen generation**. *Chemical Reviews*, **110**(11):6503–6570, 2010. 83

[142] **The absolute electrode potential: an explanatory note (Recommendations 1986)**. *Journal of Electroanalytical Chemistry and Interfacial Electrochemistry*, **209**(2):417 – 428, 1986. 83

[143] H. Kato, K. Asakura, and A. Kudo. **Highly efficient water splitting into H_2 and O_2 over lanthanum-doped $NaTaO_3$ photocatalysts with high crystallinity and surface nanostructure**. *Journal of the American Chemical Society*, **125**(10):3082–3089, 2003. 84, 87

[144] K. Mazloomi, N.B. Sulaiman, and H. Moayedi. **Electrical efficiency of electrolytic hydrogen production.** *International Journal of Electrochemical Science*, **7**(4), 2012. 84

[145] J. Yang, D. Wang, H. Han, and C. Li. **Roles of cocatalysts in photocatalysis and photoelectrocatalysis**. *Accounts of chemical research*, **46**(8):1900–1909, 2013. 84

[146] J.P. Brunelle. **Preparation of catalysts by metallic complex adsorption on mineral oxides**. *Pure and Applied Chemistry*, **50**(9-10):1211–1229, 1978. 84

[147] K.P. de Jong. *Synthesis of Solid Catalysts*. Wiley, 2009. 84

[148] Y. Sasaki, A. Iwase, H. Kato, and A. Kudo. **The effect of co-catalyst for Z-scheme photocatalysis systems with an Fe^{3+}/Fe^{2+} electron mediator on overall water splitting under visible light irradiation**. *Journal of Catalysis*, **259**(1):133–137, 2008. 86, 87

[149] M. Liu, W. You, Z. Lei, G. Zhou, J. Yang, G. Wu, G. Ma, G. Luan, T. Takata, and M. Hara. **Water reduction and oxidation on Pt–Ru/$Y_2Ta_2O_5N_2$ catalyst under visible light irradiation**. *Chemical Communications*, (19):2192–2193, 2004. 87

[150] B. Ma, F. Wen, H. Jiang, J. Yang, P. Ying, and C. Li. **The synergistic effects of two co-catalysts on Zn_2GeO_4 on photocatalytic water splitting**. *Catalysis Letters*, **134**(1-2):78–86, 2010. 87

[151] M. Long, W. Cai, J. Cai, B. Zhou, X. Chai, and Y. Wu. **Efficient photocatalytic degradation of phenol over $Co_3O_4/BiVO_4$ composite under visible light irradiation**. *The Journal of Physical Chemistry B*, **110**(41):20211–20216, 2006. 87

[152] W. Shangguan. **Hydrogen evolution from water splitting on nanocomposite photocatalysts**. *Science and Technology of Advanced Materials*, **8**(1):76–81, 2007. 87

[153] K. Maeda, K. Teramura, H. Masuda, T. Takata, N. Saito, Y. Inoue, and K. Domen. **Efficient overall water splitting under visible-light irradiation on $(Ga_{1-x}Zn_x)(N_{1-x}O_x)$ dispersed with Rh-Cr mixed-oxide nanoparticles: effect of reaction conditions on photocatalytic activity**. *The Journal of Physical Chemistry B*, **110**(26):13107–13112, 2006. 87

[154] R. Li, H. Han, F. Zhang, D. Wang, and C. Li. **Highly efficient photocatalysts constructed by rational assembly of dual-cocatalysts separately on different facets of $BiVO_4$**. *Energy & Environmental Science*, **7**(4):1369–1376, 2014. 87

[155] G. Wu, T. Chen, W. Su, G. Zhou, X. Zong, Z. Lei, and C. Li. **H_2 production with ultra-low CO selectivity via photocatalytic reforming of methanol on Au/TiO_2 catalyst**. *International Journal of Hydrogen Energy*, **33**(4):1243–1251, 2008. 87

[156] R. Abe, K. Sayama, and H. Sugihara. **Development of new photocatalytic water splitting into H_2 and O_2 using two different semiconductor photocatalysts and a shuttle redox mediator IO_3^-/I^-**. *The Journal of Physical Chemistry B*, **109**(33):16052–16061, 2005. 88

[157] C. Lo, C. Huang, C. Liao, and J.C.S. Wu. **Novel twin reactor for separate evolution of hydrogen and oxygen in photocatalytic water splitting**. *international Journal of Hydrogen Energy*, **35**(4):1523–1529, 2010. 88

[158] Frédéric Sauvage. **A review on current status of stability and knowledge on liquid electrolyte-based dye-sensitized solar cells**. *Advances in Chemistry*, **2014**, 2014. 89

[159] W. Zhao, K. Maeda, F. Zhang, T. Hisatomi, and K. Domen. **Effect of post-treatments on the photocatalytic activity of $Sm_2Ti_2S_2O_5$ for the hydrogen evolution reaction**. *Physical Chemistry Chemical Physics*, **16**(24):12051–12056, 2014. 89

[160] Y. Xu and M. A.A. Schoonen. **The absolute energy positions of conduction and valence bands of selected semiconducting minerals**. *American Mineralogist*, **85**(3-4):543–556, 2000. 89

[161] B.D. Pelatt, R. Ravichandran, J.F. Wager, and D.A. Keszler. **Atomic solid state energy scale**. *Journal of the American Chemical Society*, **133**(42):16852–16860, 2011. 89

[162] H.W. Eng, P.W. Barnes, B.M. Auer, and P.M. Woodward. **Investigations of the electronic structure of d^0 transition metal oxides belonging to the perovskite family**. *Journal of Solid State Chemistry France*, **175**:94–109, 2003. 90

[163] M.A. Alpuche-Aviles and Y. Wu. **Photoelectrochemical study of the band structure of Zn_2SnO_4 prepared by the hydrothermal method**. *Journal of the American Chemical Society*, **131**(9):3216–3224, 2009. 90

[164] O. Khaselev and J.A. Turner. **A monolithic photovoltaic-photoelectrochemical device for hydrogen production via water splitting**. *Science*, **280**(5362):425–427, 1998. 91

[165] D.J. Milliron, S.M. Hughes, Y. Cui, L. Manna, J. Li, L. Wang, and A.P. Alivisatos. **Colloidal nanocrystal heterostructures with linear and branched topology**. *Nature*, **430**(6996):190–195, 2004. 91

[166] D.C. Harris. *Quantitative Chemical Analysis*. W. H. Freeman, 2010. 92

[167] Y. Kim, S. Cook, S.M. Tuladhar, S.A. Choulis, J. Nelson, J.R. Durrant, D.D.C. Bradley, M. Giles, I. McCulloch, and C. Ha. **A strong regioregularity effect in self-organizing conjugated polymer films and high-efficiency polythiophene: fullerene solar cells**. *Nature Materials*, **5**(3):197–203, 2006. 92

[168] A. Kudo and Y. Miseki. **Heterogeneous photocatalyst materials for water splitting**. *Chemical Society Reviews*, **38**:253–278, 2009. 94

[169] B.S. Baigrie. *Electricity and Magnetism: A Historical Perspective*. Greenwood guides to great ideas in science. Greenwood Press, 2007. 94

[170] K.H.J. Buschow. *Encyclopedia of Materials: Science and Technology*. Number v. 8 in Encyclopedia of Materials: Science and Technology. Elsevier, 2001. 102

[171] A. Guinier, R. Jullien, and International Union of Crystallography. *The solid state: from superconductors to superalloys*. International Union of Crystallography texts on crystallography. International Union of Crystallography, 1989. 102

[172] J. Clarke and A.I. Braginski. *The SQUID Handbook: Applications of SQUIDs and SQUID Systems*. Number v. 2. Wiley, 2006. 105

[173] B.D. Cullity and S.R. Stock. *Elements of X-ray Diffraction*. Pearson education. Prentice Hall, 2001. 107

[174] G. Hölzer, M. Fritsch, M. Deutsch, J. Härtwig, and E. Förster. **K α 1, 2 and K β 1, 3 x-ray emission lines of the 3 d transition metals**. *Physical Review A*, **56**(6):4554, 1997. 107

[175] T.A. Ezquerra, A. Nogales, and M. Gomez. *Applications of Synchrotron Light to Scattering and Diffraction in Materials and Life Sciences*. Lecture Notes in Physics. Springer, 2009. 107

[176] G.E. Bacon. *Neutron Diffraction*. Monographs on the physics and chemistry of materials. Clarendon Press, 1975. 107

[177] P.M.B. Piccoli, T.F. Koetzle, and A.J. Schultz. **Single crystal neutron diffraction for the inorganic chemist - A practical guide**. *Comments on Inorganic Chemistry*, **28**(1-2):3–38, 2007. 108

[178] D.B. Williams and C.B. Carter. *Transmission electron microscopy: Imaging. 3*. Number v. 3. Plenum Press, 1996. 108

[179] J.I. Goldstein, D.E. Newbury, P. Echlin, D.C. Joy, C. Fiori, and E. Lifshin. *Scanning electron microscopy and X-ray microanalysis. A text for biologists, materials scientists, and geologists*. Plenum Publishing Corporation, 1981. 110

[180] P. Hanrahan and W. Krueger. **Reflection from layered surfaces due to subsurface scattering**. *Proceedings of the 20th annual conference on Computer graphics and interactive techniques*, pages 165–174, 1993. 110

[181] B.M. Weckhuysen and R.A. Schoonheydt. **Recent progress in diffuse reflectance spectroscopy of supported metal oxide catalysts**. *Catalysis Today*, **49**(4):441 – 451, 1999. 111

[182] J.F. Watts. **X-ray photoelectron spectroscopy**. *Vacuum*, **45**(6):653–671, 1994. 112

[183] T. Elsaesser and M. Woerner. **Femtosecond infrared spectroscopy of semiconductors and semiconductor nanostructures**. *Physics Reports*, **321**(6):253–305, 1999. 114

[184] S. Lowell and J.E. Shields. *Powder Surface Area and Porosity*. Chapman & Hall Series in Accounting and Finance. Springer, 1991. 115

Declaration

I herewith declare that I have produced this paper without the prohibited assistance of third parties and without making use of aids other than those specified; notions taken over directly or indirectly from other sources have been identified as such. This paper has not previously been presented in identical or similar form to any other Australian or foreign examination board.

The thesis work was conducted from March 2012 to May 2015 under the supervision of PI, Dr. Zhenguo Huang, at University of Wollongong.

Wollongong, NSW, Australia